



The University of  
**Nottingham**

UNITED KINGDOM • CHINA • MALAYSIA

# **Characterisation of Diesel Injector Deposits Using Advanced Analytical Techniques**

Thesis submitted to the University of Nottingham for the Degree of  
Doctorate of Engineering

**Sarah Jane Angel-Smith MSci**

**September 2017**

Efficient Fossil Energy Technologies Research Group

School of Chemical and Environmental Engineering

University of Nottingham

NG7 2RD

## **Abstract**

Internal diesel injector deposits (IDIDs) have become a prolific issue in the last decade, increased number of incidences have occurred since the introduction of ultra-low sulfur diesel and biodiesel. The IDIDs have caused concerns for customers such as injector systems misfiring or blocking, increased emissions and fuel consumption. Interest into the origins of the deposits has steadily grown, with identified possible causes including contaminants, degraded additives, or thermal and pressure stresses of the engine.

Most examples in previous studies only provide surface analysis of IDIDs, however, the surface only provides a relatively small part of the story. In order to understand how an IDID has formed the history needs to be explained, to do this the lower layers of the IDID need to be analysed.

Outcomes of this research include the first example of focused ion beam and secondary ion mass spectrometry being used in combination to analyse IDIDs and clearly shows different chemical layers, demonstrating that these deposits are made up of multiple complex chemistries. Raman spectroscopy can provide graphitic content information for IDIDs giving evidence of formation however, a method to remove fluorescence from carbonaceous structures was first devised and validated in order to allow this to be performed. The jet fuel thermal oxidation test (JFTOT) has been proven to be an effective method of replicating deposits on comparison with IDIDs from failed field engines, and key chemistries have been identified for B20 biodiesel and ultra-low sulfur diesel (ULSD). This work has used existing analytical methods to understand IDIDs and found novel insights that have not been previously observed in the literature.

## Publications

- Barker J., Reid J., Piggott M., Fay M., Davies A., Parmenter C., Weston N., Snape C., Scurr D. J., Angel-Smith S. “The Characterisation of Diesel Internal Injector Deposits by Focused Ion-Beam Scanning Electron Microscopy (FIB-SEM), Transmission Electron Microscopy (TEM), Atomic Force Microscopy (AFM) and Raman Spectroscopy” SAE Technical paper 2015-01-1826.
- Barker J., Reid J., Angel-Smith S., Snape C., Scurr D. J., Piggott M., Fay M., Davies A., Parmenter C., Weston N. (2017) Internal Diesel Injector Deposits (IDIDs) 11th International Colloquium Fuels Conventional and Future Energy for Automotive 2017 TAE Esslingen.
- Barker J., Reid J., Angel-Smith S., Snape C., Scurr D. J., Langley G., Patel K., Carter A., Laphorn C., Frank Pullen F. ‘The Application of New Approach to the Analysis of Deposits from the Jet Fuel Thermal Oxidation Tester (JFTOT)’. SAE Technical paper 2017-01-2293.

## Pending Publications

- Barker J., Reid J., Angel-Smith S., Snape C., Scurr D. J., Kersting R.  
Diesel Injector Needles: A Current and Historical Perspective (2017)  
SAE International Journal
- Angel-Smith S., Meredith W., Davies A., Barker J., Reid J., Scurr D. J.,  
Snape C. (2017) Removing Species Responsible Fluorescence  
Interference in Raman Spectroscopy for Carbonaceous Materials Using  
Hydropyrolysis
- Angel-Smith S., Barker J., Reid J., Snape C., Scurr D. J., (2017) Novel  
Insights into the 3D Chemical Structure of Diesel Injector Deposits  
Using Focused Ion Beam Secondary Ion Mass Spectrometry (FIB-  
SIMS)

## Conference Proceedings

- Energy Engineering Showcase, May 2015, poster presentation.  
‘Characterisation of Diesel Deposits Using Advanced Analytical Methods’. University of Nottingham. Awarded written commendation for poster.
- UKSAF Summer Meeting 2015, University of Chester, 1<sup>st</sup> July 2015, presented poster ‘Characterisation of Diesel deposits Using Advanced Analytical Methods’.
- EFET Summer School 2015, Harbin Institute for Technology, China. Awarded 2<sup>nd</sup> place for group presentation and 3<sup>rd</sup> place for oral presentation.
- MEC Conference, Loughborough University, 17<sup>th</sup> December 2015, Present poster ‘Characterisation of Diesel Deposits Using Advanced Analytical Techniques’.
- UKSAF Summer Meeting 2016, University College Dublin, 8<sup>th</sup> July 2016, presented poster ‘Analysis of Diesel Engine Deposits Using Advanced Characterisation Techniques’.
- UKSAF Summer Meeting 2017, Teignmouth, 5<sup>th</sup> July 2017, presented poster ‘Novel Insights into the 3D Chemical Structure of Diesel Injector Deposits Using Focused Ion Beam Secondary Ion Mass Spectrometry (FIB-SIMS)’. Awarded the Castle Award for the best young surface analyst poster presentation.

## **Acknowledgements**

I firstly wish to express my appreciation to Innospec for the financial support and opportunity given to me throughout undertaking this EngD. I would like to thank in particular Dr. Jim Barker and Ms. Jacqueline Reid for their support and encouragement over the last four years.

My sincere gratitude goes to my academic supervisors Professor Colin Snape and Dr. David J. Scurr. They have been incredibly patient and given thoughtful supervision throughout this process of researching and writing this thesis.

I also wish to thank Dr. Will Meredith, Dr. Chris Parmenter, Dr. Andrew Davies and Ms. Nicola Weston for training and guidance with their respective expertise. Without your patience I would not have achieved half as much as I had set out to do.

I would also like to thank my colleagues at the University of Nottingham. I really appreciate your encouragement and friendship the last four years.

Lastly, I would like to thank my parents, Beverley and Roy, for their unconditional love and support.

# Table of Contents

<b>Abstract .....</b>	<b>2</b>
<b>Publications .....</b>	<b>3</b>
<b>Pending Publications .....</b>	<b>4</b>
<b>Conference Proceedings .....</b>	<b>5</b>
<b>Acknowledgements .....</b>	<b>6</b>
<b>Table of Figures .....</b>	<b>15</b>
<b>Table of Tables.....</b>	<b>22</b>
<b>Abbreviations .....</b>	<b>24</b>
<b>1 Introduction.....</b>	<b>25</b>
<b>1.1 Context of Current Work.....</b>	<b>25</b>
<b>1.2 Diesel Fuel .....</b>	<b>26</b>
<b>1.3 History of the Diesel Engine .....</b>	<b>27</b>
<b>1.4 Emission Standards and the Future of Diesel.....</b>	<b>27</b>
<b>1.5 The History of and Types of Fuel Additives.....</b>	<b>30</b>
<b>1.6 Types of Diesel Deposits and Issues.....</b>	<b>34</b>
<b>1.7 Research into Causes of IDIDs .....</b>	<b>35</b>
1.7.1 Ultra-low Sulfur Diesel (ULSD).....	35
1.7.2 Biodiesel.....	36
1.7.3 Oxidation of Fuel .....	37
1.7.4 Polyisobutylene Succinimide (PIBSI).....	38
1.7.5 Injector Design.....	39
<b>1.8 Analysis of IDIDs .....</b>	<b>39</b>
1.8.1 Time of Flight Secondary Ion Mass Spectrometry (ToF-SIMS) .....	40
1.8.2 Dynamic Secondary Ion Mass Spectrometry (DSIMS).....	44
1.8.3 Fourier Transform Infrared (FTIR).....	45
1.8.4 X-ray Diffraction (XRD).....	46

1.8.5	Gas Chromatography Mass Spectrometry (GC-MS).....	46
1.8.6	X-ray Photoelectron Spectroscopy (XPS).....	47
1.8.7	Scanning Electron Microscopy (SEM) .....	48
1.8.8	Transmission Electron Microscopy (TEM).....	49
1.8.9	Hydropyrolysis (HyPy).....	49
1.8.10	Thermogravimetric Analysis (TGA) .....	50
1.8.11	Temperature Programmed Oxidation (TPO).....	51
1.8.12	Jet Fuel Thermal Oxidation Test (JFTOT).....	52
<b>1.9</b>	<b>Project Aim and Objectives.....</b>	<b>53</b>
<b>1.10</b>	<b>Explanation of Thesis Style .....</b>	<b>54</b>
<b>2</b>	<b>Experimental Methodology .....</b>	<b>55</b>
<b>2.1</b>	<b>Methodology.....</b>	<b>55</b>
2.1.1	Samples .....	55
2.1.2	Photographs of Samples .....	59
2.1.2.1	Injector Needle .....	59
2.1.2.2	Injector Tip .....	59
2.1.2.3	Push Rod .....	60
2.1.2.4	JFTOT Tube .....	60
<b>2.2</b>	<b>Analytical Techniques .....</b>	<b>60</b>
2.2.1	Time of Flight Secondary Ion Mass Spectrometry (ToF-SIMS) .....	60
2.2.1.1	Sample Preparation for Time of Flight Secondary Mass Spectrometry ....	61
2.2.1.2	Primary Ion Source.....	62
2.2.1.3	TOF Analyser.....	63
2.2.1.4	Sputtering and Depth Profiling .....	64
2.2.1.5	Data Acquisition and Analysis .....	64
2.2.1.6	Experimental of Time of Flight Secondary Ion Mass Spectrometry (ToF-SIMS) .....	64
2.2.1.7	Principle Component Analysis (PCA) .....	65
2.2.1.8	Experimental of Principle Component Analysis .....	65

2.2.2	Raman Spectroscopy .....	66
2.2.2.1	Principles of Raman Spectrometry .....	66
2.2.2.2	Bond Identification and $I_D/I_G$ Ratio .....	67
2.2.2.3	Lasers used in Raman Spectrometer .....	68
2.2.2.4	Sample Preparation for Raman Spectroscopy and Data Acquisition to Overcome Florescence.....	69
2.2.2.5	Raman Data Analysis.....	70
2.2.2.6	Raman Spectroscopy Experiments .....	70
2.2.3	Scanning Electron Microscopy (SEM) .....	71
2.2.3.1	Sample Preparation for Scanning Electron Microscopy .....	71
2.2.3.2	Detection of Secondary Electrons .....	72
2.2.3.3	Detection of Backscattered Electrons .....	73
2.2.3.4	Energy Dispersive X-ray Analysis and Inca Project Software .....	74
2.2.3.5	Scanning Electron Microscopy (SEM) Experimental .....	74
2.2.4	Focused Ion Beam (FIB).....	75
2.2.4.1	Sample Preparation for Focused Ion Beam.....	75
2.2.4.2	Liquid Metal Ion Source and Ion Column .....	76
2.2.4.3	Gas Delivery System.....	77
2.2.4.4	Selective Carbon Mill .....	77
2.2.4.5	Omniprobe .....	77
2.2.4.6	Scanning Electron Microscopy (SEM) and Energy Dispersive X-ray (EDX) Analysis.....	78
2.2.4.7	Experimental of Focused Ion Beam (FIB) .....	78
2.2.5	Hydropyrolysis (HyPy).....	78
2.2.5.1	Theory of Hydropyrolysis .....	78
2.2.5.2	Sample Preparation for Hydropyrolysis .....	79
2.2.5.3	Gas Supply.....	79
2.2.5.4	Experimental of Hydropyrolysis .....	80
2.2.6	Gas Chromatography Mass Spectrometry (GC-MS).....	81
2.2.6.1	Theory of Gas Chromatography Mass Spectrometry (GC-MS).....	81

2.2.6.2	Experimental of Gas Chromatography Mass Spectrometry .....	83
2.2.7	Computed Tomography .....	83
2.2.7.1	Theory of Computed Tomography .....	83
2.2.7.2	Experimental of Computed Tomography .....	84
2.2.8	Transmission Electron Microscopy (TEM).....	85
2.2.8.1	Theory of Transmission Electron Microscopy (TEM).....	85
2.2.8.2	Sample Preparation for Transmission Electron Microscopy .....	85
2.2.8.3	Experimental of Transmission Electron Microscopy (TEM).....	85
2.2.9	Profilometry.....	86
2.2.9.1	Theory of Profilometry .....	86
2.2.9.2	Roughness Measurements.....	87
2.2.9.3	Experimental of Profilometry .....	87
2.2.10	Jet Fuel Thermal Oxidation Test (JFTOT).....	87
2.2.10.1	Theory of Jet Fuel Thermal Oxidation Test.....	87
2.2.10.2	Experimental of JFTOT .....	88

<b>3</b>	<b>Evaluation of Analytical Techniques for the Application of Surface Analysis of IDIDs .....</b>	<b>90</b>
<b>3.1</b>	<b>Summary .....</b>	<b>90</b>
<b>3.2</b>	<b>Results and Discussion .....</b>	<b>91</b>
3.2.1	Computed Tomography .....	91
3.2.2	Scanning Electron Microscopy (SEM) .....	93
3.2.2.1	Secondary Electron Detection Mode.....	93
3.2.2.2	Backscattered Electron Detection Mode .....	96
3.2.3	Energy Dispersive X-ray Analysis (EDX) .....	98
3.2.4	Transmission Electron Microscopy (TEM).....	101
3.2.5	Atomic Force Microscopy (AFM) .....	103
3.2.6	Profilometry.....	105
3.2.7	Focused Ion Beam (FIB).....	107
3.2.8	Raman Spectroscopy .....	109

<b>3.3</b>	<b>Conclusions</b> .....	<b>110</b>
<b>4</b>	<b>Raman Spectroscopy Analysis of IDIDs and Comparison to Reference Carbonaceous Materials to Observe Graphitic Content</b> .....	<b>112</b>
<b>4.1</b>	<b>Summary</b> .....	<b>112</b>
<b>4.2</b>	<b>Results and Discussion</b> .....	<b>113</b>
4.2.1	Application of Raman Spectroscopy .....	113
4.2.2	Fluorescing During Raman Spectroscopy when Analysing IDIDs.....	117
4.2.3	Effects of HyPy on the Carbonaceous Structure of the Standard Materials.....	119
4.2.4	Structural Analysis of Reference Samples .....	122
4.2.5	Comparison of Hydropyrolysis and in N <sub>2</sub> .....	125
4.2.6	Validation of Thermal Treatment with Different Gas Atmospheres....	125
4.2.6.1	Structural Analysis of IDIDs .....	125
4.2.6.2	Comparison of Structural Analysis between IDIDs and Reference Standards .....	129
4.2.7	Identification of Volatile Species.....	131
<b>4.3</b>	<b>Conclusions</b> .....	<b>134</b>
<b>5</b>	<b>Development of Method to Investigation the 3D Structure of IDIDs Using Focused Ion Beam and Time of Flight Secondary Ion Mass Spectrometry</b> .....	<b>136</b>
<b>5.1</b>	<b>Summary</b> .....	<b>136</b>
<b>5.2</b>	<b>Results and Discussion</b> .....	<b>137</b>
5.2.1	Surface Analysis of Diesel Deposits on Eight Injector Needles Using ToF-SIMS .....	137
5.2.2	Principle Component Analysis (PCA) of Eight Injector Needles by ToF-SIMS .....	139
5.2.2.1	Positive Ion PC 1 .....	139
5.2.2.2	Positive Ion PC 2 .....	141
5.2.2.3	Negative Ion PC 1 .....	142

5.2.2.4	Negative Ion PC 2 .....	142
5.2.2.5	Examination of PCA of Eight Injector Needles .....	144
5.2.3	Investigation into the 3D Structure of Diesel Push Rod Deposit Using Focused Ion Beam (FIB) Lift Out and TEM EDX.....	145
5.2.4	Examination of the 3D structure of Diesel Injector Tip Deposit Using FIB SIMS, TEM EDX and Raman Spectroscopy.....	148
5.2.4.1	Raman Spectroscopy Analysis of Lift Out.....	149
5.2.4.2	Chemical Mapping with ToF-SIMS Analysis of Lift Out.....	151
5.2.4.3	TEM EDX Analysis of Lift Out.....	152
5.2.5	Application of FIB to Create Trenches for 3D Structure Analysis of IDIDs with ToF-SIMS .....	154
5.2.6	Further Investigation of IDIDs with FIB Created Trench and Analysis with ToF-SIMS .....	156
5.2.7	Analysis of 3D Structure of IDID with a FIB Created Trench and Depth Profiling with ToF-SIMS .....	160
<b>5.3</b>	<b>Conclusions.....</b>	<b>162</b>
<b>6</b>	<b>Analysing Laboratory Scale Deposits Utilising the Jet Fuel Thermal Oxidation Test (JFTOT) with ULSD and Biodiesel to Mimic IDID Formation .....</b>	<b>164</b>
<b>6.1</b>	<b>Summary .....</b>	<b>164</b>
<b>6.2</b>	<b>Results and Discussion .....</b>	<b>165</b>
6.2.1	Visual Analysis of the JFTOT Tubes .....	165
6.2.2	Profilometry of the JFTOT Tubes.....	167
6.2.3	Roughness Studies of JFTOT Tubes.....	170
6.2.4	Morphology of JFTOT Tubes Using SEM.....	172
6.2.5	Analysis of Carbonaceous Structure Determined Using Raman Spectroscopy.....	174
6.2.5.1	Initial Analysis of JFTOT Tubes with Raman Spectroscopy .....	174

6.2.5.2	Raman Spectroscopy Analysis of Carbonaceous Structure after Removal of Fluorescing Species with Hydropyrolysis .....	177
6.2.6	GC-MS Analysis of the Labile Fractions Removed from JFTOT Tubes by Hydropyrolysis .....	178
6.2.7	ToF-SIMS of JFTOT Samples.....	181
6.2.7.1	Principal Component Analysis of Deposits on JFTOT Tubes .....	183
6.2.7.1.1	Positive Ion PC 1 .....	183
6.2.7.1.2	Positive Ion PC 2.....	184
6.2.7.1.3	Negative Ion PC 1 .....	186
6.2.7.1.4	Negative Ion PC 2 .....	188
6.2.8	PCA of ToF-SIMS Data Comparing JFTOT Tubes to Failed Injector Needles from the Field.....	189
6.2.8.1	Positive Ion PC 1 .....	189
6.2.8.2	Positive Ion PC 2 .....	191
6.2.8.3	Negative Ion PC 1 .....	192
6.2.8.4	Negative Ion PC 2 .....	192
6.2.8.5	Comparison of IDIDs to JFTOT Deposits .....	194
<b>6.3</b>	<b>Conclusions.....</b>	<b>195</b>
<b>7</b>	<b>Conclusions.....</b>	<b>197</b>
<b>8</b>	<b>Future Work.....</b>	<b>199</b>
<b>8.1</b>	<b>Deposit Mechanism Formation.....</b>	<b>199</b>
<b>8.2</b>	<b>Computed Tomography .....</b>	<b>199</b>
<b>8.3</b>	<b>Hydropyrolysis.....</b>	<b>199</b>
<b>8.4</b>	<b>Raman Spectroscopy.....</b>	<b>200</b>
<b>8.5</b>	<b>FIB-SIMS .....</b>	<b>200</b>
<b>8.6</b>	<b>JFTOT .....</b>	<b>201</b>
<b>8.7</b>	<b>Blank Samples.....</b>	<b>201</b>
<b>8.8</b>	<b>Other Techniques for Analysis .....</b>	<b>201</b>
8.8.1	X-ray Photoelectron Spectroscopy (XPS).....	201

8.8.2 Synchrotron ..... 202

**References..... 203**

## Table of Figures

Figure 1.1 World map depicting where reports of IDIDs have occurred between 2007-2013 [1].	25
Figure 1.2 Examples of chemical structures found in diesel fuel. Modified from P. Richards [7]	26
Figure 1.3 A diagram showing the suspected causes of deposits that are forming different types of deposits and the complaints from customers that the deposits are causing [4-6, 27, 39, 40, 42-48].	34
Figure 1.4 A schematic of the deposit layers found on the injector redrawn from Barker et al.[40]	41
Figure 1.5 Photo of surface of JFTOT tube that has been fuelled with B0 diesel and 350 mg/kg PIBSI modified from Reid et al. [69].	52
Figure 2.1 Photo of an injector needle.	59
Figure 2.2 Photo of an injector tip.	59
Figure 2.3 Photo of a push rod.	60
Figure 2.4 Photo of a JFTOT tube.	60
Figure 2.5 Schematic of ToF-SIMS instrument (© ION-TOF GmbH).	63
Figure 2.6 Schematic of Stoke and Anti-Stoke scattering, modified from Cambridge University [127].	67
Figure 2.7 Schematic of Raman spectroscopy, modified from Cambridge University [127].	68
Figure 2.8 Schematic of a SEM, modified from Nano art [143].	72
Figure 2.9 Schematic of FIB, modified from Kant et al. [157].	76
Figure 2.10 Photo of schematic of a HyPy rig, showing where the valves, reactor and trap are in the pipeline.	80

Figure 2.11 Schematic of a GC-MS, modified from Hussain et al. [167].	82
Figure 2.12 Schematic of computed tomography, modified from Buzug et al. [172].	84
Figure 2.13 Schematic of TEM, modified from D Suneel et al. [177].	86
Figure 2.14 Photograph of the JFTOT mark III	89
Figure 3.1 Computed Tomography images of injector needle inside injector tip.	92
Figure 3.2 SEM image in secondary electron detection mode depicting the surface topography of injector needle 14.	93
Figure 3.3 SEM image in secondary electron detection mode depicting the surface topography of injector tip 8.	94
Figure 3.4 i) An optical image of the surface of push rod 1 ii) An optical of pushrod 1 iii) A SEM image in secondary electron detection mode depicting the surface topography of push rod 1.	95
Figure 3.5 i) Computed tomography image of injector needle. ii) Backscattered SEM image of needle 11. iii) Backscattered SEM image of needle 11. iv) Backscattered SEM image of needle 11.	96
Figure 3.6 SEM image in backscattered electron detection mode depicting the surface topography of an injector tip.	97
Figure 3.7 SEM image in backscattered electron detection mode depicting the surface topography of push rod 1.	98
Figure 3.8 Location of EDX data taken of Needle 2.	99
Figure 3.9 EDX analysis of push rod 1 and location of spectra 1 and 2.	100
Figure 3.10 TEM image of injector needle deposit [155].	102

Figure 3.11 AFM images various points on needle 15 i) Height mapping of needle 15 ii) Adhesion mapping of needle 15 iii) rigidity mapping of needle 15 [155].	105
Figure 3.12. i) An optical image of push rod 1. ii) A profile of deposit along push rod 1. iii) A profile of deposit along push rod 1.	106
Figure 3.13 i) Computed tomography image of an injector tip. ii) A profile of area of where deposit has been scrapped away to the surface of the shaft to identify height of deposit. iii) A profile of the area after a depth profile ToF-SIMS analysis.	107
Figure 3.14 SEM images of FIB lift out from needle 15. i) SEM of the milled trenches. ii) SEM image of the side wall of the lift out iii) SEM image of the lift out being removed from surface with an omniprobe. iv) SEM image of the lift out mounted on a TEM grid for further analysis.	109
Figure 3.15 Raman spectrum of push rod 1 showing no discernible bands ...	110
Figure 4.1 Data illustrating the ratio of $I_D/I_G$ Raman spectroscopy bands for a range of carbon black, graphite and coke samples. The error bars are one standard deviation.	114
Figure 4.2 Images of an injector needle. a) Photo of failed diesel injector needle removed from injector tip, covered in carbonaceous material at tip depicted as black matter. b) Computed tomography image needle inside injector tip before removal. c) SEM image showing surface morphology of injector needle and the deposit which is responsible for the needle sticking .	117
Figure 4.3 Raman spectra of the failed injector needle 9. a) The spectrum of the needle as received before thermal treatment by hydrolysis. b) The	

baselined Raman spectrum of the needle after thermal treatment by HyPy, the D and G bands being distinguished clearly. ....	119
Figure 4.4 $I_D/I_G$ Raman band ratios prior (i) and post (ii) hydropyrolysis biochar (A-D), Coal (E-F) Soot (G) and graphite (H) samples. The error bars are one standard deviation. ....	121
Figure 4.5 Raman spectra of needles 1-4. Needles 4 and 2 by HyPy and needles 3 and 1 by NPy. All the spectra have been baselined with OriginLab software, .....	126
Figure 4.6 Total ion chromatogram (TIC) and single ion chromatogram (SIC) $m/z$ 71 of volatiles released from needles 2, 4 and 9 in HyPy and needles 1 and 3 in NPy. ....	131
Figure 5.1 Positive ion surface analysis with ToF-SIMS of eight injector needles. The greatest differences have been highlighted and labelled as $Na^+$ , $K^+$ , $Na_2OH^+$ and $SiC_3H_9^+$ .....	138
Figure 5.2 Negative ion surface analysis with ToF-SIMS of eight injector needles. The greatest differences have been highlighted and labelled as $O^-$ , $CN^-$ $CNO^-$ and $SO_3^-$ .....	138
Figure 5.3 Principal Component Analysis of positive ion data. i) Scores of PC1 against PC2 ii) Loading on PC1, indicating the main ions iii) Loading on PC2, indicating the main ions. ....	140
Figure 5.4 Principal component analysis of negative ion data. i) Scores of PC1 against PC2 ii) Loading on PC1, indicating the main ions iii) Loading on PC2, indicating the main ions. ....	143

Figure 5.5 SEM Images of Lift out Process. i) Sectioning of deposit sample ii) Milling trenches for lift out sample iii) Lift out extracted with omniprobe iv) The lift out with thinned sections for TEM analysis .....	146
Figure 5.6 TEM images of the lift out, depicting the top platinum coating, two layered deposit and interface of the push rod surface. ....	147
Figure 5.7 EDX analysis of lift out from push rod 1. ....	148
Figure 5.8 SEM images of the lift out attached to a TEM copper grid for further analysis. ....	149
Figure 5.9 Photo of the surface of the lift out and the regions analysed with Raman spectroscopy line mapping. The green line is the software set line for analysis. ....	149
Figure 5.10 Raman spectroscopy line mapping analysis of lift out using a range of settings for the acquisition time, averages and strength of laser. ....	150
Figure 5.11 Chemical mapping of the lift out, showing positive ions $\text{Na}^+$ and $\text{SiC}_3\text{H}_9^+$ , and negative ions $\text{Cl}^-$ , $\text{PO}_2^-$ , $\text{CN}^-$ and $\text{SiO}_2^-$ ions. ....	151
Figure 5.12 TEM images of the lift out showing small amounts of ordering and uniformity throughout the sample. ....	152
Figure 5.13 EDX data of Lift out, showing the location of the analysis area and the different elements selected for analysis. ....	153
Figure 5.14 SEM image of trenches milled into injector tip 3 for ToF-SIMS analysis. ....	155
Figure 5.15 Positive ion spectra of trench. i) Overall spectrum of the area ii) Selected region of interest outside of trench iii) Selected region of interest inside of trench. ....	155

Figure 5.16 Negative of spectra of the trench. i) Overall spectrum of the area ii) Selected region of interest outside of trench iii) Selected region of interest inside of trench. ....	156
Figure 5.17 SEM Image of FIB trench created for ToF-SIMS Analysis.....	157
Figure 5.18 Chemical mapping of positive ions detected in ToF-SIMS of injector tip 4 .....	158
Figure 5.19 Chemical mapping of negative ions detected in ToF-SIMS of injector tip 4 .....	159
Figure 5.20 A SEM image of a ToF-SIMS depth profile, highlighted in yellow, and a side wall trench created by FIB of the depth profile, which is highlighted in green. ....	162
Figure 6.1 A schematic of a JFTOT tube showing the direction of flow of the fuel over the middle section of tube. The thinner centre part of the tube is the area where the fuel flowed over.....	165
Figure 6.2 Visual photos of JFTOT tube 1-3. i) JFTOT 1 was fuelled on B20 RME biodiesel fuel at 260 °C for 150 mins. ii) JFTOT 2 was fuelled on ULSD fuel at 260 °C for 150 mins. iii) JFTOT 3 was fuelled on B20 RME biodiesel and ULSD fuel at 260 °C for 450 mins. ....	166
Figure 6.3 Profilometry profiles of JFTOT tubes 1-3 over an area of 100 × 800 µm. i) Schematic of a JFTOT tube showing the locations of profiles a-e. ii) Profiles of JFTOT 1 a-e. iii) Profiles of JFTOT 2 a-e. iv) Profiles of JFTOT 3 a-e. ....	169
Figure 6.4. SEM image of JFTOT 1-3 i) A SEM image of JFTOT 1. ii) A SEM image of JFTOT 2. iii) A SEM image of JFTOT 3. ....	173

Figure 6.5. Raman spectra of JFTOT 1- 3 and the details include laser filter (%) , acquisition time (s) and averages (av).i) Raman spectra of JFTOT 1 fuelled on B20 RME biodiesel. ii) Raman spectra of JFTOT 2 fuelled on ULSD. iii). Raman spectra of JFTOT 3 fuelled on B20 RME biodiesel and ULSD. ....	176
Figure 6.6 Raman Spectra of three JFTOT tubes 1-3, B20, ULSD and Mix. The spectra are averages and have been baselined. ....	178
Figure 6.7 GC-MS total ion chromatogram for JFTOT 1-3 i) The total ion chromatogram of JFTOT 1. ii) The total ion chromatogram of JFTOT 2. iii) The total ion chromatogram of JFTOT 3. ....	180
Figure 6.8. Showing the overall ions found in the PCA analysis of the two visibly different regions along the JFTOT tubes. ....	182
Figure 6.9. Positive ion data of JFTOT tubes 1-3, B20, ULSD and MIX. i) Showing scores of PC1 and PC2 ii) loadings on PC1 and assigned ions iii) loading on PC2 and assigned ions. ....	185
Figure 6.10. Negative ion data of JFTOT tubes 1-3, B20, ULSD and MIX. i) Showing scores of PC1 and PC2 ii) loadings on PC1 and assigned ions iii) loading on PC2 and assigned ions. ....	187
Figure 6.11 Positive ion data of needles 1- 8 and JFTOT tubes 1-3, i) Showing scores of PC1 and PC2 ii) loadings on PC1 and assigned ions iii) loading on PC2 and assigned ions. ....	190
Figure 6.12 Negative ion data of Needles 1- 8 and JFTOT tubes 1-3, i) Showing scores of PC1 and PC2 ii) loadings on PC1 and assigned ions iii) Loading on PC2 and assigned ions .....	193

## Table of Tables

Table 1.1 European emission standards for euro 5 and euro 6 [16].	28
Table 1.2 Types of additives, the application and mode of action, adapted from the ATC Fuel Additives: Uses and Benefits [53]	31
Table 2.1 Table of samples	56
Table 2.2 Information on the lasers used in a Raman spectrometer including colour and wavelength	69
Table 3.1 EDX data of needle 2. Locations of spectra are shown in Figure 3.8	99
Table 3.2 EDX data collected from push rod 1.	101
Table 4.1 Elemental analysis, particle size and surface area of a range of carbon blacks, gilsonite resin, graphite and coke samples. The details of these reference samples has previously been reported [191].	116
Table 4.2 Summary of the sample details of Biochars A-D, coal samples E-F, Soot sample G and graphite H. Temperature and black carbon percentage for each biochar is recorded. The black carbon correlates to the amount of material that contains 7 or more rings [102]	120
Table 4.3 Raman spectroscopy data of reference carbonaceous samples A - H prior and post treatment. The data presents the wavenumber of highest intensity, full width half maximum (FWHM) and $I_D/I_G$ band ratio. i denotes the samples data acquisition before thermal treatment, ii denotes the samples data acquisition after thermal treatment.	123
Table 4.4 Raman spectroscopy data for needles 1-4 and 9 prior and post treatment in HyPy and NPy. The data show wavenumber of highest intensity, full width half maximum (FWHM) and $I_D/I_G$ band ratio. i denotes the samples	

data acquisition before thermal treatment, ii denotes the samples data acquisition after thermal. ....	128
Table 5.1 PCA of positive ion data of ToF-SIMS, with the positive and negative loadings and the assignment for each ion for PC1 and PC 2. ....	141
Table 5.2 PCA of Negative ion data of ToF-SIMS, with the positive and negative loadings and the assignment for each ion for PC1 and PC 2. ....	144
Table 6.1 Roughness data of JFTOT tubes 1-3. $R_{pv}$ is the maximum peak to valley difference. $R_a$ is the arithmetic average of deviations from the mean. ....	171
Table 6.2 Mass assignments for positive ion data of JFTOT tubes 1-3 showing PC 1 and PC 2 positive and negative loadings. ....	186
Table 6.3 Mass assignments for negative ion data of JFTOT tubes 1-3 showing PC 1 and PC 2 positive and negative loadings. ....	188
Table 6.4 Mass assignments for positive ion data of needle 1-8 and JFTOT tubes 1-3 showing PC 1 and PC 2 positive and negative loadings. ....	191
Table 6.5 Mass assignments for negative ion data of needle 1-8 and JFTOT tubes 1-3 showing PC 1 and PC 2 positive and negative loadings. ....	194

## Abbreviations

AFM	Atomic force microscopy
ATC	Additive technical committee
BET	Brunauer-Emmett-Teller
CARB	California air regulatory board
CNI	Cetane number improver
CTP	Coal tar pitch
DCA	Deposit control additive
DCM	Dichloromethane
DSIMS	Depth secondary ion mass spectrometry
EDX	Energy dispersive X-ray
EPA	Environmental protection agency
ESEM	Environmental scanning electron microscopy
FAME	Fatty acid methyl ester
FIB	Focused ion beam
FTIR	Fourier transform infrared
FWHM	Full width half maximum
GC-MS	Gas chromatography mass spectrometry
HyPy	Hydropyrolysis
IDID	Internal diesel injector deposit
JFTOT	Jet fuel thermal oxidation test
LMIG	Liquid metal ion gun
MN	methylnaphthalene
MW	Molecular weight
NIR	Near infrared
NPY	Nitrogen pyrolysis
PAH	Polycyclic aromatic hydrocarbon
PC	Principal component
PCA	Principal component analysis
PIBSI	Polyisobutylenesuccinimide
PDMS	Polydimethylsiloxane
RME	Rapeseed methyl ester
SEM	Scanning electron microscopy
SIC	Single ion chromatogram
TEM	Transmission electron microscopy
TGA	Thermogravimetric analysis
TIC	Total ion chromatogram
ToF-SIMS	Time of flight secondary ion mass spectrometry
TPO	Temperature programmed oxidation
ULSD	Ultra-low sulfur diesel
XPS	X-ray photoelectron spectroscopy
XRD	X-ray diffraction

# 1 Introduction

## 1.1 Context of Current Work

Internal diesel injector deposit (IDID) formation in injection systems have become a prolific problem in the last decade, occurring since the introduction of high pressure and temperature common rail systems combined with ultra-low sulfur diesel and biodiesel. Figure 1.1 illustrates where reports of IDIDs have occurred across the world between 2007 – 2013 [1]. The IDIDs have caused concerns such as injector systems misfiring and/or sticking, increased emissions, extra fuel consumption, and engines failing to start [2-5]. It has been stated that if buildup of an injector tip hole is 5% of the diameter, equating to 10% reduction in hole diameter then there will be 19% restriction in flow area, causing significant loss of power [6]. Deposits are forming on a multitude of engine parts such as the needle, tip, pushrod and filters. However, interest into what causes the deposits on the needle has steadily grown, with research persisting to identify a test method to examine the deposit material.



*Figure 1.1 World map depicting where reports of IDIDs have occurred between 2007-2013 [1].*

## 1.2 Diesel Fuel

Diesel is a fraction taken from the distillation of crude oil, which is the liquid portion of organic matter that has been trapped in underground geological reservoirs [7]. The composition of crude oil varies from different oils fields across the world. The gas oil and kerosene fraction is found to typically boiling in the diesel range, examples of chemical structures from diesel fuel can be observed in Figure 1.2 The crude oil will contain impurities such as water, solids, inorganic salts and trace metals. In order to evade fouling of equipment or poisoning of catalyst these impurities are removed. This can be achieved by electrostatic separation, chemical desalting or physical filtering. Once the crude oil has had impurities removed it then can be fractionally distilled to separate out the different fuels due to the specific boiling points.

The quality criteria of the diesel produced from a refinery depends on a number of factors. The parameters to consider are cetane number, density, sulfur content, flash point, volatility, viscosity and cold flow characteristics [7]. There is also consideration into minimising the addition of kerosene as this is more profitable as aviation fuel [7].

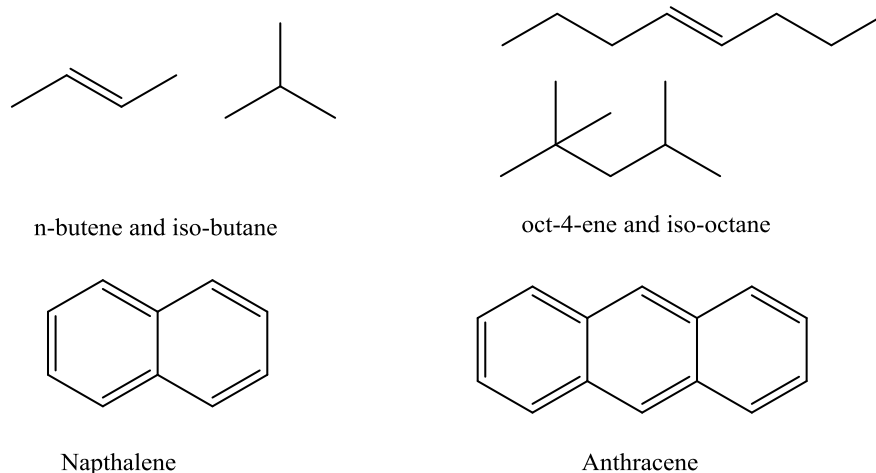


Figure 1.2 Examples of chemical structures found in diesel fuel. Modified from P. Richards [7]

### **1.3 History of the Diesel Engine**

In 1892 Rudolph Diesel filed a patent for his incorporated process into an internal combustion engine, his vision was that the engine would run on “*every kind of fuel in any state of aggregation*” and would be “*suitable for carrying out the process*”[8]. Diesel’s first attempts were to run the engine using a coal slurry, unfortunately this was unsuccessful because of the failed delivery into the combustion chamber. Diesel tried using vegetable and peanut oil, and he concluding that liquid fuels showed the most potential. He envisioned a multi fuel type engine, which would show promise once the combustion chamber delivery system was improved [9]. His patent described an engine that was seven times more efficient than the steam engine and also considered more reliable than the gasoline engine, which had been invented 20 years previous by Nikolaus Otto [10, 11].

### **1.4 Emission Standards and the Future of Diesel**

The future of energy and oil is a heavily debated topic in the current political, financial and social climate with many disputing the future of diesel [12, 13]. At the United Nations Framework Convention on Climate Change, widely known as the Paris agreement (2016) 195 countries pledged to reduce CO<sub>2</sub> emissions to stop the global average temperature increasing by 2 °C [14]. In order to achieve this a study published by Pye *et al.* stated that the UK must have a net-zero emissions by 2050 [15]. Whilst the global pledge is a step forward, if the world’s biggest polluters, namely China, India and the USA do not set targets within their countries then the global aim will not be achieved. The requirements in present day from governments and the public to improve efficiency and performance, has instigated the engine designs and fuel

composition to change dramatically. Health and safety has become more prevalent within this field in recent years, which has caused legislation restraints on diesel and its composition to become tighter by lowering emissions of NO<sub>x</sub>, SO<sub>x</sub> and particulate matter, for instance European euro 5 and euro 6 emission standard limits are stated in Table 1.1.

*Table 1.1 European emission standards for euro 5 and euro 6 [16].*

	<b>Euro 5 (2009)</b>	<b>Euro 6 (2014)</b>
<b>HC g/KWh</b>	0.46	0.13
<b>NOx g/kWh</b>	2.0	0.40
<b>PM g/kWh</b>	0.02	0.01
<b>PN /kWh</b>	-	$8.0 \times 10^{11}$

Recent controversy surround diesel as harmful to health due to NO<sub>x</sub> and particulate matter has seen a decline in diesel cars sold. In the UK during 2016 47.1% of cars sold were diesel, whilst in the first quarter of 2017 this dropped to 43.9% [17]. Even with the introduction of electric cars and the market for petrol cars maintaining a steady growth, the market percentage for diesel cars remains high. The UK government have recently pledged to ban sales of petrol and diesel cars as of 2040 [12]. There is, as yet, no indication of how this will be realised.

In the USA the Environment Protection Agency (EPA) governs the emission standards. During the time President Obama was in office the EPA stated that their targets would be an average industry fleet wide level of 163 g/mile of CO<sub>2</sub> by the year 2025 [18], this is equivalent to 54.4 mpg. During the years 2012 - 2025, 6 million tons of greenhouse gases will be cut, which will allow savings for families of over \$1.7 trillion in fuel costs and reduce America's dependence on oil by more than 2 million barrels per day by 2025 [18].

California has chosen to instate stricter regulations as defined by the California air regulation board (CARB) since 1970, due to higher levels of smog.

President Trump stated that “ *Compliance with the terms of the Paris accord and the onerous energy restrictions it has placed on the United States could cost America as much as 2.7m lost jobs by 2025*” [19]. He described the agreement as unfair and suggest that it would cripple the USA with the UN Green Climate Fund taking taxes to focus on helping less developed countries in the battle for climate change. He has proposed a new agreement could happen, which does not subject the USA to providing such financial support, “*we will start to negotiate, and we will see if we can make a deal that’s fair. And if we can, that’s great. And if we can’t, that’s fine*” [19]. This statement from the President of the USA has left the world in disappointment, however, still planning to keep up the battle for climate change. Since the USA has withdrawn from the Paris agreement, some states have made their own pledges to meet the targets.

Since the UK has triggered article 50 to leave the EU, new targets will be put in place. In June 2016 the Guardian reported that the UK announced new ambitious carbon targets of reducing carbon emissions by 57% before 2030 of the CO<sub>2</sub> levels recorded for 1990. This is stricter than the EU targets which are 40% by 2030 of the 1990 CO<sub>2</sub> levels [20].

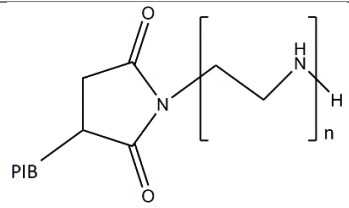
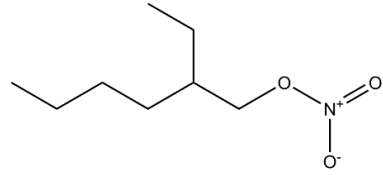
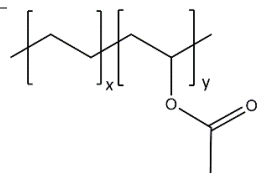
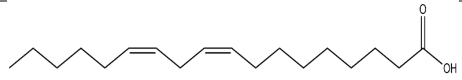
Even with the CO<sub>2</sub> emissions currently being reduced in passenger vehicles heavy duty vehicles still produce large volumes of harmful gases. Health problems from inhaling particulate matter and NO<sub>x</sub> are still an issue, particularly prevalent in built up areas. The current Mayor of London, Mr. Sadiq Khan is pushing forward with plans to heavily penalise or ban vehicles

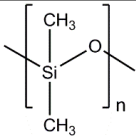
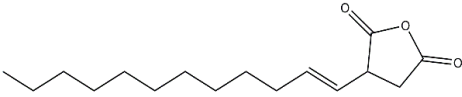
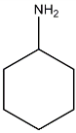
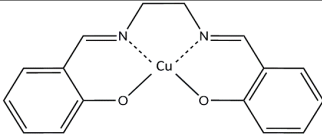
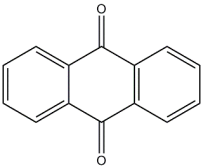
fuelled by diesel from entering Londons cleaner air zones [21]. This has been driven by reports released stating that air pollution in London has reached toxic levels [22]. It has been report as of October 2017 the ‘T-charge’ will be introduced in London, which is a charge that will apply to cars entering the congestion zone that do not meet the minimum Euro 6 emissions standards [23]. The role of fuel additives can help to make diesel more efficient and utilise the fuel supply available until a sustainable and financially viable alternative is developed.

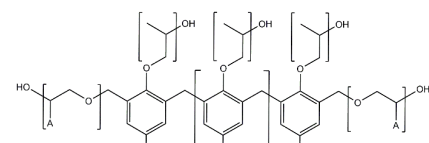
### **1.5 The History of and Types of Fuel Additives**

As diesel engine design improved there were issues that needed to be overcome, such as improving energy output of fuel, functioning in cold climates and stability for long periods of storage. In order to circumvent some of these problems fuel additives were introduced [24-35]. Research began as early as the 1920s, in additives such as lubricity improvers, detergents, dispersants, and cold start improvers [4, 5, 25, 27, 29, 36-41]. The most widely used additive currently is diesel deposit control additives and these were first researched and developed in the beginning of the 1980s [30]. Table 1.1 depicts multiple fuel additives used in the industry, the issues they address, mode of action and chemical structure. The technical committee of petroleum additive manufacturing in Europe (ATC) estimates that over 95% of on road gasoline and diesel is treated with performance additives [30]. As the use of crude oil continues as a fuel source there will remain a continued need for additives to improve performance and to prolong the use of diesel and other fuels.

Table 1.2 Types of additives, the application and mode of action, adapted from the ATC Fuel Additives: Uses and Benefits [53]

Type of Additive	Application	Mode of Action	Example
<b>Deposit Control Additive</b>	Deposit control additives (DCA) are designed to keep the engine clean and stop deposit formation and blockages at the injectors.	A DCA consists of a polar head group and a hydrophobic tail. The hydrophilic head group attaches to the deposits and the engine walls and the tail will solubilise into the fuel, creating a film.	
<b>Cetane Number Improver</b>	A cetane number improver (CNI) increases the cetane quality of the diesel, which is cost effective and reduce the ignition delay.	CNI break down in the fuel to form free radicals, these free radicals all for ignition more readily and aid in the combustion of the fuel.	
<b>Cold Flow Improver</b>	There is around 20-40% n-paraffin in middle distillate fuels. In cold weather wax crystals form, and begin to grow to form large lattices. This can lead to filter blockages.	Cold flow improvers are only partially soluble in fuel. Therefore when the temperature drops the n-paraffins are encourages to form small crystals instead.	
<b>Lubricity Improver</b>	Untreated and low sulfur fuel cause failure and wear in an	Similar to DCA in creating films over engine parts, the polar group attaches to the	

	engine. The lubricity improves act to stop wear on the engine.	walls. The film creates a barrier to keep engine parts from contacting.	
<b>Anti-Foam Additive</b>	When a vehicle is refuelled, the fuel has a tendency to foam up with contact to the air.	The anti-foam additives work by reducing surface tension of bubbles formed in the foam, therefore the bubbles readily collapse.	
<b>Corrosion Inhibitor</b>	The corrosion inhibitors act to prevent the water corroding the engine parts.	A corrosion inhibitor has a hydrophobic polar head and a hydrocarbon chain that solubilises into the fuel. This creates a protective barrier on the engine parts.	
<b>Stability improver/Antioxidant</b>	Stability improvers are used to increase the lifetime of the diesel.	The stability improvers interfere with reactions in the fuel to stop sediment forming, usually antioxidants to inhibit the actions of free radicals.	
<b>Metal Deactivator</b>	When certain metals are in fuel they can cause oxidation.	A metal deactivator works by chelating with a metal, which renders the metal incapable of acting as an oxidant.	
<b>Markers and Dyes</b>	Typically used in agriculture and off road trucks to distinguish between road and off road worthy fuel.	Markers and dyes have no mode of action but to provide a colour or marker to the fuel. They are usually included in the fuel at the refinery stage.	

<b>Dehazer/ Demulsifier/ emulsion preventative</b>	These types of additives are used to aid in water contamination. When combined with other additives water can form an emulsion.	The mode of action for these types of deposits is to interfere with the film elasticity of water found in an emulsion. Water will form together into one large droplet as opposed to throughout the fuel.	
<b>Conductivity Improvers</b>	When fuel is filled up at the pump static electricity can build up and can provide a fire hazard.	Conductivity improvers even at low treatment rate will act to stop static discharge and charge dissipation rates are increased.	Fuel soluble chromium materials, polymeric sulfur, nitrogen compound, quaternary ammonium salts or complex organic alcohols.

## 1.6 Types of Diesel Deposits and Issues

There are multiple causes, issues and types of IDIDs that have been documented. The possible origins for IDIDs are listed as suspected causes for deposits in Figure 1.3 [4-6, 27, 39, 40, 42-48]. Due to the complex nature of IDIDs and each engine having a different lifetime experience of fuel, additives, driving and weather it is unlikely that all IDIDs will be caused by the same precursors IDIDs are currently thought to be described into five different categories [4, 5, 25, 27, 29, 36-40, 49, 50], described as types of deposits in Figure.

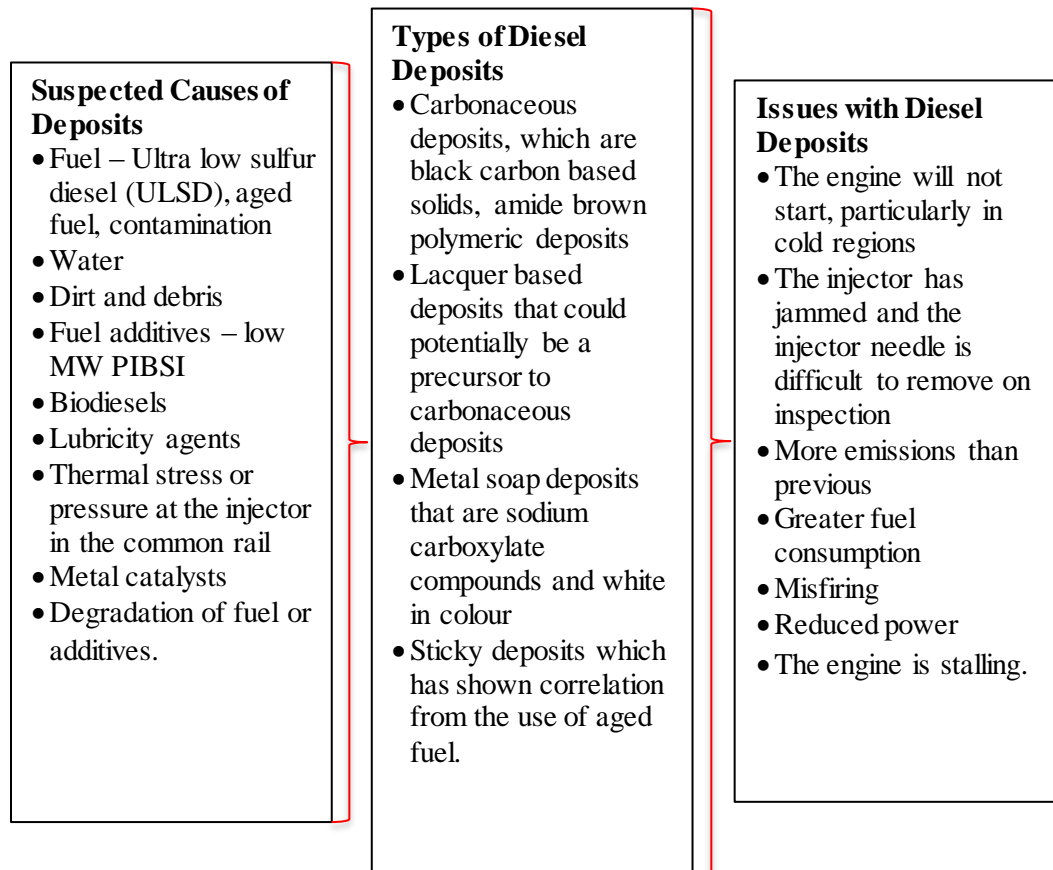


*Figure 1.3 A diagram showing the suspected causes of deposits that are forming different types of deposits and the complaints from customers that the deposits are causing [4-6, 27, 39, 40, 42-48].*

It was noted around 2006 that IDID formation on the injectors that were causing a plethora of issues [43, 44], and these have been described as issues with diesel deposits in Figure 1.3. There is presently little understanding as to how each type of IDIDs differs chemically and which suspected cause is linked to which type of IDID. It is suspected that lacquer deposits form on the injector needle and a thin structure is all that is required to block the injectors [29].

## **1.7 Research into Causes of IDIDs**

This research has broadened the list of causes to include fuel types, injector design and stability of fuel. It is possible that the combination of all of these suspected causes is the reason for deposit formation. The instigation for deposit formation will be only uncovered with identifying more sophisticated analytical methods to analyse the layering formation of deposits.

### **1.7.1 Ultra-low Sulfur Diesel (ULSD)**

In June 2006 the USA EPA stated that there must be a 97% reduction of sulfur in diesel, which is known as ULSD [51]. The change from old fuel to ULSD reduced exhaust SO<sub>x</sub> emissions from engines by 90%. Lubrizol Ltd., a fuel additives company, measured performance of engine power against ULSD with and without detergent. The results showed that after 20 test cycles the ULSD without detergent had a 7% loss of power in comparison to the treated fuel [50]. A commercially available product, MicrobMonitor® DF test kit (Lubrizol Ltd.) has been made available to check fuel systems as many problems from corrosion have been due to ULSD being susceptible to microbial attack. The cause of the increase is as yet unknown to originate from microbial contamination or the change in properties of the fuel, such as insolubility for depository precursors [52]. However, increase in problems with

deposits have also been found throughout the world, therefore ULSD is deduced to not be the only reason.

### **1.7.2 Biodiesel**

Biodiesel is a renewable alternative to conventional 'fossil' fuels and is typically produced from vegetable oils such as fatty acid methyl esters (FAME) and rapeseed methyl esters (RME). In order to reduce greenhouse gas emissions, the world is looking to renewable and CO<sub>2</sub> neutral alternatives, such as biofuels, however, biodiesel has been a suspected cause for IDIDs [26, 53, 54].

Byproducts of FAMEs are fatty acids that can react with sodium to form sodium soaps, which have been reported, the soaps are insoluble in fuel so cause a buildup of deposits and reduce the precision of the injector [2, 35, 55]. The sodium comes from contamination of water, the sodium soaps are thought to be the easiest deposits to form and a precursor to the formation of lacquered deposits. Also with biodiesel prone to instability, by containing different FAMEs, there can be issues with emissions, viscosity and cold flow [53, 54, 56].

Ullmann *et al.* also reported sodium traces found from corrosion of pipeline and catalysts reacted with acid to create the soap like deposits [2]. FAMEs are known for being unstable and having difficulty at cold temperatures, therefore require cold start additives [57]. Ullmann *et al.* have explored the possibility that molecules containing acid groups can cause deposit formation [2].

Therefore, with the change in fuel composition it is unknown if the additives, which previously prevented deposits and improved engine properties, could unintentionally contribute to their buildup. However, it should be noted that not

all FAMES come under this general rule, as some do not add to deposits, for example, Arondel *et al.* reported that it seems to be dependent on the oxidation stability of the biodiesel [29].

In conclusion to the studies from Arondel *et al.* and Ullmann *et al.* it was reported that there is a lack of suitable standard engine test for industry to conform with [29, 48]. This apparent lack of a suitable standard test is an observation which has been repeated by other researchers, for example Barker *et al.* and Muller *et al.* [38, 58]. In order for results to be consistent and transferable, a suitable test should be designed. Arondel *et al.* suggested that the problem of IDIDs was not going to be resolved without further research into fuel additives and better selection of fuel composition [29]. The challenge will be to develop an additive that combats the IDIDs but also has other properties such as lubricity and dispersant, which has been discussed in previous studies [28, 57, 59-61].

### **1.7.3 Oxidation of Fuel**

The stability of fuel during storage is a widely debated topic, for example if the fuel oxidises or reacts with the container to create depository precursors [62-66]. Clayton has given an overview of fuel degradation and concluded that storage and degradation in the injection equipment are not mutually exclusive [66]. A multitude of processes occur in the formation of depository build up in the injection system. The work described a sonication technique that causes cavitation in fuel which induces particulate formation in an attempt to mimic the soot formed. On sonication for 1 hour at 35 °C a range of samples provided evidence that aromaticity was a key parameter in forming a soot like structure, whereas aliphatic molecules created a 'gloop' [66]. The oxygen content was

also a factor in creating the soot structure and caused oxidation more readily during the sonication process. It was observed that methylnaphthalene (MN) caused the most solid precipitation, and this was compared to the material formed from a range of diesels that had been stored for 33 days and sonicated for a range of times 0-80 mins. The results showed that the MN had the highest particle number concentrations ( $\text{cm}^{-3}$ ) at around  $100,000 \text{ cm}^{-3}$  and the diesel had  $40,000 \text{ cm}^{-3}$ . Having a higher particle number would be more susceptible to deposition, because during storage more precursors could be produced. The results from this study were comparable to previously observations that stability of fuel is key for fuel performance [45, 67, 68].

#### **1.7.4 Polyisobutylene Succinimide (PIBSI)**

The use of polyisobutylene succinimide (PIBSI) has been the most prevalent deposit control additive (DCA) over the last 30 years [54, 67, 69, 70] the structure can be observed in Table 1.2. PIBSI can be synthesised in a wide range of functionality, varying molecular weight and using either the mono or bis form. As such, PIBSI can be used to describe many different chemical structures. Barker *et al.* carried out jet fuel thermal oxidation tests (JFTOT) with a range of conditions including ultra-low sulfur diesel (ULSD) doped with PIBSI [71]. The results showed that low molecular weight PIBSI was a potential cause for IDID formation, resulted in injector sticking. The deposits of PIBSI were easily detected by FTIR due to the peak identifying the amine group found in the additive [71].

It has been suggested by Ullmann *et al.* that after testing two different types of PIBSI that deposits only formed when large quantities of low molecular weight PIBSI were used. They found that when using low levels of low molecular

weight PIBSI then no deposits were formed [72]. This result was also described by Quigley *et al.* who identified depository build up in a 6.8 litre engine using low molecular weight PIBSI [73] and also Barbour *et al.* reported deposits on the internal diesel injector containing PIBSI chemistry [36].

### **1.7.5 Injector Design**

In 2017 Muller *et al.* reported that the engine used in an engine test could be crucial for the type of deposit [58]. The automotive industry use engine tests to compare performance such as the XUD9 and DW10b, which are diesel injector tests. The fuel is doped with zinc neodecanoate or dodecanyl succinic acid sodium to create IDIDs and the spray performances of the injectors are measured. It was discussed by Muller *et al.* that the XUD9 engine test created deposit internally on the injector needle [58]. Whereas the DW10b engine test is more prone to creating deposit externally on the tip and holes. In work by Muller *et al.* suggests an alternative method called the ENIAK test [58], which recirculates the fuel to induce ageing and mimics engine performance without the doped molecules which would not be found in field fuel. The findings proposed a need for a more representative test and that the deposit formation is not necessarily due to the fuel but also due to the design of the injector. This work conducted experiments with engine tests (XUD9 and DW10B), and concluded that deposits form on different regions, deposits in field engines could build up differently. Further investigation into correlations between design and deposit could be a parameter in deposit formation to consider.

### **1.8 Analysis of IDIDs**

There have been numerous analytical techniques applied to IDIDs, however, only a few have examined the layering structure of the deposit and not given

definitive proof of the suspected layering structure. It is unknown if there is a chemical interface or if the chemistries are diffused and interlaced. The prior work has majorly been the analysis of the surface, which is the last material that was positioned on the deposit. There are a small number of examples in the literature of examining the lower layers, which are the fundamental cause of the deposits to form.

### **1.8.1 Time of Flight Secondary Ion Mass Spectrometry (ToF-SIMS)**

Time of flight secondary ion mass spectrometry (ToF-SIMS) is a highly surface sensitive analytical technique used to remove the uppermost layers of a sample. ToF-SIMS was commercialised in the 1980s by Professor A Benninghoven, Dr E. Niehuis and Mr. T. Heller [74] and has been applied to analysing semiconductors [75], biomaterial surfaces [76], thin films [77] and polymer interactions [78].

Previous studies by Barker *et al.* has applied ToF-SIMS, specifically using depth profiling to investigate IDIDs structure from the surface to the injector substrate [37, 39, 79]. It was found that sodium was predominately in the  $\text{Na}^+$  and  $\text{Na}_2\text{OH}^+$ ,  $\text{Na}_2\text{SO}_4^+$  ions formed upon the surface of the IDID examined from the field. Other peaks were identified as  $\text{Ca}^+$ ,  $\text{K}^+$ , sulfates, phosphates,  $\text{Cl}^-$  and  $\text{F}^-$ . The carbon species found within the samples was a range of hydrocarbons, which was expected due to fragmentation. A crystalline carbon layer was found on the injector surface, it was suggested that this was a diamond carbon like coating to protect the injector [39]. Figure 1.4 depicts the layering structure proposed in this work. From the ToF-SIMS data it cannot be concluded that there is such distinct layers that the schematic suggests. Due to the surface of deposits being so rough and potentially porous, ions will be

detected at different sputter times and such clearly demarked layers could only be speculated from these studies.

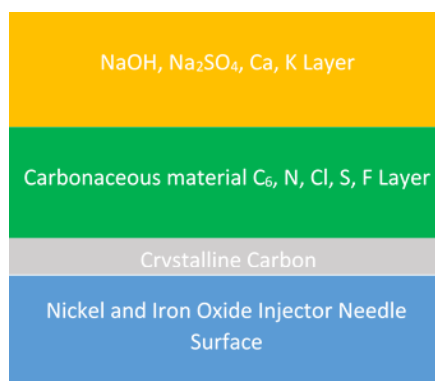


*Figure 1.4 A schematic of the deposit layers found on the injector redrawn from Barker et al.[40]*

In more recent work by Barker *et al.*, larger fragments within IDIDs were investigated, by comparing to spectra of polycyclic aromatic hydrocarbon (PAH), coronene ( $C_{12}H_{24}$ ) and coal tar pitch (CTP) [37]. Firstly for the negative polarity data, it was found that coronene was broken into fragments that had an even number of carbon fragments with masses ranging from  $C_2$  to above  $C_{10}$ . There were also ions with the elemental formula  $C_{23}H_{11}^-$  and  $C_{24}H_{11}^-$  discovered, which are very similar to the molecular formula of coronene. For CTP there were small even number carbon fragments, which indicate these are reliable markers for PAH molecules. As CTP has higher complexity with different molecular structures and masses there were many peaks for masses above  $m/z$  250. When compared to the spectra for IDIDs there were peaks above  $m/z$  250 as well, this indicated that there are PAH structures larger than coronene. For the positive ion data collected, less fragmentation of the larger ions resulted in  $C_7H_7^+$ ,  $n-C_{10}$ ,  $n-C_{12}$  and  $n-C_{20}$  ions being detected, there was

also a peak at  $C_{12}H_{24}^+$  detected when measuring coronene. With positive ion data the dimeric species were more common with masses over  $m/z$  600, therefore it was suggested that using negative ion data was more certain in defining PAH [37]. The work shows depth profile of IDIDs and shows the function of depth from sputtering of the PAH fragments and  $FeO^-$ . The depth profiling indicated that the change in organic matter decreases with depth from the surface, and an increase in  $FeO^-$  as the measurements reach the injector surface.

Dallanegra *et al.* have utilised ToF-SIMS to analyse the ratio of hydrocarbon to aromatic content within IDIDs [45, 56]. A range of conditions were tested but only three samples were analysed. Sample 2 was fuelled with B10 biodiesel (10% v/v FAME), PIBSI (1000 ppm) and fatty acid (1000 ppm). Sample 3 was fuelled with B0, PIBSI (1000 ppm) and fatty acid (1000 ppm). Sample 5 was fuelled with B10 biodiesel (10% v/v FAME), PIBSI (1000 ppm), fatty acid (1000 ppm) and fuel borne catalyst (40 ppm Fe). The fatty acid was a standard commercially available fuel lubricity additive. The results showed that there was more graphitic content in sample 3 which had no biodiesel component, the hydrocarbon was suspected to come from all of the components of the fuel. The detection of the C-N functionality was less in samples 2 and 3, suggesting there had been more degradation of PIBSI than in sample 5. The data also indicated the presence of sodium, copper and sulfur on all of the samples. In another study, Feld *et al.* applied ToF-SIMS to IDIDs [54], the injector needles and biodiesel samples were taken from failed engines from Western Europe. ToF-SIMS results from the tip of an injector needle showed sodium

hydroxide, cyanides, cyanates, carbonates and sulfates. The shaft of the needle had different chemistry which included polydimethylsiloxane (PDMS), fatty acids, calcium oxides and sulfates, alkyl sulfates, alkylbenzene sulfonate, toluene sulfonic acid quaternary ammonium compounds and formic acid [54]. Differences were noted to be from a range of countries but this observation was only highlighted and no separation in the data was discussed.

IDIDs were analysed on a metal ring near the injector needle. The deposit was described as a brown colour and the ToF-SIMS data indicated peak patterns similar to what would be expected from PIBSI, up to the mass of  $m/z$  1000. Other ions identified were alkylbenzene sulfonates and alkylsulfates, which are both surfactants. Phosphate containing molecules were also noted, specifically triarylalkylphosphates which are thought to be anticorrosive and/or anti wear additives [54].

Furthermore, the work by Feld *et al.* investigated the residue of fuel filters that had been fuelled with biodiesel [54]. The results found large intensities of the sterols, campesterol-glucoside, sitosterol-glucoside, sodium and dimer adducts, as well as oleic and linoleic acid. For completion the work also analysed biodiesel from filling stations in the region. The results showed peaks for campesterol, sitosterol, and a range of sterol esters, linoleic and oleic acid. Therefore these chemistries are present in the fuel and are proposed to be trapped in the filters, largely due to size and precipitation out of solution.

ToF-SIMS has demonstrated clear potential in the implementation of analysing IDIDs. ToF-SIMS is the only technique previously applied that can provide a depth profile, which can therefore be useful in identifying what causes the initial deposit to form. Not only can ToF-SIMS depth profile, but it can also

chemical map, creating three-dimensional images of the deposits according to the selected ion. However, ToF-SIMS does not provide a quantitative representation of the IDID. ToF-SIMS provides a large amount of data to analyse which could become a problem if there is a large data set to compare. Both examples of using ToF-SIMS from Feld *et al.* and Dallanegra *et al.* display the usefulness and sensitivity of the technique for comparing samples. The surface of the sample, however, is the only area analysed in these studies, which this not providing a comprehensive analysis of how the deposit has formed. The work described by Barker *et al.* in Figure 1.4 depicts the deposit as a clear layering structure, however, the depth profiling is not uniform and this layering structure cannot be described as such. There must be further investigation before IDIDs can be concluded as defined layers.

### **1.8.2 Dynamic Secondary Ion Mass Spectrometry (DSIMS)**

Dallanegra *et al.* applied Dynamic secondary ion mass spectrometry (DSIMS), also known as depth profiling, and found three layers within the surface of an IDID [45]. The uppermost layer consisted of carbon, nitrogen and oxygen of roughly 1  $\mu\text{m}$  thickness. The centre layer was suspected to be an oxide layer consisting of oxygen, zinc and aluminium. The lowest layer was identified when the intensity of iron increased and plateaued. It was noted that there was a clear transition between the carbonaceous deposit and the surface of the needle, suggesting that there is little to no reaction between the two layers and there is no intrusion into the metal surface.

This work compliments the work of ToF-SIMS carried out by Dallanegra *et al.* and Barker *et al.* in giving evidence of the chemistry of the surface and bulk of

the deposit and not to focus on the surface. However, this work has the same issues as previous ToF-SIMS studies by Barker *et al.* that the issues of topographical roughness could cause ions to come through at varying points and that it is difficult to assume defined and only compliments previous work rather than progressing a method for analysis IDIDs.

### 1.8.3 Fourier Transform Infrared (FTIR)

Fourier transform infrared (FTIR) is a spectroscopic technique that identifies chemical functionality within a sample, such as carbonyl and amine groups. FTIR can be used to analyse gases, liquids and solids, previous applications of FTIR include organic, inorganic and polymeric material such as proteins[80]. Trobaugh *et al.* used FTIR to analyse a range of IDIDs from Columbia, Texas and Quebec [1]. The FTIR results from the Columbia IDID showed peaks at 1440, 1550 and 2800-3000  $\text{cm}^{-1}$ . The 1440 and 1550  $\text{cm}^{-1}$  peak were from  $\text{COO}^-$  and 2800-3000  $\text{cm}^{-1}$  were from a hydrocarbon tail. The Texan IDID had the same two  $\text{COO}^-$  peaks but at 1566 and 1454  $\text{cm}^{-1}$ . The wavenumber shift was thought to be due to ligand binding to a mixture of sodium and calcium. The work explains that a shift of 100  $\text{cm}^{-1}$  suggests that the metal ligand is bonded to both oxygen atoms of the carboxylic acid group whilst a shift of 200  $\text{cm}^{-1}$  suggests there is only one oxygen atoms bonded to the metal. However, it was noted that this has not been investigated therefore would need further proving. The deposit on the needle from Quebec was reported to be pink in colour and suspected to be  $\text{Al}_2\text{SiO}_5(\text{OH})_4$ , the FTIR results showed a peaks at 911, 1006, 1033 and 3688  $\text{cm}^{-1}$ . Barker *et al.* used FTIR to analyse IDIDs and identify these functionalities and C-N stretch which is indicative of PIBSI [53, 67, 69, 81, 82].

FTIR is an efficient surface analytical technique used to identify key functionalities, which is beneficial for identifying chemistries such as the C-N bond in PIBSI. The shift position can give indication of the bonding environment. However, FTIR can only identify bonds that have a polarised dipole, therefore cannot distinguish between C-C bonding. For IDIDs which are heavily carbonaceous, information on the C-C bonding would be informative on the graphitic structure.

#### **1.8.4 X-ray Diffraction (XRD)**

X-ray diffraction (XRD) can be used to identify phase identification of crystalline material within a sample. XRD can be used to identify any sample with suspected crystallinity such as catalyst materials [83], carbon nanotubes [84] and microstructures such as metal organic frameworks [85]

For application of IDIDs XRD can identify the graphitic content, the graphitic indicative peaks reside at  $26^\circ$  and  $72^\circ$ . Barker *et al.* analysed an IDID with XRD and found neither of the peaks, suggesting there was no detectable graphitic content [6]. However, for XRD large quantities of sample are required, in the region of 50  $\mu\text{g}$ , which can be difficult to obtain from an injector needle. Additionally, the sample would be required to be removed from the surface of the needle and this would remove depository history by disrupting the layering of IDID.

#### **1.8.5 Gas Chromatography Mass Spectrometry (GC-MS)**

Gas chromatography mass spectrometry (GC-MS) is a technique that separates, identifies and quantifies molecules within a sample. GC-MS is a widely used analytical technique in identifying unknown materials and therefore highly utilised in forensics [86, 87].

Tanaka *et al.* used GC-MS to identify  $n\text{-C}_{16}$  and  $n\text{-C}_{18}$  within an IDID, the hydrocarbons were thought to be attached to a carboxylic acid group, confirmed with FTIR [88]. Cook *et al.* have tested the oxidative stability of fuel with a modified Rancimat test according to DIN EN15751 [62], and tested the products prior and post testing with GC-MS. The data shows the peaks collected at different retention times, through comparing the prior and post fuels it can be observed that for the post fuel there is no lower molecular carbonaceous material, < 8 minutes, so has likely degraded. There was no difference detected between the prior and post > 8 minutes.

GC-MS is a technique that can efficiently identify hydrocarbons within a sample, due to minimal sample needed GC-MS is advantageous for analysing IDIDs. However, for GC-MS the sample needs to be gasified and IDIDs can be difficult to fully dissolve, therefore not all of the sample can be analysed, the deposit history would also be removed.

### **1.8.6 X-ray Photoelectron Spectroscopy (XPS)**

X-ray photoelectron spectroscopy (XPS) is an analytical technique that quantifies different chemical environments in a sample. XPS is used to analyse a range of surfaces such as semiconductors [89], catalysts [90], biomaterials [91] and medical implants [92].

Venkataraman *et al.* have used XPS to analyse IDIDs and have found only carbon and oxygen were on the surface. The O/C ratio was determined to be in the region of 0.2, which was noted to be similar to jet fuel. Peaks were detected at 284.7 eV, 286.5 eV and 288.8 eV. The peak at 284.7 is responsible for aromatic carbon, the peak at 286.5 eV suggests C-O, which could come from

the present of phenolic, furan alcohol or ester groups. Finally the peak at 288.8 eV is indicative of a C=O group and is likely to be from either a carboxylic acid, anhydride or lactone group.

Dallanegra *et al.* have also applied XPS to engine test IDIDs, the difference between samples 2, 3 and 5 has already been discussed in section 1.6.1 [45]. The XPS data showed that the deposits consisted of carbon, oxygen and nitrogen. The data showed that amide, amine and carboxylic functionalities were present. The nitrogen containing functional groups were from the presence of PIBSI in the doped fuel. There were also traces of sodium, copper, sulfur, zinc and chlorine found on the needles in varying quantities. It was noted that the level of sodium was the least on sample 5 that contained the FBC.

XPS provides quantitative analysis of samples, however, is significantly improved if the suspected elements are known before analysis due to the amount of data collected and for working up the data analysis. The application of XPS would complement ToF-SIMS as it is a qualitative technique and can depth profile.

### **1.8.7 Scanning Electron Microscopy (SEM)**

Scanning electron microscopy (SEM) is a topographical analytical technique that provides images of the surface of a sample and has been extensively used to analyse surfaces across a range of disciplines [93-95]. SEM has been widely applied to IDIDs previously [1, 3, 45, 70, 96, 97]. . The SEM images show that the deposit is not homogenous and varies in thickness, colour and consistency, such as granulation.

SEM is a surface techniques, so will only provide information on the topography of the top of the sample and this work requires information on the lower deposit within the sample. Priority has been placed on identifying the chemical composition of the IDIDs, which SEM does not provide. SEM is typically used in conjunction with EDX and provides elemental analysis, however, does not give indication to how the elements are bonded.

### **1.8.8 Transmission Electron Microscopy (TEM)**

Transmission electron microscopy (TEM) uses an electron beam to give structural information for a sample and the graphitic content of a sample can be determined. Venkataraman *et al.* used TEM to analyse IDIDs and found there was little layering structure [3]. The work comments that there was less graphitic structure than jet fuel deposits, however, this was not explained in this work. If this is the case, it could be due to the tighter regulations on jet fuel which possesses less influences to create disordered structures. This work shows that TEM can be used to provide information on the graphitic content in IDIDs. Unfortunately due to TEM analysis requiring the electron beam to penetrate the sample and be detected on the other side, the sample was not analysed *in-situ*. The sample was scratched from the surface which has removed any history of the IDID. It would be suspected that the lower levels of deposit would contain more graphitic structure due to residing under the injection system environment of 260 °C and 2600 - 3000 bar for longer [98].

### **1.8.9 Hydropyrolysis (HyPy)**

Hydropyrolysis (HyPy) is the heating of a sample under a stream of high pressure hydrogen gas, which reduces functionalities and increases removal of

volatile material at lower temperature than inert atmospheres. HyPy has been applied to carbonaceous samples such as coals, oils and biomasses [99-102]. Barker *et al.* analysed an injector tip with hydropyrolysis to remove the volatile matter and analyse the labile fraction with GC-MS [42]. The sample was mixed with a molybdenum catalyst to induce molecular cracking and heated to 550 °C. The results showed a distribution of alkanes above  $n$ -C<sub>16</sub>, with a large peak for  $n$ -C<sub>18</sub>. Other ions identified were naphthalene, alkylbenzene, methylphenanthrene and methylnaphthalenes. These results were compared to the labile fraction removed from a fuel filter, however, no investigation was made into the fraction remaining on the injector tip. HyPy GC-MS analysis only analyses the labile fraction and there is no understanding of the deposit history as the material left on the IDID is not analysed and this is the bulk material that has caused the engine failure.

#### **1.8.10 Thermogravimetric Analysis (TGA)**

Thermogravimetric analysis (TGA) is the weighing of a sample during heating to determine weight loss due to loss of volatile matter. TGA is used to obtain weight percentage of water content, volatile matter and ash content of such carbonaceous materials as cellulose [103], biomass [104] and carbon nanotubes [105].

Venkataraman *et al.* used TGA to analyse IDIDs from the field and laboratory scale deposits created with  $n$ -hexadecane. The TGA results showed that the IDIDs from the field lost weight at 120 °C due to water, and then more mass in the range of 450-610 °C, this was thought to be due to the hydrogen being released from the degradation of polyaromatic arrangements and hydroxyl groups, whilst the H/C ratio was calculated to 0.4. The laboratory made deposit

produced from *n*-hexadecane began to release the majority of the weight in the temperature range 540-900 °C, the H/C ratio was calculated at 0.5.

TGA has shown use, however, it is a destructive technique and there are more sophisticated analytical techniques that could be applied to learn the carbon content. The work in this thesis has prioritised the chemical analysis of IDIDs, and therefore TGA is unlikely to be used.

### **1.8.11 Temperature Programmed Oxidation (TPO)**

Temperature programmed oxidation (TPO) heats a samples in an oxygen atmosphere and records the carbon dioxide (CO<sub>2</sub>) evolved, where greater levels of CO<sub>2</sub> produced indicates more disorder and less graphitic stable structure. As with TGA, TPO is applied to carbonaceous samples such as coal[106] and catalysts [107].

Barker *et al.* applied TPO to a needle and tip deposit, and compared to reference material [6]. The results showed that there was more CO<sub>2</sub> evolved from the needle at a higher temperature than the injector tip. The needle deposit was comparable to carbon black, as such more graphitic carbon than coke and gilsonite resin, however not comparable to the graphite samples. The level of disorder and soot like particles in the deposit on the tip is likely to have formed from the combustion process, whilst the needle deposit was suggested to be a result of the fuel quality. The results from this work was also concluded in work by Venkataraman *et al.* that injector needle deposits evolved before 750 °C [3]. This technique similar to TGA does not provide chemical information of IDIDs.

### 1.8.12 Jet Fuel Thermal Oxidation Test (JFTOT)

The jet fuel thermal oxidation test (JFTOT) was an industry test that would efficiently test the longevity of a jet fuel for further testing. The fuel is heated over a stainless steel or aluminium tube and the stability of the fuel is tested by measuring the thickness of deposits on the tube, this method has been applied to diesel fuels in recent studies [46, 67]. The outcome of this test indicates further investigation of additives and fuels in the early stages of research screening. By using the JFTOT the time frame for testing a fuel and/or an additives is cost and time effective, a JFTOT test is 2.5hr and one tube costs £60 whereas an engine test can be days, require a team of specialist and cost in the region of £10,000 per single test.

Reid *et al.* has used the JFTOT to provide evidence on the growing issue of poorly manufactured low molecular weight PIBSI is a cause for depository build up [69], an optical image of deposit formation on a JFTOT tube can be observed in Figure 1.5. Multiple test conditions were tested with reference fuel RF06, biodiesel with fatty acids, and the samples that contained the low molecular weight PIBSI caused the most deposit.

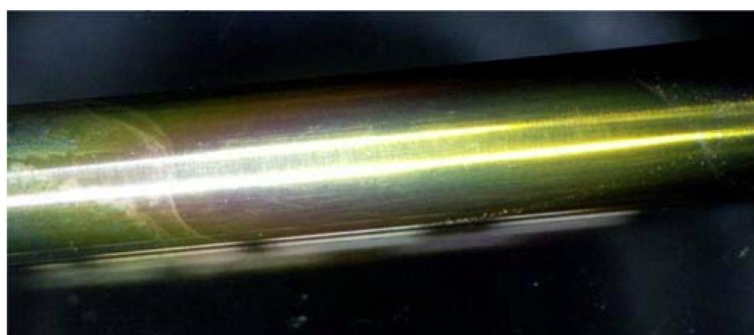


*Figure 1.5 Photo of surface of JFTOT tube that has been fuelled with B0 diesel and 350 mg/kg PIBSI modified from Reid et al. [69].*

Lacey *et al.* have used the JFTOT to investigate different temperatures at which sodium carboxylate salts begin to form, which was deemed to be at 140 °C [46]. Further JFTOTs included doping the fuel with nitrogen species and zinc containing species. The height profile were then measured to identify at what temperatures the thickest deposit was forming.

Initial research into analysing deposits on JFTOT shows potential for screening diesel fuels and for an industry test, the JFTOT indicates quickly and efficiently if a fuel and/or additive are viable for further tests. However, analysis of the JFTOT currently has only been visual, height profiles and FTIR measurements. There could be more in depth analysis of the deposit and there could be a comparison to field deposits to verify the replication of deposits.

## **1.9 Project Aim and Objectives**

Currently there has been various examples in the literature of analysis of IDIDs. However, limited investigation has been carried out to identify the layering structure of the deposit and therefore the initial cause for deposition. There has also been no comparison of deposits from different geographical locations and therefore identifying if there is a universal problem or many different factors for deposit formation. The overall aim of this research is to develop a test method for analysing IDIDs that have come from failed engines from the USA, China, Europe, engine tests and from laboratory bench scale tests. In order to accomplish this aim a number of objectives have been devised as follows:

- To explore a range of analytical techniques to develop a test method that would investigate the chemical difference with the thickness of the

deposit or uncovering layers, and therefore keeping the deposits history intact. Therefore understanding how the deposit has formed over time.

- To compare injector needles from different geographical locations, engine test and laboratory tests.
- To identify different chemistries that come from different fuel types such as ultra-low sulfur diesel or biodiesel.
- To investigate if the deposit on the injector needle is altered when removed from the injector tip.
- To find a suitable method of removing fluorescing material from the injector needles to allow for Raman spectroscopy analysis. Then to also test the volatile matter removed and find the cause for the fluorescence.

### **1.10 Explanation of Thesis Style**

For ease of reading this thesis will not follow the recognised IMRAD format (introduction, method, results and discussion). This thesis will be similar to European-style theses where the research chapters will be divided into four separate research chapters. Due to the nature of this work being exploratory into a variety of analytical techniques each chapter will take on one technique and discuss the results. To conclude, there will be a conclusions chapter that will aim to bring together the results of this thesis and a further work chapter. The further work chapter will discuss the proposed experiments and analytical instruments that could be developed to widen the extent of this research.

## **2 Experimental Methodology**

### **2.1 Methodology**

This chapter describes the experimental techniques used during this work, the advantages the techniques provide and how the data was analysed. Therefore for ease of reading this chapter will give an overview of the technique and each result chapter will refer back to the relevant section.

Initially the approach was to expand on the work carried out utilising ToF-SIMS, which has been previously discussed [37, 67, 79, 108]. The initial focus was to investigate analysing the injector needles as this is a current topic of research in the industry, largely due to injector ‘jamming’ causing the most problems for the customers. However, due to the needle deposits being relatively thin there was also interest in analysing the push rods and injector tips, which had more depository material to utilise for analysis.

#### **2.1.1 Samples**

For this work the samples will be detailed by their identification assigned for this work not the Innospec identification. Samples that start with the same number are from the same engine set. In Table 2.1 the information on the samples used are given, with details on the identification for this thesis, Innospec identification, the engine part, the fuel used and the geographical location.

Table 2.1 Table of samples

<b>Part of Engine</b>	<b>Identification</b>	<b>Innospec Ltd. Identification</b>	<b>Information</b>
<b>Needles</b>	Needle 1	NEEDLE 5	The needle was from Norway where the heavy truck was fuelled on EN590 reference fuel. The complaint was no start and the injector was stuck. This was from the same engine as tip 8.
	Needle 2	DWISSI	This was a DW10B engine test needle using low MW (non-commercial) PIBSI. After 16 hours there was a severe failure due to the injector being stuck. It was a light duty engine fuelled on RF06 reference fuel.
	Needle 3	ID4	The needle was from the mid-west USA and fuelled with ULSD.
	Needle 4	USILLID	The needle was from a heavy duty truck from Illinois fuelled on ULSD. The complaints were insufficient power due to injector sticking.
	Needle 5	1517	This needle was from Louisiana and complaints included power loss and a workshop tow required. In the workshop engine misfired after 40 mins and stopped, then there was no start. This needle was from the same engine as tip 7.
	Needle 6	4999	This needle was from New York and complaints were no start due to unable to remove needle.
	Needle 7	4998	This needle was from New York and complaints were no start due to unable to remove needle.
	Needle 8	China 1	This needle was from China.
	Needle 9	1514	The engine was fuelled with Californian air resources board (CARB) diesel. The complaints were of the engine not starting. This needle is from the same engine as injector tip 5.
	Needle 10	10b	The needle was from Indiana USA and complaints were that the engine would not start, which was due to the injector sticking. This needle is from the same engine as injector tip 3 (10a).

	Needle 11	DET1	The injector was from Louisiana and the complaints were of insufficient power. This injector needle came from the same engine as tip 4.
	Needle 12	9a	The injector was from Minnesota and the complaints were poor drivability. This needle was from the same engine as tip 2.
	Needle 13	1516	This needle was from a highway truck from Colorado. The engine would crank but there was it would not start. This needle was from the same engine as injector tip 6.
	Needle 14	NC1	The needle was from North Carolina in the USA and the highway truck engine would not start due to the injector needle sticking.
	Needle 15	KYOTO	The needle was from a stuck injector from the USA which had only been fuelled on ULSD. The problem manifested as power loss, poor drivability, no start and particulate production.
<b>Injector Tips</b>	Tip 1	8b	The injector was from an off road truck from the USA and complaints were that the engine would not start. This injector tip is from the same engine as Push rod 1 (8c).
	Tip 2	9b	The injector was from Minnesota and the complaints were poor drivability. This tip was from the same engine as needle 12.
	Tip 3	10a	The injector was from Indiana USA and complaints were that the engine would not start, which was due to the injector sticking. This injector tip was from the same engine as needle 3 (10b).
	Tip 4	DET1	The injector was from Louisiana and the complaints were of insufficient power. This injector tip came from the same engine as needle 11.
	Tip 5	1514	The engine was fuelled with Californian air resources board (CARB) diesel. The complaints were of the engine not starting. This injector tip was from the same engine as needle 14.
	Tip 6	1516	This needle was from a highway truck from Colorado. The engine would crank but there was it would not start. This injector tip was from the same engine as needle 13.

	Tip 7	1517	Needle was from Louisiana and complaints included power loss and a workshop tow required. The needle misfired after 40 mins and stopped, then there was no start. This injector tip was from the same engine as injector needle 6 (1517).
	Tip 8	Injector 5	The tip was from Norway where the heavy truck was fuelled on EN590 reference fuel. The complaint was no start and the injector was stuck. This was from the same engine as needle 1.
<b>Push Rod</b>	Push rod 1	8c	The push rod was from an off road truck from the USA and complaints were that the engine would not start. This injector is from the same engine as injector tip 1 (8b).
<b>JFTOT Tubes</b>	JFTOT 1	B20	JFTOT test fuelled for 150 mins at 260°C on B20 biodiesel (20% rapeseed methyl ester, 80% diesel).
	JFTOT 2	ULSD	JFTOT test fuelled for 150 mins at 260°C on ULSD.
	JFTOT 3	Mix (B20 & ULSD)	JFTOT test fuelled for 450 mins at 260°C, two cycles of B20 and 1 cycle of ULSD, 150 mins each.

## 2.1.2 Photographs of Samples

The photos in this section are an example of the samples used in this work, the images also include measurements of the samples.

### 2.1.2.1 Injector Needle

Figure 2.1 shows a photo of an injector needle. Although there are different designs the principle design of the injector needle is the same. The injector needle resides inside the injector tip where the needle puts the diesel fuel under high pressure for ignition.



*Figure 2.1 Photo of an injector needle.*

### 2.1.2.2 Injector Tip

Figure 2.2 depicts a photo of an injector tip. It is here where the fuel is injected from under such high pressure that causes combustion. It is also a key area of reduced efficiency in engine performance as these holes become blocked with deposit [97, 109].



*Figure 2.2 Photo of an injector tip.*

### 2.1.2.3 Push Rod

Figure 2.3 shows a photo of a push rod, this resides behind the injector needle and pushes the injector needle in and out of the injector tip.



*Figure 2.3 Photo of a push rod.*

### 2.1.2.4 JFTOT Tube

Figure 2.4 shows a photo of a jet fuel thermal oxidation test or JFTOT tube.

This is a lab scale test used to mimic IDID formation.

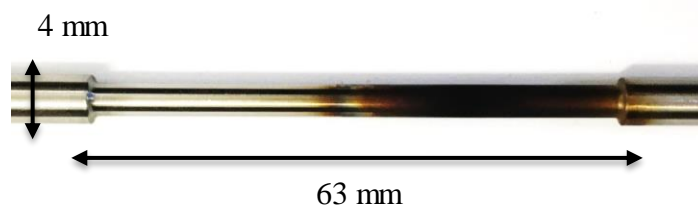


*Figure 2.4 Photo of a JFTOT tube.*

## 2.2 Analytical Techniques

The majority of this work utilised ToF-SIMS, Raman spectroscopy, SEM, FIB and HyPy therefore the theory behind these techniques will be more in depth.

### 2.2.1 Time of Flight Secondary Ion Mass Spectrometry (ToF-SIMS)

ToF-SIMS is an analytical technique that examines the chemical composition of surfaces. In ToF-SIMS the surface of a sample is bombarded with a pulsed high energy (keV) primary ion beam to collide with surface molecules of the sample [110-112]. As the primary ions hit the sample surface this releases

secondary ions, which are then accelerated in to the time of flight (TOF) analyser [113, 114]. The mass of the secondary ions can then be measured according to the time of flight taken to reach the detector. The principle of the ToF-SIMS technique is that the time of flight for a molecule is proportional to the square root of its mass [115]. Depending on the ion source the technique is delicate enough to allow non-volatile secondary ions up to masses of approximately 10000 Daltons to be detected without much fragmentation occurring [116, 117]. ToF-SIMS is able to surface image and depth profile, therefore is able to provide a three-dimensional mass resolved ion image of the surface.

#### *2.2.1.1 Sample Preparation for Time of Flight Secondary Mass Spectrometry*

When analysing samples with ToF-SIMS generally there is no sample preparation needed. Due to the instrument probing the chemical composition of a sample any alterations to the sample surface will affect the spectra seen by the detector. Therefore any modifications should be avoided. However, as ToF-SIMS is a surface analytical technique, consideration should be made of contamination on the surface, topography of the sample and stability in a vacuum. The sample will likely have air borne contaminants on the upmost surface and this will show in the spectra. It could be suggested to remove of surface contaminants by sputtering the sample prior to ToF-SIMS analysis. Alternatively when depth profiling a sample then discounting an initial sputter time will remove the contaminants and enter into the bulk of the sample, giving a 'real' representation of the sample.

Analysis with ToF-SIMS is favored when a sample has a flat surface [113].

This is due to the close proximity of the analysers and the sample. If a sample

surface is rough with varying peaks and valleys, the efficiency of which the secondary ions reach the TOF analyser will be compromised. The peaked areas on a sample will have higher intensities detected and areas of valleys and rapid slopes will have lower intensities of ions detected.

A final consideration when analysing with ToF-SIMS is that analysis must occur in a vacuum, typically less than  $\sim 10^{-6}$  mbar [113]. Samples that contain large quantities of volatile matter may have difficulty reaching adequate pressure. However, for the samples in this work, this was not an issue.

#### *2.2.1.2 Primary Ion Source*

The primary ion source is used to create a focused beam of short ion pulses that can effectively hit a point on a sample surface with precision, a schematic of a ToF-SIMS instrument can be observed in Figure 2.5. For the instrument used in this work a liquid metal ion gun (LMIG) is used. A tip covered in a thin layer of metal is heated above the melting point and then an electrostatic field induces the emission of ions [113]. The most common pulsed primary ion beam are any of the following ions  $\text{In}^+$ ,  $\text{Bi}_3^+$ ,  $\text{Au}^+$ , or  $\text{Ga}^+$ , for this work  $\text{Bi}_3^+$  was used. In order to have higher resolution of analysis the diameter of the primary ion beam is very important. The time that the beam pulses hit the surface limit the mass resolution. The length of time adds an uncertainty in the calculation of the flight time through the TOF analyser. Therefore the primary ion pulses needs to arrive at the same time of the surface of the sample. The initial ions in the pulse are slowed down to arrive at the same time as the later ions in the pulse, this is known as ‘bunching’. By bunching the pulses the beam diameter is increased, therefore this will give sharp spectra peaks but low resolution or fuzzy chemical mapping images. In order to get clearer chemical

maps bunching needs to be switched off and then the diameter of the primary ion beam will be reduced to detect better lateral spatial resolution. However, the spectra peaks will be compromised and widened.

### 2.2.1.3 TOF Analyser

Once the primary ion source dislodges ions from the surface of the sample, the secondary ions are focused and accelerated into the TOF analyser by electrostatic potentials. The ions are then electrostatically attracted to the detector. The ions will travel at a constant kinetic energy until reaching the detector [113]. The flight time is determined by [113]:

$$\frac{mv^2}{2} = \frac{ms^2}{2t^2} = zeU$$

Where  $m$  = ion mass,  $v$  = ion velocity,  $s$  = length of flight tube,  $t$  = time of flight,  $z$  = charge of ion,  $e$  = elementary charge and  $U$  = electrostatic potential. The equation demonstrates that the flight time of each ion is proportional to the square root of the mass ( $m/z$ ). It therefore takes longer for a heavier mass to reach the detector compared to lighter masses, even after leaving the surface of the sample at the same time.

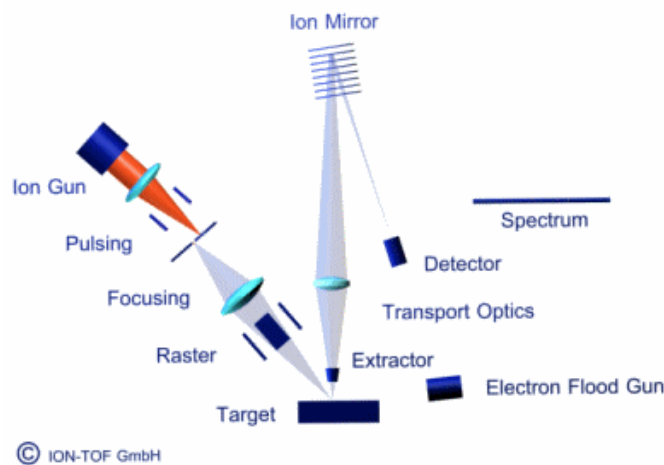


Figure 2.5 Schematic of ToF-SIMS instrument (© ION-TOF GmbH).

#### *2.2.1.4 Sputtering and Depth Profiling*

Many ToF-SIMS instruments will be equipped with a second ion source with the main purpose of sputtering or removing surface material. Using a sputtering ion source depth profiling can remove contamination, identify lower chemistries in a sample and create 3D images. Analysis is carried out in a dual beam manner where the beams alternate between sputtering and analysing [113]. The instrument in this work was equipped with a monatomic  $\text{Cs}^+$  and  $\text{Ar}_n^+$  cluster source. The  $\text{Ar}_n^+$  cluster source is considered to be less destructive because the ions are larger and therefore have a larger surface impact when compared to the  $\text{Cs}^+$  ion source. By using an ion source that has a larger surface area of impact there will be less fragmentation of secondary ions.

#### *2.2.1.5 Data Acquisition and Analysis*

SurfaceLab 6 (IONTOF GmbH) was the software used in this work to analyse data acquired with the ToF-SIMS. Data collected is saved in a raw data file where each pixel and scan have a separate mass spectra. The data can be manipulated after acquisition such as selecting region of interests, creating 3D profiles and chemical maps of selected ions. The software can also output selected ion intensities which can be used for principle component analysis.

#### *2.2.1.6 Experimental of Time of Flight Secondary Ion Mass Spectrometry (ToF-SIMS)*

A ToF-SIMS IV (ION-TOF GmbH, Münster, Germany) instrument was used to acquire spectra and depth profiles in this work. The instrument was equipped with a 20 keV gas cluster ion beam (GCIB) operated at 10 keV with  $\text{Ar}_{1455}^+$  clusters. A 25 keV  $\text{Bi}_3^{++}$  analysis beam was used to analyse the central area between sputtering pulses, All of the samples were sputtered with  $\text{Ar}_{1455}^+$

which was rastered at  $400 \times 400 \mu\text{m}$  area. The  $\text{Bi}_3^+$  analysis beam was rastered over a  $200 \times 200 \mu\text{m}$  area. All points analysed were rastered over areas of  $200 \times 200 \mu\text{m}$  at a resolution of  $128 \times 128$  pixels. An electron flood gun was also employed for charge compensation, using approximately 2.6 A, -30 V extraction bias and -38 V reflector voltage. Data acquisition, data processing and analysis were performed using SurfaceLab 6 (ION-TOF GmbH).

#### *2.2.1.7 Principle Component Analysis (PCA)*

Principle component analysis (PCA) is a statistical transformation of a large data set of possibly correlated variables into linear uncorrelated variables, these are called principle components (PC). The PCs define the differences in the data set and identify key variables that differ. In the instance that PCA was applied to ToF-SIMS data it will identify the biggest differences in ion intensities detected. Whereas manually analysing a large number of spectra will be time consuming and can indicate that there are differences in different ions. Using PCA a larger number of ions can be investigated and could pick out ions that manually could be missed without prior knowledge.

#### *2.2.1.8 Experimental of Principle Component Analysis*

The positive and negative ion intensity data were collected from three points on eight injector needles, which were divided into four regions of interest. Each data matrix was square root mean scaled and mean-centred to the mean of the training set prior to analysis. PCA was carried out using PLS Toolbox 5.2 software (Eigenvector, Wenatchee, WA, USA), an add-on to MATLAB R2009b. The number of principal components was determined from an eigenvalue plot using a screen test.

## 2.2.2 Raman Spectroscopy

Raman spectroscopy is an analytical technique that observes change in the polarisation of a molecule, which can be vibrational, rotational, and other low-frequency modes in an environment [118-120]. The scattering patterns obtained are unique fingerprints to each molecule. For each molecule the vibrational energy level is different and the photons emitted have a different wavelength shift. The initial laser of monochromatic light can be detected to give details of the different Raman excitations [111]. Due to Raman spectroscopy being a scattering process, samples of any size or shape can be examined. Very small amounts of material can be studied.

### 2.2.2.1 Principles of Raman Spectrometry

When a beam of photons strikes a molecule, the photons are scattered elastically, which is called Rayleigh scattering, elastic scattering is the photon energy is return to original state, as the name suggests. The inelastic scattering of photons is called Raman scattering [119-123], which is when the energy is altered so does not return to original the energy state. Only a small proportion of the scattered light, approximately,  $1 \times 10^{-7}$  is Raman [124]. Due to Raman scattering changing photon energy, then Stokes and anti-Stokes lines are generated. Stokes lines are present when material absorbs the energy and emit photons at a lower energy than the absorbed photons, the final state is higher in energy than the original state. Whereas anti-Stoke lines are present when material absorbs photon energy and emit photons at a higher energy than the absorbed photons, then the final state is lower in energy that the original state, this is detailed schematically in Figure 2.6. The stronger of the two processes is Stoke lines, as Raman spectrometry is used at room temperature and the

molecule will be in its ground vibrational state, therefore more likely to be emitted at a lower energy [125, 126].

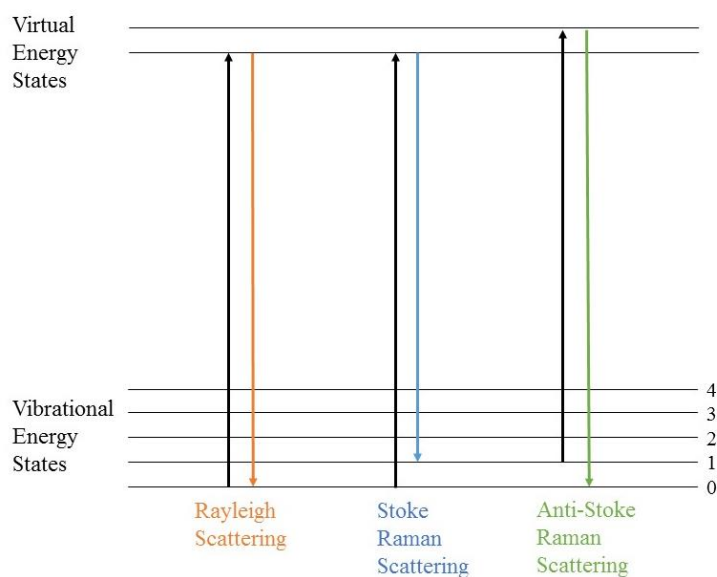


*Figure 2.6 Schematic of Stoke and Anti-Stoke scattering, modified from Cambridge University [127].*

#### 2.2.2.2 Bond Identification and $I_D/I_G$ Ratio

The energy difference experienced with each photon interaction can indicate the nature of each bond present within the sample. The vibration of each bond will be slightly different depending on the atoms and the strength of the bond. Due to carbon being able to bond in a variety of manners, Raman spectroscopy can identify different bonding orientations [128-130]. The bands of interest are the D and G bands. The D band is found at  $1380\text{ cm}^{-1}$  and is reported from disordered  $\text{sp}^2$  carbon [131-133]. This when there are imperfections in the structure such as heteroatoms, edges of graphite sheets, or adjacent  $\text{sp}^3$  or  $\text{sp}^1$  hybridised carbons. The G band found at  $1552\text{ cm}^{-1}$ , is indicative of graphitic carbon, where the  $\text{sp}^2$  hybridised carbon is in perfect graphitic order with no

defects [134-137]. The ratio of the  $I_D/I_G$  bands gives evidence of the graphitic content of a sample and provides comparison among a collection of samples. By observing the full width half maximum (FWHM) this also gives further information on the structure of a sample. A larger FWHM suggests that there are a variety of environments responsible. For instance graphite will have a sharp peak because the structure is uniform, whereas a carbonaceous material such as biochar there will be a number of disordered and ordered structures. The trend in the  $I_D/I_G$  ratio need to be interpreted separately of the trends seen in the FWHM of the D and G bands [131-133].

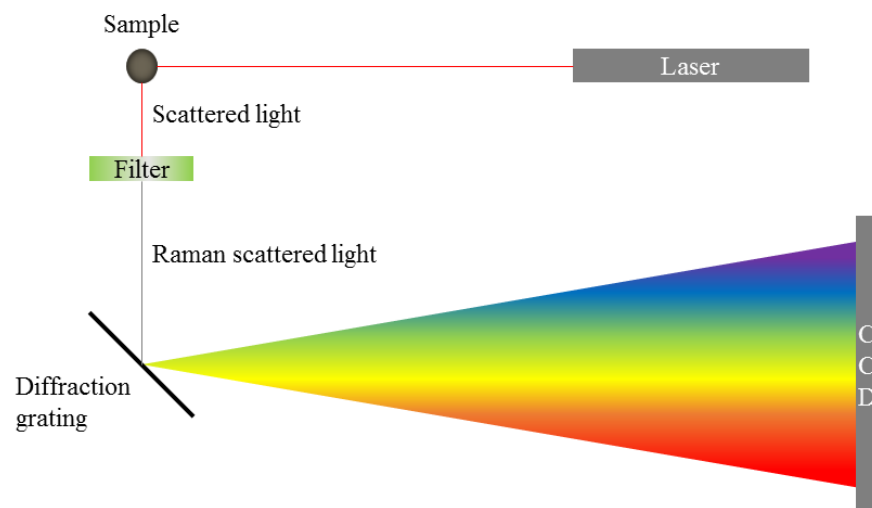


*Figure 2.7 Schematic of Raman spectroscopy, modified from Cambridge University [127].*

### 2.2.2.3 Lasers used in Raman Spectrometer

Determining the correct laser to use can be important based on sample type due to some samples readily fluorescing. Biological and organic samples have a tendency to fluoresce therefore it is standard for a Raman spectrometer to have

a range of lasers, some typical configurations can be found below in Table 2.2 and include information such as colour and wavelength. There is a trade off when selecting the correct laser for a given sample. By using a longer wavelength such as red or NIR the risk of fluorescence is reduced, however, there is a need to increase laser strength or acquisition time to excite photons for detection. For the carbonaceous samples analysed in this work a green 532 nm laser was used as it provided the best results with reducing fluorescence and detecting the D and G bands. The same laser wave length must be used throughout the samples range otherwise the D and G bands will shift and/or give different intensities rendering a comparison between samples impossible.

*Table 2.2 Information on the lasers used in a Raman spectrometer including colour and wavelength*

<b>Colour</b>	<b>Wavelength (nm)</b>
UV	325
Green	532
Red	660
Near Infrared (NIR)	785

#### *2.2.2.4 Sample Preparation for Raman Spectroscopy and Data Acquisition to Overcome Florescence*

Samples analysed in Raman spectroscopy do not need any sample preparation. However, if a sample has a tendency to fluoresce then there are options to explore before acquiring any spectra. Photo bleaching is powering the laser onto the analysis area and hopefully eradicating the fluorescing matter for a length of time. Other options include reducing acquisition time whilst increasing laser strength. As discussed in section 2.2.2.3, lasers used in Raman spectrometry give varying results with regards to overcoming fluorescence,

changing to a lower wavelength can aid in data acquisition but this compromises sensitivity. The same wavelength must be used to compare band shift or intensity of two samples.

#### *2.2.2.5 Raman Data Analysis*

The software used to analyse data from the Raman spectrometer was LabSpec 6 (Horiba UK Ltd). The software controls the acquisition time, filter of laser, averages and data processing of the acquired spectra. The Raman spectrometer can also line map, surface map and has confocal ability. For this work the line mapping application was used, where LabSpec 6 (Horiba UK Ltd) creates a path along a sample for the Raman spectrometer to take spectra at given distance intervals and then provide graphical interpretation of the change in intensities for selected bands. The confocal microscope uses an aperture to focus below the surface and as the light is diffracted back only information from below the surface is detected, however, because the samples used in this work were very dark in colour this was unable to be used. For graphical analysis and baselining data, Origin (OriginLab Ltd) was used.

#### *2.2.2.6 Raman Spectroscopy Experiments*

The Raman data was collected on a Horiba LabRAM HR. equipped with confocal imaging capability and with laser wavelengths available of 325, 532, 660 or 785 nm and a 600 lines/mm grating. The detector was a Synapse CCD detector. The spectra were collected by recording multiple acquisitions for each spectral window. The Raman shift was calibrated using the Raleigh peak and the  $520.7\text{ cm}^{-1}$  silicon line from a Si (100) reference sample.

### **2.2.3 Scanning Electron Microscopy (SEM)**

A scanning electron microscope (SEM) is an instrument that generates images of a sample by scanning with a focused beam of electrons [138, 139]. The electrons interact with the surface of the sample and the scattered signals are detected and an image is interpreted [140]. The resolution of a SEM image can be better than 10 nm [141]. This technique has been a common tool in discovering the topography of many sample types including IDIDs. The SEM used in this work was an environmental scanning electron microscope (ESEM), this means that analysis of samples do not have to occur in a vacuum [142]. The use of an ESEM is advantageous if samples are prone to containing volatile matter.

#### *2.2.3.1 Sample Preparation for Scanning Electron Microscopy*

In the instance that samples charge and build up current on the surface, then the sample must be coated. Coating can be either carbon, platinum or gold which allows for obtaining a better quality image of the topography. However, consideration of which coating needs to be considered for further analysis.

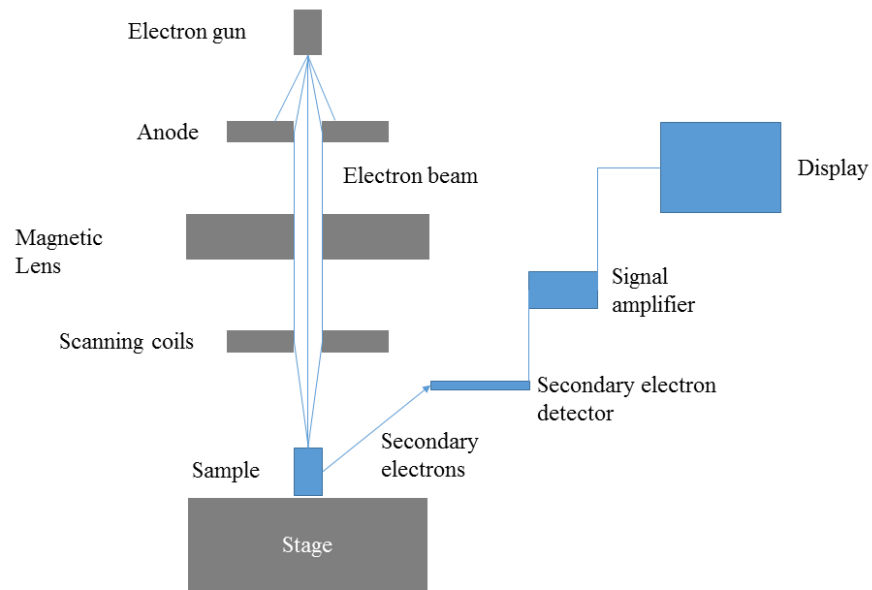


Figure 2.8 Schematic of a SEM, modified from Nano art [143].

### 2.2.3.2 Detection of Secondary Electrons

A SEM functions by scanning a sample with a beam of electron over the region of interest [144]. The electrons are generated at the top of the column and then accelerated and focused with apertures and lenses to hit the surface of the sample with precision, observed in the schematic in Figure 2.8. The electron beam scans over the sample and the interactions cause secondary electrons to be produced [139, 145]. These secondary electrons are collected by the detector and an image is interpreted. The interaction incident of an electron beam on a sample surface penetrates a few microns in a drop manner. With the incident beam spreading out from the initial contact point into a round drop shape. The secondary electrons, backscattered electrons and characteristic X-rays are generated at a lower depth of the drop shaped interaction [146]. The secondary electrons are the shallowest, which is why when detecting these

electrons the topographical information is interpreted with such precision and topographical information is subsequently lost for backscattering detection as elemental information is substituted.

The contributing factors affecting the quality of each image are spot size, scanning rate, and beam strength [145]. The spot size is determined by the lens size used to change the diameter of the analysis point on the surface of the sample. The higher the spot size the larger the diameter. The spot size used will alter the resolution of the image acquired and the number of electrons generated. There is a tradeoff between resolution of image and magnification. At a lower magnification a higher spot size will be needed. When obtaining images the scan rate of a SEM will dictate the quality of the image collected. A lower scan rate will make for a better quality image once a region of interest has been identified.

#### *2.2.3.3 Detection of Backscattered Electrons*

For the images taken in backscattered detection mode, the electrons interact with atoms lower into the surface than secondary electron imaging [138]. It is backscattered electrons that are generated from lower within the sample, creating a tradeoff of topographical data for elemental information. In replacement of this information is the benefit of elemental analysis, showing different compositions as different brightness. The higher the atomic number the brighter the area appears in the images, for IDIDs this is indicative of alkali, alkali earth metals and surface metals of injector parts and areas of darker regions typically are carbonaceous based.

Using both secondary and backscattered modes can aid in creating a better understanding of the topography of a sample and then with elemental information why certain topographies have occurred.

#### *2.2.3.4 Energy Dispersive X-ray Analysis and Inca Project Software*

Energy dispersive X-ray (EDX) analysis provides elemental analysis [147, 148]. And is the detection of detection of characteristics X-rays. Excited particles such as electron, protons or X-rays collide with the atoms in the top 2  $\mu\text{m}$  of the sample and the interaction results in X-rays being emitted. The X-rays can then be detected and are specific to different energy levels in an element [148, 149]. It is typically the K and L lines at a given keV that are detected from elements. The K line is from the excitation of the electron in the shell closest to the nucleus, whereas the L line is the next electron orbital shell. The lines are also noted in importance from  $\alpha$  to  $\beta$  and so on, for all versions of the K and L lines. These lines will be detected and at different keV [139, 140, 142, 146], therefore providing further evidence of each element as different K and L lines will be detected at different keV, providing a fingerprint like distribution of detected lines. The Inca software will suggest the elements detected from EDX analysis.

#### *2.2.3.5 Scanning Electron Microscopy (SEM) Experimental*

Scanning Electron Microscopy (SEM) analysis of the samples was carried out with a FEI XL30 FEG-ESEM, equipped with an energy dispersive X-ray (EDX) detection system, which was used for EDX chemical analysis. The accelerating voltage used was between 10-15 kV and for the scattered and back scattered electron modes the spot size was 3.0. However, for detection in the 'wet mode' the spot size was 4.0. The working distance ranged between 8.8 -24

mm. SEM analyses of the JFTOT tubes was carried out with a JEOL 6490LV SEM. The accelerating voltages used were between 10-20 kV. For the scattered electron mode the spot size used was 3.0.

#### **2.2.4 Focused Ion Beam (FIB)**

Focused ion beam (FIB) is a technique that uses a precise ion beam to alter sections on the surface of a sample [150-152]. This includes milling out sections to isolate areas for depth profiling, and to deposit electrically insulating regions or conducting contact areas large enough to analyse [153-155]. Applications of FIB have been used in material science, semiconductors and more recently for application with biological samples. For this work FIB was used to mill lift outs of deposit for further analysis and to create trenches to reveal a wall of sample which allowed for further analysis of the deposit layers. A FIB can be a standalone instrument, however, adaptations have included FIB to be combined with SEM, auger electron spectrometry, transmission electron microscopy and secondary electron mass spectrometry [156].

A FIB instrument consists of a vacuum system, chamber, liquid metal ion source, an ion column, sample stage, a gas delivery system [152] and a SEM instrument. The stage can move in *xyz* planes, rotate and tilt, providing full access to the sample.

##### *2.2.4.1 Sample Preparation for Focused Ion Beam*

There is no specific sample preparation needed for the FIB, however, similar to ToF-SIMS the instrument requires a high vacuum. The samples therefore need to have low volatile content so that the instrument can reach an appropriate vacuum.

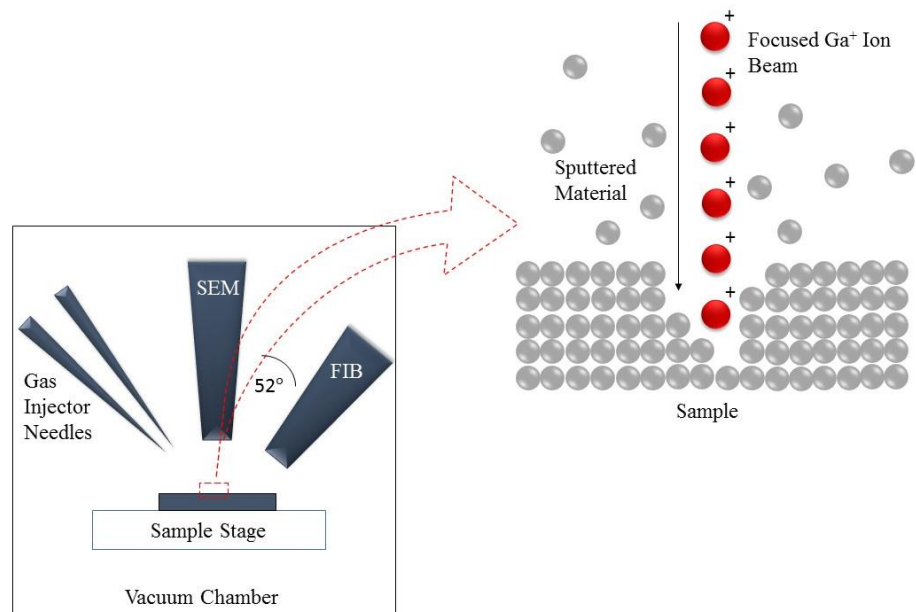


Figure 2.9 Schematic of FIB, modified from Kant et al. [157].

#### 2.2.4.2 Liquid Metal Ion Source and Ion Column

A FIB instrument uses gallium ( $\text{Ga}^+$ ) as the ion source. The advantages of using gallium as the ion source include a low melting point ( $30^\circ\text{C}$ ), low volatility and vapour pressure, small energy spread and advantageous mechanical, electrical and vacuum properties [158].

When the Gallium is heated the metal begins to melt, and then is contacted by a tungsten filament where the liquid metal flows along causing surface tension and creates an electric field. When the liquid Gallium reaches the end of the filament the electric field that has been created causes ionisation and field emission of the  $\text{Ga}^+$  ions. The ion beam can be focused onto the surface of the sample by electrostatic lenses and accelerated at an energy of 1-50 keV [157]. The FIB is as precise as an area size in the order of a few nanometers. The energy of the beam can be low voltage which is useful when analysing delicate

material or a high voltage which will sputter through more dense material such as metals.

#### *2.2.4.3 Gas Delivery System*

When obtaining a lift out, the area that has been chosen will then have platinum deposited on the section [151, 152]. By using a gas delivery system a thin layer of platinum can be deposited onto the surface and with high levels of accuracy. The platinum is for protection of the material from the ion beam but also to create a flat surface for the beam to mill through the material in a uniform manner. This is particularly crucial for uneven surfaces, such as the deposits analysed in this research.

#### *2.2.4.4 Selective Carbon Mill*

A selective carbon mill is a milling ion beam specifically for carbon based material. The source uses  $\text{MgSO}_4 \cdot 7\text{H}_2\text{O}$ , and produces a focused beam of water ions to mill through the sample. By using this milling tool, contamination and deposited  $\text{Ga}^+$  ions are reduced.

#### *2.2.4.5 Omniprobe*

When a lift out is ready for removal the sides have been milled and there is only a small attachment to the lift out and the sample, then an Omniprobe micro tweezer must be inserted to attach to the lift out. For removal platinum is deposited onto the connection between the lift out and the tweezers. Finally the section still holding the lift out in place must be milled through to cleave any attachments, then the tweezer can freely move the lift out away from the sample.

#### 2.2.4.6 *Scanning Electron Microscopy (SEM) and Energy Dispersive X-ray (EDX) Analysis*

The FEI Quanta 200 3D is equipped with SEM and EDX analysis, which uses Inca project software to collect data. The area in a sample that has been milled by the Ga<sup>+</sup> ion beam or a lift out can then have the SEM images and EDX data collected.

#### 2.2.4.7 *Experimental of Focused Ion Beam (FIB)*

Analysis was carried out using a FEI Quanta 200 3D, equipped with dual beam to combine focused ion beam (FIB) with scanning electron microscopy (SEM). The accelerating voltages used were 1-15 kV. The sections were cut at 5 micron thickness and deposited onto a copper transmission electron microscopy (TEM) grid. The samples were mounted on a TEM holder stub for the SEM and imaged at a tilt of 0-20 degrees, using secondary imaging mode. The lift outs were rough 5 × 5 μm and 50 × 50 μm in size.

### **2.2.5 Hydropyrolysis (HyPy)**

#### 2.2.5.1 *Theory of Hydropyrolysis*

Hydropyrolysis (HyPy) is a technique of pyrolysis under a high pressure of hydrogen, usually at a pressure of 150 bar. Using high-pressure hydrogen releases volatile matter by reducing chemical functionality and strips away the matter in a high pressure environment which is more effective than an inert atmosphere and/or under atmospheric pressure [100, 159-161]. The application of hydropyrolysis at 550 °C with a nickel/molybdenum or cobalt/molybdenum based catalyst removes biomarkers from a sample. The catalyst acts to remove weaker heteroatomic functionalities and prevent fragmentation and rearrangement of the volatile matter removed [99, 102]. The hydropyrolysis rig

is a closed system and collects volatile matter in a trap. Further analysis on the labile fraction with gas chromatography mass spectrometry (GC-MS) aids the analysis of samples by giving a comprehensive chemical description of the sample. HyPy has been applied to analyse the release of certain biomarkers, rendering this technique useful when looking at the composition of petroleum source rocks and heavy oil fractions [99, 101, 162]. By removing the labile fraction the recent history of the matter is removed and then the earlier material can be analysed.

For work in this thesis the temperatures applied in hydrolysis were up to 350 °C, this was to act as a thermal treatment to remove volatiles rather than extracting biomarkers from the sample. As carbon rich samples are heated to above 500 °C, there is a risk of altering the structure of the carbon environments. Due to not taking the sample to temperatures above 350 °C no catalyst was required. Hydrolysis is typically used up to 550 °C with a molybdenum catalyst, the labile fraction removed can be indicative of the sample upon GC-MS analysis. However, for this work analysis of the remaining material on the IDID was of higher priority.

#### *2.2.5.2 Sample Preparation for Hydrolysis*

There is no sample preparation required for hydrolysis, however, as the thermal treatment heats up to 350°C, one consideration to make is if the sample will be stable up to this temperature. The reactor vessel is roughly 1 cm in diameter so this restricts the sample size that can be analysed.

#### *2.2.5.3 Gas Supply*

The gas usually used in the hydrolysis rig is hydrogen, however, the rig can be altered to inlet any gas that is fitted with a regulator adjusted for 30-50

bar. The rig boosts the pressure of the gas to 150 bar for treatment of samples. A schematic of the HyPy rig can be observed in Figure 2.10. Pressure in the system is set at 30 bar before opening valve 5 and boosting pressure to 150 bar.

#### 2.2.5.4 Experimental of Hydrolysis

For test conditions of hydrolysis, each sample was rapidly heated to 250 °C at a rate of 300 °C/min and then at a rate of 8 °C/min until reaching 350 °C under a hydrogen stream at 150 bar, with a flow rate of 5 L/min. Once at 350 °C, the temperature was held for 5 mins. No silica trap was required for the carbonaceous reference samples as it was only the change in  $I_D/I_G$  ratio that was of interest and not the chemistry of the volatile matter. A silica trap and dry ice was used to trap the volatile matter from the five injector needles. The labile fraction was subsequently analysed with GC-MS. The apparatus has been described in detail previously [99, 162].

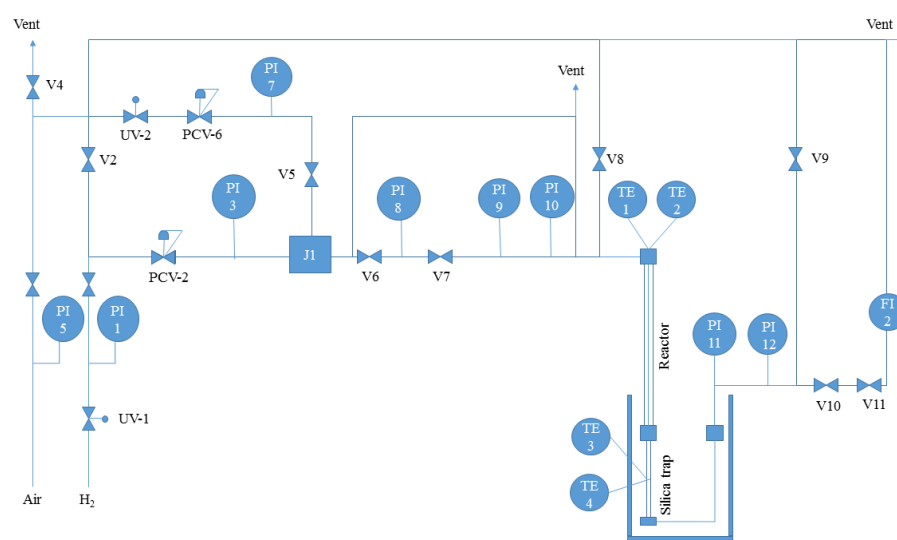


Figure 2.10 Photo of schematic of a HyPy rig, showing where the valves, reactor and trap are in the pipeline.

## 2.2.6 Gas Chromatography Mass Spectrometry (GC-MS)

### 2.2.6.1 Theory of Gas Chromatography Mass Spectrometry (GC-MS)

Gas chromatography mass spectrometry (GC-MS) is a partition technique that uses the combination of gas chromatography (GC) and mass spectrometry (MS) to analyse a sample [163, 164]. The gas chromatography uses a carrier gas which is called the mobile phase, in this work the gas was helium, an inert gas must be used so that it does not interact with the sample. The sample and carrier gas is then eluted through a column, called the stationary phase, and separates molecules based on their volatility, intermolecular forces or ease with which they evaporate into a gas. A schematic of a GC-MS can be observed in Figure 2.11. Generally the smaller the molecule the faster it will travel up the column for detection. The detector generates chromatograms of retention time against relative abundance, where the intensity of the peaks are proportional to the concentration of the component [165]. The output from a GC will show a peak at a given retention time for a given molecule, however, molecules that are structurally and chemically different can have the same retention time but not be distinguished in GC. At this stage the mass spectrometer will produce a mass spectrum to identify the molecules in a peak of a given retention time, ruling out the possibility for molecules to be wrongly identified. It is possible for a GC to identify a sample less than 1 ng [166].

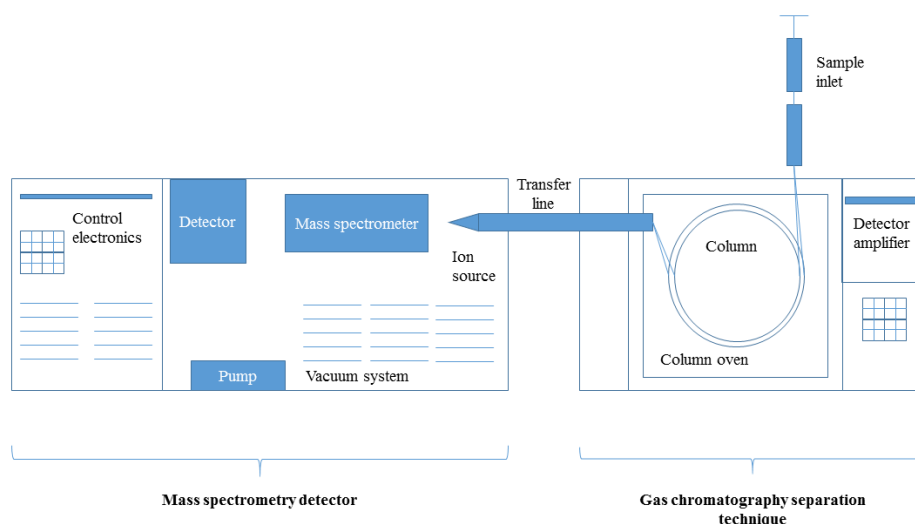


Figure 2.11 Schematic of a GC-MS, modified from Hussain et al. [167].

The second stage is the mass spectrometry, the mass spectrometer used in this work was an electron ionization and quadrupole analyser. The electron ionization creates ions which are then separated by the quadrupole mass analyser. The molecules enter and are hit with free electrons generated from a filament, this causes fragmentation and is known as ‘hard ionisation’. The energy given to the electrons will dictate the fragmentation pattern however this can be compared to a known spectra of masses to aid identification. The next stage of a mass analyser is the quadrupole mass spectrometer. As the name implies there are found cylinder rods which filter the sample ions based on the mass to charge ratio ( $m/z$ ). The rods have an applied voltage to them which then dictates which mass of ions reach the detector. The quadrupole rods will disrupt the trajectory of any other mass not within the set limits and therefore not let that ion reach the detector. .

### 2.2.6.2 *Experimental of Gas Chromatography Mass Spectrometry*

The thermally labile products from the injector needles were desorbed from the silica and recovered from the hydrolysis trap with 10 mL dichloromethane (DCM). The extraction was then evaporated to 100  $\mu$ L under a stream of nitrogen at room temperature prior to analysis. GC-MS analyses in full scan mode ( $m/z$  40-400) were performed on an Agilent 7890 MGC gas chromatograph, interfaced to an Agilent 5977 MSD spectrometer. Separation was achieved on a HP-5MS fused silica capillary column (30 m  $\times$  250  $\mu$ m  $\times$  0.25  $\mu$ m), with helium as the carrier gas, and an oven setting of 50  $^{\circ}$ C (hold for 2 min) to 300  $^{\circ}$ C (hold for 20.5 min) at 4  $^{\circ}$ C min<sup>-1</sup>. The assignments for the spectra were verified by a mass library attached to the OpenLAB software.

## 2.2.7 **Computed Tomography**

### 2.2.7.1 *Theory of Computed Tomography*

Computed tomography uses X-rays to create cross sections of a sample to provide a 3D image without destroying the sample [168-170], a schematic of computed tomography can be observed in Figure 2.12. Due to its non-destructive nature, low harm and risk to patients and/or sample it has many applications. This technique has been used for medical imaging, biomedical samples, industrial applications such as foods, microfossils, and other samples with tiny detail [171].

There are two ways for the technique to be set up, both the X-ray source and detector are stationary during the scan while the sample/patient rotates, or the sample/patient is stationary in space while the X-ray tube and detector rotate around. Computed tomography can image dense material such as metals and alloys and differentiate between these densities to provide images of

contrasting material. There was no sample preparation needed to obtain computed tomography images.

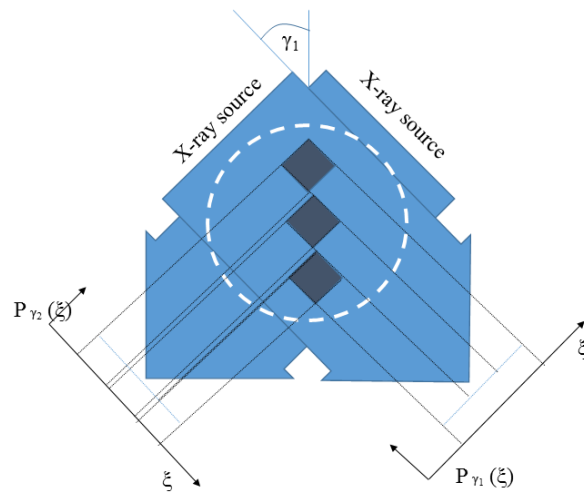


*Figure 2.12 Schematic of computed tomography, modified from Buzug et al. [172].*

#### 2.2.7.2 Experimental of Computed Tomography

The injectors were scanned with a Pheonix V|tomex| M 240 X-ray computed tomography system (GE Sensing and Inspection Technologies, GmbH, Wunsdorf, Germany) with a maximum electron acceleration energy of 300 kV and lateral resolution beyond down to  $< 1 \mu\text{m}$ . Settings for the sample were as follows 220kV, 110  $\mu\text{A}$ , 29  $\mu\text{m}$  resolution, 500 ms detector exposure time, 1800 radiograph images over 360 degree rotation where, each radiograph was 1 image. The X-ray beam was filtered with 0.5 mm of copper. The total scan time was 25 mins. The software used to analyse sample data was datos|x rec, and visualised using Volume Graphics VG StudioMax (Volume Graphics, GmbH, Heidelberg, Germany).

## **2.2.8 Transmission Electron Microscopy (TEM)**

### *2.2.8.1 Theory of Transmission Electron Microscopy (TEM)*

Transmission electron microscopy (TEM) can be used to depict nanoscale structures within samples [173-175]. In this work the application of TEM is used to analyse carbonaceous material for graphitic structures, where ordering in the bonding of such material can be depicted. TEM uses a tungsten filament to produce an electron beam within a vacuum chamber, a schematic of a TEM instrument can be observed in Figure 2.13. The electrons are then accelerated through an electromagnetic field and into a focused beam [144, 176]. The beam is then passed through the sample material, the transmitted signals are detected and an image is defined. TEM provides morphology, crystallisation, stress or even magnetic domain information. A schematic of a TEM instrument can be observed in Figure 2.13.

### *2.2.8.2 Sample Preparation for Transmission Electron Microscopy*

For analysis with TEM the sample must be thin enough for the beam of electrons to penetrate through the sample. The material must be less than 5  $\mu\text{m}$  thick.

### *2.2.8.3 Experimental of Transmission Electron Microscopy (TEM)*

High resolution TEM was carried out using a JEOL 2100F microscope (JEOL, Japan) at an acceleration voltage of 200 kV.

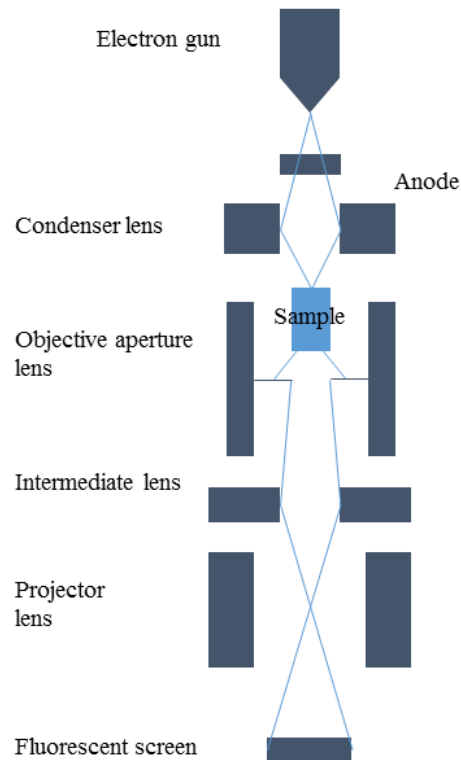


Figure 2.13 Schematic of TEM, modified from D Suneel et al. [177].

## 2.2.9 Profilometry

### 2.2.9.1 Theory of Profilometry

A profilometer uses an optical microscope to give 3D imaging. Different to a conventional microscope that has limited ability to focus on a sample with depth, the Zeta 20 3D will scan over a set vertical range [178, 179]. The profilometer will scan down the  $z$  plane for a given  $xy$  area and create a 3D image of the surface of a sample. The optical microscope also records images in true colour, to give a 3D image as well as variations in sample surface colour. The Zeta software can then be used to measure varying peaks and troughs in a sample, and also gives information on the roughness of a sample.

### *2.2.9.2 Roughness Measurements*

The Zeta 3D software can use the optical images taken by the profilometer and give roughness measurements of samples. The measurements are given in a range of ways, for this work it was reported as  $R_a$  and  $R_{pv}$ .  $R_a$  is arithmetic average of deviations from the mean and  $R_{pv}$  is the maximum peak to valley difference

### *2.2.9.3 Experimental of Profilometry*

Profiles and roughness data was collected with a Zeta 20 3D Optical Profiler and analysed with Zeta 3D software. The sample areas analysed were  $100 \times 800 \mu\text{m}$  with a  $50 \times$  optical lens.

### **2.2.10 Jet Fuel Thermal Oxidation Test (JFTOT)**

The jet fuel thermal oxidation test (JFTOT) was designed as a bench scale test to assess thermal stability of jet fuel [180-186]. More recently, the JFTOT has been applied to analysing the thermal stability of diesel fuels [46, 69, 82]. The instrument is shown in Figure 2.14. The JFTOT is representative of IDIDs found in a diesel engine because the JFTOT mimics the fuel flows in an injector. The fuel in an injector has not yet reached the combustion chamber and is flowing over a hot metal surface, as such in the JFTOT. The JFTOT is a more efficient and cheaper option to screen fuel and additive combinations before moving on to the more expensive engine test.

#### *2.2.10.1 Theory of Jet Fuel Thermal Oxidation Test*

The aerated fuel flows in through the inlet filter, over the tube located at the thermocouple and then out into the waste sample beaker. The conditions at the JFTOT tube are  $260 \text{ }^\circ\text{C}$  at 30 bar [69, 82]. Whilst the fuel comes into contact with the tube it is likely to degrade slightly due to the conditions of temperature

and pressure. As the fuel flows over the tube from bottom to top, material is deposited on the surface of tube [180-183]. Once the test is over the tube profile is measured to determine the thickness of the deposit. The profile can then be compared to other fuels to determine which fuel is more thermally stable. It was suggested that this would also be a suitable bench scale test for diesel. The model used in this work was a mark III, therefore the conditions can be changed to suit jet or diesel fuel. In Figure 2.14 a photo of a JFTOT mark III can be observed, the two beakers show the inlet and outlet of fuel. Where the part is labelled heater section is where the test tube is found, with the thermocouple placed down the inside of the tube. The fuel flows from the inlet beaker through the system over the test tube from the bottom to the top and then back out to the waste beaker.

#### *2.2.10.2 Experimental of JFTOT*

An Alcor JFTOT III was adapted to assess deposit formation from diesel fuels. A volume of fuel was pumped at a fixed rate of 3 mL/min through an initial filter unit containing a 4  $\mu$ m filter paper cut from a new diesel fuel filter. The fuel was then passed over a stainless steel test piece heated to 260 °C. The total test time was 150 or 450 mins and at the end of tests the metal test piece was cleaned with analytical grade toluene and acetone and dried in an oven.

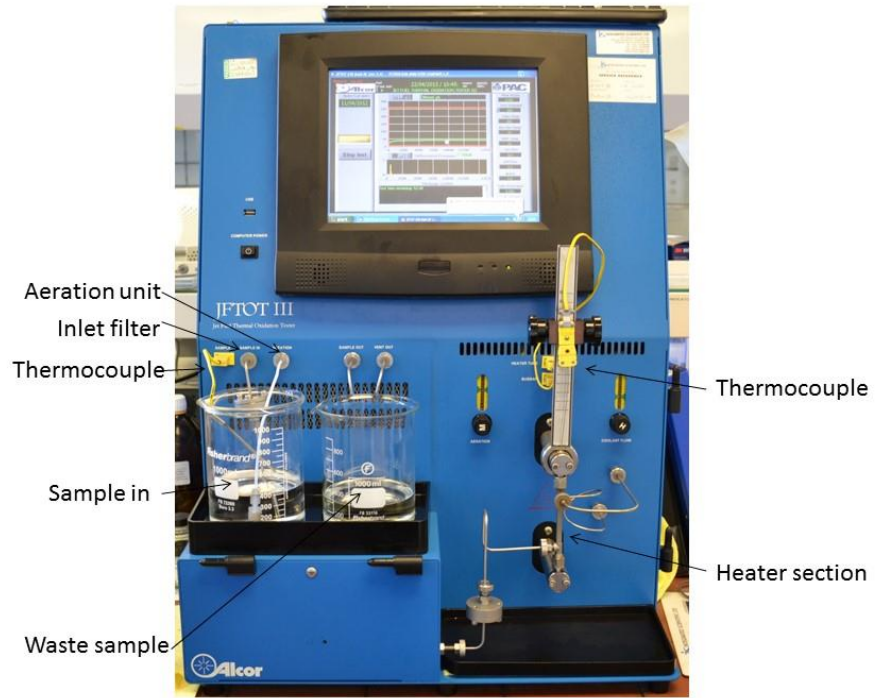


*Figure 2.14 Photograph of the JFTOT mark III*

## **3 Evaluation of Analytical Techniques for the Application of Surface Analysis of IDIDs**

### **3.1 Summary**

In this chapter, well established analytical techniques have been applied to analysing IDIDs, by overcoming the unconventional nature of these topographically difficult samples. The techniques that have been applied include: computed tomography, scanning electron microscopy energy dispersive X-ray (SEM EDX), transmission electron microscopy (TEM), atomic force microscopy (AFM), profilometry, focused ion beam (FIB) and Raman spectroscopy.

The results observed elemental differences observed within a sample with backscattered detection SEM images and EDX analysis. Profilometry and AFM has shown that the diesel deposits differ in rigidity, height and adhesion, providing evidence that there are variations on the surface and areas where bonding of debris is more likely to occur. The graphitic structure has been investigated with TEM and Raman spectroscopy, showing that there is pseudo graphitic structure in the IDIDs. However, Raman data could not be obtained due to extensive fluorescence, if this could be overcome the technique might provide insight into the graphitic content of IDIDs and demonstrate that the deposit forms ring structures over time on the needle. This has created a need for further investigation for a method to remove the fluorescing material. The technique that shows the most promise is FIB which has been used for sample preparation by obtaining a lift out which creates a wall of sample uncovering the lower layers and creates a surface to analyse. The surface

techniques that have shown promise could be used in conjunction with FIB to provide a comprehensive analysis. The premise of this chapter is to apply conventional surface analytical techniques to IDIDs, in which it will be devised which techniques to pursue and the best methods of application.

## **3.2 Results and Discussion**

### **3.2.1 Computed Tomography**

Computed tomography images can provide three dimensional images of a samples, a variety of images from injector tips 4, 5 and 6 can be observed in Figure 3.1. The computed tomography image in Figure 3.1i depicts the needle inside the injector tip and has been highlighted in yellow, the spring that aids in maintaining the high pressure has been coloured in red. The computed tomography images show the tight tolerances experienced in the injector system, seen in Figure 3.1iii. Figure 3.1ii shows the top of the injector tip where the holes reside to the combustion chamber. This is where the fuel is injected into the combustion chamber at extreme pressures and causes ignition. The holes are a crucial location where fuel deposits build up and cause inefficiencies in engine output. Figure 3.1iii-iv are cross sections through the length of an injector. The needle has again been emphasised in yellow to highlight the tight tolerances and indicate how little deposit would be required to restrict the flow of fuel and block the needle. Figure 3.1iv shows the needle as a brighter area in the image, this is due to the needle being made of a more dense material than the injector tip, this is because the needle would need to withstand greater mechanical force.

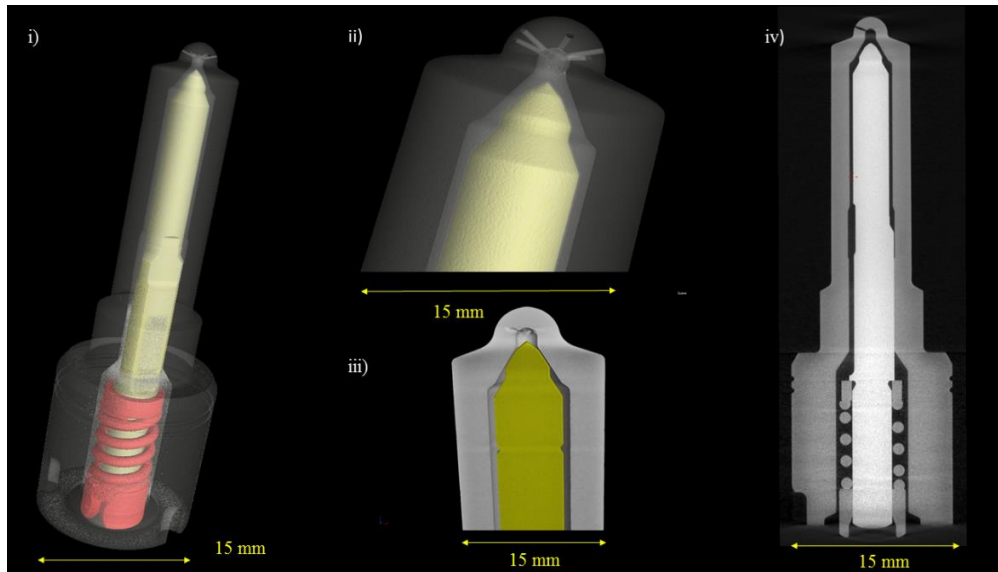


Figure 3.1 Computed Tomography images of injector needle inside injector tip.

The images shown in Figure 3.1 give a novel understanding of how an injector needle resides inside of an injector tip. These images demonstrate previously unobserved visual representation of how the injector resides inside the tip to create high pressure to inject the fuel through the holes shown in Figure 3.1ii. The deposits that are causing problems in the field are found on the surface of the needle coloured in yellow in Figure 3.1i-iii. With the tight restrictions around the needle it can be observed that not a lot of debris would be required to fill the space.

The aim of this work, described in chapter 1, was to determine if the deposit was altered in removing the needle from the injector tip. The injector system must be forcefully opened to remove the injector tip and occasionally due to the needle being stuck inside, it cannot be removed by hand and require machinery to extract the needle. Therefore, it was described as an objective to image the needle deposit *in situ* before removal. However, due to the deposit

potentially being too thin, the injector material being too dense or the spatial resolution of this equipment, the deposit could not be seen. This aim was deemed to not be of high priority so this was not explored any further, however, an instrument with higher spatial resolution could be explored in future work.

### 3.2.2 Scanning Electron Microscopy (SEM)

SEM is a standard technique to look at the topographical differences on a sample's surface. There are two detection modes, secondary electron and back scattered electron mode, discussed in, section 2.2.3.

#### 3.2.2.1 Secondary Electron Detection Mode

Secondary electron SEM images of injector needle 14 can be observed in Figure 3.2 and the computed tomography image of the needle depicting the location. The images show three points along the needle and how the deposit can topographically vary. The images show that deposit has built up along the needle. Due to secondary electron SEM imaging giving topographical information and the deposits being a low thickness there are not many topographical features to identify.

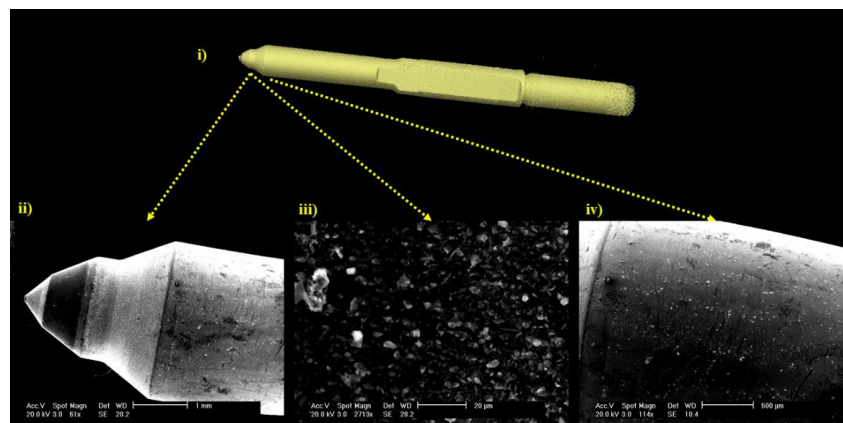
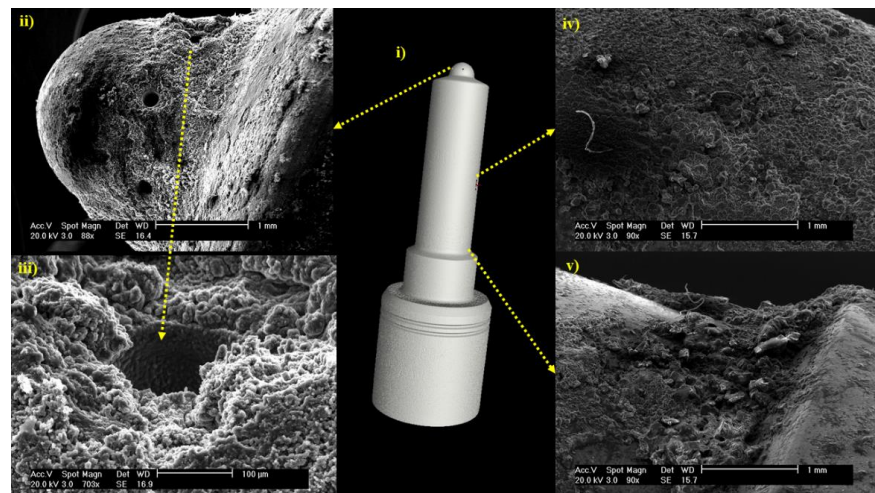


Figure 3.2 SEM image in secondary electron detection mode depicting the surface topography of injector needle 14.

Secondary electron images of injector tip 8 can be seen in Figure 3.3. The computed tomography image in the centre shows where the SEM images have been taken from. An injector tip resides inside the combustion chamber, therefore thick carbonaceous deposits are common, which give clear topographical differences with SEM images. The deposit appears to be granular and disordered in appearance observed in Figure 3.3. Figure 3.3i and iii show the tip and holes, it can be seen that there is a lot of deposited debris around and inside the holes, which reduce engine efficiency [6]. Figure 3.3ii and iv show the depository build up on the shaft of the tip, which has occurred over time due to the deposit not hindering the combustion process. For samples like an injector tip that has a lot of deposit built up on the surface then secondary electron imaging is useful in showing how topographically different areas on the sample can be and observing the restrictions of the injector tip holes as seen in Figure 3.3iii.



*Figure 3.3 SEM image in secondary electron detection mode depicting the surface topography of injector tip 8.*

The deposit found on push rod 1 is in Figure 3.4 and has cracks within the deposit. It is not known if the deposit formed as one structure and then cracked or if the deposit grew as a column like structure. It is speculated that the deposit appears to be peeling away from the surface, the surface of the push rod can be seen in the centre of the SEM image Figure 3.4iii, where a piece of the deposit has thought to have broken away. The push rod is a surface encountered in the early stages of the combustion process.

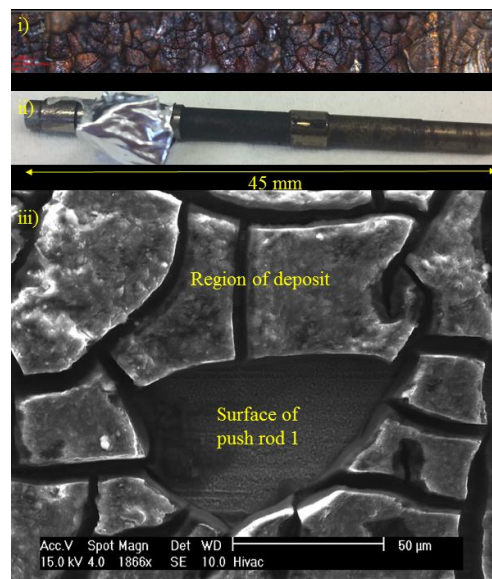


*Figure 3.4 i) An optical image of the surface of push rod 1 ii) An optical of pushrod 1 iii) A SEM image in secondary electron detection mode depicting the surface topography of push rod 1.*

Secondary electron SEM provides clear images of the topography of samples and is more applicable to the injector tip and push rod, where there is thicker deposit and more topographical differences. Secondary electron SEM imaging is not as beneficial for samples such as the needle, due to the deposit being thin. SEM is regarded as a surface analytical technique so there is no information given about the lower layers of deposit or the chemical

composition. The SEM images in the section are similar to topography to the images shown in section 1.8.7. Therefore no further information can be obtained from continually pursuing SEM imaging of IDIDs.

### 3.2.2.2 Backscattered Electron Detection Mode

Backscattered electron SEM images of injector needle 12 can be observed in Figure 3.5. From Figure 3.5i the different chemistries at the tip can be seen, it appears that there are three different regions. Some needles are coated in a diamond like coating [130, 187], which would appear dark in backscattered detection. This is likely to be what this image is showing and the deposits contains alkali metals and contaminants that have a higher average atomic mass, and therefore appear brighter. The brightest area is at the end of the needle, it could be due to the diamond like coating being worn away from the mechanical stress placed on the end and showing the more dense material underneath.

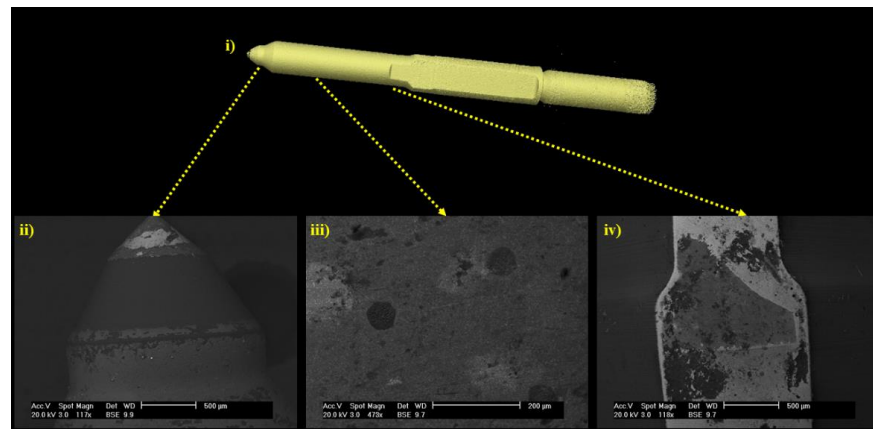


*Figure 3.5 i) Computed tomography image of injector needle. ii) Backscattered SEM image of needle 11. iii) Backscattered SEM image of needle 11. iv) Backscattered SEM image of needle 11.*

The surface of injector tip 3 is visible beneath the deposit as a brighter material, evident in Figure 3.6ii and iv. The deposit appears to be uniform in the elemental information being given. The deposit is a lot darker than the surface of the injector tip therefore suggesting a lower atomic mass, which is most likely to be carbon rich. For the injector tip where the deposit appears to be elementally uniform then the use of back scattered imaging is not as useful.

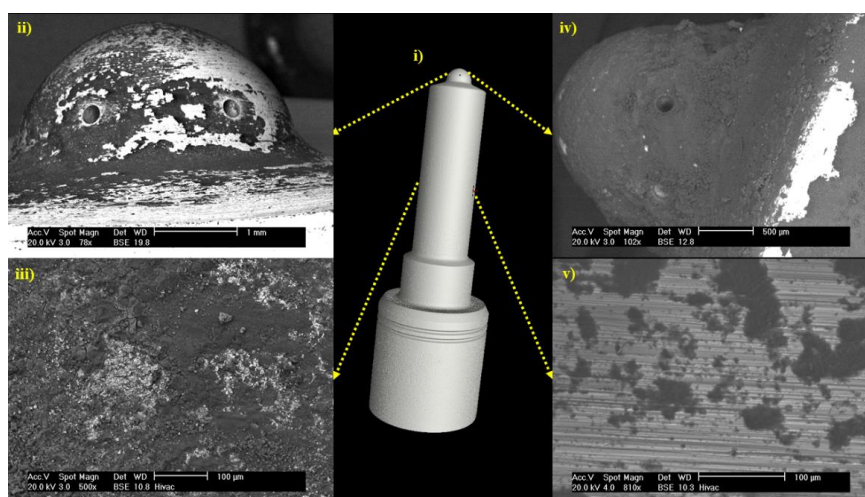


*Figure 3.6 SEM image in backscattered electron detection mode depicting the surface topography of an injector tip.*

The backscattered images of push rod 1 shows that there was a layering effect in the deposit, observed in Figure 3.7. The lower layer was a brighter colour in the image, giving evidence that the atomic weight of the material on the bottom of the deposit was higher than the uppermost deposit. The higher atomic mass was likely to have come from the surface of the push rod. The top layer is darkest which would suggest this is the lowest atomic mass material, which is most likely to be carbon based.

The images of needle 11 and push rod 1 in Figure 3.5 and Figure 3.7 show that there are elemental differences in the deposit, whereas for the injector tip

observed in Figure 3.6 there is no chemical difference in the deposit. Using back scattered detection is only beneficial for samples that have chemical differences, and as seen for push rod 1 in Figure 3.7, the layering structure can be observed. However, as previously discussed this is only a surface technique and it was fortunate that the side profile of the deposit on push rod 1 in Figure 3.7 could be observed.

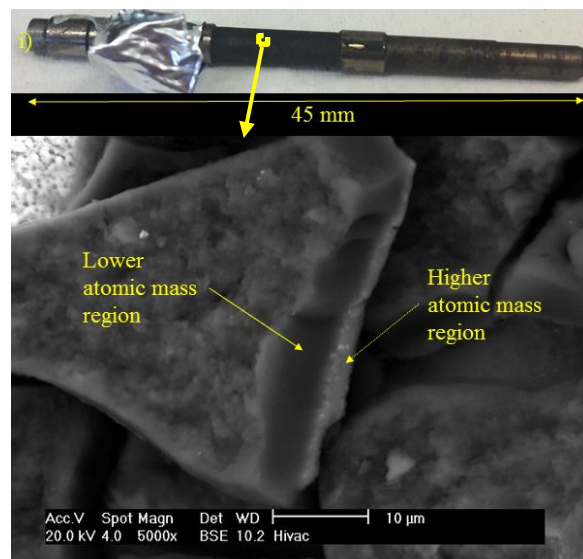


*Figure 3.7 SEM image in backscattered electron detection mode depicting the surface topography of push rod 1.*

### **3.2.3 Energy Dispersive X-ray Analysis (EDX)**

Energy dispersive X-ray (EDX) analysis is typically attached to a SEM to compliment the topographical and elemental information of SEM. EDX uses X-rays to identify which elements are present in the sample. A SEM image of needle 2, shown in Figure 3.8, shows the location of where the EDX data was collected, the EDX data is detailed in Table 3.1

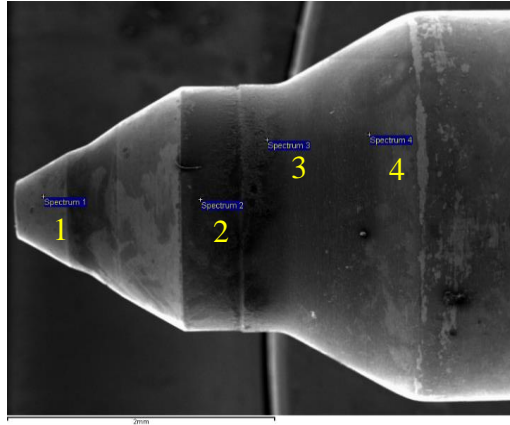


Figure 3.8 Location of EDX data taken of Needle 2.

Table 3.1 EDX data of needle 2. Locations of spectra are shown in Figure 3.8

Element	Spectrum 1	Spectrum 2	Spectrum 3	Spectrum 4
<b>C</b>	30.97	76.54	17.08	68.93
<b>O</b>	19.18	18.63	16.9	0
<b>Na</b>	1.11	2.13	1.68	0
<b>Si</b>	5.29	0	0	0
<b>P</b>	0	0	1.38	0
<b>S</b>	0	0	0.07	0
<b>Cl</b>	0	0.39	0	0
<b>V</b>	0	0	1.25	0
<b>Cr</b>	36.6	2.3	31.94	28.5
<b>Fe</b>	6.85	0	23.12	1.62
<b>Mo</b>	0	0	3.09	0
<b>Ag</b>	0	0	0	0.95
<b>W</b>	0	0	3.49	0
<b>Total</b>	100	100	100	100

From the backscattered SEM images seen in section 3.2.2.2 Figure 3.5, there was a range of areas that had different chemistries. In order to capture the range of potential information, the EDX analysis of needle 2 investigated four different points along the tip, shown in Figure 3.8 and the variation in EDX has

been tabulated in Table 3. All of the analysis points include C, Na and O. The amount of C detected was highest at point 2, which also has high levels of O and Na, therefore it is possible that there is a bonding structure with these elements, such as a sodium carboxylic acid group. There was only Si detected on point 1, whilst the detection of Fe, Mo, S, Ag, W and Cr were found in points 3 and 4, towards the back end of the tip.

It was observed in Figure 3.4 that push rod 1 had suspected deposit removed. There were two EDX data points taken for push rod 1 shown in Figure 3.9, the EDX data can be observed in Table 3.2. One analysis point was taken from the lower layer, the surface of the push rod (spectrum 1) and the second from the top deposit layer (spectrum 2).

The EDX data from spectrum 1 shows the surface of pushrod 1 to consist of more O, Si, Ca, Cr, and Fe. The EDX data for spectrum 2 shows that the deposit layer consists of more C, N, Na, S and Cl. Spectrum 1 is higher in composition of metals which are to be expected to be the material of the push rod. Spectrum 2 consisting of large quantities of C, N and S, which is indicative of carbonaceous deposit and additive contamination [67, 69].

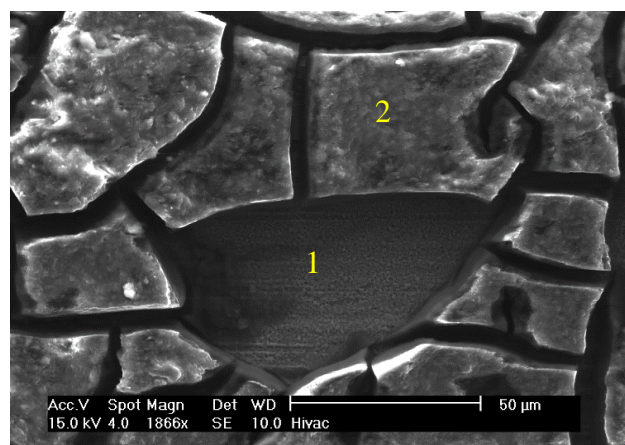


*Figure 3.9 EDX analysis of push rod 1 and location of spectra 1 and 2.*

Table 3.2 EDX data collected from push rod 1.

<b>Element</b>	<b>Spectrum 1</b>	<b>Spectrum 2</b>
<b>C</b>	12.12	55.81
<b>N</b>	0	21.09
<b>O</b>	17.58	16.44
<b>Na</b>	0.31	0.77
<b>Si</b>	1.43	0.18
<b>S</b>	0.19	0.42
<b>Cl</b>	0	0.08
<b>Ca</b>	0.2	0.13
<b>Cr</b>	0.67	0.09
<b>Fe</b>	67.5	5
<b>Total</b>	100	100

The EDX data provides evidence of the elements found in the sample which is advantageous to provide a comparison of a range of different regions in a SEM. However, only the elements are identified and there is no information as to how the elements are bonded. As with SEM only the surface is analysed and there are more sophisticated analytical techniques that provide more information. Therefore it was concluded that SEM EDX was not a priority analytical technique to further explore with IDIDs.

#### **3.2.4 Transmission Electron Microscopy (TEM)**

Transmission electron microscopy (TEM) is an electron microscopy technique that analyses on a smaller scale to SEM and identifies bonding structures within a sample. The deposit on needle 15 was scrapped from the surface and analysed with TEM. The image shows that there was some pseudo graphitic structure in the deposit due to the patterning and regular bonding of the atoms. Owing to the needle environments experiencing up to 260 °C [98], the formation of such graphitic structure would not be anticipated. This finding

therefore suggests that the pressure in the injector system is having an effect on the deposit formation process. The TEM work from Venkataraman *et al.* did not show any graphitic structure. This would indicate that there is variation in deposits as there appears to be a difference in the structuring and as suspected deposits are unlikely to be all the same.

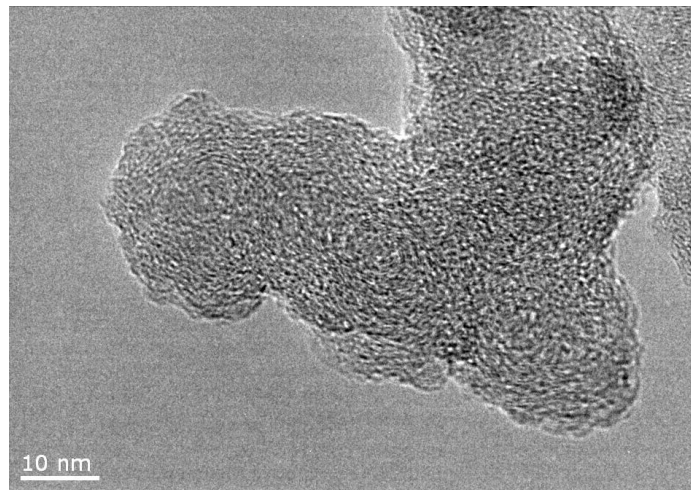


*Figure 3.10 TEM image of injector needle deposit [155].*

TEM shows future potential for analysing the graphitic structure within a sample. For the analysis of needle 15 due to the deposit being forcefully removed from the surface of the needle there is no evidence as to where the graphitic structure was within the sample, removing all history of the graphitic formation. The sample is required to be thin enough for the electron beam to penetrate through. Therefore for analysing deposit it must be scrapped or thinned, there are many examples in the literature where TEM has been used in combination with FIB, [188-190]. The combination of FIB and TEM could be a consideration for future work.

### 3.2.5 Atomic Force Microscopy (AFM)

Atomic force microscopy (AFM) is a topographical imaging technique that scans a cantilever over the surface of a sample whilst a laser interprets the differences experienced and creates an image. AFM images of needle 15 can be observed in Figure 3.11. The three images shown in Figure 3.11i-iii illustrate height, rigidity and adhesion measurements of the same area of needle 15. Figure 3.11i depicts an area of  $10 \times 10 \mu\text{m}$  and shows the height mapping of an area displaying the varying difference in topography of the surface of the needle and this is where debris can adhere onto the surface. Figure 3.11ii shows the adhesion mapping of a different area of  $1 \times 1 \mu\text{m}$ . The flatter surface to the left of the image has the highest adhesion. Incidentally this is the area of lowest rigidity observed in Figure 3.11iii. This is the more likely point for formation of more material to occur as it is a 'tacky' surface. These images show that there is large variation in the surface of these deposits and germination points for debris adhesion. The advantages of AFM are that it provides topographical, height, rigidity and adhesion measurements which provides evidence that deposits are not uniform and have large variances in all measurements. The area analysed with regards to rigidity and adhesion was  $1 \times 1 \mu\text{m}$ , which provided high resolution of the surface of this small area. The reason that the measurement for adhesion and stiffness were in volts is that both adhesion and stiffness / strain were kept as the basic output from the experiments. This would be because relative measurements of both were considered adequate and avoided some of complex cantilever calibrations to provide absolute values.

Both outputs are products of 'force curves' performed by the AFM. The basic output of a force curve is the deflection of the cantilever against height of the scanner. That deflection is measured initially in volts. It is the photodetector signal consequent to movement of the laser occurring under cantilever flex. In order to convert this signal to a 'real' value several additional pieces of information are required. Primarily the deflection sensitivity of the cantilever (the distance the cantilever actually deflects for a measured change in photodetector voltage) and the spring constant of the cantilever. Additionally however, for adhesion you also need to know / provide a model for the tip. If accurate values are required then the tip must be calibrated on reference materials with known stiffnesses. Therefore if you are primarily just interested in relative spatial differences in adhesion and stiffness these processes are often left out and the raw data values reported (which are in volts) as a relative variation.

AFM provides no chemical information, and the IDIDs cover a large surface area and due to AFM analysing small sections it would be time consuming to analyse a large surface. It was therefore decided that AFM was not a high priority technique to pursue as this was only a small area surface analytical technique and gave no chemical information, which was considered more important for the future of this research.

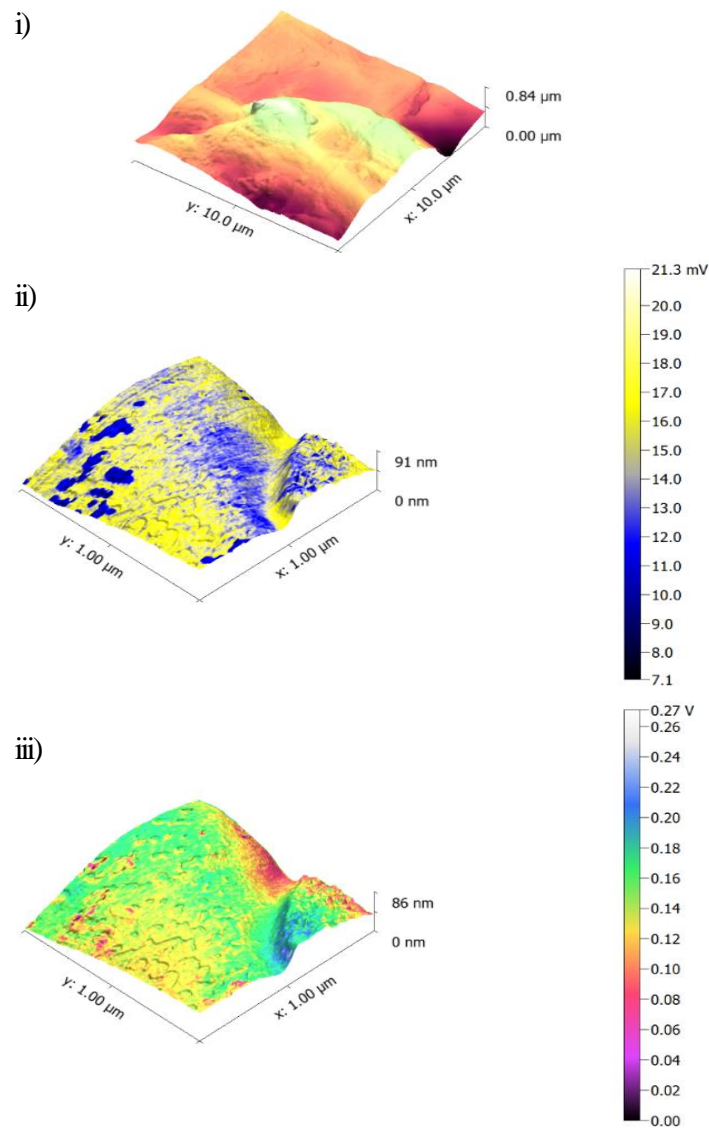


*Figure 3.11 AFM images various points on needle 15 i) Height mapping of needle 15 ii) Adhesion mapping of needle 15 iii) rigidity mapping of needle 15 [155].*

### 3.2.6 Profilometry

Profilometry is the application of an optical microscope that focusses on the surface of a sample and creates a three dimensional image. Data was collected from push rod 1 shown in Figure 3.12 and injector tip 6 shown in Figure 3.13. The images from the two samples displayed the variation that can be seen with

diesel injector samples. The push rod has experienced high pressures of near 3000 bar and temperatures of 260 °C [98]. The injector tip would have experienced much higher temperatures in the combustion chamber and lower pressures, this has affected the deposit formed. Profilometry gives true colour images of the deposits, the push rod is brown in colour. Figure 3.12i is photograph of the surface of the push rod and the profile is shown in Figure 3.12iii, showing the realistic information gained from profilometry. The deposit on the push rod had large cracks and parts have broken away, potentially suggesting that the deposit had resided on the needle for some time. The images in Figure 3.12 show points along the push rod with varying degrees of thickness and in Figure 3.12iv there are features of the push rod observed and deposit has broken away.

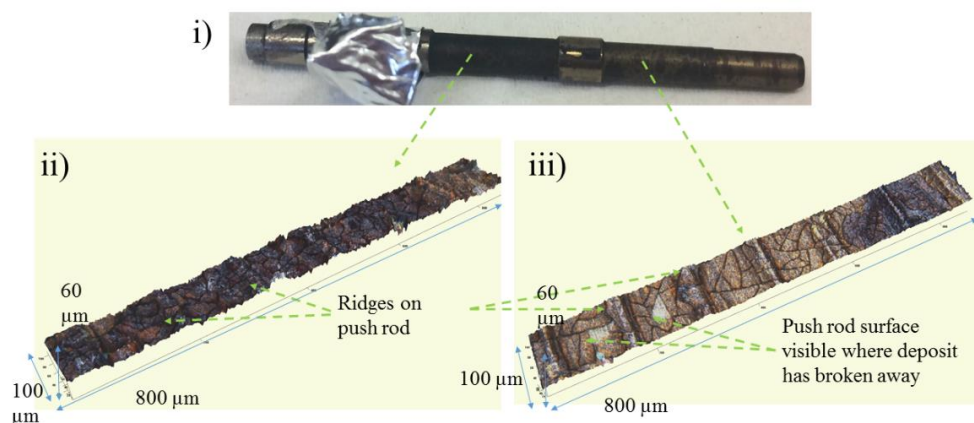


*Figure 3.12. i) An optical image of push rod 1. ii) A profile of deposit along push rod 1. iii) A profile of deposit along push rod 1.*

In Figure 3.13ii the area to the left has been scraped to reveal the surface of the injector tip. This was to allow for a step height measurement which was recorded at 90 μm, therefore for further analysis of these deposit a method that

can reach the interface would be required. In Figure 3.13iii there is a profile of an area where a depth profile with time of flight secondary ion mass spectrometry (ToF-SIMS) has been milled, this is a useful way to identify the depth that has been analysed because it is measured as a function of sputter time.

Profilometry has been deemed to be more advantageous than AFM due to analysing a larger area. Although AFM provides rigidity and adhesion mapping, profilometry can be used to create roughness measurements. Neither AFM nor profilometry provide chemical or depth information however, do give evidence that the surface of IDIDs are not smooth and uniform.

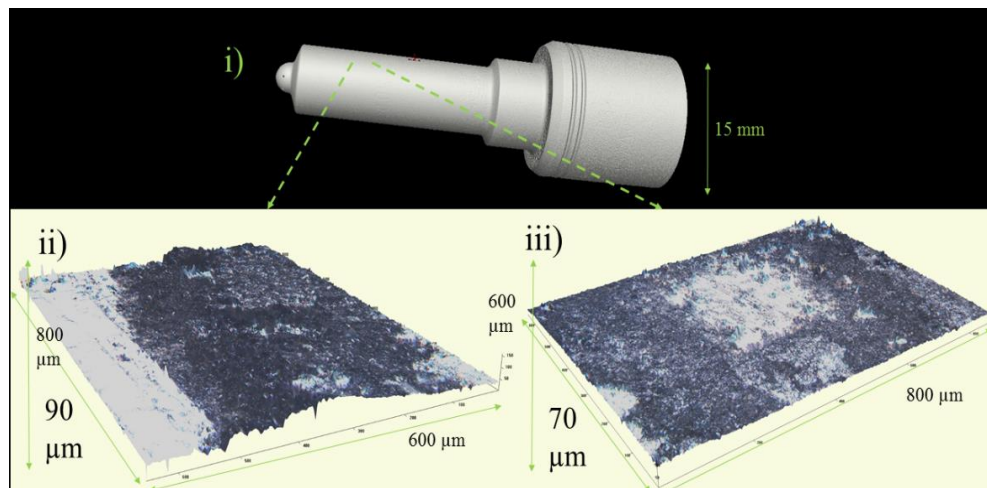


*Figure 3.13 i) Computed tomography image of an injector tip. ii) A profile of area of where deposit has been scrapped away to the surface of the shaft to identify height of deposit. iii) A profile of the area after a depth profile ToF-SIMS analysis.*

### **3.2.7 Focused Ion Beam (FIB)**

Focused ion beam (FIB) is focused beam of gallium ions ( $\text{Ga}^+$ ) that can be used to manipulate or sputter the surface of samples. FIB is typically used to create

lift outs which are walls of sample that display the lower levels of sample, the other method is creating trenches to again expose the lower levels. Most FIB instruments are equipped with SEM EDX to collect topographical and elemental information.

Initial work with a focused ion beam (FIB) created a 'lift out' from the deposit on needle 15 which is shown in Figure 3.14. The lift out is 10.63  $\mu\text{m}$  in width and 4.15  $\mu\text{m}$  in height. This aim of the work was to further analyse the side wall with Raman spectroscopy, however, due to the lift out detaching from the TEM holder, no further analysis could occur. For analysis with Raman this size would be sufficient as the area analysis size is 1  $\mu\text{m}$  diameter. This FIB lift out did provide evidence that a lift out could be obtained and it would be advantageous to further investigate the method. The images in Figure 3.14i-iv show the process of removing the lift out, creating trenches either side of the selected area, undercutting and cutting the side of the lift out, removal with an omniprobe and attachment to a TEM stub. Although this lift out was obtained from an injector needle where deposit is typically not as thick from an injector tip, the size of lift out is crucial. It is essential that the lift out is representative of the deposit. The profilometry data collected from injector tip 6 (Figure 3.13ii) showed that the deposit was 90  $\mu\text{m}$  thick. Therefore a lift out of this size would not show the full deposit history.

FIB shows great potential for the analysis of IDIDs, as previously highlighted in chapter 1 it is vital to understand how the deposit is forming from the bottom to the top. The application of FIB will provide this information, however, the size of the lift out used in this work would not be representative of thicker

deposits. It will need to be investigated if a larger lift out is viable and attempting to create a FIB trench.

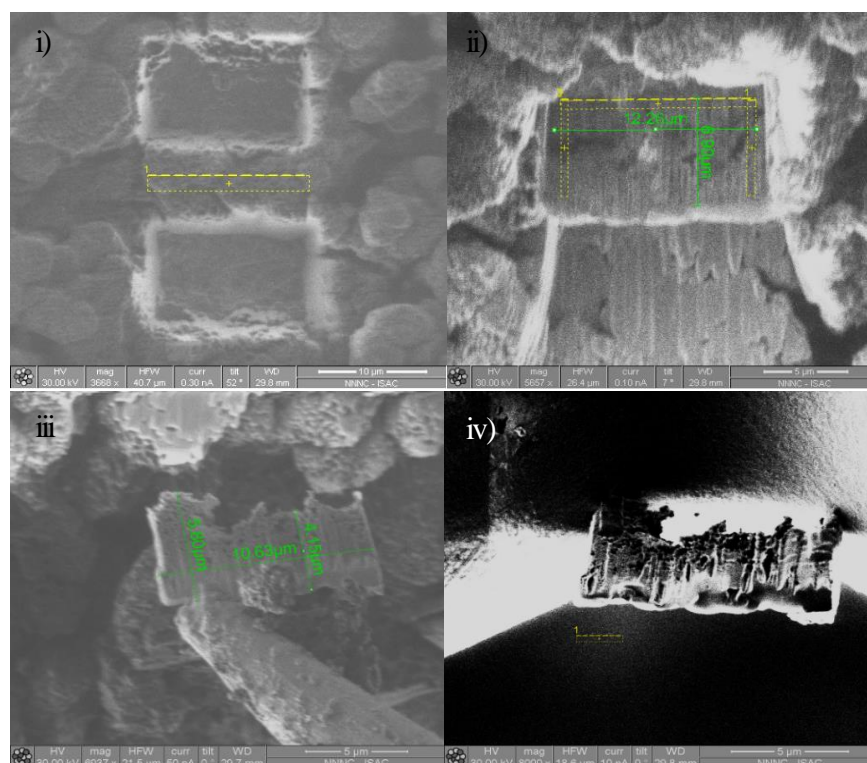


*Figure 3.14 SEM images of FIB lift out from needle 15. i) SEM of the milled trenches. ii) SEM image of the side wall of the lift out iii) SEM image of the lift out being removed from surface with an omniprobe. iv) SEM image of the lift out mounted on a TEM grid for further analysis.*

### 3.2.8 Raman Spectroscopy

Data was collected from sample push rod 1 with Raman spectroscopy. Unfortunately as shown in Figure 3.15, the data does not illustrate any significant peaks and exhibits a spectra that appears symptomatic of fluorescence. The two bands of interest should have appeared at 1380 and 1552  $\text{cm}^{-1}$  which are the D and G bands, and indicate the ratio of ordered to disorder carbon [125]. The sample heavily fluoresced even with varying the laser

strength and acquisition time. This also occurred when many of the other samples including injector tip 2 from Minnesota and needle 13 from Colorado. Raman spectroscopy shows promise for providing information on the graphitic content of a sample, which will determine if the deposit has resided on the needle for a long period. However, the problem with fluorescence needs to be addressed.

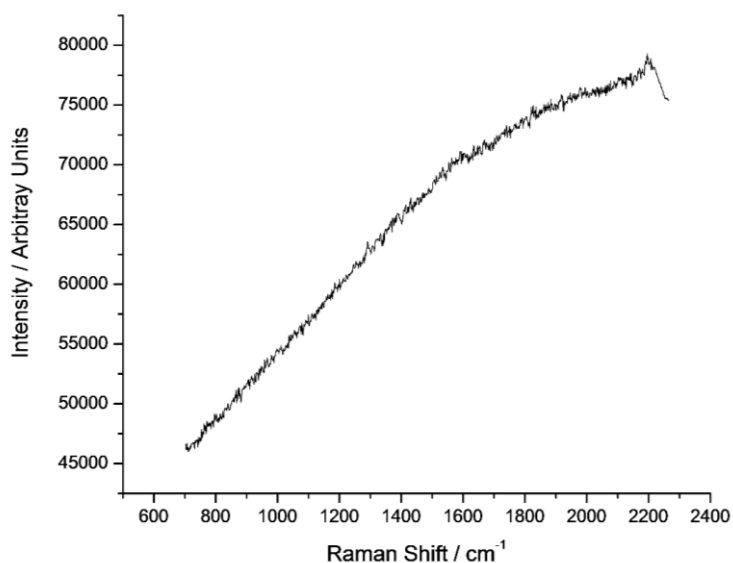


*Figure 3.15 Raman spectrum of push rod 1 showing no discernible bands*

### **3.3 Conclusions**

This chapter has explored a range of techniques to begin expanding on previous work analysing IDIDs. The techniques discussed in this chapter included computed tomography, SEM/EDX, TEM, AFM, profilometry, FIB and Raman spectroscopy.

Computed tomography was valuable in creating 3D images of the needle within the injector tip before removal and demonstrating the structure of the injector tip holes, vital for combustion. However, the deposit on the needle

could not be observed, likely due to the deposit being beyond the resolving capabilities of this particular instrument. The other technique not taken forward for further application in this study was AFM, which was due to the small scale of area analysed and the chemistry information was considered more important rather than topography which AFM provides. Furthermore, SEM/EDX and profilometry were considered useful to provide surface information however, not critical in the evaluation of analysing the IDIDs.

The techniques that were prioritised and taken further for method development were FIB, Raman spectroscopy and TEM. The use of FIB in conjunction with some of the surface techniques discussed in chapter 2, such as ToF-SIMS would create a valuable test method to understand the deposit formation.

Whereas Raman spectroscopy and TEM offer information on the carbon structure with regards to graphitic structure, however, fluorescence prevented analysis with Raman spectroscopy. Therefore a treatment method would be required to overcome this. This work has created the foundations in highlighting areas of further investigation into the composition of IDIDs.

## 4 Raman Spectroscopy Analysis of IDIDs and Comparison to Reference Carbonaceous Materials to Observe Graphitic Content

### 4.1 Summary

Raman spectroscopy is an effective analytical method to measure the ratio of graphitic to disordered carbon in carbonaceous samples. IDIDs have been an evolving problem for the last decade and understanding the carbonaceous mechanism of formation will uncover novel information into how the deposit is structured and bonded. However, on initial analysis the deposits heavily fluoresced with Raman spectroscopy.

Interference from fluorescent species is a major issue and current methods to circumvent this are not always effective. Heating under high hydrogen pressures, known as hydrolysis (HyPy), is demonstrated here to be effective in removing fluorescing species at 350 °C, while not altering the aromatic structure of the carbonaceous material. This was qualified through the analysis of a series of reference samples with HyPy and pyrolysis under nitrogen (NPy) whereby, after HyPy the intensity ratio and peak width of the D and G bands remained unchanged. It was found that NPy removed volatile species however, altered the disorder structure. The analysis of volatile species removed by hydrolysis from diesel injector needle deposits where engine failures have occurred suggested that functionalised  $n\text{-C}_{16}$  and  $n\text{-C}_{18}$  species were responsible for the fluorescence. Analysis of IDIDs demonstrated a high

graphitic content on comparison to reference material, which is thought to be a result of the high pressures experienced in the injector systems.

## **4.2 Results and Discussion**

### **4.2.1 Application of Raman Spectroscopy**

When analysing carbon rich samples with Raman spectroscopy there are two bands of interest, namely the D and the G band, located at  $1380\text{ cm}^{-1}$  and  $1552\text{ cm}^{-1}$  respectively. By using the same wavelength, a comparison of carbon structure can be calculated by looking at the ratio between the intensities of the D and G bands. Bands overlapping will occur if there is a complex mixture of environments, which are difficult to distinguish.

Two carbon blacks, three graphite, a gilsonite resin and two cokes, were analysed to demonstrate a variety in  $I_D/I_G$  ratios, as shown in Figure 4.1, the  $I_D/I_G$  ratios range between 0.14-1.05. As would be expected the graphite (micro 450, micro 850 and 146) have the lowest ratios between  $0.14 \pm 0.06$  and  $0.23 \pm 0.06$ , whilst the coke and carbon black samples (calcined coke, degussa carbon black, green coke, gilsonite resin and sigma carbon black) have the highest  $I_D/I_G$  ratios  $0.72 \pm 0.03 - 1.05 \pm 0.09$ . This indicated that the graphite samples had the greater amount of ordering in the sample.

When analysing pure graphite only the G band would be identified, however, realistically there will be imperfections in the structure which results in the D band being observed. This range of carbon samples demonstrates the varying structures of carbon that can be produced and are useful in analysing other carbon rich samples so the graphitic content can be compared. The surface area and elemental analysis for the samples can be seen in Table 4.1. The carbon

black samples (Degussa and sigma) have large surface areas in the range of 205 - 417 m<sup>2</sup>/g. Carbon black samples are typically large particles with mesopores and large amounts of disorder in the structure, which is reflected in the relatively large I<sub>D</sub>/I<sub>G</sub> ratios of 1.05 ± 0.09. The gilsonite resin and green coke were the smallest surface areas, observed in Table 4.1, and have the lowest I<sub>D</sub>/I<sub>G</sub> ratio meaning there is more ordering in the structure.

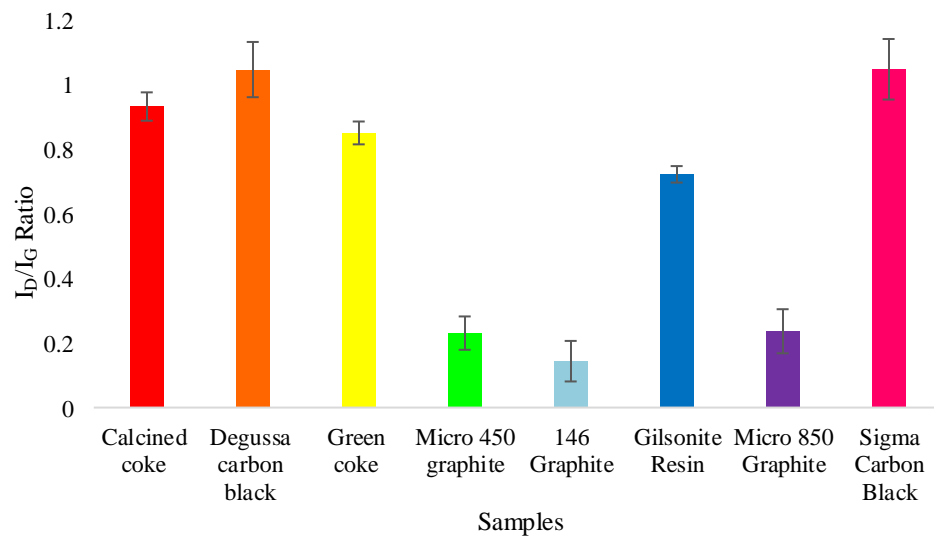


*Figure 4.1 Data illustrating the ratio of I<sub>D</sub>/I<sub>G</sub> Raman spectroscopy bands for a range of carbon black, graphite and coke samples. The error bars are one standard deviation.*

The elemental data for the two carbon blacks, three graphite, a gilsonite resin and two cokes, shown in Table 4.1, only provided percentages of carbon, hydrogen and nitrogen and typically will not add up to 100%. This is because other elements are in the sample, such as oxygen and sulfur. The introduction of oxygen and sulfur into the sample will cause an imperfection and therefore affect the I<sub>D</sub>/I<sub>G</sub> ratio. The degussa carbon black sample has a total carbon content of 82.73%, therefore 17.27% of the sample is not carbon, hydrogen or

nitrogen. This is likely why it had the highest  $I_D/I_G$  ratio, as the other elements present in the sample will cause imperfections. The graphite samples had a high carbon content above 98% and 0% nitrogen, shown in Table 4.1, having a higher carbon content confirms less other elements in the sample, which could cause imperfections.

*Table 4.1 Elemental analysis, particle size and surface area of a range of carbon blacks, gilsonite resin, graphite and coke samples. The details of these reference samples has previously been reported [191].*

<b>Samples</b>	<b>Elemental Analysis</b>			<b>Average Particle Size (<math>\mu\text{m}</math>)</b>	<b>Surface (<math>\text{m}^2/\text{g}</math>)</b>	<b>Area</b>
	<b>C (%)</b>	<b>H (%)</b>	<b>N (%)</b>			
<b>Sigma Carbon Black</b>	99.95	0.00	0.00	45	205	
<b>Gilsonite Resin</b>	84.86	10.14	3.23	74	0.3	
<b>Calcined Coke</b>	95.69	0.07	1.26	6	20	
<b>Green Coke</b>	85.94	2.84	2.53	2	10	
<b>Degussa Carbon Black</b>	81.27	0.89	0.57	43	417	
				(From particle size analysis)	(From BET analysis)	
<b>Micro 450</b>	98.04	0.05	0.00	5	17	
<b>Micro 850</b>	98.10	0.01	0.00	5	13	
<b>Graphite 146</b>	98.61	0.02	0.00	21	6	

#### 4.2.2 Fluorescing During Raman Spectroscopy when Analysing IDIDs

An image of a failed diesel injector needle with a carbonaceous deposit on the tapered end is shown in Figure 4.2a. The computed tomography image shown in Figure 4.2b, illustrates the small tolerance of space between the needle and the injector tip, which are required to put diesel under high pressure. The image shown in Figure 4.2c is a SEM image of the upper portion of a contaminated needle and shows the deposit built up on the surface.

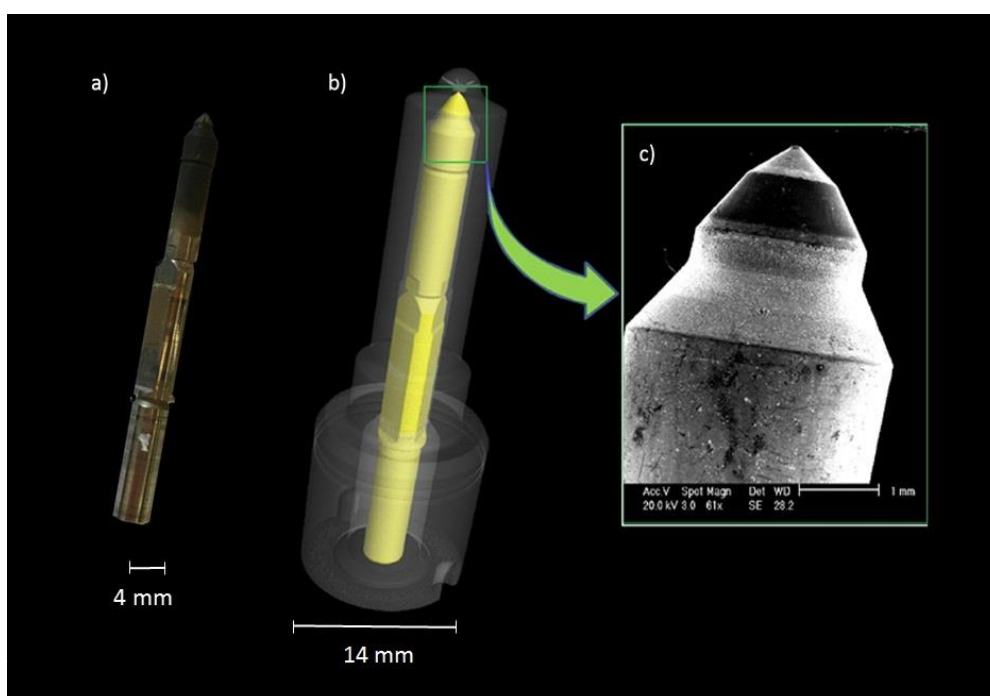


*Figure 4.2 Images of an injector needle. a) Photo of failed diesel injector needle removed from injector tip, covered in carbonaceous material at tip depicted as black matter. b) Computed tomography image needle inside injector tip before removal. c) SEM image showing surface morphology of injector needle and the deposit which is responsible for the needle sticking*

The Raman data collected from an injector needle would provide evidence into the mechanism of carbonaceous material. In theory the longer the deposit has resided on the needle the longer the deposit has been under a harsh

environment and thereby would contain more graphitic structuring. The diesel fuel that enters the injector system is mixture of aliphatic hydrocarbons with a small number of ring structures, such as naphthalene. Previous work by Clayton *et al.* has suggested that the deposit formation is dependent on the ring structures in the original fuel [66]. The information collected from Raman spectra would give evidence of the graphitic content and the growth of ring structures that have formed. Raman would be able to give evidence of how disordered the content of a sample is.

A Raman spectrum acquired from injector needle 9 is shown in Figure 4.3 for which fluorescence prevents the observation of any meaningful Raman data with no D and G bands discernible. The IDID was thermally treated with hydrolysis, which is the rapid heating to 350 °C and held for 5 mins under a high pressure stream of hydrogen gas [99, 102]. Figure 4.3b shows the baseline corrected spectrum from needle 9 following hydrolysis and clearly shows two distinct bands which correlate to disordered (D) and graphitic (G) carbon, located at 1380 cm<sup>-1</sup> and 1552 cm<sup>-1</sup> respectively [125]. Thus HyPy successfully removed the fluorescent material, thought to be contaminants in the fuel, and thereby allowing subsequent Raman analysis. This is the first known data obtained by Raman spectroscopy for an IDID and can be used to better understand the chemical structure of these systems. The TPO data collected by Barker *et al.* found that the deposit on an injector needle had more graphitic content than the injector tip [6]. The Raman data compliments this finding that high graphitic content is found on the needle.

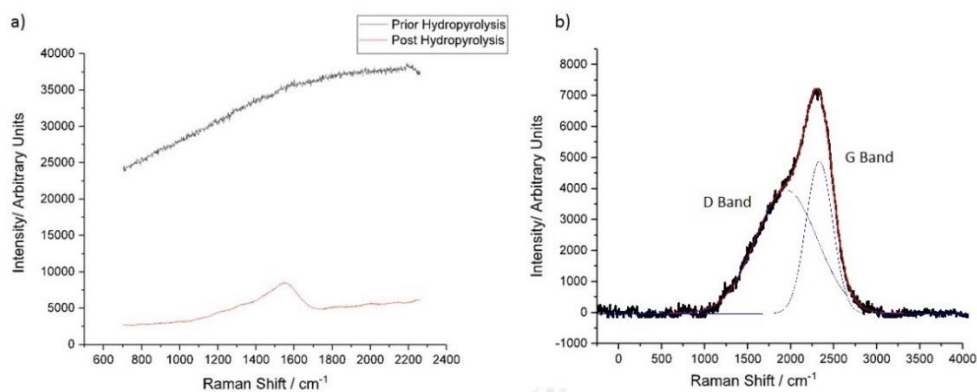


*Figure 4.3 Raman spectra of the failed injector needle 9. a) The spectrum of the needle as received before thermal treatment by hydroxyprolysis. b) The baselined Raman spectrum of the needle after thermal treatment by HyPy, the D and G bands being distinguished clearly.*

#### **4.2.3 Effects of HyPy on the Carbonaceous Structure of the Standard Materials**

In order to confirm that the HyPy treatment did not have an impact on carbonaceous structure and subsequently the  $I_D/I_G$  ratio, eight carbonaceous reference samples were analysed with Raman spectroscopy prior and post HyPy treatment, details of the reference samples can be observed in Table 4.2. The data shown in Figure 4.4 indicates that, within experimental error, the  $I_D/I_G$  ratios were unaltered by HyPy meaning that data acquired from IDID samples would be expected to be a true representation of the structures.

*Table 4.2 Summary of the sample details of Biochars A-D, coal samples E-F, Soot sample G and graphite H. Temperature and black carbon percentage for each biochar is recorded. The black carbon correlates to the amount of material that contains 7 or more rings [102]*

<b>Carbon Sample</b>	<b>Feedstock/Detail</b>	<b>Type</b>	<b>Temperature (°C)</b>	<b>HyPy black carbon (%)</b>	<b>Total Carbon (%)</b>
<b>A</b>	Wheat Straw	Biochar	550	66	
<b>B</b>	Wheat Straw	Biochar	700	97	
<b>C</b>	Pine Chips	Biochar	400	45	
<b>D</b>	Durian Shell	Biochar	400	32	
<b>E</b>	Beulah-Zap lignite Coal	Coal		4	58.5
<b>F</b>	Pocahontas Bituminous Coal	Coal		46	85.9
<b>G</b>	Hexane Soot	Diesel engine soot		83	92.9
<b>H</b>	Graphite	Graphite			100

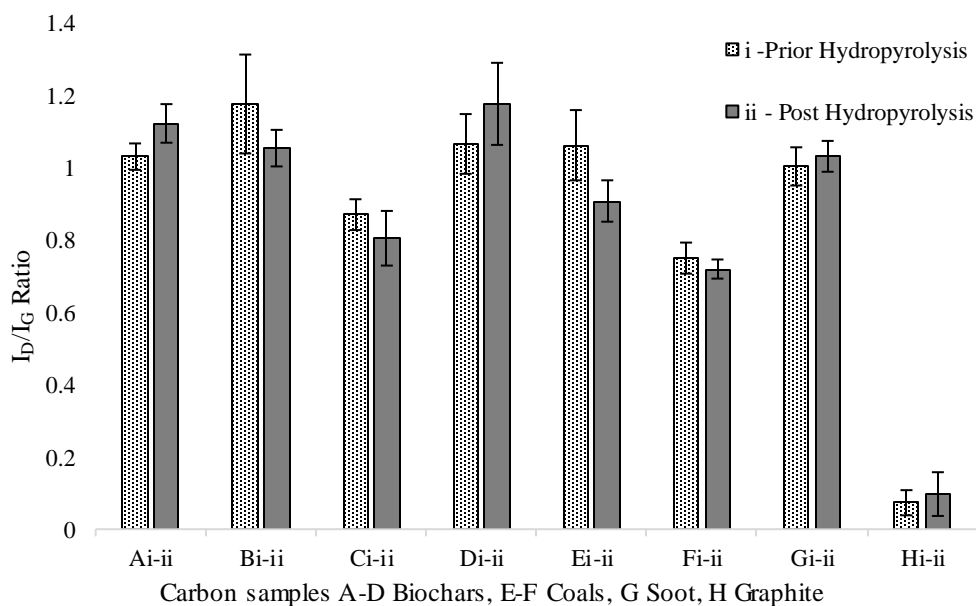


*Figure 4.4  $I_D/I_G$  Raman band ratios prior (i) and post (ii) hydropyrolysis biochar (A-D), Coal (E-F) Soot (G) and graphite (H) samples. The error bars are one standard deviation.*

Pocahontas bituminous coal (sample F) exhibited the lowest  $I_D/I_G$  band ratio of the biochar and coal samples, at  $0.75 \pm 0.04$  and  $0.72 \pm 0.02$ , for the initial and HyPy treated samples, respectively. This correlates to the highest proportion of aligned or graphitic carbon for samples investigated. Pocahontas coal is a medium volatile bituminous coal containing on average 4-5 rings in vitrinite and larger structures in inertinite as has been shown using  $^{13}\text{C}$  NMR [192]. The lignite (sample E) has a comparable ratio of  $I_D/I_G$  bands that were similar to biochars C and D. Intuitively the biochars would be expected to contain less ordered carbon than the bituminous coal but not necessarily the lignite, which contained much smaller aromatic rings. However, the biochars and coals are within range of each other and there was no distinction between the two carbon types.

The graphite (sample H) exhibited a low  $I_D/I_G$  ratio, as expected, being  $0.07 \pm 0.03$  and  $0.10 \pm 0.06$  for prior and post hydrolysis respectively. Overall the reference samples show minimal change in  $I_D/I_G$  band ratios but band widths also need to be considered, which will be discussed in section 4.2.4.

#### 4.2.4 Structural Analysis of Reference Samples

The band position and full width half maximum (FWHM) of the G and D bands are reported in Table 4.3. The band position for the carbonaceous reference samples ranged over  $20 \text{ cm}^{-1}$  for the D band and  $27 \text{ cm}^{-1}$  for the G band. The band shift position did not change substantially between the prior and post thermal treatment of samples when taking into consideration instrument error, therefore suggesting minimal structural change. A shift in band would suggest structural change in the sample. The biomass char samples A-D had higher FWHM than the coal and soot samples E-G, showing more disorder in the biomass chars than the coal and soot samples.

The trends of the D and G band FWHM and  $I_D/I_G$  ratios are independent of one another and must be interpreted separately. A given sample could have a low  $I_D/I_G$  ratio but have a high D band FWHM, this would mean the sample is heavily ordered but there is variation in the disordered content. There is a clear difference between the graphite and the collection of biochars, coals and soot. The graphite sample exhibited a FWHM of  $44 \text{ cm}^{-1} \pm 7$  for the D band and  $23 \text{ cm}^{-1} \pm 2$  for the G band. When this is compared to the other carbonaceous samples that have FWHM of  $242 \pm 16 - 363 \pm 13 \text{ cm}^{-1}$  for the D band and  $68 \pm 5 - 95 \pm 5 \text{ cm}^{-1}$  for the G band. The  $I_D/I_G$  ratios and the D and G band FWHM of the carbonaceous samples display very little change prior and post HyPy (Table 4.3).

Table 4.3 Raman spectroscopy data of reference carbonaceous samples A - H prior and post treatment. The data presents the wavenumber of highest intensity, full width half maximum (FWHM) and  $I_D/I_G$  band ratio. *i* denotes the samples data acquisition before thermal treatment, *ii* denotes the samples data acquisition after thermal treatment.

<b>Samples</b>	<b>Gas Atmosphere</b>	<b>D Band Position</b>	<b>FWHM</b>	<b>G Band Position</b>	<b>FWHM</b>	<b><math>I_D/I_G</math></b>
<b>Ai</b>	Hydropyrolysis (HyPy)	1352 ± 2	318 ± 21	1586 ± 2	88 ± 2	1.03 ± 0.01
<b>Aii</b>		1343 ± 4	327 ± 24	1579 ± 5	87 ± 4	1.12 ± 0.04
<b>Bi</b>		1338 ± 8	310 ± 10	1577 ± 7	90 ± 2	1.18 ± 0.11
<b>Bii</b>		1346 ± 2	318 ± 11	1585 ± 2	88 ± 2	1.05 ± 0.04
<b>Ci</b>		1358 ± 6	332 ± 24	1585 ± 2	88 ± 5	0.87 ± 0.04
<b>Cii</b>		1353 ± 2	309 ± 18	1586 ± 5	82 ± 7	0.80 ± 0.14
<b>Di</b>		1356 ± 2	346 ± 11	1579 ± 2	95 ± 5	1.07 ± 0.07
<b>Dii</b>		1349 ± 2	362 ± 14	1576 ± 4	87 ± 3	1.18 ± 0.09
<b>Ei</b>		1357 ± 2	308 ± 12	1582 ± 2	95 ± 2	0.96 ± 0.08
<b>Eii</b>		1355 ± 2	311 ± 13	1583 ± 3	94 ± 4	0.90 ± 0.04
<b>Fi</b>		1349 ± 2	263 ± 13	1590 ± 2	68 ± 5	0.75 ± 0.04
<b>Fii</b>		1349 ± 4	260 ± 3	1591 ± 2	69 ± 4	0.72 ± 0.04
<b>Gi</b>		1343 ± 2	243 ± 12	1585 ± 2	80 ± 2	1.00 ± 0.00
<b>Gii</b>		1341 ± 2	242 ± 16	1584 ± 2	79 ± 2	1.03 ± 0.01
<b>Hi</b>		1336 ± 2	43 ± 10	1564 ± 2	23 ± 2	0.07 ± 0.03

<b>Hii</b>		$1342 \pm 2$	$44 \pm 7$	$1570 \pm 4$	$22 \pm 4$	$0.10 \pm 0.05$
<b>Ei*</b>	Nitrogen	$1353 \pm 5$	$162 \pm 5$	$1568 \pm 6$	$102 \pm 6$	$0.59 \pm 0.15$
<b>Eii*</b>	pyrolysis (NPy)	$1349 \pm 2$	$187 \pm 7$	$1574 \pm 7$	$100 \pm 3$	$0.65 \pm 0.07$
<b>Fi*</b>		$1356 \pm 5$	$179 \pm 11$	$1584 \pm 4$	$75 \pm 6$	$0.67 \pm 0.10$
<b>Fii*</b>		$1358 \pm 7$	$223 \pm 15$	$1582 \pm 2$	$76 \pm 4$	$0.67 \pm 0.02$

#### **4.2.5 Comparison of Hydropyrolysis and in N<sub>2</sub>**

For further confirmation of justifying the use of hydrogen as the gas medium, nitrogen was also tried. To compare HyPy against nitrogen pyrolysis (NPY), the two coals, Beulah-zap lignite (sample E) and Pocahontas (sample F), details observed in Table 4.3 were selected since the biochars had already experienced temperatures above 350 °C and have lost the majority of any volatile matter, whereas the coals have not. The I<sub>D</sub>/I<sub>G</sub> ratio and FWHM of the G bands for the two coal samples (Table 4.3) exhibited minimal change for HyPy. However, on contrast, the FWHM of the D bands after NPY increased significantly from 162 cm<sup>-1</sup> ± 5 to 187 cm<sup>-1</sup> ± 7 for Beulah-zap lignite (sample E) and from 179 cm<sup>-1</sup> ± 11 to 223 cm<sup>-1</sup> ± 15 for Pocahontas coal (sample F), although the position of the bands did not change. The FWHM of the D band after HyPy went from 308 cm<sup>-1</sup> ± 12 to 311 cm<sup>-1</sup> ± 13 for sample E and for sample F 263 cm<sup>-1</sup> ± 13 to 260 cm<sup>-1</sup> ± 3. Clearly there was a significant change in the FWHM of the D band in the NPY treatment which was not seen in the HyPy. The larger FWHM of the D band demonstrated that the disordered environments in the coal samples increased during NPY, and not in HyPy. This therefore shows that using hydrogen as the gas medium is more advantageous than nitrogen as there was no increase in the FWHM of the HyPy and therefore is no structural change displayed.

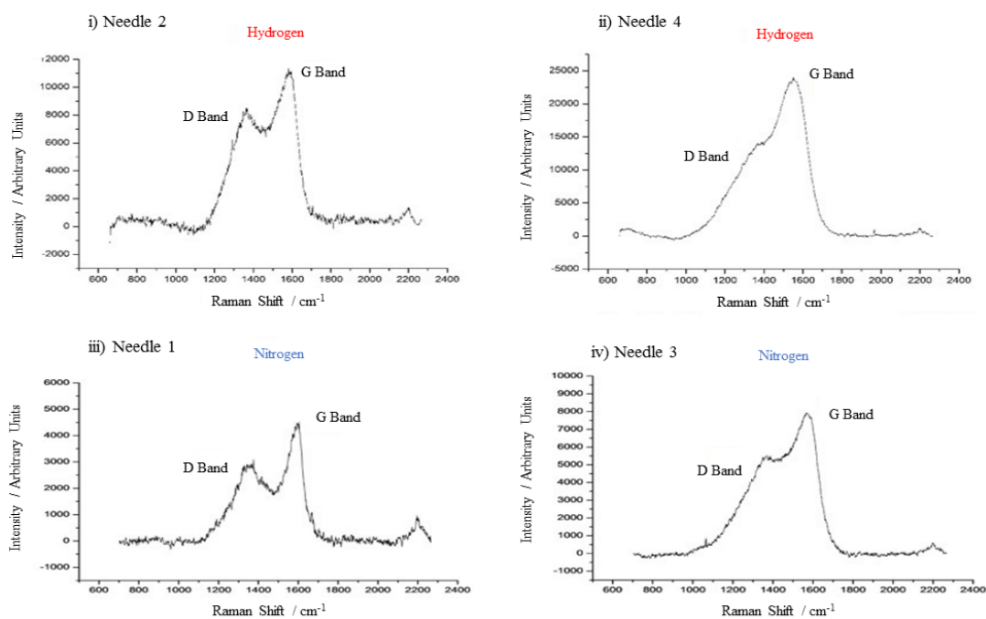
#### **4.2.6 Validation of Thermal Treatment with Different Gas Atmospheres**

##### *4.2.6.1 Structural Analysis of IDIDs*

To further investigate and compare the application of HyPy and NPY needles, 2, 4 and 9, were treated in a hydrogen by HyPy and needles 1 and 3 were treated by NPY. As nitrogen is inert, pressure and temperature would be the

only causes of volatile matter being released. Although gas atmospheres remove volatile matter, it is hydrogen that is the more effective gas medium, as this reduces functional groups to release volatile matter.

The Raman spectra obtained for the hydrogen treated needles, 2, 4 and 9, demonstrates that the D and G bands are observable following HyPy treatment, observed in Figure 4.5i-iv. Using this data the ratios of  $I_D/I_G$  were calculated as  $0.76 \pm 0.13$  for needle 2,  $0.50 \pm 0.18$  for needle 4, and  $0.62 \pm 0.03$  for needle 9, showing significant differences. It is unlikely that the graphitic content on a needle would be within error range of each other. Each needle has been subjected to different fuelling conditions, which means different fuels, additives and driving conditions. Therefore the graphitic content is expected to



be different.

*Figure 4.5 Raman spectra of needles 1-4. Needles 4 and 2 by HyPy and needles 3 and 1 by NPy. All the spectra have been baselined with OriginLab software,*

For NPy conducted on needles 1 and 3, the procedure appears to remove the fluorescence whereby all subsequent Raman data demonstrated an observable D and G bands (Figure 4.5iii and 4iv). The ratios of  $I_D/I_G$  were  $0.72 \pm 0.01$  for needle 1 and  $0.81 \pm 0.02$  for needle 3. It was observed that the  $I_D/I_G$  ratio reported was similar for needle 1 and needle 2, irrespective of the thermal treatment used. However, in order to obtain Raman data of sufficient quality a longer acquisition time of 60 s was required as compared to the HyPy (needles which took 20 s. For the NPy needles the spectra were not suitable for presenting with an acquisition time of 20 s and required an increase to 60 s). A longer acquisition time is needed to excite the photons for detection but risks the data becoming saturated and thereby invalid. This could be due to some of the volatile species remaining on the NPy treated needles and effecting the excitation of detectable photons. During the HyPy process the molecules in the sample are reduced by the hydrogen gas and therefore a higher proportion is removed.

*Table 4.4 Raman spectroscopy data for needles 1-4 and 9 prior and post treatment in HyPy and NPy. The data show wavenumber of highest intensity, full width half maximum (FWHM) and  $I_D/I_G$  band ratio. *i* denotes the samples data acquisition before thermal treatment, *ii* denotes the samples data acquisition after thermal.*

	<b>Thermal Treatment</b>	<b>D Band Position</b>	<b>FWHM</b>	<b>G Band Position</b>	<b>FWHM</b>	<b><math>I_D/I_G</math></b>
<b>Needle 2</b>	Hydropyrolysis (HyPy)	$1373 \pm 6$	$186 \pm 13$	$1572 \pm 12$	$117 \pm 9$	$0.76 \pm 0.13$
<b>Needle 4</b>		$1370 \pm 6$	$252 \pm 20$	$1548 \pm 11$	$134 \pm 12$	$0.50 \pm 0.18$
<b>Needle 9</b>		$1386 \pm 6$	$140 \pm 2$	$1555 \pm 2$	$67 \pm 2$	$0.62 \pm 0.03$
<b>Needle 1</b>	Nitrogen	$1363 \pm 2$	$216 \pm 5$	$1584 \pm 2$	$91 \pm 4$	$0.72 \pm 0.01$
<b>Needle 3</b>	Pyrolysis (NPy)	$1368 \pm 3$	$255 \pm 6$	$1582 \pm 2$	$102 \pm 9$	$0.81 \pm 0.02$

#### 4.2.6.2 Comparison of Structural Analysis between IDIDs and Reference Standards

The  $I_D/I_G$  ratio of the injector needles ranged between  $0.50 \pm 0.18$  -  $0.81 \pm 0.02$ , compared to  $0.72 \pm 0.04$  -  $1.18 \pm 0.18$  for the reference coal, soot and biochar reference samples in Table 4.3. When comparing the ratios of IDIDs and carbon samples, the IDIDs are most similar to biochars C and the bituminous coal F. Needles 1, 4 and 9 had lower  $I_D/I_G$  ratios than sample F, thereby suggesting a more ordered structure. The aligned aromatic structure could have resided on the needle surface for some time before manifestation of the issues with engine function. An injector system rarely experiences temperatures above  $250\text{ }^\circ\text{C}$  but pressures are between 2400 - 3000 bar [98]. Therefore, the inference is that the extreme high pressure can promote the formation of graphitic structure. Other techniques that can observe graphitic structure include X-ray diffraction (XRD) and TEM. Barker *et al.* used XRD to analyse IDIDs however, found no indicative peak of graphitic carbon [6]. However, the same authors found that TEM analysis of an IDID showed some pseudo graphitic structure with TEM [155].

The D band FWHM for the reference samples except graphite were all higher than that of the injector needles, whilst the G band FWHM values for the injector needles were larger than the carbon samples. Thus the imperfections in the non-aligned structures giving rise to the D bands for the diesel injector samples were less than for all the reference samples. In contrast, for the G band the injector needles exhibit a higher FWHM therefore a greater range of carbonaceous environments (which are giving signals for the G band) are present when compared to the carbonaceous samples. Needle 4 had the lowest

$I_D/I_G$  ratio but has the highest G band FWHM and the second highest D band FWHM. Similar trends where G and D band FWHM do not correlate with  $I_D/I_G$  ratios have also been observed for a range of ranked coals reported by Ulyanova *et al.* [193].

The D band FWHM of the NPy treated needles are  $216\text{ cm}^{-1} \pm 5$  and  $255\text{ cm}^{-1} \pm 6$ , which were both higher than the HyPy treated needles, which were  $140\text{ cm}^{-1} \pm 2$  and  $186\text{ cm}^{-1} \pm 13$  with exception of needle 4 which was  $252\text{ cm}^{-1} \pm 20$ , however, needle 4 also has the highest G band FWHM, therefore had the most disorder overall. The FWHM of the needles compared to the reference samples show that the NPy causes the alteration of environments responsible for the D band. This data aids in understanding the bonding structure in the injector needles, that there is more different environments in the ordered carbon. Due to the harsh environments and tight orifices experienced in an injection system the deposit will be constantly breaking away and forming new structures. The high pressure will force the graphitic content to increase and due to the diverse chemistries entering the injection system then a range of graphitic structures are likely to form. The difference could occur due to sheer force of the mechanics, running time of the engine, fuel, additives and weather conditions. When comparing the FWHM of the needles to the reference samples it suggests that during the process of formation there is a lower number of disorder environments. The material that is considered for the D band is likely to be deposited and then transformed into graphitic structures, or be washed away with incoming fuel or until the engine fails. This is why there are less disordered environments compared to the reference samples and more

ordered environments as the deposit is forced to form graphitic structures to withstand the pressures of the injection system,

#### 4.2.7 Identification of Volatile Species

Gas chromatography mass spectrometry (GC-MS) was used to analyse the material desorbed from the silica trap during hydropyrolysis up to 350°C from needles 1-4 and 9. The HyPy GC-MS of the volatile matter from needles 2, 4 and 9 are shown in Figure 4.6i-viii. The NPy GC-MS of the volatile matter from needles 1 and 3 are shown in Figure 4.6, v, ix and x. Figure 4.6 shows both the total ion chromatogram (TIC) and the  $m/z$  71 single ion chromatogram (SIC), to help to identify the major alkane fragments in the sample.

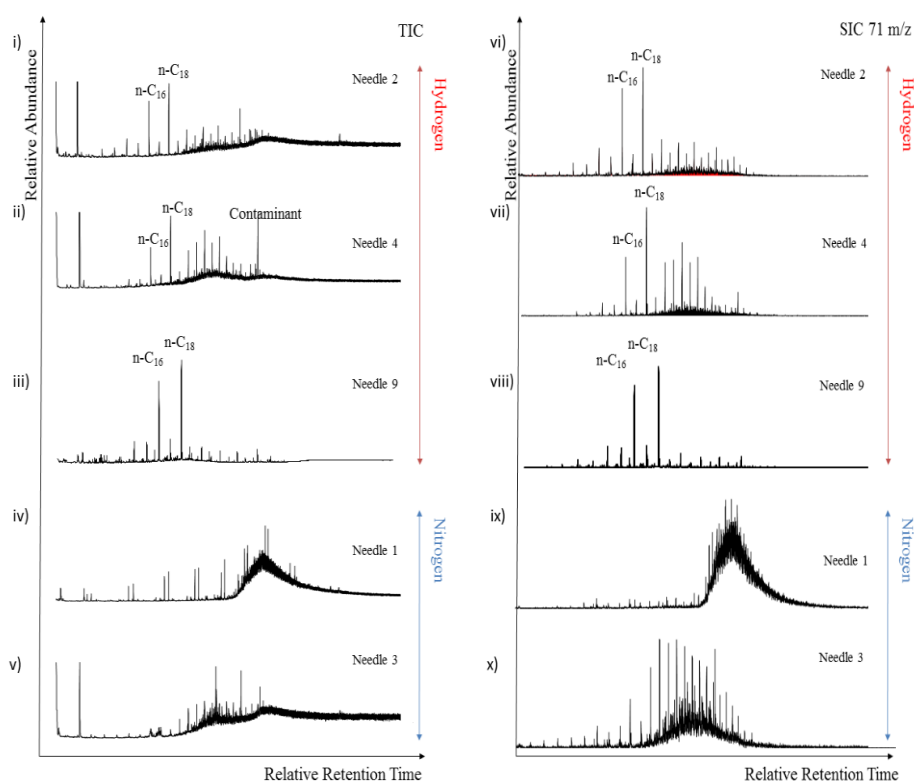


Figure 4.6 Total ion chromatogram (TIC) and single ion chromatogram (SIC)  $m/z$  71 of volatiles released from needles 2, 4 and 9 in HyPy and needles 1 and 3 in NPy.

The HyPy products of needles 2, 4 and 9 consist mainly of n-hexadecane, n-octadecane, n-alkanes (C<sub>14</sub>-C<sub>26</sub>), as shown in Figure 4.6i, iii, v, and more clearly in the *m/z* 71 in SIC Figure 4.6 vi, vii, viii. Diesel fuel is the likely origin of the C<sub>12</sub>-C<sub>20</sub> *n*-alkanes within the sample, giving a reasonably equal distribution and intensity of peaks, seen in many examples in previous studies [194, 195]. This pattern of hydrocarbon distribution is typical for diesel and heavier oils [196]. Therefore it is suggested that the high levels of n-hexadecane and n-octadecane arise from other species, notably the triglycerides in biodiesel [197]. The assignments for the spectra were verified by a mass library attached to the OpenLAB software.

The engine from which needle 9 was obtained was run on California air regulatory board (CARB) fuels, where typically this fuel meets the strictest guidelines for emissions. It can be concluded that the fluorescence arises from unsaturated chain species that are fully reduced during HyPy [198]. Needle 4 was fuelled with ultra-low sulfur diesel (ULSD), it is unknown if any additives were in the fuel, however, due to the lubricity properties of ULSD it is likely there would have been an additive package. The GC-MS data shows a large distribution of high molecular weight carbon chains mostly above *n*-C<sub>18</sub>.

Needle 2 was obtained from a DW10B engine test performed with RF06 reference fuel with no additives but with added low molecular weight PIBSI, which has been known to cause sticking [67]. Needle 2 shows more material lower than *n*-C<sub>16</sub> compared to the other samples, which is possibly from fragmentation of the PIBSI. The fuel has contributed to the higher molecular species [198].

The GC-MS data for needles 1 and 3 shown in Figure 4.6iv, v, ix and x, which were thermally treated in NPy, showed both an increased proportion of column bleed in the TIC traces and a lower signal to noise ratio on the  $m/z$  71 mass chromatogram than for the HyPy experiments. As the volatile products from each needle were dissolved in an equal volume of solvent prior to analysis this suggest that less volatile material was removed under NPy conditions than with HyPy. The SIC shows a uniform distribution of the hydrocarbons found in the sample and UCM. Needle 3 and 4 were both taken from engines fuelled with ULSD so it would be expected to show similar results, however, they do not. Needle 1 showed 9 double peaks, indicative of isomers, in the TIC Figure 4.6iv, the doublet was identified as a polymer of 2, 4, 4, 6, 6, 8, 8 heptamethyl nonene from its mass spectra and assignment from OpenLAB library. The doublet is due to the isomers of the molecule, where the double bond starts at the 1 or 2 carbon position. The origin of this polymer is unknown, however, it is possible that it may be represent a contaminant in the fuel. The data for needle 1, Figure 4.6iv, also consists of an unresolved complex matrix which would be anticipated to arise from polar species, such as lube oils, aliphatics or high molecular mass aromatics in diesel This needle was obtained from a failed engine in Norway with no additives package, further suggesting the doublet was a contaminant in the fuel.

The labile fractions from needles 1-4 and 9 have different compositions. The material suspected of causing fluorescence from the GC-MS data is not the same for each sample. For the three needles treated with hydropyrolysis increased levels of  $n$ -C<sub>16</sub> and  $n$ -C<sub>18</sub> were released. The data collected from the HyPy and NPy data show similar results with the I<sub>D</sub>/I<sub>G</sub> ratios being between

$0.50 \pm 0.02$  and  $0.81 \pm 0.02$ , however, the intensity of the data from the GC-MS of the NPy was lower. The NPy does not successfully remove as much material as HyPy as seen in the GC-MS data and the difficulty with obtaining spectra from NPy treated needles. Although some material is being removed there appears to be a transition in the structure of the deposit on the NPy needles. The heating energy of the NPy is not releasing any volatile matter however, is enough energy for the disordered carbon to change into new and different environments. Whereas the energy input from the HyPy is utilised to release volatile matter, thereby proving this is the better gas medium.

### **4.3 Conclusions**

HyPy has been demonstrated to be a successful pre-treatment for removal of fluorescing species to facilitate characterisation of carbonaceous deposits in IDIDs by Raman spectroscopy. Establishing the extent of ordered carbon present in IDIDs provides evidence as to how long the deposit has resided on the needle before causing issues by indicating to what extent ring growth and ordering has occurred.

Analysis of a range of carbonaceous reference materials has demonstrated that there is negligible change in the  $I_D/I_G$  ratio following the HyPy treatment.

Although NPy is capable of removing volatiles and the  $I_D/I_G$  band ratio remains unchanged, the FWHM of the D band is increased suggesting that structural change occurs in NPy, providing evidence that hydrogen is the gas medium of choice over nitrogen. The  $I_D/I_G$  ratio may remain unchanged for the injector needles because the temperatures of NPy is not high enough to create ordered carbon however, does cause structural variance to occur in the disordered

carbon. This does not occur in HyPy because the volatile material is removed rather than structurally changed.

The IDIDs had a greater G band FWHM and lower D band FWHM than the carbon samples, showing a greater variety of environments in the ordered carbon and lower variety in the disordered carbon for the injector needles than the carbon samples. The deposits on the needles are likely to have occurred over a short time period in the range of months compared to the coals which have taken millions of years. Therefore the types of environments being forced into a graphitic arrangement would be high due to the high pressure, which is shown in the results, where there is a higher graphitic variance.

For the IDID deposits, GC-MS analysis of the volatile species realised by HyPy has indicated that the fluorescence arises from unsaturated  $n$ -C<sub>16</sub> and  $n$ -C<sub>18</sub> molecules, this is likely to have come from contaminants in the fuel.

The intensity  $I_D/I_G$  ratio found for the carbonaceous deposit of needles 9 and 1 were similar to that for a low volatile bituminous coal where previous work has shown that partially aromatic units comprise 4-6 rings.

This work successfully removed fluorescence from IDIDs with HyPy as the advantageous gas medium to allow for Raman data collection which gives insight into the structural formation of deposit. The application of HyPy has the potential to be applied to a variety of other carbonaceous samples, including petroleum source rocks and heavy crudes recovered as where fluorescence arises from species in drilling muds.

## **5 Development of Method to Investigation the 3D Structure of IDIDs Using Focused Ion Beam and Time of Flight Secondary Ion Mass Spectrometry**

### **5.1 Summary**

The previous applications of FIB and ToF-SIMS have shown promising results when applied to IDIDs [37, 79, 108, 155]. Therefore it was a natural progression to begin to develop a test method combining the two. The application of FIB can mill samples to create lift outs and trenches which will expose the lower chemical composition of a sample [153-155, 199-203].

Whilst ToF-SIMS can collect mass spectra and chemically map sample surfaces. Different methods of application were explored in this chapter, from initially attempting a lift out of a deposits, to finally creating an *in situ* trench for analysis.

The combination of FIB and ToF-SIMS is a well-established technique [200-203]. However, this is the first example of the analysis method being applied to IDIDs. Due to the deposits being porous and topographical difficult to analyse, the application of FIB-SIMS was the most appropriate to analyse these samples and identified layers with a defined structure. The work in section 5.2.6 shows that polysiloxanes [204-207] were layered onto the surface of the injector tip and further phosphate and sodium rich layers formed on top, these assignments were made with SurfaceLab 6 library. The research in this chapter definitively verify that there is a process occurring to form the deposits, they are not homogenous and that FIB-SIMS is the optimal test method to analyse these deposits.

## 5.2 Results and Discussion

### 5.2.1 Surface Analysis of Diesel Deposits on Eight Injector Needles Using ToF-SIMS

The surface of eight injector needles were analysed to identify the chemistry with ToF-SIMS. The needles used in this section were needles 1-8, in Table 2.1 there are details as to the location of each needle and the reasons for failure. Figure 5.1 shows the positive ion data of the eight needles. It was observed that there were differences in the ions identified, these include a variety of hydrocarbons ( $m/z$  57, 41 and 43),  $\text{Na}^+$ ,  $\text{K}^+$ ,  $\text{Na}_2\text{OH}^+$  and  $\text{SiC}_3\text{H}_9^+$ , these ions were not unexpected as they have previously been reported [37, 45, 46, 67, 79]. It appears that needle 3 has the most sodium on the surface, compared to the other 7 needles, this can be observed in Figure 5.1, and the peaks at  $m/z$  22.99 and  $m/z$  62.98 are at higher intensities. Polysiloxane,  $\text{SiC}_3\text{H}_9^+$ , is found on needles 2-6 [204-207], these assignments were made with SurfaceLab 6 library. The assignments were made with the best statistical confidence of the library and own judgement.

Figure 5.2 shows the negative ion data of the eight needles. It was observed that there were differences in the ions, these include nitrogen containing species  $\text{CN}^-$  and  $\text{CNO}^-$ , carbon and oxygen species such as  $\text{O}^-$ ,  $\text{C}^-$ ,  $\text{CH}^-$ ,  $\text{OH}^-$  and sulfate and phosphate species. The nitrogen containing peaks at  $m/z$  26.00 and  $m/z$  42.00 were found on needles 1, 2, 4, 6-8, whilst oxygen ions,  $\text{O}^-$ , and sulfate ions,  $\text{SO}_x^-$ , were found on all of the needles in varying intensities.

Nitrogen, sulfur and phosphorus containing species regularly occur in IDIDs and are suspected to be indicative of poorly manufactured additives [67, 71], however, nitrogen can occur in fuel [208].

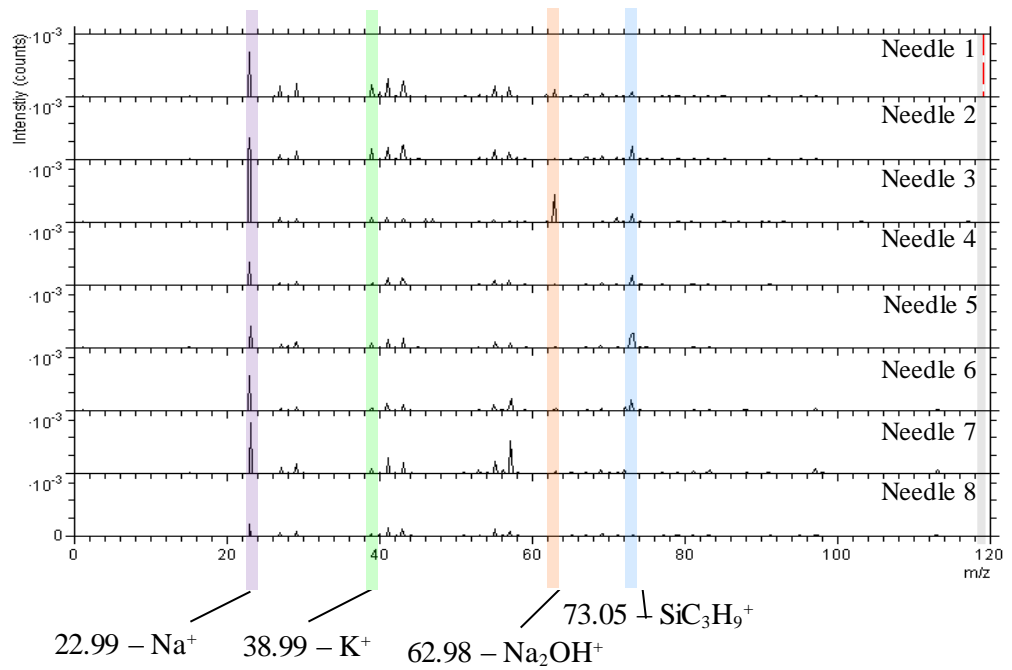


Figure 5.1 Positive ion surface analysis with ToF-SIMS of eight injector needles. The greatest differences have been highlighted and labelled as  $\text{Na}^+$ ,  $\text{K}^+$ ,  $\text{Na}_2\text{OH}^+$  and  $\text{SiC}_3\text{H}_9^+$ .

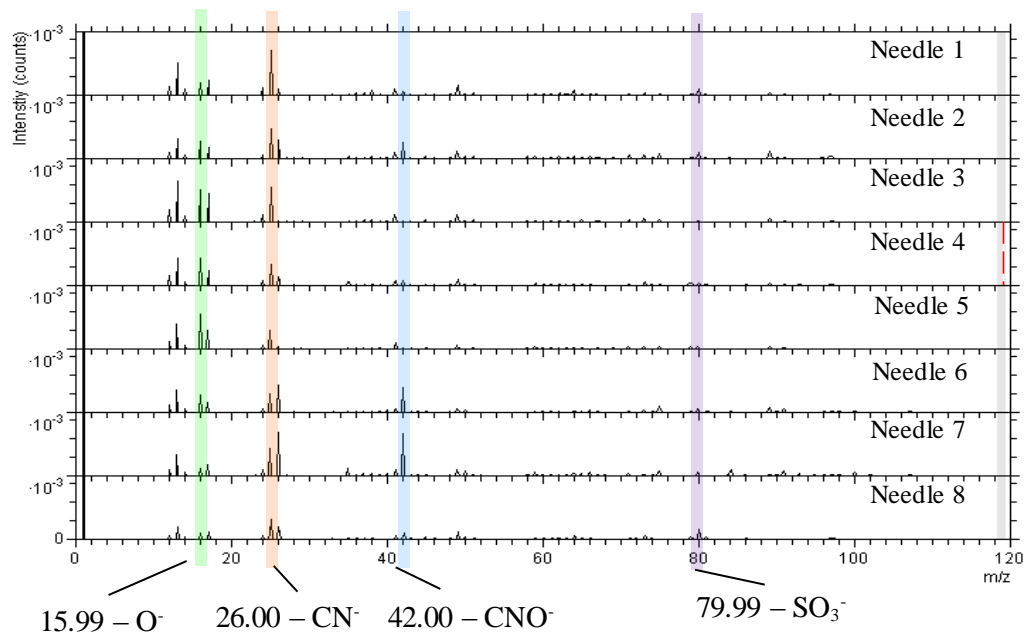


Figure 5.2 Negative ion surface analysis with ToF-SIMS of eight injector needles. The greatest differences have been highlighted and labelled as  $\text{O}^-$ ,  $\text{CN}^-$ ,  $\text{CNO}^-$  and  $\text{SO}_3^-$ .

## 5.2.2 Principle Component Analysis (PCA) of Eight Injector Needles by ToF-SIMS

Data was collected at a further two points on each needle from section 5.2.1, totaling three points from each of the eight needles, 2 mm apart. The analysis points were then collected into four regions of interest, creating twelve data points for each needle. The data set was so large that manual analysis of the data would be too arduous. Therefore principle component analysis (PCA) was applied to aid analysis of the data. PCA gives statistical evidence showing differences and similarities in large data sets, which is advantageous with large data sets and requires more substantial evidence of a variance. The principal component (PC) number indicates the severity of the difference. For ToF-SIMS this method is valuable to examine all ions and observe differences that would have been overlooked by manual examination. Only PC1 and PC 2 have been reported due to no trend occurring from the PC 3 data.

### 5.2.2.1 Positive Ion PC 1

The positive ion data is shown in Figure 5.3. In Figure 5.3i the data for PC 1 and PC 2 is shown, the data shows that on PC 1 there is an outlying sample set, which is needle 3, this was visually observed in the spectra in Figure 5.1. It can be observed from Figure 5.3ii that the ions responsible for the difference were  $\text{Na}^+$  and  $\text{Na}_2\text{OH}^+$ . Although  $\text{Na}^+$  was found on all sample, shown in Figure 5.1, the intensity difference for needle 3 compared to all the other samples was vastly greater. The negative loading on PC 1 was identified to be a range of hydrocarbon, this data can be viewed in Table 5.1, where the visibly higher and lower loadings have been manually identified and the masses assigned.

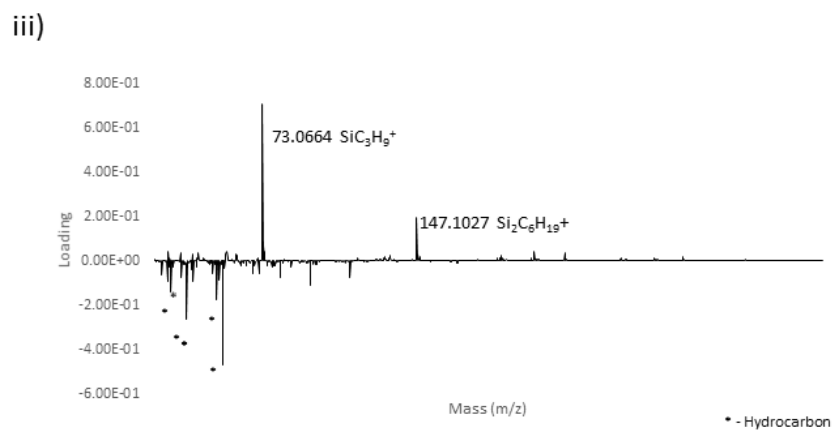
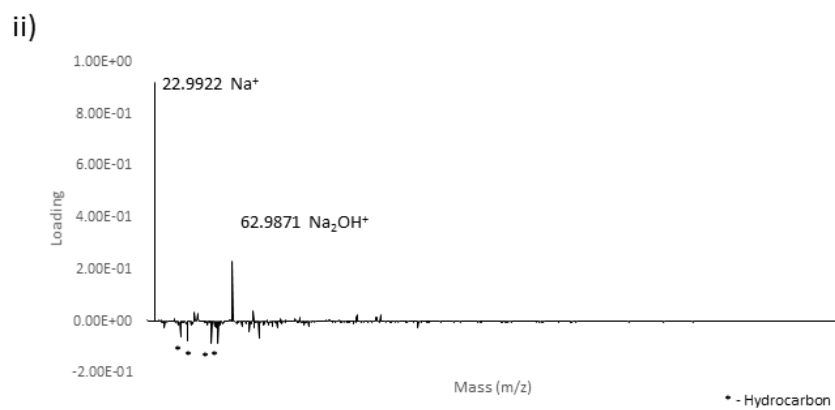
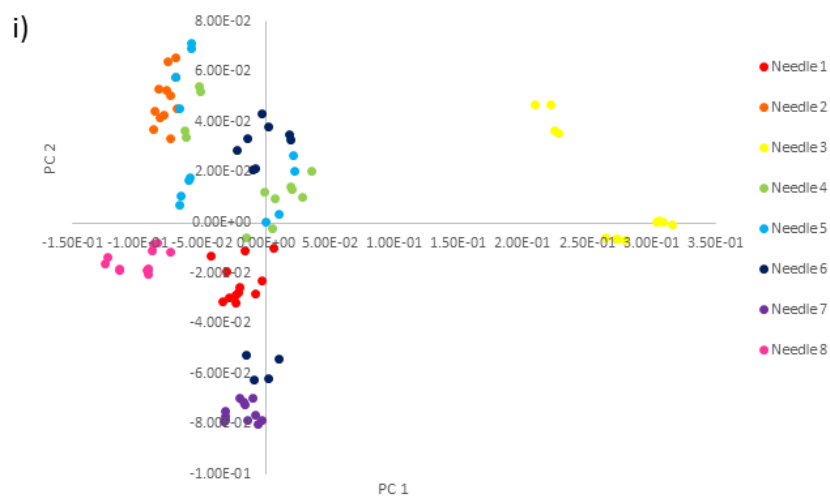


*Figure 5.3 Principal Component Analysis of positive ion data. i) Scores of PC1 against PC2 ii) Loading on PC1, indicating the main ions iii) Loading on PC2, indicating the main ions.*

### 5.2.2.2 Positive Ion PC 2

In Figure 5.3i the data for positive ions for PC 2 can be observed, although there is no visual split, as with PC1, it can be seen that needles 2, 3, 4, 5 and partially 6 are positive for PC 2, whereas needles 7 and 8 are negative. Figure 5.3iii shows that for PC 2 the positive loading was identified as polysiloxanes  $\text{SiC}_3\text{H}_9^+$  and  $\text{Si}_2\text{C}_6\text{H}_{19}^+$  [204-207], and the negative loading was from hydrocarbons,  $\text{n-C}_4\text{H}_y$  and  $\text{n-C}_5\text{H}_y$ . Needles 1, 2, 7 and 8 have tight groupings, which means there is evidence of repeatability of the data and the deposit was uniform over the needle.

*Table 5.1 PCA of positive ion data of ToF-SIMS, with the positive and negative loadings and the assignment for each ion for PC1 and PC 2.*

PC 1			PC 2		
Mass	Positive Loading	Assignment	Mass	Positive Loading	Assignment
22.99	9.21E-01	$\text{Na}^+$	73.07	7.07E-01	$\text{SiC}_3\text{H}_9^+$
62.99	2.32E-01	$\text{Na}_2\text{OH}^+$	147.10	1.98E-01	$\text{Si}_2\text{C}_6\text{H}_{19}^+$
70.99	3.96E-02	$\text{C}_5\text{H}_{11}^+$	59.04	4.48E-02	$\text{C}_4\text{H}_{11}^+$
45.98	3.36E-02	$\text{Na}_2^+$	27.97	4.38E-02	$\text{Si}^+$
46.99	2.92E-02	$\text{Na}_2\text{H}^+$	207.06	4.14E-02	$\text{Si}_3\text{C}_5\text{H}_{15}\text{O}_3^+$
117.02	2.53E-02	$\text{C}_9\text{H}_9^+$	221.15	3.59E-02	$\text{Si}_3\text{C}_7\text{H}_{21}\text{O}_4^+$
128.96	2.51E-02	$\text{C}_{10}\text{H}_8^+$	38.96	3.58E-02	$\text{K}^+$
Mass	Negative Loading	Assignment	Mass	Negative Loading	Assignment
29.04	-2.34E-02	$\text{C}_2\text{H}_5^+$	113.14	-7.33E-02	$\text{C}_8\text{H}_{17}^+$
83.09	-2.42E-02	$\text{C}_6\text{H}_{11}^+$	83.09	-7.61E-02	$\text{C}_6\text{H}_{11}^+$
147.10	-2.44E-02	$\text{Si}_2\text{C}_6\text{H}_{19}^+$	56.06	-8.53E-02	$\text{C}_4\text{H}_8^+$
69.07	-4.11E-02	$\text{C}_5\text{H}_9^+$	27.02	-9.22E-02	$\text{C}_2\text{H}_3^+$
41.04	-6.20E-02	$\text{C}_4\text{H}_5^+$	43.05	-9.24E-02	$\text{C}_3\text{H}_7^+$
73.06	-6.33E-02	$\text{SiC}_3\text{H}_9^+$	97.11	-1.10E-01	$\text{C}_7\text{H}_{13}^+$
43.06	-7.63E-02	$\text{C}_3\text{H}_7^+$	29.04	-1.36E-01	$\text{C}_2\text{H}_5^+$
57.07	-8.26E-02	$\text{C}_4\text{H}_9^+$	55.04	-1.76E-01	$\text{C}_4\text{H}_7^+$
55.05	-8.35E-02	$\text{C}_4\text{H}_7^+$	41.04	-2.62E-01	$\text{C}_3\text{H}_5^+$
			57.07	-4.67E-01	$\text{C}_4\text{H}_9^+$

On analysis of needles 3, 4, 5 and 6 there was a chemical difference along the length of the needle which is seen as the data points splitting. This is suspected to be due to the stability of the chemistry coming into contact with the harsh environment of the engine. The other ions observed for PC 2 depicted in Figure 5.3iii, that are indicating a high or low loading have been identified and assigned in Table 5.1. A range of ions were detected with varying masses up to  $m/z$  221.15, which is suspected to be a polysiloxane [204-207].

#### 5.2.2.3 *Negative Ion PC 1*

The findings of the negative ion PCA data are depicted in Figure 5.4i, the graph shows the data for PC 1 and PC 2. For the PC 1 data it was observed that needles 6 and 7 are a positive score and the ions identified for this are  $\text{CN}^-$  and  $\text{CNO}^-$ , shown in Figure 5.4ii. Needles 3, 4 and 5 have a negative score and this is due to a greater intensity of  $\text{PO}_x^-$  and  $\text{SO}_x^-$  ions. Needles 1, 2 and 8 were clustered around zero loading for PC 1, which means that the ions are present on the needles but are not in high intensities compared to the other needles.

#### 5.2.2.4 *Negative Ion PC 2*

The negative ion data for PC 2 is depicted in Figure 5.4iii. Needle 3, 6 and 7 are positive had a positive score for PC 2. The positive loading for PC 2 was due to oxygen and nitrogen species, including  $\text{O}^-$ ,  $\text{OH}^-$ ,  $\text{CN}^-$  and  $\text{CNO}^-$ . Needles 2 and 8 had a negative score for PC 2. The negative loading on PC 2 identified that sulfates and phosphates were the main ion intensity difference, the ions identified were  $\text{SO}_3^-$ ,  $\text{PO}_3^-$  and sulfate and phosphate groups attached to hydrocarbon chains. For needles 1, 4 and 5 there were analysis points with positive and negative scores, the points split, therefore showing that there were

different chemistries along the needle and that both ions that were assigned for positive and negative scoring were found on these needles.

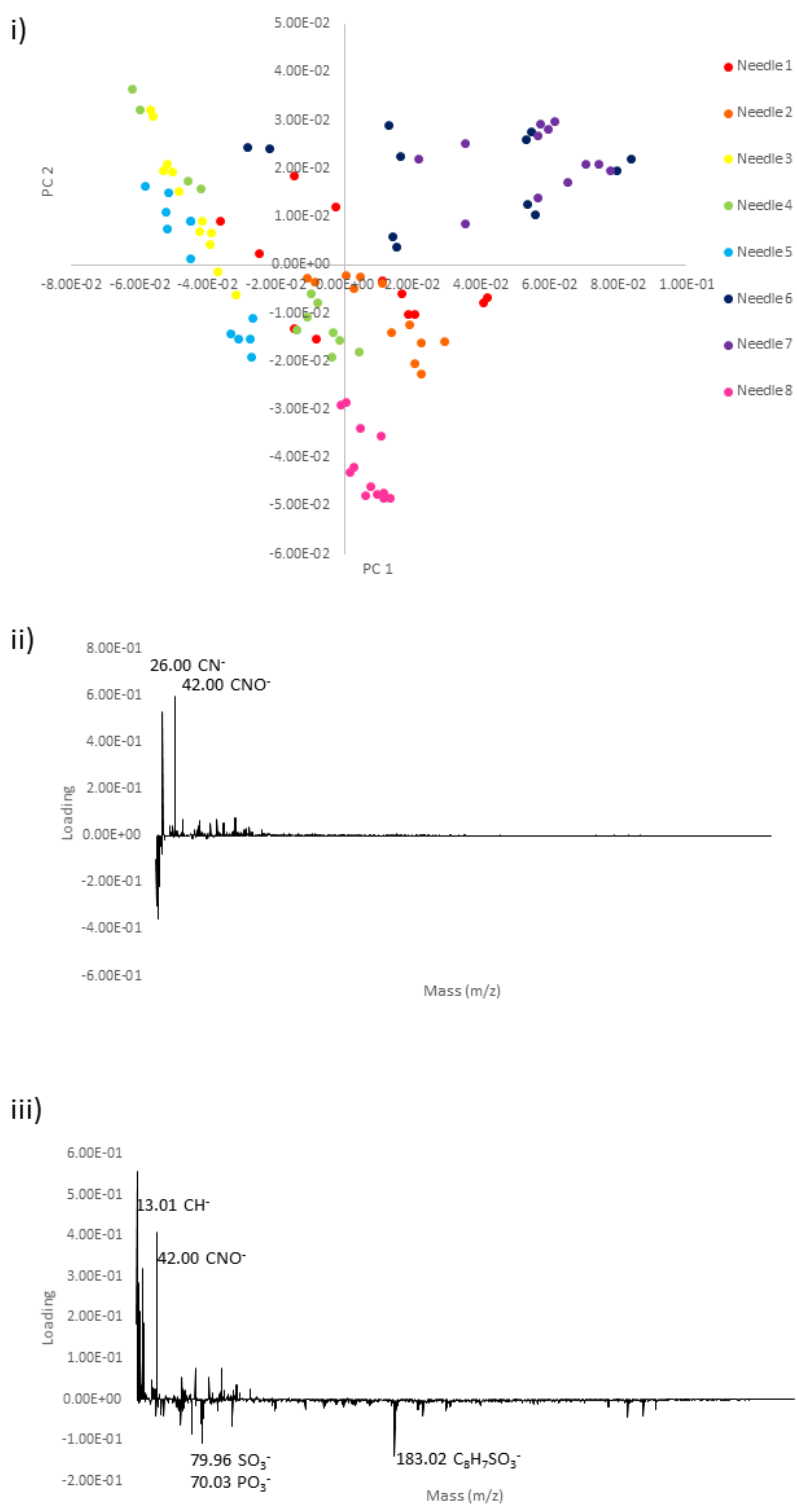


Figure 5.4 Principal component analysis of negative ion data. i) Scores of PC1 against PC2 ii) Loading on PC1, indicating the main ions iii) Loading on PC2, indicating the main ions.

Table 5.2 PCA of Negative ion data of ToF-SIMS, with the positive and negative loadings and the assignment for each ion for PC1 and PC 2.

PC1			PC2		
Mass	Positive Loading	Assignment	Mass	Positive Loading	Assignment
42.00	5.97E-01	CNO <sup>-</sup>	13.01	5.58E-01	CH <sup>-</sup>
13.01	5.28E-01	CH <sup>-</sup>	42.00	4.08E-01	CNO <sup>-</sup>
26.00	5.28E-01	CN <sup>-</sup>	25.01	3.21E-01	C <sub>2</sub> H <sup>-</sup>
91.00	7.39E-02	C <sub>7</sub> H <sub>7</sub> <sup>-</sup>	15.99	2.86E-01	O <sup>-</sup>
79.96	7.07E-02	SO <sub>3</sub> <sup>-</sup>	17.00	2.15E-01	OH <sup>-</sup>
50.00	6.91E-02	C <sub>4</sub> H <sub>2</sub> <sup>-</sup>	26.00	1.87E-01	CN <sup>-</sup>
66.00	6.76E-02	C <sub>3</sub> NO <sup>-</sup>	12.00	1.82E-01	C <sup>-</sup>
83.97	5.54E-02	SiC <sub>3</sub> H <sub>4</sub> O <sup>-</sup>	24.00	1.06E-01	C <sub>2</sub> <sup>-</sup>
75.00	5.21E-02	SiC <sub>2</sub> H <sub>7</sub> O <sup>-</sup>	75.00	7.72E-02	SiC <sub>2</sub> H <sub>7</sub> O <sup>-</sup>
			91.00	7.55E-02	C <sub>7</sub> H <sub>7</sub> <sup>-</sup>
			65.01	5.33E-02	C <sub>4</sub> HO <sup>-</sup>
			83.97	4.58E-02	SiC <sub>3</sub> H <sub>4</sub> O <sup>-</sup>
Mass	Negative Loading	Assignment	Mass	Negative Loading	Assignment
25.01	-7.81E-02	C <sub>2</sub> H <sup>-</sup>	299.16	-2.59E-04	C <sub>15</sub> H <sub>25</sub> PO <sub>4</sub> <sup>-</sup>
12.00	-9.99E-02	C <sup>-</sup>	344.97	-2.79E-04	C <sub>19</sub> H <sub>22</sub> PO <sub>4</sub> <sup>-</sup>
17.00	-2.15E-01	OH <sup>-</sup>	325.30	-4.01E-02	C <sub>18</sub> H <sub>29</sub> SO <sub>3</sub> <sup>-</sup>
13.01	-3.03E-01	CH <sup>-</sup>	311.35	-4.57E-02	C <sub>17</sub> H <sub>27</sub> SO <sub>3</sub> <sup>-</sup>
15.99	-3.58E-01	O <sup>-</sup>	79.03	-5.96E-02	PO <sub>3</sub> <sup>-</sup>
			64.00	-6.19E-02	SO <sub>2</sub> <sup>-</sup>
			97.02	-6.59E-02	C <sub>8</sub> H <sup>-</sup>
			73.01	-8.47E-02	C <sub>6</sub> H <sup>-</sup>
			79.96	-1.06E-01	SO <sub>3</sub> <sup>-</sup>
			183.02	-1.27E-01	C <sub>8</sub> H <sub>7</sub> SO <sub>3</sub> <sup>-</sup>

#### 5.2.2.5 Examination of PCA of Eight Injector Needles

The purpose of this investigation was to identify similarities and differences in the chemistries of the eight needles that were analysed. Needle 3 has the greatest difference, with regards to the sodium levels detected and phosphate and sulfate groups, there were no needles scoring similarly to needle 3.

Needles 6 and 7 scored comparably for the positive ion data and had alike negative data except for the split of the needle 7 points on PC 2. This was to be

expected as both of these needles were from New York, so would have likely experienced comparable fuel and additive packages. There was also a similarity observed for needles 2 and 8, both scoring negatively for PC1 with the positive ion data which was an increased intensity for hydrocarbons and a lower sodium count. Both needles also had a negative score for PC 2 with the negative ion data which was assigned to be phosphate and sulfate groups. This was not to be expected at needle 2 was a DW10B engine test and needle 8 was from China, both have different regulations with fuel and additives. There was also a similarity seen in the data observed for needles 1 and 4, needle 1 was from Norway and needle 4 was from Illinois USA, therefore again a similarity was not expected, levels of the sodium species and hydrocarbons were not in high intensities on these needles. The data shows that there was more phosphate and sulfate groups on needle 1 and more nitrogen containing species on needle 4.

To conclude, PCA has been successfully used to analyse the ions from eight injector needles and has identified similarities and differences in chemistries. However, this was surface analysis and further differences in chemistry could lie under the surface, therefore the 3D structure must be investigated.

### **5.2.3 Investigation into the 3D Structure of Diesel Push Rod Deposit**

#### **Using Focused Ion Beam (FIB) Lift Out and TEM EDX**

A lift out was obtained from sample push rod 1, details can be found in Table 2.1. The push rod resides behind the injector needle, the deposits that form on the push rod are suspected to be similar to injector needle deposits because they are under high pressure and low temperatures and have not entered into the combustion chamber. Figure 5.5 shows SEM images of the lift out at

different stages of removal from the pushrod surface. The lift out was  $5 \times 15$   $\mu\text{m}$ , exact measurement is difficult due to the angle of the lift out.

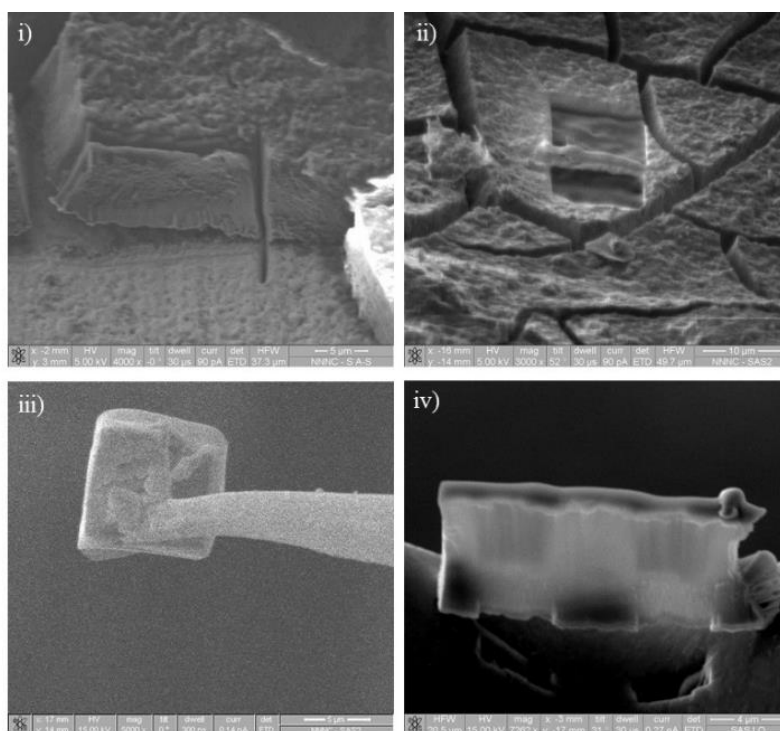


*Figure 5.5 SEM Images of Lift out Process. i) Sectioning of deposit sample ii) Milling trenches for lift out sample iii) Lift out extracted with omniprobe iv) The lift out with thinned sections for TEM analysis*

The size of the lift out was considered too small for analysis with ToF-SIMS so it was suggested that it would be more suitable for analysis with transmission electron microscopy (TEM). TEM can be used to look at the structuring of a sample, as seen in Figure 3.10. The TEM images of the lift out shows four distinct layers, shown in Figure 5.6. The lowest layer was from the surface of the pushrod and the top layer was the platinum deposited protection layer. The two middle layers were from the deposit that formed on the push rod. The TEM images show that there is an interface and at the interface there was more graphitic structure.

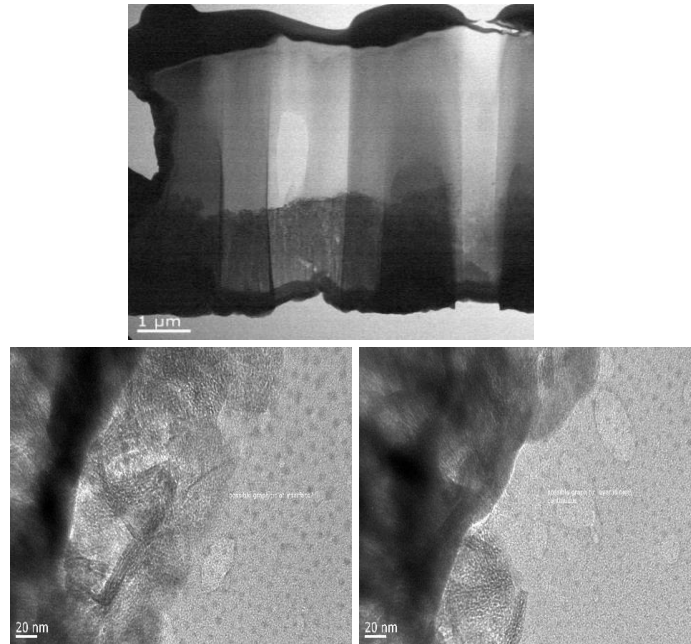


*Figure 5.6 TEM images of the lift out, depicting the top platinum coating, two layered deposit and interface of the push rod surface.*

Further analysis of the lift out with EDX analysis shows that the lower deposit layer consisted of Fe, O, S and Cl. Then a carbonaceous deposit has formed on top. The EDX data can be seen in Figure 5.7. It is likely that an oxide layer consisting of iron, chromium and oxygen had formed on the top of the push rod. During the lifetime of the engine the oxide layer could have created rough nucleation points for carbonaceous material to grow upon. It was observed that Cl and S had migrated into the oxide layer and also looked to be diffusing through the carbon layer, it appeared that the Fe was not diffusing through the carbon material and maintaining the interface. The stress of the mismatching lattice structures of the two layers has likely caused the deposit to delaminate from the push rod. This is further suggested in the rough bottom edge of the lift out seen in Figure 5.6. If this deposit was to delaminate full it would cause

large piece of insoluble debris to be carried by the fuel and is likely to cause problems further in the engine.

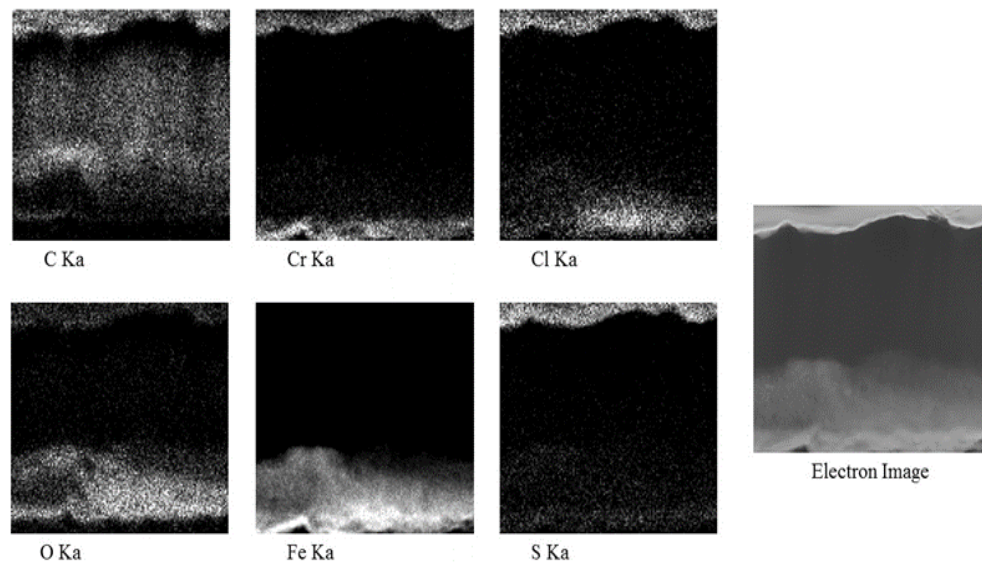


*Figure 5.7 EDX analysis of lift out from push rod 1.*

#### **5.2.4 Examination of the 3D structure of Diesel Injector Tip Deposit**

##### **Using FIB SIMS, TEM EDX and Raman Spectroscopy**

A lift out was obtained from injector tip 2, details can be found in Table 2.1.

For this analysis there was a clear objective to create the lift out an appropriate size for a range of analytical techniques. The lift out from injector tip 2 can be seen in Figure 5.8i, it is approximately  $50 \times 50 \mu\text{m}$  in size. The image with the ruler bars are incorrect due to the tilt of the lift out so cannot be used as accurate measurements of the lift out. The lift out was square in shape, seen in Figure 5.8ii.

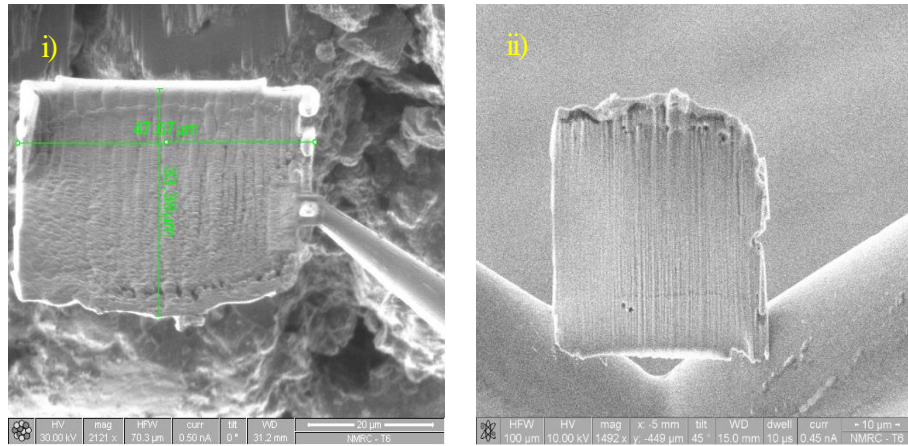


Figure 5.8 SEM images of the lift out attached to a TEM copper grid for further analysis.

#### 5.2.4.1 Raman Spectroscopy Analysis of Lift Out

The lift out from injector tip 2 was line mapped with Raman spectroscopy. In Figure 5.10 the line map started at the bottom of the lift out and moved in 2 μm increments taking a Raman spectrum at each step to reach the top, shown in green. The actual line of analysis by the laser can be seen to the right of the green line as the laser has moved from top to bottom.

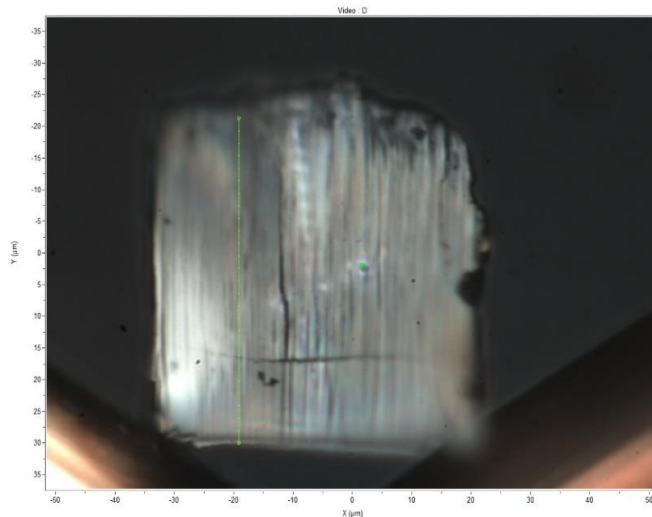
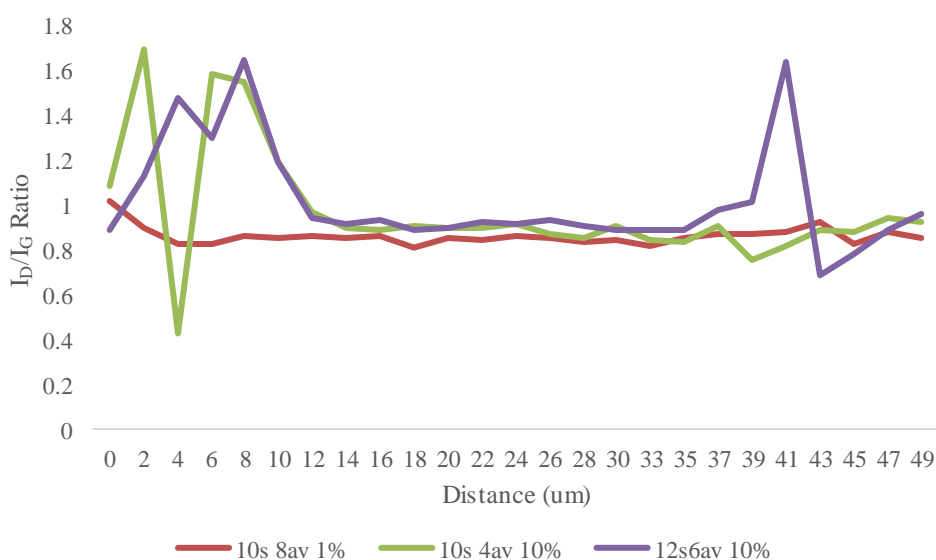


Figure 5.9 Photo of the surface of the lift out and the regions analysed with Raman spectroscopy line mapping. The green line is the software set line for analysis.

The graph, shown in Figure 5.11 shows the change in ratio of the  $I_D/I_G$  band. The graph shows three series with varying settings of the Raman laser and acquisition. The initial analysis was the red line at a longer acquisition time, more averages and lower power laser, this was to try to not damage the sample. The next analysis was with a stronger laser power and the same acquisition time with less averages. There is a trade-off between damaging the sample and having a strong enough laser to excite the photons, using the 10% laser did leave marks on the surface of the lift out. However, all three series show no difference in the  $I_D/I_G$  ratio. It was suspected that the lower part of the deposit would have a lower  $I_D/I_G$  ratio because there would be greater graphitic content. The spikes and trough at the bottom and top of the analysis could be due to interference from the edge of the lift out. The analysis point indicated by the software did not match up to the analysis point on the lift out. This was particularly obvious when using the 10% laser and the analysis points created marks on the surface, seen in Figure 5.10.



*Figure 5.10 Raman spectroscopy line mapping analysis of lift out using a range of settings for the acquisition time, averages and strength of laser.*

#### 5.2.4.2 Chemical Mapping with ToF-SIMS Analysis of Lift Out

The ToF-SIMS chemical maps of injector tip 2 for the positive and negative ions can be observed in Figure 5.9. The lift out was attached to the middle of the TEM holder, however, the holder was thicker than the lift out. Therefore there was an issue obtaining signal from the surface of the lift out. This is depicted in the negative ion data of  $\text{CN}^-$  and  $\text{Cl}^-$  where the section of the holder is bright at the bottom of the analysis area, seen in Figure 5.9. Due to this issue, it was difficult to chemically map the lift out and distinguish any layering.

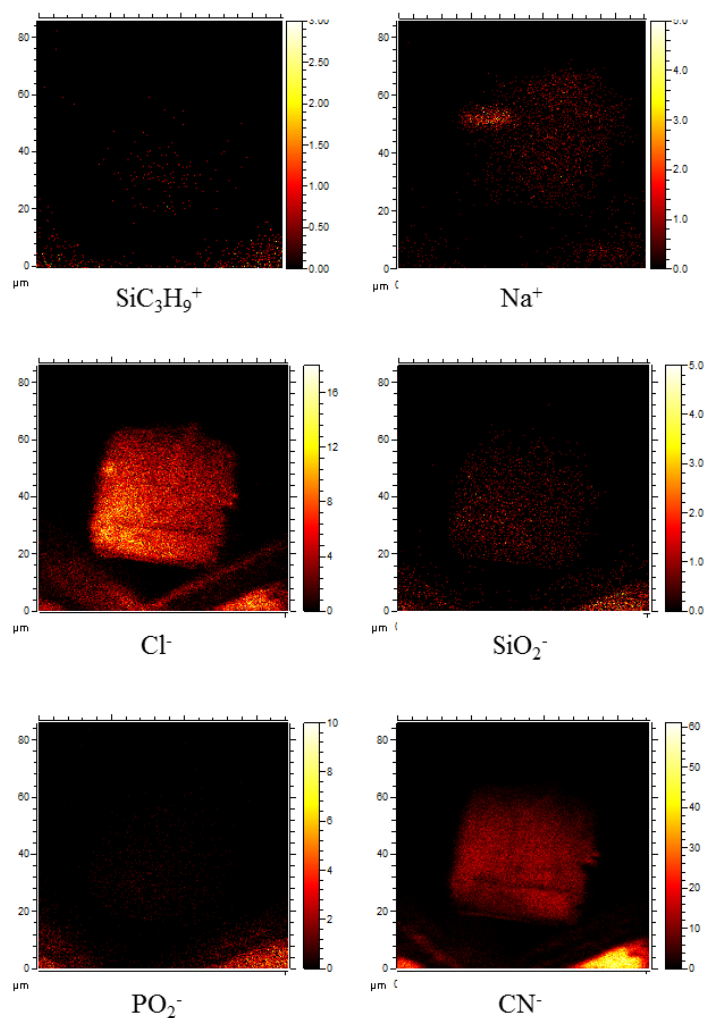
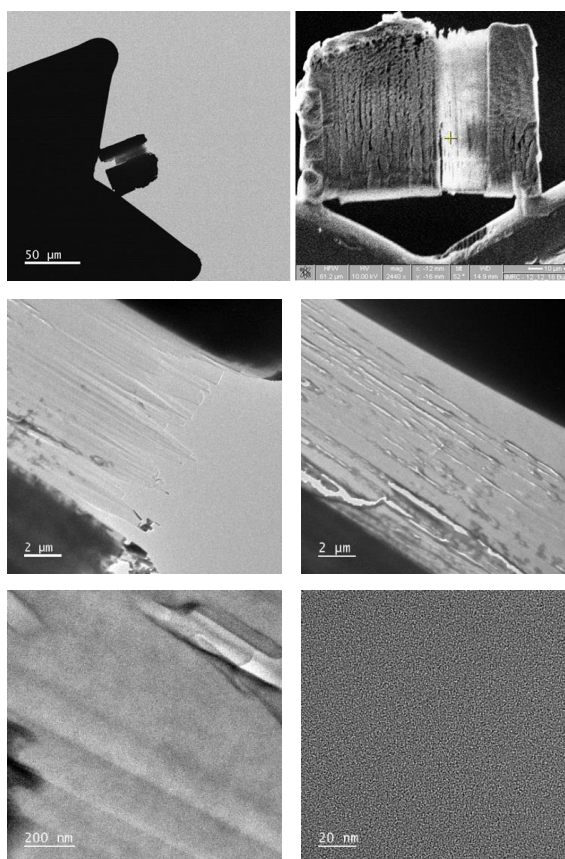


Figure 5.11 Chemical mapping of the lift out, showing positive ions  $\text{Na}^+$  and  $\text{SiC}_3\text{H}_9^+$ , and negative ions  $\text{Cl}^-$ ,  $\text{PO}_2^-$ ,  $\text{CN}^-$  and  $\text{SiO}_2^-$  ions.

### 5.2.4.3 TEM EDX Analysis of Lift Out

TEM analysis of the lift out from injector tip 2 shows small areas of ordering and it was uniform though out the lift out. This was to be expected after analysis with Raman spectroscopy and the ToF-SIMS data shows no difference with depth. The electron images can be observed in Figure 5.12. The bottom section of the thinned area for TEM analysis had broken away due to the brittle nature of the deposit.



*Figure 5.12 TEM images of the lift out showing small amounts of ordering and uniformity throughout the sample.*

The energy dispersive X-ray (EDX) analysis of the lift out shows a uniform distribution of a range of elements, shown in Figure 5.13. Deposits found on the tips can be over 100 μm thick. Therefore from this EDX data it was

concluded that there was no difference in chemistry. This could have been for a number of reasons, such as this was not a true representation of the deposit because it did cover the full depth of the deposit. Another reason could be that for this deposits there was no layering and that the chemistry did not change. It is unlikely to find the same layering structure in a range of deposits.

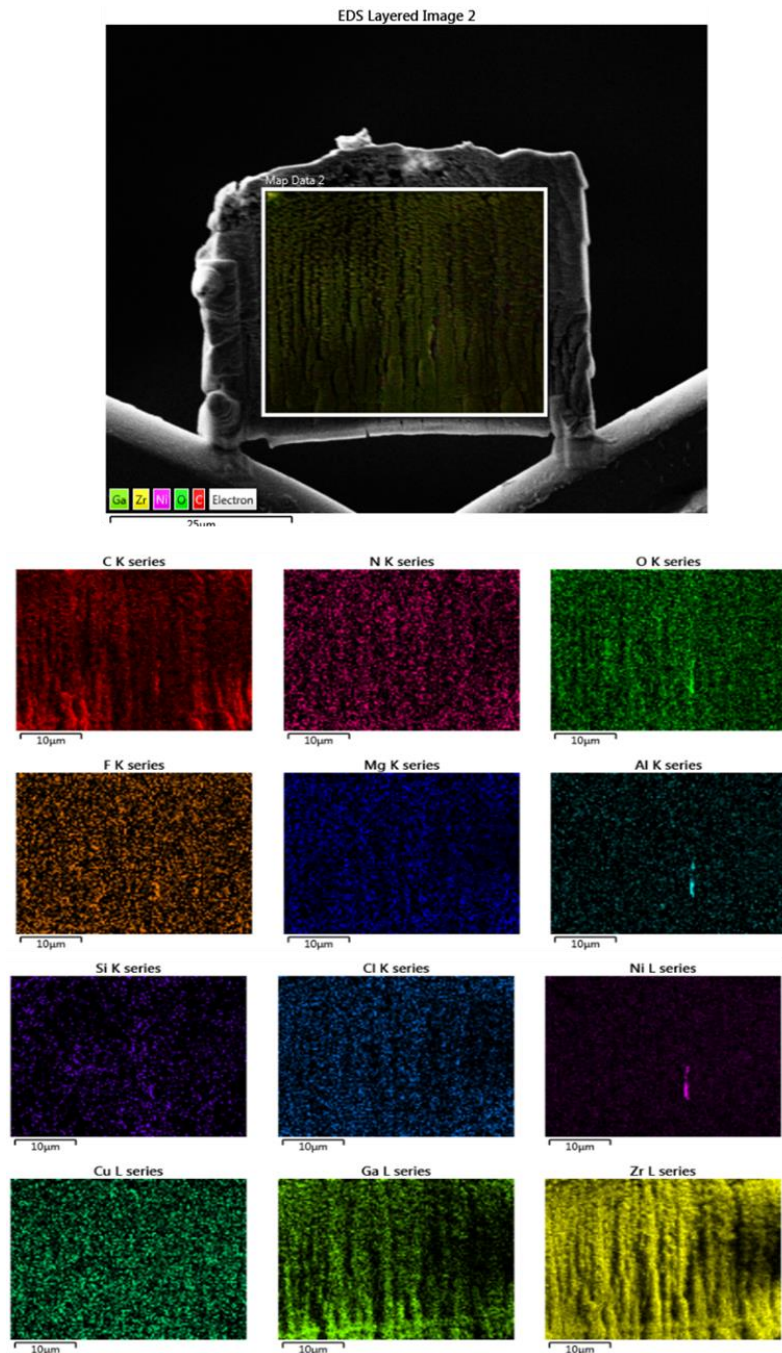


*Figure 5.13 EDX data of Lift out, showing the location of the analysis area and the different elements selected for analysis.*

In order to obtain a true representation of the deposits, the lift out would need to be in the order of 100  $\mu\text{m}$  in height. The width of the lift out would not have to be the same as the height, however, the trenches required on either side of the lift out to observe the bottom of the lift out would need to be substantial to reach a depth of 100  $\mu\text{m}$ . Another issue that would arise with a lift out is that because these deposits are porous they are liable to break during the milling process or extraction. Therefore it was finally concluded that a lift out was not suitable for these thicker deposits. Another disadvantage to FIB lift outs is the amount of time required to create a lift out, care must be taken to not break the lift outs. Once a suitable method for analysing IDIDs has been identified then it will be important to begin comparing a range of different deposits.

#### **5.2.5 Application of FIB to Create Trenches for 3D Structure Analysis of IDIDs with ToF-SIMS**

A new test method for analysing the IDIDs was proposed, that instead of creating lift outs, FIB could be applied to mill trenches into the deposit. The sample was angled so that the FIB would mill into the sample to create a 'ramp'. By removing the top layers it would expose the lower parts of the deposit for surface analysis. Then ToF-SIMS would be able to chemically map the exposed surface. The benefit to this method is that the analysis area can be much greater than what a lift out could achieve. The sample used for the trench investigation was injector tip 3, the details can be found in Table 2.1. In Figure 5.14 two trenches can be observed.

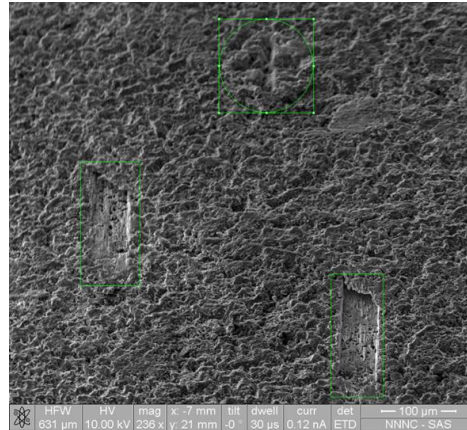


Figure 5.14 SEM image of trenches milled into injector tip 3 for ToF-SIMS analysis.

The positive ion spectra can be seen in Figure 5.15. The spectrum in Figure 5.15i shows the overall area spectrum, whilst Figure 5.15ii is from the selected region around the trench and Figure 5.15iii the region inside the trench. It can be seen for the spectra that there are little to no differences between them. The only ion of difference can be seen in the positive data in Figure 5.15, where  $\text{Na}^+$  and  $\text{K}^+$ ,  $m/z$  22.99 (Purple bar) and  $m/z$  38.98 (green bar), are found in the trench at a higher intensity. This would indicate that  $\text{Na}^+$  and  $\text{K}^+$  are below the surface of the deposit.

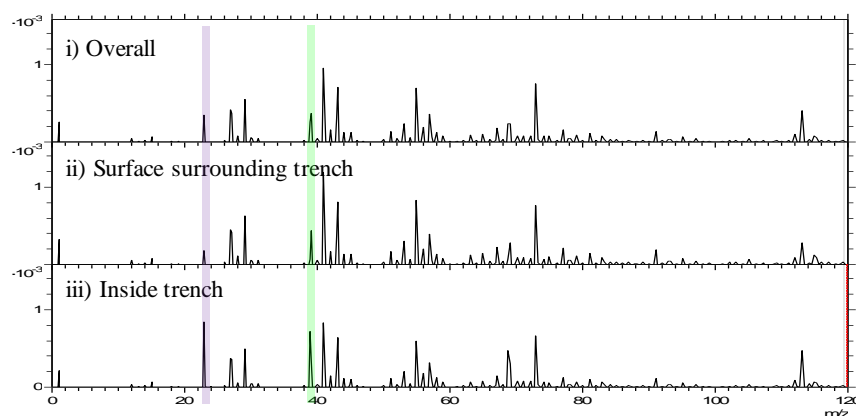
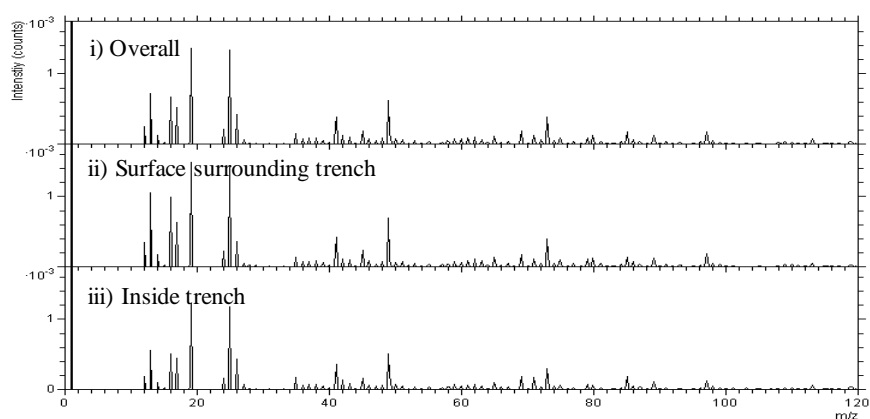


Figure 5.15 Positive ion spectra of trench. i) Overall spectrum of the area ii) Selected region of interest outside of trench iii) Selected region of interest inside of trench.

The negative ion spectra for the overall area, surround surface and inside the trench can be observed in Figure 5.16. There was no difference between the three spectra identified.

It was concluded that milling trenches was the best method of analysing the samples. However, for this piece of work the FIB trench did not mill far enough down into the material because there was no variation observed in the spectra. For future consideration the interface between the deposit and the metal surface must be exposed. The area that was analysed was far larger than the lift out, therefore would be more representative of the deposits and easier for ToF-SIMS analysis. Another advantage to creating a trench is that not so much care is required as with the delicate lift outs.



*Figure 5.16 Negative ion spectra of the trench. i) Overall spectrum of the area ii) Selected region of interest outside of trench iii) Selected region of interest inside of trench.*

## **5.2.6 Further Investigation of IDIDs with FIB Created Trench and Analysis with ToF-SIMS**

Further investigation into the application of FIB milled trenches and analysis with ToF-SIMS was carried out in an all in one system, where the equipment combined FIB and ToF-SIMS in piece of equipment. The main advantage to

this is that there is no risk of contamination by removing the sample from the vacuum. Therefore all ions identified were from the sample. The sample used was injector tip 4 and the details can be found in Table 2.1. The trench was milled to expose the lower chemical composition, observed in Figure 5.17. From the SEM image a horizontal crack in the deposit was seen. It was here that there was a chemical division perceived with ToF-SIMS analysis.

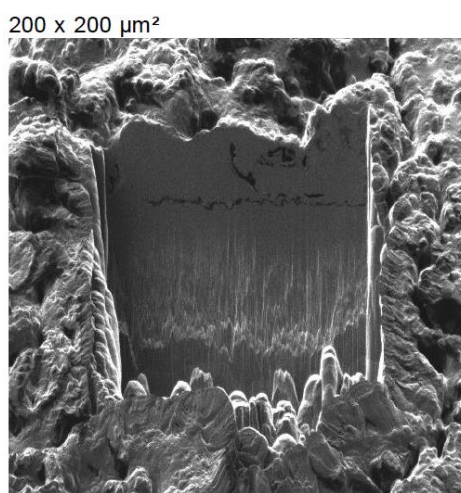


*Figure 5.17 SEM Image of FIB trench created for ToF-SIMS Analysis.*

The positive ion data collected, observed in Figure 5.18, shows the different chemistries of the layers in the deposit. The bottom layer consisted of polysiloxanes [204-207], aliphatic and aromatic hydrocarbons, shown in Figure 5.18ii-iv. The silicone containing material is likely to have come from anti-foam additives, shown in Table 1.2, these are used in diesel fuel to prevent foaming of the fuel at filling stations, which is adverse for the customer. The chemical mapping shows that the top layer of deposits is sodium rich. Sodium is likely to be in the form of salts bonded to carboxylates in the deposit. Sodium dissolves readily in water, which could have contaminated the fuel.

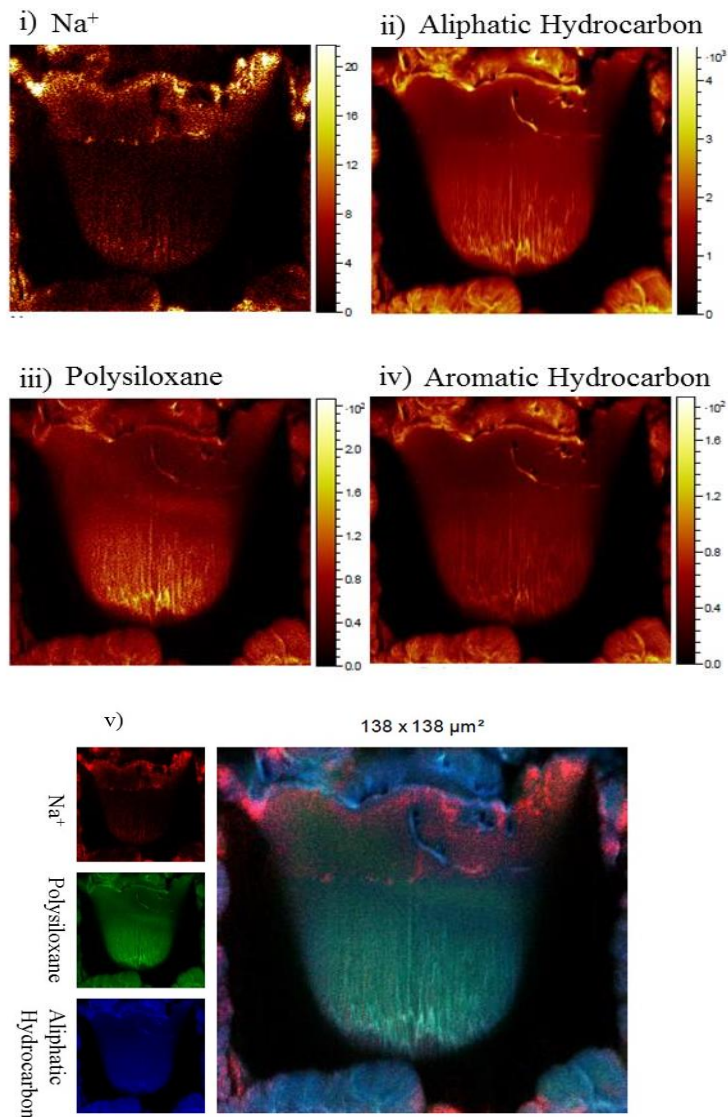


*Figure 5.18 Chemical mapping of positive ions detected in ToF-SIMS of injector tip 4*

The negative ion chemical mapping of the trench is shown in Figure 5.19. The ions detected were  $\text{H}^-$ ,  $\text{OH}^-$ ,  $\text{O}^-$ ,  $\text{C}_x\text{H}_y^-$ , polysiloxanes,  $\text{PO}_x^-$  and  $\text{Cl}^-$ . The chemical mapping shows that polysiloxanes [204-207], oxygen species and hydrocarbons were found in the lower layer of the deposit. The horizontal crack in the deposit depicted in Figure 5.17, had levels of  $\text{PO}_x^-$  and  $\text{Cl}^-$  present. The phosphate ions are likely to have come from lubricant oil additives,

however, Feld *et al.* has suggested that phosphate containing species come from anti-corrosive additives [54]. There was no distinct negative ion data for the uppermost layer.

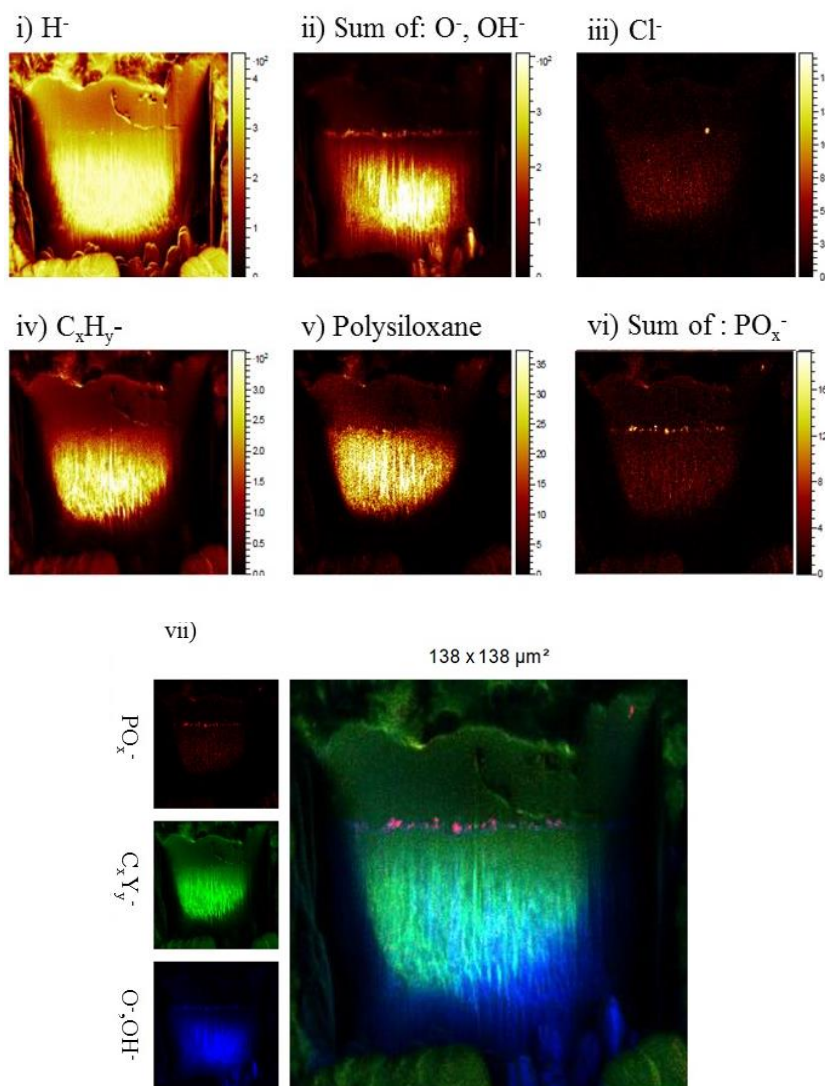


Figure 5.19 Chemical mapping of negative ions detected in ToF-SIMS of injector tip 4

This work gives novel insight into the formation of the diesel deposit on injector tip 4. Prior work to this had speculated that there was a layering structure which was discussed in CHAPTER 1 carried out by barker *et al.* Depth profiling with ToF-SIMS was the first example of IDIDs not being

homogenous, however, this is the first example with clear chemical images that there are distinct interfaces between chemistries. The SEM image in Figure 5.17 shows that there is a horizontal crack and it is here that the phosphate ions are found. It could be speculated that once the phosphate layer settles on top of the polysiloxane [204-207] and carbonaceous material then this creates an optimal surface for sodium salts to form on top.

The crack in the deposit shows that the different chemistries that are seen for this sample do not bind together very well. It is likely that deposit formation will not remain on the surface for the entire lifetime of the injector. The deposit will form and break away in a cyclic motion causing either no problem to the engine function, reduce efficiency of engine or stop engine performance all together. The debris that breaks away could be removed to a location further in the engine, especially if the uppermost layer does not adhere well to the lower levels, and cause issues further down the fuel flow. As the engine experiences different fuels and additives then this would also have an effect in the adherence and removal of deposit.

The bottom of the deposit is not visible so it is unknown if these are the only layers. For future work the interface between the deposit and the tip surface must be reached to observe if there are any more layers to the deposit.

### **5.2.7 Analysis of 3D Structure of IDID with a FIB Created Trench and Depth Profiling with ToF-SIMS**

The work of section 5.2.6 has demonstrated that there is layering structure however, did not reach the interface of the injector tip and the deposit. The aim of this work was to reach the interface to observe layering, and to also compare

data collected from a depth profile with an ion source to a trench wall chemical mapping analysis.

In Figure 5.20 there is a SEM image of a depth profile with a secondary ion source where material has been sputtered away and analysis has been taken in conjunction, the area is highlighted in yellow. This method has been previously applied by Barker *et al.* and Dallanegra *et al.* [37, 45, 79, 108] and has been discussed in Chapter 1. It is believed that the surface of the tip has been sputtered because the area is rough as this is due to the alloy grains being different densities and therefore removed at different rates. The SIMS data collected was also indicating a higher intensity of Fe<sup>+</sup> ions, which is a clear indication of reaching the tip. To combine the work of section 5.2.6, the side wall of the depth profile in Figure 5.20 was milled with a FIB to create a 'ramp' similar to the trench, which will provide a surface area to analyse and expose the layering structure. The trench that has skimmed over the depth profile is highlighted in green. The 'ramp' at the top of the SEM image clearly shows three areas of variation. The green box to the bottom of the picture shows 'patches' of different coloration in the metal, this is likely due to the grain of the alloy metal, however, on chemical analysis this could be determined.

This work demonstrated great potential for analysing IDIDs and comparing the FIB trench milling technique to ToF-SIMS depth profiling. However, time constraints did not allow for further analysis. Therefore this is an area of research that would be high priority for future work.

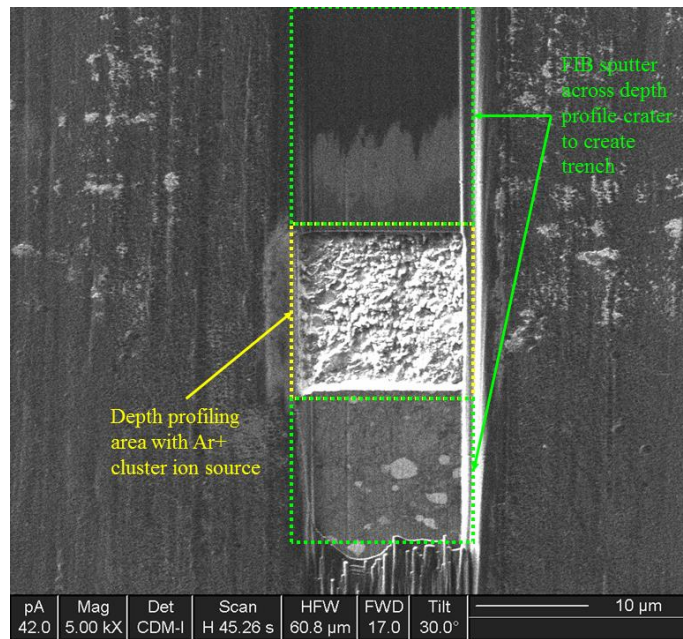


Figure 5.20 A SEM image of a ToF-SIMS depth profile, highlighted in yellow, and a side wall trench created by FIB of the depth profile, which is highlighted in green.

### 5.3 Conclusions

The application of ToF-SIMS has evolved from initial surface and depth profiling of diesel injector deposits, to unite with FIB to create *in situ* analysis of lower depository layers. Through developing the combination of FIB and ToF-SIMS, two method were explored, which were creating lift outs and trenches. This work has proven that a lift out is not the method of choice for IDIDs and that creating trenches is far more advantageous. Due to the thickness of some of these samples the application of a trench was preferable to reach the interface and not compromise the structure, whereas breakages were likely to occur when creating lift outs.

The use of an all in one system reduce risk of contamination and the sample was analysed more efficiently *in situ*. The findings in section 5.2.6 shows that

there were distinct layers of polysiloxane [204-207], a phosphate rich thin middle section and the uppermost layer being sodium rich. Carbonaceous material was found throughout the sample with aromatic carbon being more towards the lower layers as suspected.

The combination of FIB and ToF-SIMS has been used to identify clear distinctions in the formation process of IDIDs. The sophisticated application of depth profiling and creating a side wall trench with FIB has indicated an area of further work with high priority, shown in Figure 5.20.

## **6 Analysing Laboratory Scale Deposits Utilising the Jet Fuel Thermal Oxidation Test (JFTOT) with ULSD and Biodiesel to Mimic IDID Formation**

### **6.1 Summary**

The jet fuel thermal oxidation test (JFTOT) has been used to investigate stability of jet fuel for many decades [180-183]. Adaptions to settings such as temperature and duration of test, have allowed for testing of diesel fuel to now become a discussed method and various work has been published [46, 82, 209]. The JFTOT provides a cost and time efficient method of exploring a variety of fuels and/or additives before progressing to engine scale testing.

Three JFTOT deposits were created with B20 biodiesel, ULSD and a mixture of the two. The JFTOT deposits were a valuable analytical tool when analysing the field IDIDs as it gave evidence of where certain chemistries have come from with regards to fuels. The JFTOT tube deposits were analysed with scanning electron microscopy (SEM), profilometry, hydrolysis, Raman spectroscopy and principle component analysis (PCA) of time of flight secondary ion mass spectrometry (ToF-SIMS).

On analysis of JFTOT deposits similarities were found to IDIDs seen in failed engines. By using one fuel type to form deposits, key chemical markers for each fuel were identified. From the ToF-SIMS negative ion data it was observed that biodiesel degraded at the ester bond to produce  $C_xH_yO^-$  ions and that phosphates and sulfate ion were found more prominently in ULSD deposits. The positive ion data indicated that the ULSD deposit (JFTOT 2)

consisted of higher amounts of  $K^+$  and  $Ca^+$  and B20 biodiesel contained higher intensities of  $Na^+$ .

## 6.2 Results and Discussion

In this work three JFTOT tubes were tested with two types of fuel, B20 biodiesel and ULSD, the area that comes into contact with the fuel is shown in Figure 6.1. For JFTOT 1 the test was fuelled with B20 biodiesel, whilst for JFTOT 2 the test was fuelled with ULSD. The final tube, JFTOT 3 was fuelled with alternating cycles of B20 and ULSD. The full details of the test conditions can be observed in the methodology section 2.2.10.

Due to the direction of flow, the fuel begins to deposit on the final end of the tube, this was discussed in Chapter 1, section 1.8.12. The JFTOT tube was vertical in the test rig therefore with regards to Figure 6.1 this is shown left to right.

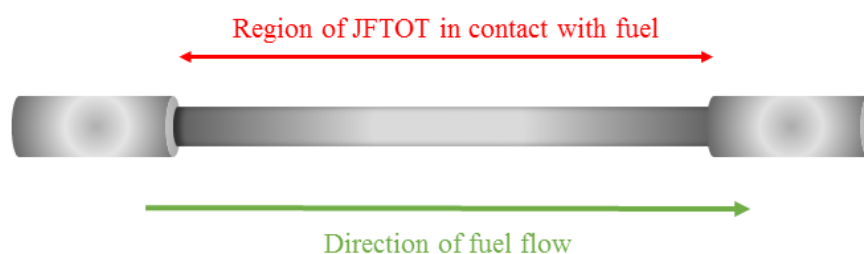


*Figure 6.1 A schematic of a JFTOT tube showing the direction of flow of the fuel over the middle section of tube. The thinner centre part of the tube is the area where the fuel flowed over.*

### 6.2.1 Visual Analysis of the JFTOT Tubes

In Figure 6.2 the photos of JFTOT tubes 1-3 can be observed. All three tubes have deposited in the same region, which is the second half of the tube.

Sander's thesis has investigated the computational fluid dynamics of the flow

of fuel through the JFTOT to demonstrate that the position of where there is the most build-up of deposit on the tube is the hottest point [210]. Although the thermocouple is set to a temperature of 260 °C there was not uniform heating of the JFTOT tubes[210]. The area of greatest deposit forms around the same area for all three samples, indicating this area was crucial in conditions for deposit formation. Whether this is the highest temperature or the optimum path time for the fuel to degrade and deposit at this point is unclear for this work. It has been suggested by Lacey *et al.* that certain chemistries will form at certain temperatures [46], this has been discussed in section 1.8.12.



*Figure 6.2 Visual photos of JFTOT tube 1-3. i) JFTOT 1 was fuelled on B20 RME biodiesel fuel at 260 °C for 150 mins. ii) JFTOT 2 was fuelled on ULSD fuel at 260 °C for 150 mins. iii) JFTOT 3 was fuelled on B20 RME biodiesel and ULSD fuel at 260 °C for 450 mins.*

JFTOT 1 can be seen in Figure 6.2i, the deposit was brown in appearance with areas of different colours towards the middle of the tube, and the deposit

appears to become thicker towards the right side of the tube. JFTOT 2 can be seen in Figure 6.2ii and is heavily carbonaceous in appearance with areas of difference colours in the middle, this deposit varied and was shinier in appearance in the centre section, than the matte appearance of the black carbonaceous deposit further along the tube. JFTOT 3 shown in Figure 6.2iii, appears to be heavily carbonaceous in appearance, where there is less colourful fringing observed in this deposit as there was more carbonaceous deposit observed.

The JFTOT is considered a representative of IDID formation, this is due to in the formation of IDIDs the fuel has not reaching the combustion chamber so therefore is just moving over metal surface at high temperatures and pressures, like the JFTOT. The JFTOT 3 is likely to be more representative of deposits from the field as it is unlikely only one type of fuel will be used in an engines lifetime and the effects of using two types of fuel will be identified in this test. However, the comparison between the three tubes will identify the characteristics in the deposits from the two fuel stocks and if there is any interaction when using different fuels on one tube.

### **6.2.2 Profilometry of the JFTOT Tubes**

Profilometry analysis of the JFTOT samples were taken at five points along the length of the tubes, shown in Figure 6.3i. The profiles show how varied the formed deposit were for the three JFTOT tubes. The varying heights and roughness of the deposit show that the pathway over the JFTOT tubes degraded the fuel and deposited at different points along the tube, mostly at points iii-v. This is thought to be because of varying temperatures along the tube proposed through computational fluid dynamics from Sander's thesis

[210]. The profilometer acquires the images in true colour, therefore this technique can display the different iridescent effects of the deposit at various points, which could indicate different chemistries depositing along the tube. For all three tubes the first profile Figure 6.3iia, Figure 6.3iia and Figure 6.3iva appears to be similar with little to no visible deposit. The profiles show the surface of the tubes to be rough, which is advantageous in building deposit upon. Injector needles surfaces can also be very similar to the JFTOT surfaces in appearance and roughness. The final profiles Figure 6.3iie, Figure 6.3iie and Figure 6.3ive show that the material deposit is less, clearly showing there is a distribution of material. The 4<sup>th</sup> point, Figure 6.3iid, Figure 6.3iid and Figure 6.3ivd, shows the area with the most deposited material. This point was previously proven with computational fluid dynamics that due to the flow of the fuel there was an optimum point for deposition [210].

Figure 6.3ii indicates the sections of analysis acquired along JFTOT 1, which was fuelled with B20 biodiesel. Figure 6.3iic-e shows that the deposit is beginning to form at this point and displays different colours likely indicating variation in the chemistry of the deposit or could be due to different thicknesses of deposit. Figure 6.3iic illustrates this well, exhibiting almost a 'rainbow' effect across the analysed area. Visually JFTOT 1 is different to JFTOT 2 and 3, as there does not appear to be any thick black carbonaceous deposit. JFTOT 1 was fuelled with B20 biodiesel, therefore this could indicate that biodiesel creates alternative chemistry in the deposit to ULSD.

Figure 6.3iii shows the profiles of deposit along JFTOT 2, which was fuelled with ULSD. Figure 6.3iiib-c are visibly colourful deposit formations, as the fuel flowed up to the hottest point. Figure 6.3iiib shows the deposit as a yellow

to pink lacquer on the surface, the groves and scratches of the surface are still visible. Figure 6.3iiid was where the greatest deposit build up occurred, the deposit was almost black in colour and have no features of the steel tube surface, therefore indicating this was the most deposited region.

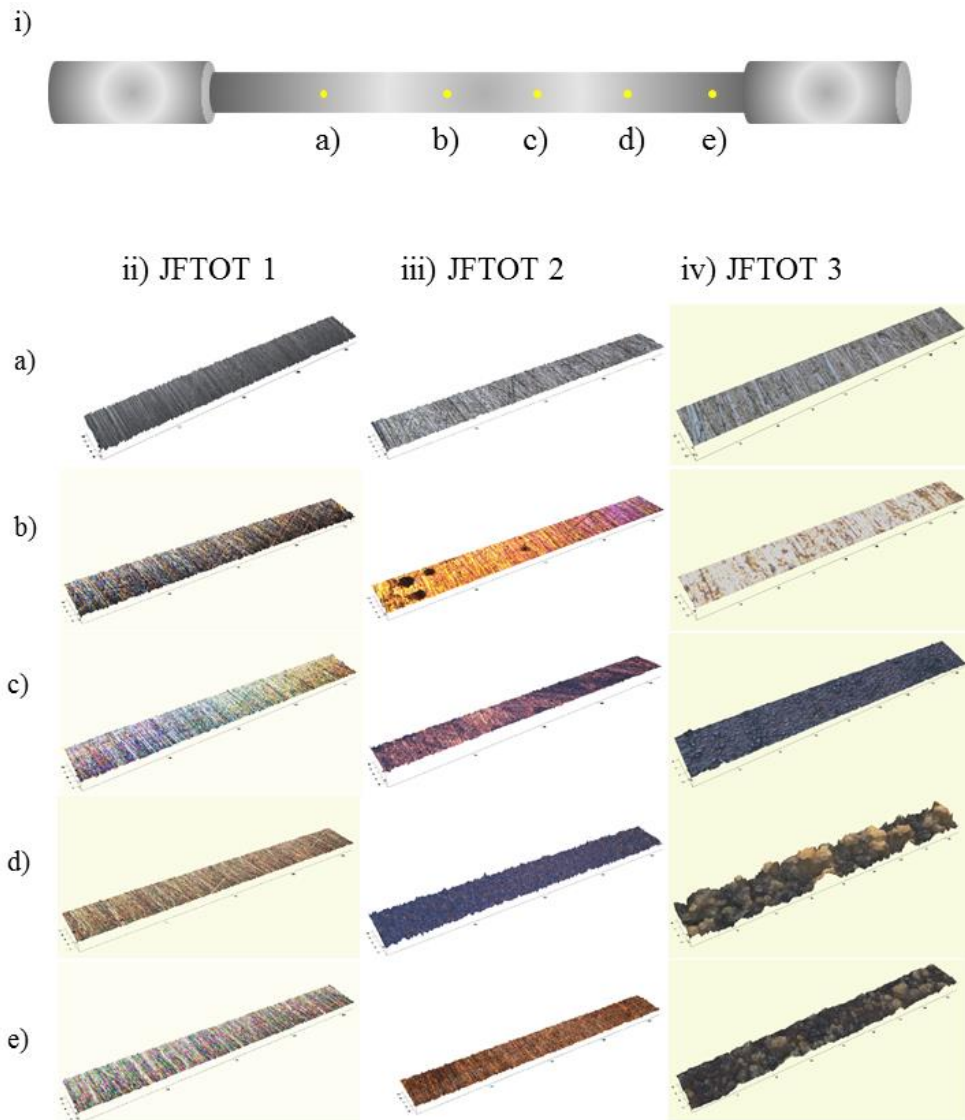


*Figure 6.3 Profilometry profiles of JFTOT tubes 1-3 over an area of  $100 \times 800 \mu\text{m}$ . i) Schematic of a JFTOT tube showing the locations of profiles a-e. ii) Profiles of JFTOT 1 a-e. iii) Profiles of JFTOT 2 a-e. iv) Profiles of JFTOT 3 a-e.*

Figure 6.3iv shows the profiles of deposit along the JFTOT 3. Figure 6.3ivd observes the thickest part of the deposit, which was thicker and more carbonaceous in appearance than the other two tubes. This was to be expected as the tube was tested for three times longer than the other tubes. Figure 6.3ivc shows dark carbonaceous material on the surface, which is similar to the deposit observed in Figure 6.3iiid. This could be the initial layering of deposit that forms and then from observing Figure 6.3ivd, which has a clear thicker deposit which has formed on top.

### **6.2.3 Roughness Studies of JFTOT Tubes**

Analysis with the profilometer provided statistical analysis of the acquired 3D images to give roughness measurements. Roughness data was taken from the same areas as the profiles previously shown in Figure 6.3i.  $R_a$  is the arithmetic average of deviations from the mean and  $R_{pv}$  is the maximum peak to valley difference.

The roughness data collected from the three JFTOT tubes can be observed in Table 6.1. The data shows JFTOT 1 has little change in peak to valley difference and roughness measurements across the tube, which ranged from  $7.8 \pm 0.8$  to  $17.4 \pm 1.0$  and  $0.0 \pm 0.0$  to  $1.9 \pm 0.0$  respectively. The profilometry images shows that the surface of the tubes are not smooth and have many ridges and 'bumps'. It is suspected that when the biodiesel lays down a thin lacquer on the surface of the tube it was settling in between the ridges, and this is why the roughness data shows that the non-contaminated end of the tube is the most rough. For JFTOT 2 and JFTOT 3 there appears to be a trend to the values for  $R_{pv}$  and  $R_a$  measurements. It is observed that position d for both JFTOT 2 and 3, observed in Figure 6.3iiid and Figure 6.3ivd, has the highest

$R_{pv}$  and  $R_a$ . The data from Table 6.1 indicates that the deposits build up in thickness until reaching the highest point and then deposit less material past this point, this is suspected due to position e measures a lower value for  $R_a$  and  $R_{pv}$  than position d on JFTOT 2 and 3.

It was suspected that JFTOT 3 would have the most deposit and be the roughest deposit, due to being tested for three times that of the other tubes, which is what was observed. All of the profiles from Figure 6.3ii-iv and data from Table 6.1 show that there is a difference between the three samples. JFTOT 1 is the least deposited, and does not have the carbonaceous soot-like material that is observed on JFTOT 2 and 3. Both biodiesel and ULSD have been suspected as causes for deposition. From this data it is speculated that ULSD is more likely to be a cause for deposition, due to JFTOT 2 and 3 displaying more deposit. It cannot be speculated from the profiles if JFTOT 3 is different from JFTOT 2 due to the time scale of the test being three times longer or if there is an interaction between using ULSD and B20 biodiesel for the deposit formation.

*Table 6.1 Roughness data of JFTOT tubes 1-3.  $R_{pv}$  is the maximum peak to valley difference.  $R_a$  is the arithmetic average of deviations from the mean.*

	<b>Position</b>	<b>JFTOT 1</b>	<b>JFTOT 2</b>	<b>JFTOT 3</b>
<b><math>R_{pv}</math></b>	a	17.4 ± 1.0	7.2 ± 0.8	1.1 ± 0.1
	b	7.8 ± 0.8	9.5 ± 7.2	3.6 ± 1.0
	c	10.8 ± 1.1	6.4 ± 1.3	2.4 ± 0.4
	d	9.6 ± 1.1	11.2 ± 0.3	10.9 ± 0.6
	e	12.2 ± 1.3	4.8 ± 0.3	6.4 ± 1.0
<b><math>R_a</math></b>	a	1.9 ± 0.0	0.8 ± 0.0	0.1 ± 0.0
	b	0.9 ± 0.0	1.1 ± 0.1	0.2 ± 0.0
	c	1.3 ± 0.1	0.6 ± 0.0	0.3 ± 0.0

d	$1.1 \pm 0.0$	$1.2 \pm 0.1$	$2.0 \pm 0.4$
e	$1.4 \pm 0.1$	$0.6 \pm 0.0$	$1.0 \pm 0.1$

#### 6.2.4 Morphology of JFTOT Tubes Using SEM

The morphology of the surface of JFTOT 1-3 was analysed with SEM, observed in Figure 6.4. The images were taken in the deposited region of the tubes, shown in Figure 6.2.

The deposit of JFTOT 1, observed in Figure 6.4i show that the surface was covered in small pieces of debris and light scratches. The surface has minimal features highlighting the morphology of the deposit. The SEM image of JFTOT 2 seen in Figure 6.4ii illustrates that the deposit is very different in appearance from the JFTOT 1. The deposit on the JFTOT 2 was granular in appearance and uniform in distribution and particle size across the area analysed.

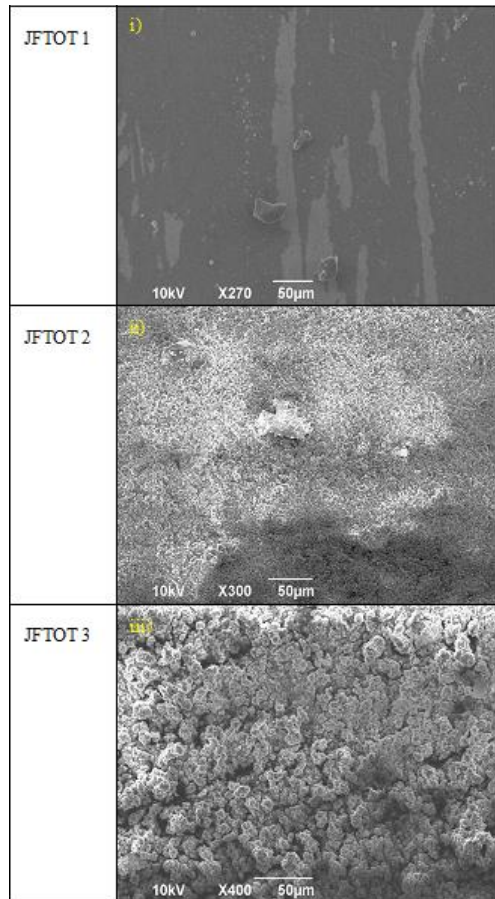


*Figure 6.4. SEM image of JFTOT 1-3 i) A SEM image of JFTOT 1. ii) A SEM image of JFTOT 2. iii) A SEM image of JFTOT 3.*

The morphology of JFTOT 3 shown in Figure 6.4 similar granular structure to JFTOT 2. However, the particles within JFTOT 3 deposit, seen in Figure 6.4iii are larger than on JFTOT 2 observed in Figure 6.4ii. The deposit on JFTOT 3 is suspected to be the thickest deposit because this tube was under test conditions for three times that of JFTOT 1 and 2. The JFTOT 3 deposit appeared uniform in the size and distribution of particles. As the fuel flows over the aggregates stuck on the surface, more deposition would occur as the fuel degrades. This is likely why there is more deposit on JFTOT 3 as more fuel has flowed over the tube.

JFTOT tubes 2 and 3 were the most similar in morphology as there did not appear to be any carbonaceous deposit on JFTOT 1. The SEM images in

Figure 6.4 show similar SEM images that have previously been seen with IDIDs in Chapter 3 section 3.2.2. There have been SEM images similar to the thin lacquer observed on JFTOT 1 and the thicker deposits of JFTOT 2 and 3.

## **6.2.5 Analysis of Carbonaceous Structure Determined Using Raman Spectroscopy**

### *6.2.5.1 Initial Analysis of JFTOT Tubes with Raman Spectroscopy*

As previously discussed in Chapter 4, Raman spectroscopy can be used to describe the graphitic content of a sample through measurements of the D and G band. Speculation from Chapter 4 was that contaminants and/or additives in the fuel were the causes for the fluorescence, which rendered valuable analysis unobtainable. On analysis of the JFTOT tubes, which were only fuelled with biodiesel and ULSD it was unexpected to observe fluorescence and difficulty in obtaining informative data. Due to the fluorescence affecting the spectra a range of parameters were trialed, including the laser filter, acquisition time and averages, this was to improve the quality of the data. The spectra were taken at random points along the tube in the deposited region observed in Figure 6.2.

Figure 6.5 shows the Raman spectroscopy spectra taken of JFTOT 1-3.

Analysis of JFTOT 1, observed in Figure 6.5i, shows that the D and G band to be present when the laser filter strength was set to 10%. A higher power laser was required to excite the photons and the spectra, as no bands were observed when the laser was at 1%. Raman analysis of the JFTOT 2 was extremely difficult to obtain data from, as clearly seen in Figure 6.5ii, this sample fluoresced heavily in comparison to JFTOT 1. Analysis was difficult to keep intensity under 60,000 arbitrary units. The filter was therefore reduced to 1% and different acquisition times were trialed. One run with the filter at 10%

remained under the 60,000 arbitrary unit threshold and small D and G bands can be seen, however, this was not replicated on another area of the tube and heavily fluorescing spectra were common. Raman spectroscopy analysis of JFTOT 3 was the easiest to obtain, maybe this was due to more carbonaceous deposit material being on the tube and/or less volatile material. Raman spectra for JFTOT 3 can be seen in Figure 6.5iii where the D and G bands can be observed and the  $I_D/I_G$  ratio was calculated as  $0.55 \pm 0.06$ . This was comparable to the IDIDs  $I_D/I_G$  ratio reported from Chapter 4 section 4.2.6.2. From analysis of JFTOT 1 and JFTOT 2 tubes this was not to be expected of JFTOT 3, however, because the test was 450 mins, then potentially more stable carbonaceous structures were able to form and drive off some volatile matter.

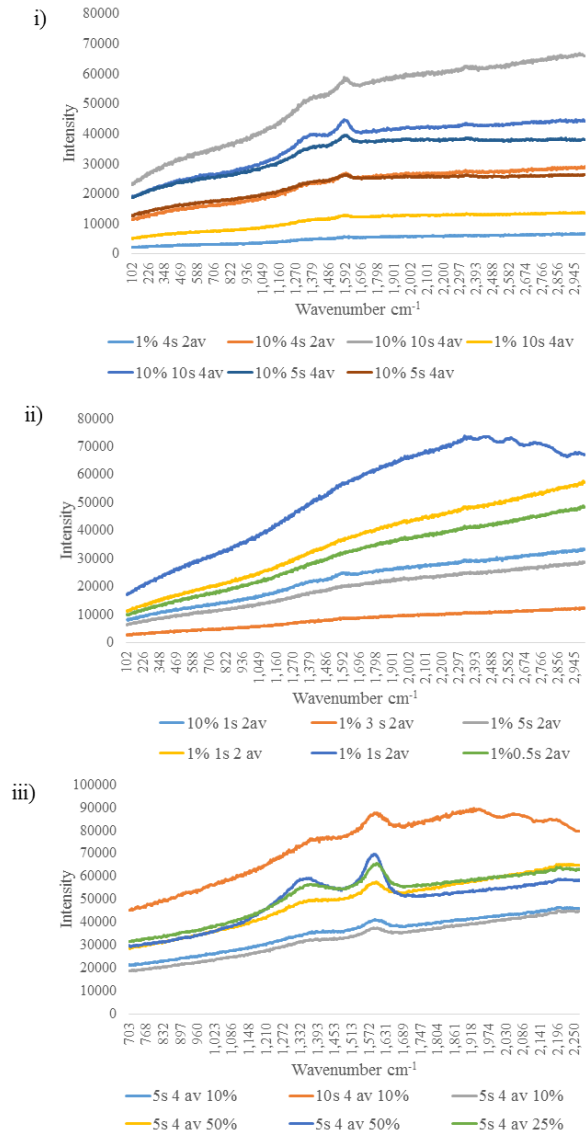


Figure 6.5. Raman spectra of JFTOT 1- 3 and the details include laser filter (%), acquisition time (s) and averages (av). i) Raman spectra of JFTOT 1 fuelled on B20 RME biodiesel. ii) Raman spectra of JFTOT 2 fuelled on ULSD. iii). Raman spectra of JFTOT 3 fuelled on B20 RME biodiesel and ULSD.

This work potentially demonstrates that previous speculations from Chapter 4 that the biodiesel could be a cause for fluorescing is not completely true, JFTOT 1 was far easier to obtain a spectrum from and the D and G bands were more readily visible than from JFTOT 2. As such potentially the ULSD could be a cause for fluorescence. Further tests would need to be carried out on the

initial fuel and doped fuel JFTOT tests to identify the cause. This could be a consideration for work in the future. The Raman analysis of the JFTOT tubes shows that the fuel could be contributing to fluorescence. For further analysis and to be able to compare the D and G band ratios of the fuels thermal treatment using hydrolysis should be adopted.

#### *6.2.5.2 Raman Spectroscopy Analysis of Carbonaceous Structure after Removal of Fluorescing Species with Hydrolysis*

Following HyPy treatment of the JFTOT samples the D and G band were discernible for all of the tubes. The lowest  $I_D/I_G$  ratio was JFTOT 2 at  $0.29 \pm 0.02$ , indicating this has the highest graphitic content, when compared to JFTOT 1 and 3 which were similar with  $I_D/I_G$  ratios of  $0.45 \pm 0.02$  and  $0.49 \pm 0.09$  respectively. It could be speculated that the biodiesel reduces the graphitic content, this could be due to the heteroatoms in the ester bond in biodiesel, which could influence imperfections in the graphitic structures that form. It would be advantageous to further investigate graphitic content of another set of JFTOT tubes with different test conditions.

When comparing to IDIDs formed in the field, discussed in Chapter 4, the  $I_D/I_G$  ratios ranged between  $0.50 \pm 0.18$  and  $0.81 \pm 0.02$ . The ratio calculated from JFTOT 2,  $0.29 \pm 0.02$ , contained more graphitic content than the IDIDs, however, JFTOT 1 and 3 were within experimental error of needle 4. It is likely that ULSD is optimal for forming graphitic structures when compared to biodiesel. However, in reality no engine would be fuelled with just ULSD and contain no additive packages. JFTOT 3 has the highest ratio of  $I_D/I_G$  and this is the nearest value to the ratios of the IDIDs, therefore it can be speculated that JFTOT 3 is the most representative of an IDID out of the three JFTOT tubes,

due to being fuelled with different fuel types and having a comparable  $I_D/I_G$  ratio. Further investigation with the JFTOT tubes and doping the fuel used could observe if this alters  $I_D/I_G$  ratio.

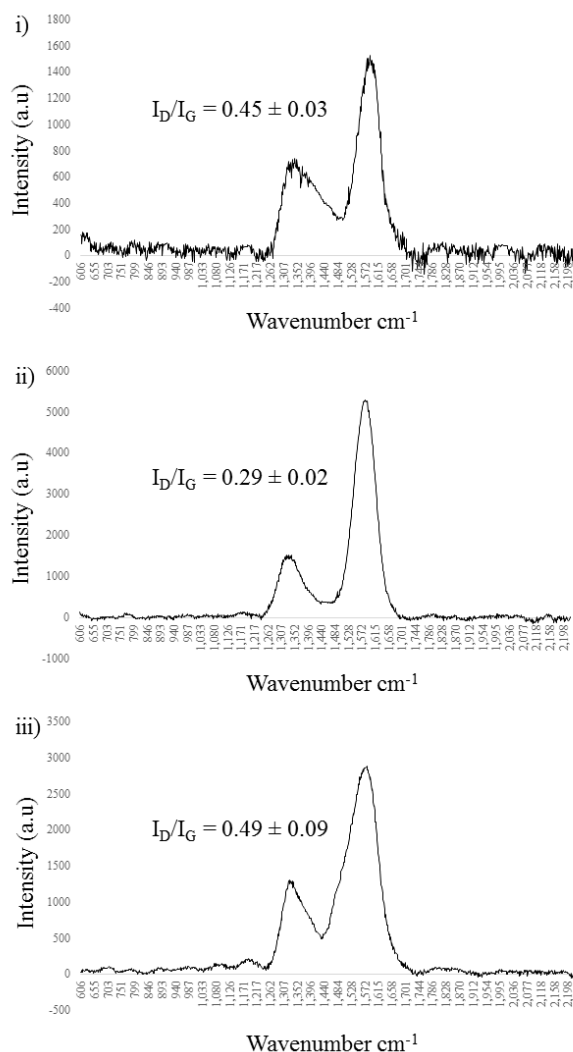


Figure 6.6 Raman Spectra of three JFTOT tubes 1-3, B20, ULSD and Mix. The spectra are averages and have been baselined.

## 6.2.6 GC-MS Analysis of the Labile Fractions Removed from JFTOT Tubes by Hydropyrolysis

The labile fraction from the HyPy treatment of JFTOT 1-3 was analysed with GC-MS, the data can be observed in Figure 6.7. It was suspected that there

would be different ions in JFTOT 1 and 2 due to JFTOT 1 being fuelled with B20 biodiesel and JFTOT 2 being fuelled with ULSD. For JFTOT 3 it was suspected that there would be similarities between JFTOT 1 and 2 because it was fuelled with B20 biodiesel and ULSD. The data shows that there were ions indicative of JFTOT 1 and JFTOT 2 that were found in the JFTOT 3 deposit. It was identified that *n*-C<sub>18</sub> ions found in all three samples, however, only *n*-C<sub>16</sub> were found in JFTOT 1 and JFTOT 3. Polysiloxanes with masses of *m/z* 73 and *m/z* 371 were found on JFTOT 2 and JFTOT 3. The trend of *n*-C<sub>16</sub>, *n*-C<sub>18</sub> and polysiloxane was expected to occur [204-207]. From the GC-MS data collected from the IDIDs analysed in Chapter 4 section 4.2.6.2, *n*-C<sub>16</sub> and *n*-C<sub>18</sub> were identified as the main components of the labile fraction. Therefore this could suggest that for field deposits the fluorescence is affected by a range of causes because JFTOT 1 and 3 identified both of these ions but JFTOT 2 did not. JFTOT 3 is a mixture of fuels which is highly likely for the fuels used in the formation of an IDID and an engine will not be fuelled on only B20 biodiesel. Therefore a multiple of causes is most like to contributing to creating the deposits.

However, there are ions that are only seen in JFTOT 1 and 2, and none present in JFTOT 3. In Figure 6.7i the peaks assigned to only be found in JFTOT 1 and 2 were three and four ring structures, which have been provided in Figure 6.7i. This could be because the ions are unstable and degraded in the longer heating process of JFTOT 3 which has been heated for three times that of JFTOT 1 and 2. The origin of the ions is unknown, and have not been identified in the work carried out in Chapter 4. Therefore with more expansion on the JFTOT samples set, further investigation could uncover the origin.

The highest retentive time peak that was found in all of the samples was assigned as hexanedioic acid bis (2 ethyl hexyl) ester, seen in Figure 6.7, is thought to be a contaminant from the storage of the samples because it was present in all of the samples. This contaminant was not observed in the IDIDs, however, the samples are stored differently, so further work could easily identify if this is the cause by storing the JFTOT tubes in different containers.

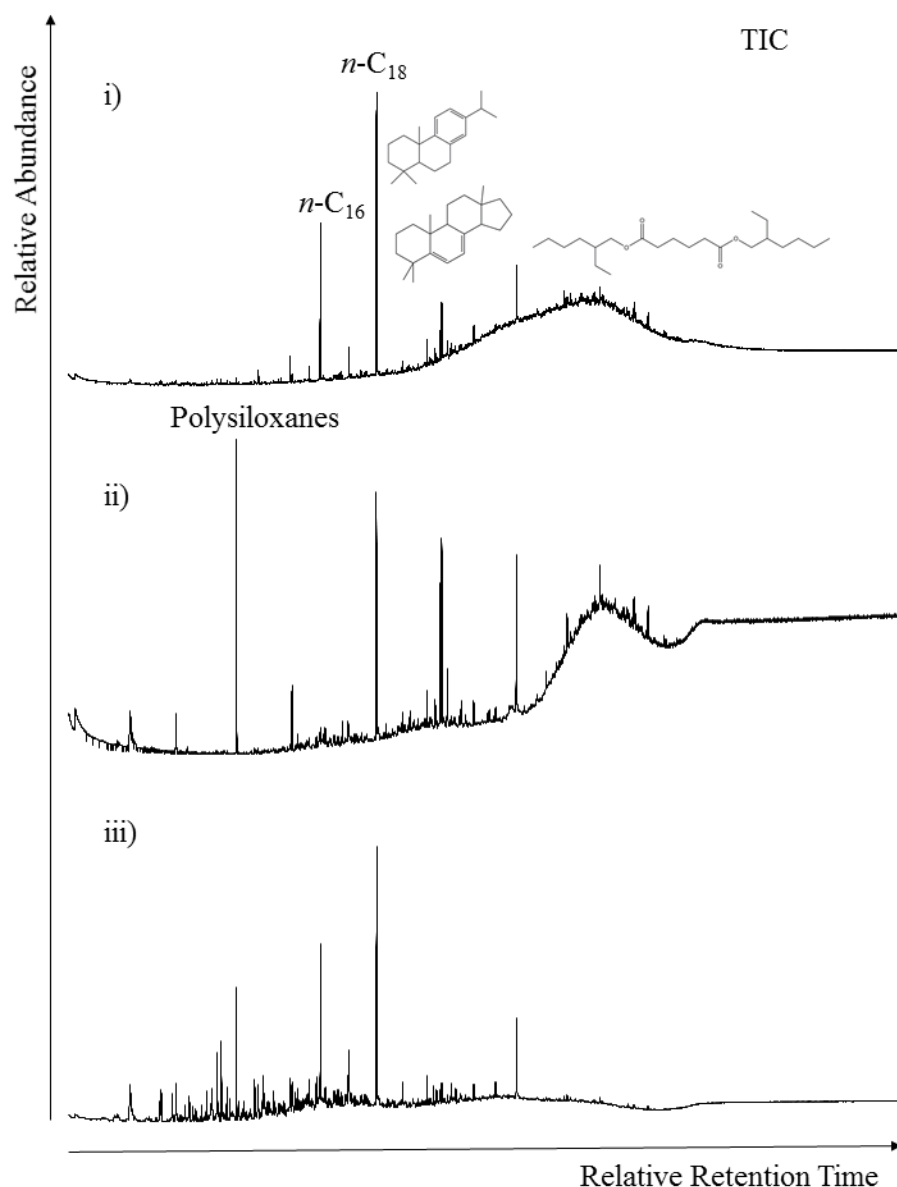


Figure 6.7 GC-MS total ion chromatogram for JFTOT 1-3 i) The total ion chromatogram of JFTOT 1. ii) The total ion chromatogram of JFTOT 2. iii) The total ion chromatogram of JFTOT 3.

### 6.2.7 ToF-SIMS of JFTOT Samples

The previous work in this chapter has identified the morphology and graphitic content of the JFTOT tubes. The GC-MS data from section 6.2.6 has analysed the volatile material, therefore this section will investigate the chemistry of the deposit on tubes with ToF-SIMS as previously applied to IDIDs in Chapter 5. The ToF-SIMS data collected in Chapter 5 was analysed using PCA, which was considered optimal for the data collection from the JFTOT tubes. Only PC 1 and PC 2 are reported here, as there were no significant differences in data for PC 3, this was determined through eigenvalues, variance and manual observation of the data.

Principal component analysis (PCA) was used to analyse the ions identified with time of flight secondary ion mass spectrometry (ToF-SIMS) on four different locations along each of the JFTOT tubes, observed in Figure 6.8. There were areas of analysis acquired from the visibly uncontaminated area on the tubes and another two points in the visibly carbonaceous deposited regions on the tubes, specific analysis area are highlighted by blue squares shown in Figure 6.8. These areas were then divided into four regions of interest for enabling the assessment of reproducibility. The PCA was performed on the SIMS data in order to identify the largest significant differences in ion intensities for the two different regions. This assessment is therefore to provide an overview of the three JFTOT tubes 1-3, comparing the contaminated areas against the visibly uncontaminated area on the tubes. The differences between the two regions has been shown, as the next section will investigate further.

Figure 6.8 summarises the positive and negative ions collectively found in the two different regions for the three JFTOT tubes, these assignments were made with SurfaceLab 6 library. The assignments were made with the best statistical confidence of the library and own judgement. The visually non-contaminated area on the left in Figure 6.8 was where the fuel first comes into contact with the tube. It is in this area that siloxanes [204-207] and larger hydrocarbons have been deposited, however, not in large enough quantities for there to be any visible deposit. As the fuel continued along the tube the deposit was laid down and became thicker and more carbonaceous in appearance. The hydrocarbon ions that were found in this area are smaller as the fuel begins to break down. The deposited region identified the following ions:  $K^+$ ,  $Ca^+$  and  $Na^+$  based,  $PO_x^-$ ,  $SO_x^-$  and nitrogen containing ions such as  $CNO^-$  and  $CN^-$ . All of these ions have been previously reported by Barker *et al.* [37, 39]. Nitrogen species has been previously reported to come from diesel fuel [208]. Further investigation between the three tubes was required to identify the different ions associated with the different fuel sources.

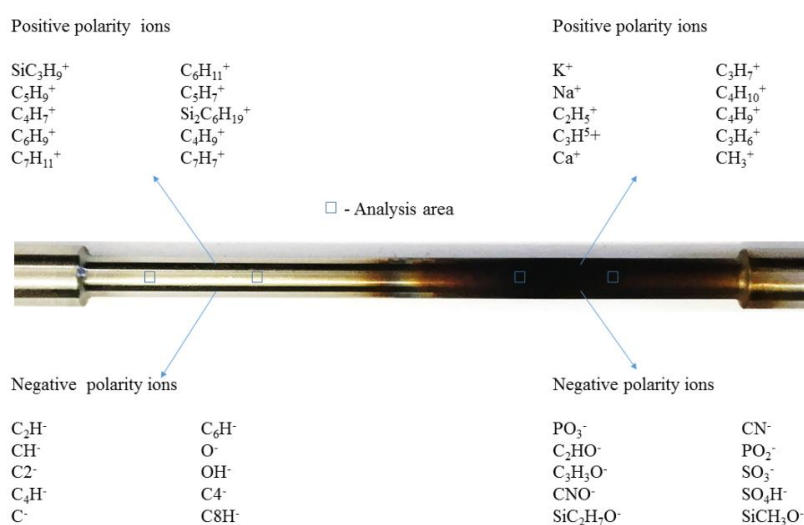


Figure 6.8. Showing the overall ions found in the PCA analysis of the two visibly different regions along the JFTOT tubes.

### 6.2.7.1 Principal Component Analysis of Deposits on JFTOT Tubes

This work identified the collective differences between the two regions on the three JFTOT tubes, this demonstrates that different chemistries are forming along the tube, as reported by Sander and Lacey *et al.* [46, 210]. The next progression of this work is to identify the differences and/or similarities between the deposits formed on the tube from the three different test conditions of using B20 and ULSD on the JFTOT tubes. Analysis of the deposited region on the tubes (two analysis areas on right) shows differences in chemistry for the three JFTOT tubes, observed in Figure 6.9 and Figure 6.10. For this the two analysis areas in the deposited area were cut into four regions of interest. Only PC 1 and PC 2 are reported here, as there were little to no trends in the data, this was determined through eigenvalues and manual observation of the data.

#### 6.2.7.1.1 Positive Ion PC 1

Figure 6.9 shows the data for PC 1 and PC 2 for the positive ion data of the JFTOT tubes. The PC 1 data shows that JFTOT 2 has a positive score which correlated to higher intensities of  $\text{Ca}^+$  and  $\text{K}^+$  ions, which shows that ULSD could cause alkali and alkali earth metal deposits. The JFTOT 3 tube has a negative score on PC 1, from Figure 6.9ii it can be observed that the ions identified as negative loadings were  $\text{SiC}_3\text{H}_9^+$  and  $\text{Si}_2\text{C}_6\text{H}_{19}^+$ , which are polysiloxanes [211]. This was not to be expected, as JFTOT 3 has chemistry on the tube that neither indicates chemistry of JFTOT 1 or JFTOT 2. Therefore a combination of B20 biodiesel and ULSD used for JFTOT 3 could cause a process of forming more deposited polysiloxanes on the surface than on just

JFTOT 1 or JFTOT 2. The masses that have positive and negative loadings for PC 1 and PC 2 are assigned in Table 6.2.

#### 6.2.7.1.2 Positive Ion PC 2

The data collected for PC 2, shown in Figure 6.9, indicates that there was negligible difference between JFTOT 2 and JFTOT 3. The analysis areas for JFTOT 1, which was fuelled with B20 biodiesel, split with the first area that was analysed (JFTOT 1-1) showing higher levels of  $\text{Na}^+$ , displayed in Figure 6.9ii. The area of higher intensity of  $\text{Na}^+$  ions was likely to be the region where the fuel reached optimal temperature for the  $\text{Na}^+$  species to deposited, Lacey *et al.* reported sodium depositing at 140 °C. The profilometry work from section 6.2.2 discussed different colouration along the JFTOT tubes and it was speculated that this could be due to different chemistry. The split of JFTOT 1-1 and JFTOT 1-2 indicate that there is instability and different degradation points along the tube.

The ions that score negative for PC 2, which were JFTOT 1-1 and JFTOT 3-2, were at the later contact point on the tube and the ions were assigned to be  $\text{K}^+$ ,  $\text{SiC}_3\text{H}_9^+$  and  $\text{Si}_2\text{C}_6\text{H}_{19}^+$  ions. It can be concluded that these ions are more thermally stable or soluble in the fuel than sodium species. JFTOT 3 has identified higher intensity for polysiloxanes [204-207] on the surface of the tube than JFTOT 1 and JFTOT 2. The JFTOT 3 deposit did not show specific chemistry that match either of the other samples. Therefore it could be concluded that both the biodiesel B20 RME and ULSD were contributing to create the deposit on JFTOT 3 and there is an interaction or 'washing' process of the two fuels.

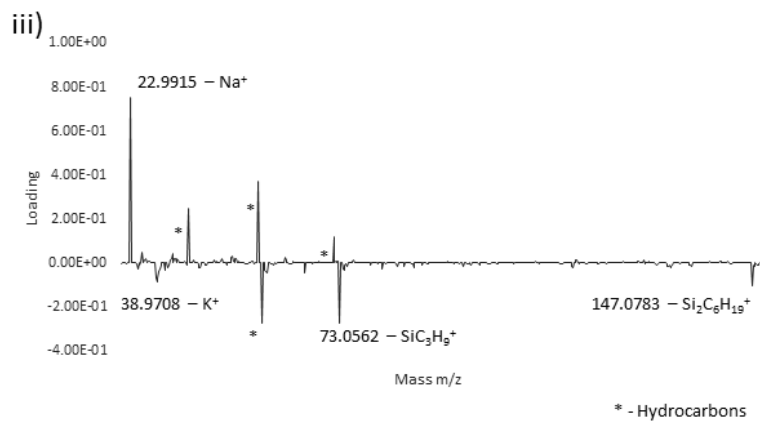
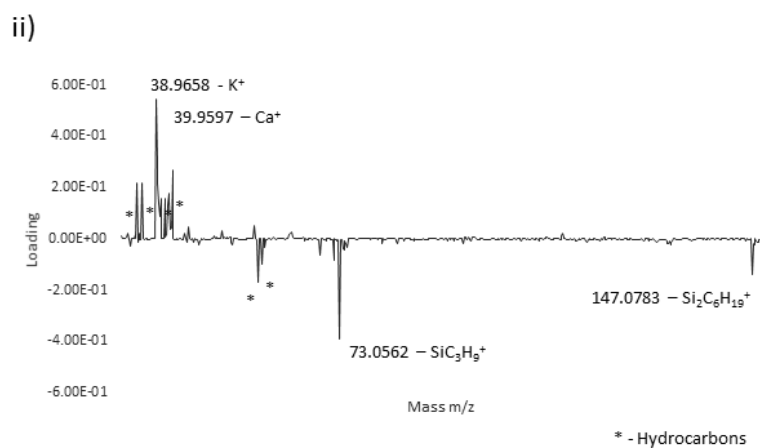
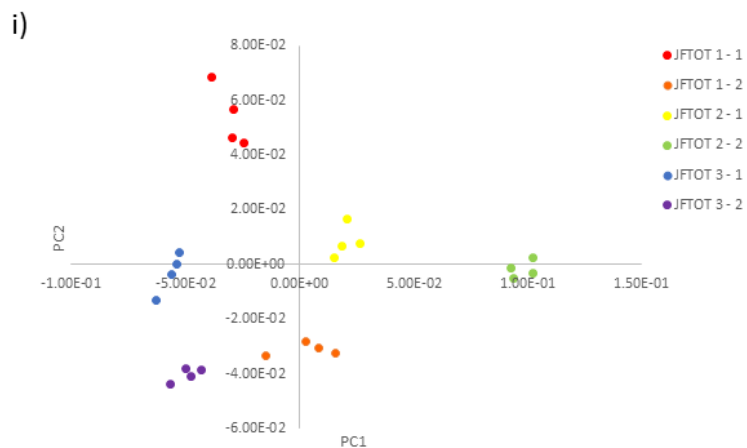


Figure 6.9. Positive ion data of JFTOT tubes 1-3, B20, ULSD and MIX. i) Showing scores of PC1 and PC2 ii) loadings on PC1 and assigned ions iii) loading on PC2 and assigned ions.

Table 6.2 Mass assignments for positive ion data of JFTOT tubes 1-3 showing PC 1 and PC 2 positive and negative loadings.

PC 1			PC 2		
Mass	Positive Loading	Assignment	Mass	Positive Loading	Assignment
<b>38.97</b>	5.45E-01	K <sup>+</sup>	<b>22.99</b>	0.750869	Na <sup>+</sup>
<b>41.03</b>	2.69E-01	C <sub>3</sub> H <sub>5</sub> <sup>+</sup>	<b>57.07</b>	0.371151	C <sub>4</sub> H <sub>9</sub> <sup>+</sup>
<b>27.02</b>	2.19E-01	C <sub>2</sub> H <sub>3</sub> <sup>+</sup>	<b>43.05</b>	0.247968	C <sub>3</sub> H <sub>7</sub> <sup>+</sup>
<b>29.04</b>	2.17E-01	C <sub>2</sub> H <sub>5</sub> <sup>+</sup>	<b>71.09</b>	0.119285	C <sub>5</sub> H <sub>11</sub> <sup>+</sup>
<b>39.96</b>	1.59E-01	Ca <sup>+</sup>			

PC 1			PC 2		
Mass	Negative Loading	Assignment	Mass	Negative Loading	Assignment
<b>74.01</b>	-4.38E-02	SiC <sub>3</sub> H <sub>10</sub> <sup>+</sup>	<b>38.97</b>	-0.08883	Ca <sup>+</sup>
<b>69.01</b>	-6.46E-02	C <sub>5</sub> H <sub>9</sub> <sup>+</sup>	<b>147.07</b>	-0.1048	Si <sub>2</sub> C <sub>6</sub> H <sub>19</sub> <sup>+</sup>
<b>71.09</b>	-8.29E-02	C <sub>5</sub> H <sub>11</sub> <sup>+</sup>	<b>73.05</b>	-0.27277	SiC <sub>3</sub> H <sub>9</sub> <sup>+</sup>
<b>58.07</b>	-9.79E-02	C <sub>4</sub> H <sub>10</sub> <sup>+</sup>	<b>58.07</b>	-0.27462	C <sub>4</sub> H <sub>10</sub> <sup>+</sup>
<b>147.07</b>	-1.37E-01	SiC <sub>6</sub> H <sub>19</sub> <sup>+</sup>			
<b>57.07</b>	-1.69E-01	C <sub>4</sub> H <sub>9</sub> <sup>+</sup>			
<b>73.05</b>	-3.91E-01	SiC <sub>3</sub> H <sub>9</sub> <sup>+</sup>			

#### 6.2.7.1.3 Negative Ion PC 1

The negative loading for PC 1 is assigned as CN<sup>-</sup> and polysiloxanes found in higher intensity on JFTOT 2 and JFTOT 3, which is indicative that these chemistries are coming from ULSD. The JFTOT 1 deposit was positive on PC 1 and assigned as hydrocarbons, namely C<sup>-</sup>, C<sub>4</sub>H<sup>-</sup> and C<sub>5</sub>H<sub>7</sub>O<sup>-</sup>, observed in Figure 6.10ii. The masses that have positive and negative loadings for PC 1 and PC 2 are assigned in Table 6.3.

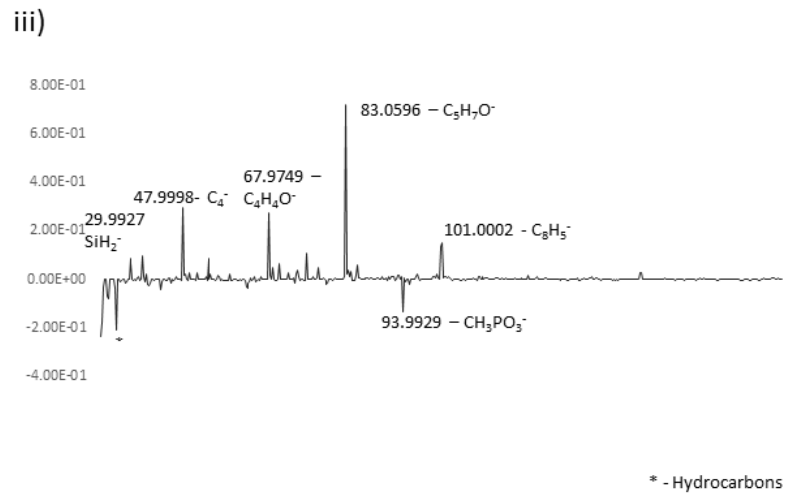
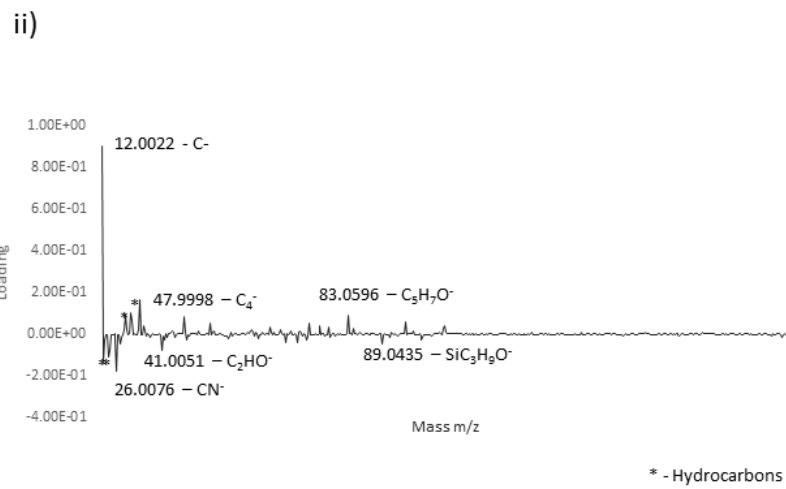
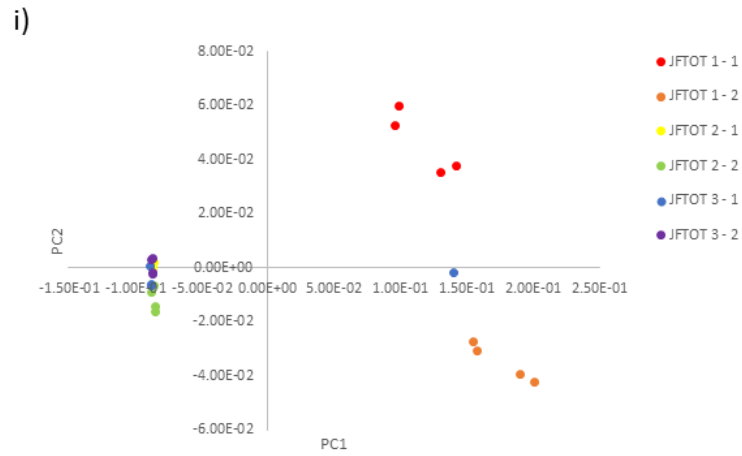


Figure 6.10. Negative ion data of JFTOT tubes 1-3, B20, ULSD and MIX. i) Showing scores of PC1 and PC2 ii) loadings on PC1 and assigned ions iii) loading on PC2 and assigned ions.

#### 6.2.7.1.4 Negative Ion PC 2

The data from PC 2 with regards to JFTOT 1 suggests that the deposit is not uniform and some chemistries in the fuel will deposit faster than others, likely due to thermal stability and solubility. The analysis for JFTOT 1 split along PC 2, the analysis points JFTOT 1-1 has a positive score and has been assigned as hydrocarbons and  $C_5H_7O^-$ ,  $C_4H_4O^-$  and  $C_{12}H_7O^-$ . The  $C_5H_7O^-$ ,  $C_4H_4O^-$  and  $C_{12}H_7O^-$  ions are presumed to arise from the degradation of the ester bond in the RME biodiesel. The analysis points from JFTOT 1-2 identify that the ions were phosphates, suggesting phosphate ions are more stable components within the fuel.

*Table 6.3 Mass assignments for negative ion data of JFTOT tubes 1-3 showing PC 1 and PC 2 positive and negative loadings.*

PC 1			PC 2		
Mass	Positive Loading	Assignment	Mass	Positive Loading	Assignment
<b>12.00</b>	0.90169	$C^-$	<b>83.05</b>	0.722065	$C_5H_7O^-$
<b>31.99</b>	0.167821	$O_2^-$	<b>48.00</b>	0.29507	$C_4^-$
<b>29.97</b>	0.104089	$SiH_2^-$	<b>67.97</b>	0.275995	$C_4H_4O^-$
<b>27.98</b>	0.091055	$Si^-$	<b>101.00</b>	0.15332	$C_8H_5^-$
<b>83.05</b>	0.088549	$C_5H_7O^-$	<b>75.95</b>	0.109287	$C_5O^-$
<b>47.99</b>	0.085534	$C_4^-$	<b>34.97</b>	0.098962	$Cl^-$
<b>93.99</b>	0.058874	$Si_2H_6O_2^-$	<b>55.96</b>	0.089704	$SiCO^-$
<b>75.95</b>	0.053021	$C_5O^-$	<b>29.99</b>	0.066726	$SiH_2^-$

PC 1			PC 2		
Mass	Negative Loading	Assignment	Mass	Negative Loading	Assignment
<b>89.04</b>	-0.04732	$SiC_3H_9O^-$	<b>15.99</b>	-0.07053	$O^-$
<b>41.00</b>	-0.07818	$C_2OH^-$	<b>17.00</b>	-0.07874	$OH^-$
<b>17.00</b>	-0.07965	$OH^-$	<b>167.04</b>	-0.10263	$C_{12}H_7O^-$
<b>15.99</b>	-0.10981	$O^-$	<b>93.99</b>	-0.13038	$CH_3PO_3^-$
<b>13.00</b>	-0.12714	$CH^-$	<b>13.00</b>	-0.17509	$CH^-$
<b>25.00</b>	-0.17799	$C_2H^-$	<b>25.00</b>	-0.20917	$C_2H^-$
			<b>12.00</b>	-0.23548	$C^-$

The positive and negative ion data show that the JFTOT 1 deposit has more variation than the deposits analysed on JFTOT 2 and 3 (as illustrated by their tight grouping in Figure 6.10ii). Conversely, there is a clear difference in chemistry along JFTOT 1, indicating that there are different degradation points to biodiesel as it flows through the JFTOT equipment.

## **6.2.8 PCA of ToF-SIMS Data Comparing JFTOT Tubes to Failed Injector Needles from the Field**

The differences between the deposited regions on the JFTOT tubes has been investigated in section 6.2.7. However, a comparison between the JFTOT deposits and IDIDs. By comparing IDIDs to JFTOT deposits it can be observed if chemistries from biodiesel or ULSD are seen in these deposits and then identify which fuels have been used. In this section PCA is applied to the three JFTOT tubes and the eight injector needles that were analysed in Chapter 5 section 5.2.2, details of the needles can be found the methodology section 2.1.1.

### *6.2.8.1 Positive Ion PC 1*

The positive ion data that compared needles 1-8 and JFTOT tubes 1-3 shows that needle 3 is outlying from the data, observed in Figure 6.1i. This was previously seen in Chapter 5 section 5.2.2.1. The difference is due to an increased detection of sodium species on needle 3. The other needles and JFTOT tube 1-3 score similarly, with the JFTOT tubes scoring the lowest on PC 1, shown in Figure 6.11ii. This would indicate that sodium species do not enter the fuel line through fresh fuel, it is a contaminant that is picked up along the lifespan of the fuel. Sodium has been regularly identified in the literature

and it has been speculated that it was picked up [46, 67, 82]. This is the first example of a JFTOT deposit being compared to field injector deposits.

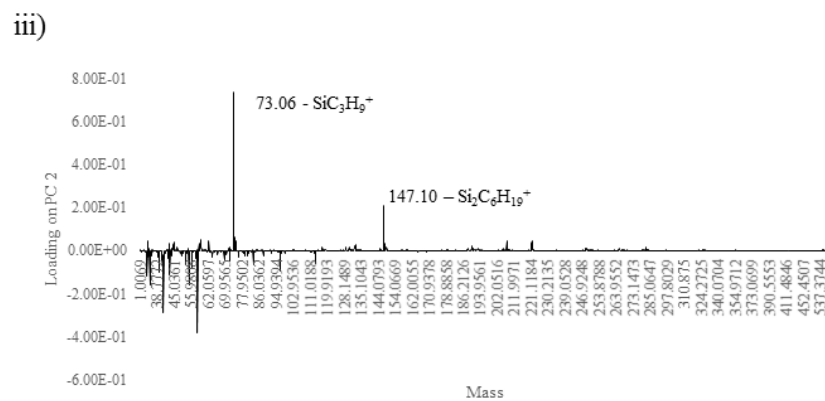
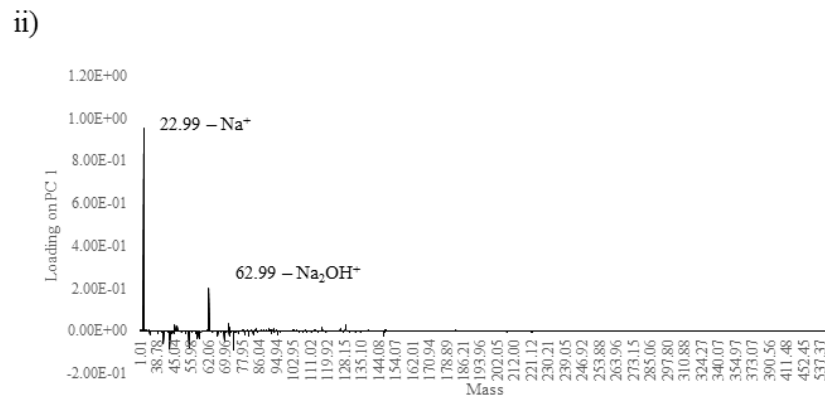
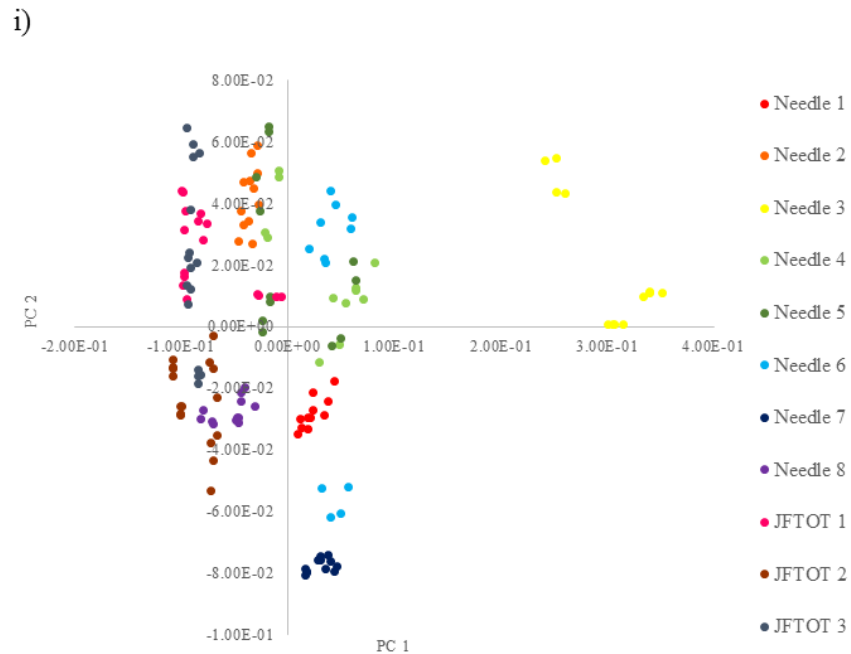


Figure 6.11 Positive ion data of needles 1- 8 and JFTOT tubes 1-3, i) Showing scores of PC1 and PC2 ii) loadings on PC1 and assigned ions iii) loading on PC2 and assigned ions.

### 6.2.8.2 Positive Ion PC 2

The analysis of PC 2 indicates that needles 2, 4, 5 and JFTOT 1 scored positively with Needle 6 and JFTOT 3 splitting along PC2, the assignment is as increased intensity for polysiloxane species [204-207], shown in Figure 6.11iii. Needles 1, 7 and 8 and JFTOT 2 scored negatively for PC 2 and this was identified to be due to hydrocarbons, the mass assignments can be observed in Table 6.4.

*Table 6.4 Mass assignments for positive ion data of needle 1-8 and JFTOT tubes 1-3 showing PC 1 and PC 2 positive and negative loadings.*

PC 1			PC 2		
Mass	Positive Loading	Assignment	Mass	Positive Loading	Assignment
<b>22.99</b>	0.955028	Na <sup>+</sup>	<b>73.06</b>	0.734706	SiC <sub>3</sub> H <sub>9</sub> <sup>+</sup>
<b>62.98</b>	0.202474	Na <sub>2</sub> OH <sup>+</sup>	<b>147.01</b>	0.207073	Si <sub>2</sub> C <sub>6</sub> H <sub>19</sub> <sup>+</sup>
			<b>74.07</b>	0.062595	SiC <sub>3</sub> H <sub>10</sub> <sup>+</sup>
			<b>59.04</b>	0.051475	C <sub>4</sub> H <sub>11</sub> <sup>+</sup>
			<b>62.98</b>	0.046988	Na <sub>2</sub> OH <sup>+</sup>
			<b>75.01</b>	0.045901	SiC <sub>2</sub> H <sub>7</sub> O <sup>+</sup>
			<b>221.02</b>	0.044274	Si <sub>3</sub> C <sub>7</sub> H <sub>21</sub> O <sub>4</sub> <sup>+</sup>
			<b>27.98</b>	0.043414	C <sub>2</sub> H <sub>3</sub> <sup>+</sup>
			<b>207.05</b>	0.042996	Si <sub>3</sub> C <sub>5</sub> H <sub>15</sub> O <sub>3</sub> <sup>+</sup>

PC 1			PC 2		
Mass	Negative Loading	Assignment	Mass	Negative Loading	Assignment
<b>147.01</b>	-0.02712	Si <sub>2</sub> C <sub>6</sub> H <sub>9</sub> <sup>+</sup>	<b>83.01</b>	-0.06481	C <sub>6</sub> H <sub>11</sub> <sup>+</sup>
<b>81.07</b>	-0.02732	C <sub>6</sub> H <sub>9</sub> <sup>+</sup>	<b>56.05</b>	-0.0769	C <sub>4</sub> H <sub>8</sub> <sup>+</sup>
<b>67.05</b>	-0.02805	C <sub>5</sub> H <sub>7</sub> <sup>+</sup>	<b>97.01</b>	-0.09624	C <sub>7</sub> H <sub>13</sub> <sup>+</sup>
<b>57.07</b>	-0.03433	C <sub>4</sub> H <sub>9</sub> <sup>+</sup>	<b>39.02</b>	-0.09945	K <sup>+</sup>
<b>58.07</b>	-0.03502	C <sub>4</sub> H <sub>10</sub> <sup>+</sup>	<b>43.05</b>	-0.10939	C <sub>3</sub> H <sub>7</sub> <sup>+</sup>
<b>69.07</b>	-0.04906	C <sub>5</sub> H <sub>9</sub> <sup>+</sup>	<b>27.02</b>	-0.12089	C <sub>2</sub> H <sub>3</sub> <sup>+</sup>
<b>41.03</b>	-0.05953	C <sub>3</sub> H <sub>5</sub> <sup>+</sup>	<b>55.05</b>	-0.15895	C <sub>4</sub> H <sub>7</sub> <sup>+</sup>
<b>43.05</b>	-0.0851	C <sub>3</sub> H <sub>7</sub> <sup>+</sup>	<b>29.03</b>	-0.15947	C <sub>2</sub> H <sub>5</sub> <sup>+</sup>
<b>55.05</b>	-0.08584	C <sub>4</sub> H <sub>7</sub> <sup>+</sup>	<b>41.03</b>	-0.28797	C <sub>3</sub> H <sub>5</sub> <sup>+</sup>
<b>73.06</b>	-0.0926	SiC <sub>3</sub> H <sub>9</sub> <sup>+</sup>	<b>57.07</b>	-0.38398	C <sub>4</sub> H <sub>9</sub> <sup>+</sup>

#### 6.2.8.3 Negative Ion PC 1

The negative ion data shows increased intensities of nitrogen species, specifically  $\text{CN}^-$  and  $\text{CNO}^-$ , for needles 1, 2, 4, 6, 7 and 8. The JFTOT tubes scored low for nitrogen species, this provides evidence that nitrogen does not enter through the fuel, and it must be via another source. Needles 3, 5 and JFTOT 1-3 scored negatively which suggested the presence of nitrogen species was low and that there were higher intensities of smaller ions such as  $\text{C}^-$ ,  $\text{CH}^-$ ,  $\text{C}_2^-$ ,  $\text{O}^-$  and  $\text{OH}^-$ .

#### 6.2.8.4 Negative Ion PC 2

The PC 2 information for the negative ion score data is shown in Figure 6.12iii. The data shows that small ions such as  $\text{CH}^-$ ,  $\text{C}_2\text{H}^-$ ,  $\text{C}^-$  and nitrogen species were found on needles 1, 3, 6, 7 and JFTOT 2, with partial points from needles 4, 5 and JFTOT 3, due to a positive scoring on PC 2. There were higher intensities of phosphates, sulfates and polysiloxanes ions found on needles 2, 8 and JFTOT 1 [204-207].

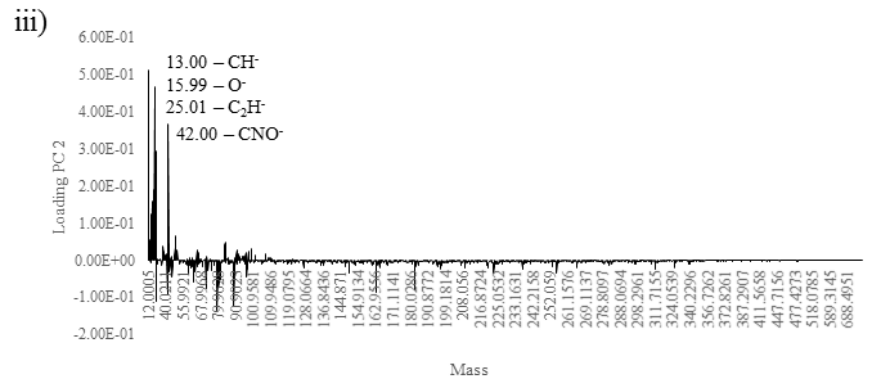
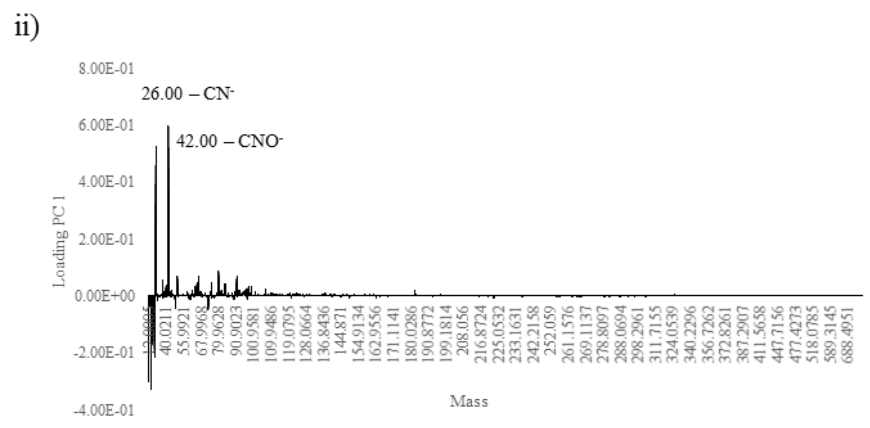
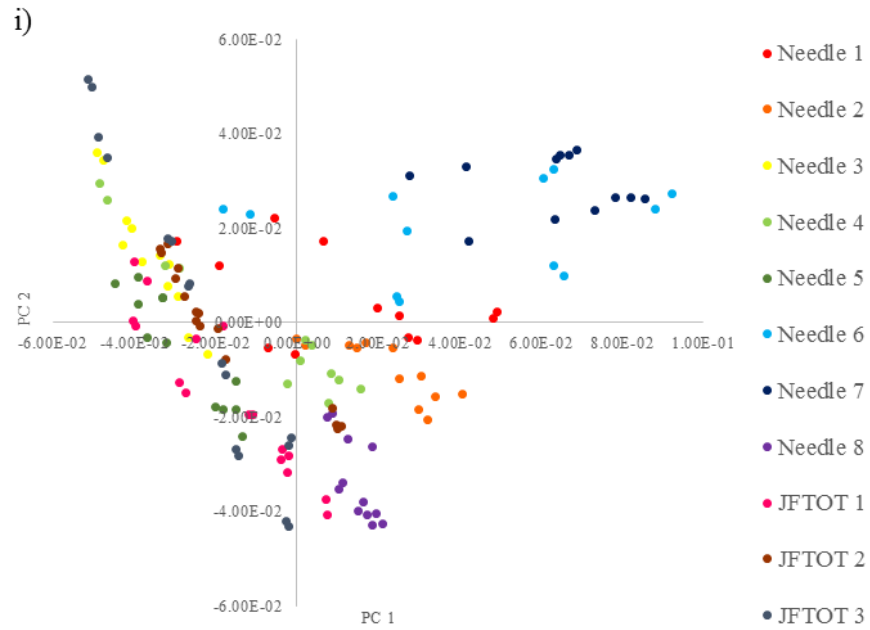


Figure 6.12 Negative ion data of Needles 1- 8 and JFTOT tubes 1-3, i) Showing scores of PC1 and PC2 ii) loadings on PC1 and assigned ions iii) Loading on PC2 and assigned ions

Table 6.5 Mass assignments for negative ion data of needle 1-8 and JFTOT tubes 1-3 showing PC 1 and PC 2 positive and negative loadings

PC 1			PC 2		
Mass	Positive Loading	Assignment	Mass	Positive Loading	Assignment
42.00	0.598849	CNO <sup>-</sup>	13.00	0.511281	CH <sup>-</sup>
26.00	0.525747	CN <sup>-</sup>	25.00	0.466476	C <sub>2</sub> H <sup>-</sup>
79.96	0.087051	SO <sub>3</sub> <sup>-</sup>	42.00	0.365307	CNO <sup>-</sup>
66.00	0.071227	C <sub>3</sub> NO <sup>-</sup>	26.00	0.293714	CN <sup>-</sup>
50.00	0.068695	C <sub>4</sub> H <sub>2</sub> <sup>-</sup>	24.00	0.190856	C <sub>2</sub> <sup>-</sup>
90.99	0.067337	C <sub>7</sub> H <sub>7</sub> <sup>-</sup>	12.00	0.185015	C <sup>-</sup>
			17.00	0.157586	OH <sup>-</sup>
			15.99	0.124636	O <sup>-</sup>
			49.00	0.066957	C <sub>4</sub> H <sup>-</sup>
			14.01	0.056606	CH <sub>2</sub> <sup>-</sup>
			83.97	0.048917	SiC <sub>3</sub> H <sub>4</sub> O <sup>-</sup>

PC1			PC 2		
Mass	Negative Loading	Assignment	Mass	Negative Loading	Assignment
24.00	-0.08677	C <sub>2</sub> <sup>-</sup>	45.00	-0.04422	CHO <sub>2</sub> <sup>-</sup>
12.00	-0.11073	C <sup>-</sup>	96.96	-0.04453	C <sub>8</sub> H <sup>-</sup>
17.00	-0.16816	OH <sup>-</sup>	81.03	-0.05181	SO <sub>3</sub> H <sup>-</sup>
25.00	-0.21599	C <sub>2</sub> H <sup>-</sup>	62.97	-0.05858	SO <sub>2</sub> <sup>-</sup>
13.00	-0.30113	CH <sup>-</sup>	79.96	-0.0746	SO <sub>3</sub> <sup>-</sup>
15.99	-0.32701	O <sup>-</sup>	71.02	-0.0752	C <sub>3</sub> H <sub>3</sub> O <sub>2</sub> <sup>-</sup>
			183.01	-0.07826	C <sub>8</sub> H <sub>7</sub> SO <sub>3</sub> <sup>-</sup>
			163.07	-0.08594	SiC <sub>9</sub> H <sub>11</sub> O <sup>-</sup>
			41.01	-0.09235	C <sub>2</sub> OH <sup>-</sup>
			26.01	-0.10925	C <sub>2</sub> H <sub>2</sub> <sup>-</sup>
			89.04	-0.12544	SiC <sub>3</sub> H <sub>6</sub> O <sup>-</sup>
			78.96	-0.13473	PO <sub>3</sub> <sup>-</sup>

#### 6.2.8.5 Comparison of IDIDs to JFTOT Deposits

The JFTOT tubes scored within similar ranges to the IDIDs in the PCA data.

The biggest difference was that the JFTOT tubes have the lowest intensities of sodium species, observed in Figure 6.11i. However, this was not a huge

difference with needle 8 scoring particularly close. With the exception of the sodium species there was no obvious difference to the chemistry detected on the JFTOT tubes. For the positive ion data, the JFTOT tubes were most similar to needles 2 and 8 for PC1. For positive ion PC 2 JFTOT 2 was most similar to needles 1 and 8. Whilst JFTOT 1 and 3 were similar to needles 2, 3, 4 and 6. The negative ion data shows that for PC 1 the JFTOT chemistry was most similar to needles 3 and 5. For PC 2 JFTOT 1 was similar to needle 8. There were a range of similarities for the JFTOT tubes but no distinct alignment to one needle. This is to be expected as the injector needles were unlikely to only have one fuel type. This work shows that the chemistry identified on the JFTOT tubes is comparable to the chemistry on the injector needles. This work suggests that the JFTOT method is therefore a viable tool in future work of creating pseudo diesel injector deposits for subsequent study and analysis.

### **6.3 Conclusions**

Profilometry and SEM images of the three JFTOT tubes fuelled with different fuel stocks shows visual and chemical differences in the formed deposits, demonstrating a variation in topography and roughness.

Analysis of the JFTOT tubes with ToF-SIMS demonstrate that different chemistries of deposits forming along the tubes, which correlate to different temperatures experienced. This was also suspected from the colour variation observed in the profiles in section 6.2.2.

Fluorescence from the deposits prevented usable data to be collected, shown in section 6.2.5.1, therefore it is suspected that fuel is having an effect on the fluorescence formation. On removal of fluorescence with HyPy the  $I_D/I_G$  ratios were between 0.29 – 0.49, JFTOT 2 fuelled with

ULSD had the lowest  $I_D/I_G$  ratio and therefore the greatest graphitic content. The  $I_D/I_G$  ratios of JFTOT 1 and 3 are most similar to  $I_D/I_G$  ratios measured in the IDIDs of Chapter 4. The GC-MS data collected on thermal treatment of the samples shows that biodiesel and ULSD contribute different chemistries to deposit formation, therefore providing evidence that different deposit mechanisms are occurring and there could be a number of factors that contribute to formation.

ToF-SIMS analysis of the JFTOT tubes was compared to failed field injector needles and shows similar chemistries. The JFTOT can reliably create pseudo diesel injector deposits that mimic failed engine deposits. Therefore this is a viable test method for creating lab scale deposits and creating future work of doping the fuel used with suspect deposit precursors.

## 7 Conclusions

Analysis of IDIDs has been shown to be challenging due to the nature of the deposit. The samples had little information known about them with regards to lifetime, fuel samples and driving conditions. This has resulted in it being difficult to correlate the chemistries uncovered in the deposit to a specific source. Further work is required to analyse more controlled samples to identify the similarities and differences in chemistry. This could be utilising the JFTOT with base fuel and then doping in identified deposit precursors.

For this work, analysis of IDIDs was carried out with a range of analytical methods, including SEM EDX, TEM, computed tomography, AFM, FIB-SIMS, profilometry, hydrolysis, GC-MS and Raman spectroscopy.

Chemical analysis of the IDIDs was considered of high importance and this aided in prioritising which techniques to further explore. The combination of FIB and ToF-SIMS was considered to be the most successful method to use for analysis IDIDs. FIB has successfully been applied to IDIDs to manipulate the surface structure to reveal the lower layers. The application explored creating lift outs and found that creating trenches was the optimum analysis method. A trench provides a larger surface area to analyse and reduce risks associate with milling a lift out, such as breakage of the porous material of the IDIDs.

The combination of FIB and SIMS have shown that the deposits from injector 4 was a three layered structure, which had previously been suspected by Barker *et al.* from the depth profiling work. Furthermore, the combination of HyPy, GC-MS and Raman spectroscopy was useful in breaking the deposit down into volatiles and labile fraction to further understand the deposit formation.

Other methods of analysis used were profilometry, AFM, SEM/EDX and TEM, these were considered of less importance to the analysis method due to the information collected. Profilometry has been deemed more useful than AFM due to analysing a larger surface area, however, neither provided chemical analysis of the IDIDs. Other techniques provide limited chemical information including SEM and computed tomography. The applications of Raman, FIB and ToF-SIMS showed great potential for analysing the complex structures by analysing the lower levels and giving chemical information. A key focus to this research was to begin understanding the deposit mechanism of formation. For the injector needle it is suspected that a lacquering forms first which is indicative of a colourful layer and then if this has not caused the engine to stick then carbonaceous material can form on top. The layering structure of IDIDs suggests that there is a formation process, the solubilising ability of the fuel is a key parameter to the deposits mechanism and there is a washing and depository effect occurring until the maximum tolerance is reached.

This work has provided a comprehensive analysis of IDIDs from the field, engine tests and laboratory scale testing, and has given novel insight into the complex process of formation. The aim of this work has been proven by the combination of FIB-SIMS proving that there is a layering structure occurring and the deposits analysed are not homogenous, this is crucial in understanding how deposits form. By identifying where the intervention points of deposition are then there is better understanding into how deposits can be mitigated, in order to create cleaner injectors which would lead to better fuel economy.

## **8 Future Work**

### **8.1 Deposit Mechanism Formation**

This work has begun a discussion of best methods for analysing deposits.

However due to the history of the sample being relatively unknown, forming a hypothesis on deposits formation is difficult. The deposits analysed here have varied in chemical and topographical composition. Further samples would need to be analysed and controlled samples created to better understand what has caused certain deposit formations.

### **8.2 Computed Tomography**

Computed tomography was used to obtain novel 3D images of the injector needle inside the injector tip, however, were unsuccessful in imaging the deposit. This could have been due to the material being too dense on the outside or due to the deposit not being thick enough. The orifice of the injector tip is extremely tight around the needle due to the pressures required for ignition of the diesel fuel, therefore it does not take large quantities to block an injector. The objective of identifying if removing the needle from the injector tip disrupts the deposits still needs to be addressed.

### **8.3 Hydropyrolysis**

The hydropyrolysis reactor has a diameter of about 1 cm, therefore only certain samples will fit. For samples such as the injector tip which would not fit, an alternative method would need to be devised. Perhaps, a method of cutting the samples or altering the reactor would need to be addressed before analysing bigger samples.

For samples that have previously experienced high temperatures, the method of thermal treatment with hydropyrolysis was adequate for removing volatile

fluorescing material. Further investigation for a new test method will be required to treat less thermally stable samples, such as fuel filters.

#### **8.4 Raman Spectroscopy**

The premise of using Raman spectroscopy was to understand the carbonaceous mechanism of formation. In theory it was thought that the longer the deposits had resided on the needle then the more graphitic content it would have. This work has compared the graphitic content of the needles to coals, biochars and soot, however, no indication as to how long the deposit has resided on the needle has been identified. Further investigation into providing evidence potentially with engine tests could estimate how much graphitic content is formed and with fuel types and/or additives promote and decelerate formation. The work from the JFTOT had suggested difference graphitic content for different fuels, however, this also needs to be explored.

#### **8.5 FIB-SIMS**

The combination of FIB-SIMS has proven to be a useful analytical tool to reach the interface between the deposit and the metal surface. Therefore continuing analysis with FIB-SIMS to analyse deposits and look at other deposits from parts of the engine will provide further knowledge of the deposit composition.

Due to the FIB procedure being destructive, it is unknown if the application of the high energy beam causes any structural alterations to the deposit. The ion beam could potentially move chemistries from the place of origin when creating a lift out or trench. This is thought to be overcome by sputtering the selected area, but could be investigated.

Profilometry can be used to analyse the depth of the analysis area created with FIB-SIMS. This has been discussed in Chapter 3, however was not implemented in Chapter 5. Profilometry could give indication of the thickness of the layers, which would overcome the measurements in SEM being incorrect due to tilting as seen in Figure 5.8.

## **8.6 JFTOT**

In order to expand on the work carried out in this thesis further JFTOT samples would be required with different conditions and doping the fuel with a range of suspected contaminations and/or additives such as varying molecular weights of PIBSI. It was suspected that from the previous work that antifoam additives could have been the cause of the initial layer of deposits. Through utilising the JFTOT, analysis could identify how antifoam behaves and if it creates a similar deposit to the one analysed from the field.

## **8.7 Blank Samples**

This research has only analysed deposited and contaminated needles and JFTOT tubes. This has been due to difficulty of acquiring a clean needle. The injection system costs over £3000, so in order to analyse a fresh needle it would be too costly. From analysing a new needle then the chemistry that is already on the needle could be identified. This was not considered a priority during this work, however, could be a consideration for future work to be sure of origin of some chemistries.

## **8.8 Other Techniques for Analysis**

### **8.8.1 X-ray Photoelectron Spectroscopy (XPS)**

Whilst ToF-SIMS is qualitative data, XPS would provide quantitative data. An instrument with an  $\text{Ar}_n^+$  cluster ion source could be used to depth profile

samples. This would make for a comparison between ToF-SIMS and XPS, to analyse the chemistries both instrument identify.

### **8.8.2 Synchrotron**

Synchrotron radiation analysis would be useful to probe the lower levels of the deposit without physically manipulating the surface of the material.

## References

1. Trobaugh, C., Burbrink, C., Zha, Y., Whitacre, S., Corsi, C., Blizard, N., *Internal Diesel Injector Deposits: Theory and Investigations into Organic and Inorganic Based Deposits*. SAE International Journal of Fuels and Lubricants, 2013. 6(3): p. 772-784.
2. Ullmann, J., Geduldig, M., Stutzenberger, H., *Investigation into the Formation and Prevention of Internal Diesel Injector Deposits*. SAE International, 2008. 01-0926.
3. Venkataraman, R., Eser, S., *Characterization of deposits formed on diesel injectors in field test and from thermal oxidative degradation of n-hexadecane in a laboratory reactor*. Chemistry Central, 2008. 2(25).
4. Barker, J., Richards, P., Snape, C., Meredith, W., *A Novel Technique for Investigating the Nature and Origins of Deposits Formed in High Pressure Fuel Injection Equipment*. SAE International, 2009. 01-2637.
5. Barker, J., Richards, P., Goodwin, M., Wooler, J., *Influence of High Injection Pressure on Diesel Fuel Stability: A study of Resultant Deposits*. SAE International, 2009. 01-1877.
6. Barker, J., Richards, P., Pinch, D., Cheeseman, B., *Temperature Programmed Oxidation as a Technique for Understanding Diesel Fuel System Deposits*. SAE International, 2010. 01-1475.
7. Richards, P., *Automotive Fuels Reference Book*. 3rd Edition ed, ed. S. international. 2014.
8. Diesel, R., *Arbeitsverfahren und Ausführungsart für Verbrennungskraftmaschinen*. Patentschrift, 1892(67207).
9. Diesel, R., *Method of igniting and regulating combustion for internal-combustion engines*. 1901, Google Patents.
10. Otto, N.A., *Improvement in gas-motor engines*. 1877, Google Patents.
11. Otto, N.A., *Nicolaus august otto*. 1887, Google Patents.
12. Swinford, S., *Diesel and petrol car ban: Plan for 2040 unravels as 10 new power stations needed to cope with electric revolution*, in *The Telegraph*. 2017, The Telegraph: <http://www.telegraph.co.uk/news/2017/07/25/new-diesel-petrol-cars-banned-uk-roads-2040-government-unveils/>.
13. Brignall, M., *Will the diesel car you are driving be worthless in five years' time?*, in *The Guardian*. 2017: <https://www.theguardian.com/money/2017/mar/04/diesel-environment-ban-tax-duty-emissions-values>.
14. United Nations. [http://unfccc.int/paris\\_agreement/items/9485.php](http://unfccc.int/paris_agreement/items/9485.php). 2016 [cited 2017 26th May].
15. Pye S., L.F.G.N., Price J., Fais B., *Achieving net-zero emissions through the reframing of UK national targets in the post-Paris Agreement era*. Nature Energy, 2017. 2(17024).
16. Ltd., I. <http://www.infineuminsight.com/insight/april-2017/lower-emissions-by-design#heading-0>. 2017 [cited 2017 23rd August].
17. Julia Kollewe, D.C., *UK new car sales speed to record high*, in *The Guardian*. 2017:

- <https://www.theguardian.com/business/2017/apr/05/uk-new-car-sales-record-tax-rates>.
18. EPA. *Regulations for greenhouse gas emissions from passenger cars and trucks*. 2017 [cited 2017 9th May].
  19. Guardian, T., *Full Text of Trump's Speech - 'Draconian' Paris accord Dump*, in *The guardian*. 2017: <https://www.theguardian.com/us-news/2017/jun/02/full-text-of-trumps-speech-draconian-paris-accord-dumped>.
  20. Vaughan, A., *UK Sets ambitious new 2030s target*, in *The Guardian*. 2016, Thw Guardian: <https://www.theguardian.com/environment/2016/jun/30/uk-sets-ambitious-new-2030s-carbon-target>.
  21. Morley, K., *Drivers of Older Diesel Cars to be Charged extra £10 to Enter London* in *The Telegraph*. 2017: <http://www.telegraph.co.uk/news/2017/02/17/drivers-older-diesel-cars-charged-extra-10-enter-london/>.
  22. Forster, K., *London toxic air alert: 'very high' pollution warning issued for the first time by Mayor of Lodn Sadiq Khan*, in *The independent*. 2017: <http://www.independent.co.uk/news/uk/home-news/london-toxic-air-alert-very-high-pollution-sadiq-khan-mayor-of-london-warning-system-latest-a7542036.html>.
  23. Mills, J. *Check if your car is effectd by the London T-charge and ultra low emission zone*. 2017 [cited 2017 9th May].
  24. Quigley, R., Barbour, R., Fahey, E., *A Study of the Internal Diesel Injector Deposit Phenomenom*, in *TAE 9th International Colloquium Fuels*. 2013: Esslingen.
  25. Ambrosio, A., Ferrari, A. , *Diesel Injector Coking: Optical-Chemical Analysis of Deposits and Influence on Injected Flow-Rate, Fuel Spray and Engine Performance*. *Journal of engineering for Gas Turbines and Power*, 2012. 134(062801-1).
  26. A.M. Liaquat, A., Masjuki, H., Kalama, M., Fazal, M. A., Abdul Faheem Khanb, Fayaz, H., Varman, M., *Impact of palm biodiesel blend on injector deposit formation*. *Applied Energy*, 2013. 11: p. 882-893.
  27. Barker, J., Richards, P., Snape, C., Meredith, W., *Diesel Injector Deposits- An issue That has Evolved with Engine Technology*. SAE International, 2011. 01-1923.
  28. Cook, S., Barker, J., Reid, J., Richards, P., *Possible Mechanism for Poor Diesel Fuel Lubricity in the Field*. SAE International, 2012. 01-0867.
  29. Arondel, M., Rodeschini, H., Lopes, M., Dequenne, B., *Fuel Additives for Reduction of Internal Diesel Injectors Deposits (IDID, 'Lacquering'): A Critical and Priority Route*. Sae International, 2012. 01-1687.
  30. ATC, *Fuel Additives: Uses and Benefits*, t.T.C.f.P.A.M.i. Europe, Editor. 2013.
  31. Patel, M., Ricardo, C. L. A., Scardi, P., Aswath, P. B., *Morphology, structure and chemistry of extracted diesel soot-Part I: Transmission electron microscopy, Raman spectroscopy, X-ray photoelectron spectroscopy and synchrotron X-ray diffraction study*. *Tribology International*, 2012. 52: p. 29-39.

32. Ribeiro, N., Pinto, A., Quintella, C., O. da Rocha, G., L. Teixeira, Guarieiro, L., Rangel, M., Veloso, M., Rezende, M., Serpa da Cruz, R., and A. de Oliveira, Torres, E., Jailson, R., Andrade, B, *The Role of Additives for Diesel and Diesel Blended (Ethanol or Biodiesel) Fuels: A Review*. American Chemical Society, 2007. 21: p. 2433-2445.
33. Richard, P., Reid, J., *The Emerging Market for Biodiesel and the Role of Fuel Additives*. SAE International, 2007. 01-2033.
34. Ullmann, J., Geduldig, M., Stutzenberger, H., Caprotti, R., *Investigation into the Formation and Prevention of Internal Diesel Injector Deposits*. SAE International, 2008. 04-14.
35. Zerda, T.W., X. Yuan, and S.M. Moore, *Effects of fuel additives on the microstructure of combustion engine deposits*. Carbon, 2001. 39(10): p. 1589-1597.
36. Barbour, R., Quigley, R., Panesar, A., Payne, J., *Finding a Solution to Internal Diesel Injector Deposits*, in *TAE 9th International Colloquium Fuels*. 2013: Esslingen.
37. Barker, J., Snape, C., Scurr, D., *Information on the Aromatic Structure of Internal Diesel injector Deposits From Time of Flight Secondary Ion Mass Spectrometry*. SAE International, 2014. 01-1387.
38. Barker, J., Snape, C., Scurr, D., *Diesel Deposits*. 9th International Colloquium Fuels Conventional Future Energy for Automobile J, 2013.
39. barker, J., Snape, C., Scurr, D., *A Novel Technique for Investigating the Characteristics and History of Deposits Formed Within High Pressure Fuel Injection Equipment*. SAE International, 2012. 01-1685.
40. Barker, J., Langley, G., Richards, P., *Insight into Deposits Formation in High Pressure Diesel Fuel INjection Equipment*. SAE International, 2010. 01-2243.
41. Diaby, M., Singhal, P., Ousmane, M., Sablier, M., Le Négrate, A., El Fassi, M., Zymła, V., *Impact factors for the degradation of engine oil causing carbonaceous deposits in the piston's grooves of Diesel engines*. Fuel, 2013. 107(0): p. 90-101.
42. Barker, J., et al., *A Novel Technique for Investigating the Nature and Origins of Deposits Formed in High Pressure Fuel Injection Equipment*. SAE Int. J. Fuels Lubr., 2009. 2(2): p. 38-44.
43. Caprotti, R., Breakspear, A., Graupner, O., Klaua, T., Kohnen, O., *Diesel Injector Deposits Potential in Future Fueling Systems*. SAE International, 2006. 2006-01-3359.
44. Ullmann, J., Geduldig, M., Stutzenberger, H., Caprotti, R., Balfour, G., *Investigation into the Formation and Prevention of Internal Diesel Injector Deposits*. SAE International, 2008. 2008-01-0926.
45. Dallanegra, R. and R. Caprotti, *Chemical Composition of Ashless Polymeric Internal Diesel Injector Deposits*. SAE International, 2014. 2014-01-2728.
46. Lacey, P., Gail, S., Grinstead, D., Daveau, C., Caprotti, R., Dallanegra, R., Pigeon, D., *Use of a Laboratory Scale Test to Study Internal Diesel Injector Deposits*. 2016, SAE International.
47. Schwab, S., Bennett, J., Dell, S., Galante-Fox, J., Kulinowski, A., Miller, K., *Internal Injector Deposits in High-Pressure Common Rail Diesel Engines*. SAE Int. J. Fuels Lubr., 2010. 3(2): p. 865-878.

48. Schwab, S., Bennett, J., Dell, S., Galante-Fox, J., Kulinowski, A., Miller, K., *Internal Injector Deposit in High-Pressure Common Rail Diesel Engines*. SAE International, 2010. 01-2242.
49. Li, H., Lea-Langton, A., Biller, P., Andrews, G. E., Hadavi, S., Charlton, A., Richard, P., *Effect of Multifunctional Fuel Additive Package on Fuel Injector Deposits, Combustion and Emissions using Pure Rape seed Oil for DI Diesel*. Sae International, 2009. 01-2642.
50. Lubrizol, *Will ULSD fuels increase injector deposits?* 2010: file:///C:/Users/enxsa23/Downloads/Lubrizol\_IDID-Deposits-Article%20rev624.pdf.
51. Quality, O.o.T.a.A., *Heavy-Duty Engine and Vehicle Standards and Highway Diesel Fuel Sulfur Control Requirements*, E.P. Agency, Editor. 2006.
52. Barker J., R.J., Angel-Smith S., Snape C., Piggott M., Fay M., Davies A., Parmenter C., Weston N., *IDIDs: internal diesel deposits*, in *TAE Esslingen*, T. Esslingen, Editor. 2017: Esslingen
53. Barker, J., S. Cook, and P. Richards, *Sodium Contamination of Diesel Fuel, its Interaction with Fuel Additives and the Resultant Effects on Filter Plugging and Injector Fouling*. SAE International Journal of Fuels and Lubricants, 2013. 6(3): p. 826-838.
54. Feld, H. and N. Oberender, *Characterization of Damaging Biodiesel Deposits and Biodiesel Samples by Infrared Spectroscopy (ATR-FTIR) and Mass Spectrometry (TOF-SIMS)*. 2016.
55. Zerda, T.W., Yuan, X., Moore, S. M., Leon y Leon, C. A., *Surface area, pore size distribution and microstructure of combustion engine deposits*. Carbon, 1999. 37(12): p. 1999-2009.
56. Lacey, P., Gail, S., Kientz, J., Milovanovic, N., Gris, C., *Internal Fuel Injector Deposits*. SAE International Journal of Fuels and Lubricants, 2011. 5(1): p. 132-145.
57. Delphi, B., Stanadyne, Denso, Continental, *Fuel Requirements for Diesel Fuel Injection Systems Diesel Fuel Injection Equipment Manufacturers Common Position Statement 2009*. 2009.
58. Muller M., C.S., Lucka K., Hoffmann H., Feldhoff S., *Future Requirements for Diesel Additives - Current Application Tests*, in *Fuels - Conventional and Future Energy for Automobiles* T. Esslingen, Editor. 2017: Esslingen Germany.
59. Barsic, N., Humke, A., *Performance and Emissions Characteristics of a Naturally Aspirated Diesel Engine With Vegetable Oil Fuels*. SAE International, 1981. 810262.
60. Clague A.D.H, D.J.B., Wang T. K., Peng J. C. M., *A comparison of diesel engine soot with carbon black*. Carbon, 1999. 37(10): p. 1553-1565.
61. Cook, S., Richards, P., *Possible Influence of High Pressure on Diesel Fuel Stability: A review and Preliminary Study*. SaE International, 2009. 01-1878.
62. Cook, S. and P. Richards, *Possible Influence of High Injection Pressure on Diesel Fuel Stability: A Review and Preliminary Study*. 2009, SAE International.
63. Hartikka, T., Kiiski, U., Kuronen, M., Mikkonen, S., *Diesel Fuel Oxidation Stability: A Comparative Study*. 2013, SAE International.

64. Shiotani, H. and S. Goto, *Studies of Fuel Properties and Oxidation Stability of Biodiesel Fuel*. 2007, SAE International.
65. Jackson, M.M., K.C. Corkwell, and C.C. DeGroot, *Study of Diesel and Ethanol Blends Stability*. 2003, SAE International.
66. Clayton, C., *IDIDs: Overview and Use of Power Ultrasound (Sonication) Model Fuel Degradation by Hydrodynamics Cavitation Within Fuel Injection Equipment*, in *TAE Esslingen*, S.G. Solutions, Editor. 2017: Esslingen Germany.
67. Barker, J., Reid, J., Snape, C., Scurr, D., Meredith, W., *Spectroscopic Studies of Internal Injector Deposits (IDID) Resulting from the Use of Non-Commercial Low Molecular Weight Polyisobutylenesuccinimide (PIBSI)*. *SAE Int. J. Fuels Lubr.*, 2014. 7(3): p. 762-770.
68. Frauscher M., D.N., Besser C., Rogner A., *Oxidation Characteristics of Fuel and Fuel Components Identified by Mass Spectrometry*, in *TAE Esslingen*. 2017, TAE: Esslingen Germany.
69. Reid, J. and J. Barker, *Understanding Polyisobutylene Succinimides (PIBSI) and Internal Diesel Injector Deposits*. 2013, SAE International.
70. de Goede, S., Barbour, R., Velaers, A., Sword, B., Burton, D., Mokheseng, K., *The Effect of Near-Zero Aromatic Fuels on Internal Diesel Injector Deposit Test Methods*. 2017.
71. Reid, J., Barker, J., *Understanding Polyisobutylene Succinimides (PIBSI) and Internal Diesel Injector Deposits* SAE International, 2013. 01-2682.
72. Ullmann, J., Stutzenberger, H., *Internal Diesel Injector Deposits Formation - Reproduction in Laboratory, System Bench and Engine Test*, in *TAE 9th International Colloquium Fuels*. 2013: Esslingen.
73. Quigley, R., Barbour, R., *Understanding the Spectrum of Diesel Injector Deposits*, in *TAE 9th International Colloquium Fuels*. 2013: Esslingen.
74. IONTOF. <https://www.iontof.com/history-ion-tof-sims.html>. 2017 [cited 2017 14th September].
75. van Duren, J.K.J., Yang, X. N., Loos, J., Bulle-Lieuwma, C. W. T., Sieval, A. B., Hummelen, J. C., Janssen, R. A. J., *Relating the morphology of poly(p-phenylene vinylene)/methanofullerene blends to solar-cell performance*. *Advanced Functional Materials*, 2004. 14(5): p. 425-434.
76. Belu, A.M., D.J. Graham, and D.G. Castner, *Time-of-flight secondary ion mass spectrometry: techniques and applications for the characterization of biomaterial surfaces*. *Biomaterials*, 2003. 24(21): p. 3635-3653.
77. Benninghoven, A., *Chemical-analysis of inorganic and organic-surfaces and thin-films by static time-of-flight secondary-ion mass-spectrometry (tof-sims)*. *Angewandte Chemie-International Edition in English*, 1994. 33(10): p. 1023-1043.
78. Pasche, S., De Paul, S. M., Voros, J., Spencer, N. D., Textor, M., *Poly(L-lysine)-graft-poly(ethylene glycol) assembled monolayers on niobium oxide surfaces: A quantitative study of the influence of polymer interfacial architecture on resistance to protein adsorption by ToF-SIMS and in situ OWLS*. *Langmuir*, 2003. 19(22): p. 9216-9225.

79. Barker, J., Snape, C., Scurr, D., *Diesel Deposits*. SAE International, 2013. 01-1517.
80. Byler, D.M. and H. Susi, *Examination of the secondary structure of proteins by deconvolved ftir spectra*. Biopolymers, 1986. 25(3): p. 469-487.
81. Barker J., R.J., *Injector and Fuel System Deposits*, in *TAE Esslingen*, TAE, Editor. 2015, TAE: Esslingen Germany.
82. Reid, J., S. Cook, and J. Barker, *Internal Injector Deposits From Sodium Sources*. 2014.
83. Rohrbaugh, W.J. and E.L. Wu, *Xrd characterization of catalyst materials*. Abstracts of Papers of the American Chemical Society, 1988. 196: p. 86-PETR.
84. Rinzler, A.G., Liu, J., Dai, H., Nikolaev, P., Huffman, C. B., Rodriguez-Macias, F. J., Boul, P. J., Lu, A. H., Heymann, D., Colbert, D. T., Lee, R. S., Fischer, J. E., Rao, A. M., Eklund, P. C., Smalley, R. E., *Large-scale purification of single-wall carbon nanotubes: process, product, and characterization*. Applied Physics a-Materials Science & Processing, 1998. 67(1): p. 29-37.
85. Saha, D. and S.G. Deng, *Structural Stability of Metal Organic Framework MOF-177*. Journal of Physical Chemistry Letters, 2010. 1(1): p. 73-78.
86. Smith, R.M., *Some applications of gc-ms in forensic laboratory*. International Laboratory, 1978(MAY-): p. 115-&.
87. Wiarda, W., R.P. de Bruijn, and G.J.Q. van der Peijl, *Analytical chemistry for environmental forensics*. Forensic Science International, 2003. 136: p. 109-110.
88. Tanaka, A., Yamada, K., Omori, T., Bunne, S., Hosokawa, K., *Inner Diesel Injector Deposit Formation Mechanism*. SAE International Journal of Fuels and Lubricants, 2013. 6(3): p. 755-761.
89. Battistoni, C., Gastaldi, L., Mattogno, G., Viticoli, S., *An xps study of layered ab2x4 semiconductors*. Surface and Interface Analysis, 1986. 9(1-6): p. 342-342.
90. Reucroft, P.J. and J.Y. Kim, *An xps study of liquefaction catalysts and catalyst impregnated coals*. Abstracts of Papers of the American Chemical Society, 1992. 203: p. 77-FUEL.
91. McArthur, S.L., *Applications of XPS in bioengineering*. Surface and Interface Analysis, 2006. 38(11): p. 1380-1385.
92. Shchukarev, A., Malekzadeh, B. O., Ransjo, M., Tengvall, P., Westerlund, A., *Surface characterization of insulin-coated Ti6Al4V medical implants conditioned in cell culture medium: An XPS study*. Journal of Electron Spectroscopy and Related Phenomena, 2017. 216: p. 33-38.
93. Cuevas, L., Herrera, M. I., Maria, I. S., Hermann, R., Luna, M., Colchero, J., Baro, A., *Surface imaging of viral architectures by three different scanning microscopies: High resolution scanning electron microscopy, high voltage scanning transmission electron microscopy and atomic force microscopy*. Electron Microscopy 1994, Vol 1: Interdisciplinary Developments and Tools, ed. B. Jouffrey and C. Colliex. 1994, Les Ulis: Editions Physique. 113-114.

94. Fourcy, A., J.P. Bossy, and C. Brambilla, *X-ray-microanalysis in transmission and scanning electron microscopies - study of human alveolar macrophages*. *Biologie Cellulaire*, 1979. 35(2): p. A2-A2.
95. MacPhee, J.A., Hutny, W. P., Giroux, L., Palmer, A. D., Price, J. T., Haythornthwaite, R. F., *Characterization of coal injection chars by thermogravimetric analysis, scanning electron and optical microscopies and surface analysis*, in *Coal Science, Vols I and II*, J.A. Pajares and J.M.D. Tascon, Editors. 1995, Elsevier Science Publ B V: Amsterdam. p. 539-542.
96. Cardenas Almena, M., Lucio Esperilla, O., Martin Manzanero, F., Murillo Duarte, Y., Quintero Toscano, L., Wolff, G., *Internal Diesel Injector Deposits: Sodium Carboxylates of C12 Succinic Acids and C16 and C18 Fatty Acids*. 2012, SAE International.
97. Rounthwaite, N., Williams, R., McGivery, C., Jiang, J., Giulliani, F., Britton, B., *A Chemical and Morphological Study of Diesel Injector Nozzle Deposits - Insights into their Formation and Growth Mechanisms*. 2017.
98. Jaclyn E. Johnson, S.H.Y., Jeffrey D. Naber, Seong-Young Lee, Gary Hunter, Russell Truemner, Tony Harcombe and *Characteristics of 3000 bar Diesel Spray Injection under Non-Vaporizing and Vaporizing Conditions* ICLASS 2012, 12th Triennial International Conference on Liquid Atomization and Spray Systems, Heidelberg, Germany, September 2-6, 2012 2012.
99. Meredith, W., C.E. Snape, and G.D. Love, *Development and Use of Catalytic Hydropyrolysis (HyPy) as an Analytical Tool for Organic Geochemical Applications*, in *Principles and Practice of Analytical Techniques in Geosciences*, K. Grice, Editor. 2015, Royal Soc Chemistry: Cambridge. p. 171-208.
100. Meredith, W., C.E. Snape, and G.D. Love, *CHAPTER 6 Development and Use of Catalytic Hydropyrolysis (HyPy) as an Analytical Tool for Organic Geochemical Applications*, in *Principles and Practice of Analytical Techniques in Geosciences*. 2015, The Royal Society of Chemistry. p. 171-208.
101. Dayton, D., Carpenter, J., Farmer, J., Turk, B., Gupta, R., *Biomass Hydropyrolysis in a Pressurized Fluidized Bed Reactor*. *Energy & Fuels*, 2013. 27(7): p. 3778-3785.
102. Meredith, W., Ascough, P. L., Bird, M. I., Large, D. J., Snape, C. E., Sun, Y., Tilston, E. L., *Assessment of hydropyrolysis as a method for the quantification of black carbon using standard reference materials*. *Geochimica et Cosmochimica Acta*, 2012. 97: p. 131-147.
103. Yang, H.P., Yan, R., Chen, H. P., Lee, D. H., Zheng, C. G., *Characteristics of hemicellulose, cellulose and lignin pyrolysis*. *Fuel*, 2007. 86(12-13): p. 1781-1788.
104. Yaman, S., *Pyrolysis of biomass to produce fuels and chemical feedstocks*. *Energy Conversion and Management*, 2004. 45(5): p. 651-671.
105. Datsyuk, V., Kalyva, M., Papagelis, K., Parthenios, J., Tasis, D., Siokou, A., Kallitsis, I., Galiotis, C., *Chemical oxidation of multiwalled carbon nanotubes*. *Carbon*, 2008. 46(6): p. 833-840.

106. Lacount, R.B., Kern, D. G., King, W. P., Miltz, D. J., Stewart, A. L., Trulli, T. K., Walker, D. K., Wicker, R. K., *Advances in coal characterization by programmed-temperature oxidation*. Abstracts of Papers of the American Chemical Society, 1991. 202: p. 58-FUEL.
107. Paryjczak, T., P. Zielinski, and W.K. Jozwiak, *Temperature programmed reduction and oxidation of ir/al<sub>2</sub>o<sub>3</sub> catalysts*. Reaction Kinetics and Catalysis Letters, 1985. 29(1): p. 167-173.
108. Barker J., S.C.E., Scurr D. J., *A novel technique for investigating the characteristics and history of deposits formed within high pressure fuel injection equipment*. SAE Int. J Fuels Lubr., 2012. 5 (3) 2012-01-1685.
109. Behrendt, C. and A. Smith, *A Study of Diesel Fuel Injector Deposit Effects on Power and Fuel Economy Performance*. 2017, SAE International.
110. Vickerman J. C., G.I., *Surface Analysis The Principle Techniques*. 2nd ed, ed. Wiley. 2009.
111. Rouessac F., R.A., *Chemical Analysis*. 2nd ed, ed. Wiley. 2007.
112. Vickerman, J.C. and D. Briggs, *TOF-SIMS: Materials Analysis by Mass Spectrometry*. 2013: SurfaceSpectra/IM Publications.
113. Thiel, V. and P. Sjoval, *CHAPTER 5 Time-of-Flight Secondary Ion Mass Spectrometry (TOF-SIMS): Principles and Practice in the Biogeosciences*, in *Principles and Practice of Analytical Techniques in Geosciences*. 2015, The Royal Society of Chemistry. p. 122-170.
114. Spool, A.M., *The Practice of TOF-SIMS: Time of Flight Secondary Ion Mass Spectrometry*. 2016: Momentum Press.
115. Fearn, S., *An Introduction to Time-of-Flight Secondary Ion Mass Spectrometry (ToF-SIMS) and its Application to Materials Science*. 2015, Morgan & Claypool Publishers.
116. McDonnell, L.A. and R.M.A. Heeren, *Imaging mass spectrometry*. Mass Spectrometry Reviews, 2007. 26(4): p. 606-643.
117. Weibel, D., Wong, S., Lockyer, N., Blenkinsopp, P., Hill, R., Vickerman, J. C., *A C-60 primary ion beam system for time of flight secondary ion mass spectrometry: Its development and secondary ion yield characteristics*. Analytical Chemistry, 2003. 75(7): p. 1754-1764.
118. Yvon, H.J., *Raman Application Note Fluorecence 01 - Raman Scattering and Fluorescence*, in <http://www.horiba.com/fileadmin/uploads/Scientific/Documents/Raman/Fluorescence01.pdf>, Horiba, Editor.
119. Tuinstra, F. and J.L. Koenig, *Raman Spectrum of Graphite*. The Journal of Chemical Physics, 1970. 53(3): p. 1126-1130.
120. Grasselli, J.G., M.K. Snavely, and B.J. Bulkin, *Applications of Raman spectroscopy*. Physics Reports, 1980. 65(4): p. 231-344.
121. Asher, S.A. and C.R. Johnson, *Raman spectroscopy of a coal liquid shows that fluorescence interference is minimized with ultraviolet excitation*. Science, 1984. 225(4659): p. 311-313.
122. Fodor, S., Rava, R., Copeland, R., Spiro, T., *H<sub>2</sub> Raman-shifted YAG laser ultraviolet Raman spectrometer operating at wavelengths down to 184 nm*. Journal of Raman Spectroscopy, 1986. 17(6): p. 471-475.

123. Asher, S.A., *UV Resonance Raman Studies of Molecular Structure and Dynamics: Applications in Physical and Biophysical Chemistry*. Annual Review of Physical Chemistry, 1988. 39(1): p. 537-588.
124. Camp Jr, C.H. and M.T. Cicerone, *Chemically sensitive bioimaging with coherent Raman scattering*. Nat Photon, 2015. 9(5): p. 295-305.
125. Ferraro, J.R., K. Nakamoto, and C.W. Brown, *Chapter 1 - Basic Theory*, in *Introductory Raman Spectroscopy (Second Edition)*. 2003, Academic Press: San Diego. p. 1-94.
126. Gardiner, D.J., *Introduction to Raman Scattering*, in *Practical Raman Spectroscopy*, D.J. Gardiner and P.R. Graves, Editors. 1989, Springer Berlin Heidelberg: Berlin, Heidelberg. p. 1-12.
127. University, C. <http://www.doitpoms.ac.uk/tlplib/raman/printall.php>. [cited 2014 18/8]; Available from: <http://www.doitpoms.ac.uk/tlplib/raman/printall.php>.
128. Zhang, S., Zeng, X. T., Xie, H., Hing, P., *A phenomenological approach for the Id/Ig ratio and sp<sup>3</sup> fraction of magnetron sputtered a-C films*. Surface and Coatings Technology, 2000. 123(2-3): p. 256-260.
129. Bokobza, L., J.-L. Bruneel, and M. Couzi, *Raman spectroscopy as a tool for the analysis of carbon-based materials (highly oriented pyrolytic graphite, multilayer graphene and multiwall carbon nanotubes) and of some of their elastomeric composites*. Vibrational Spectroscopy, 2014. 74: p. 57-63.
130. Dorner-Reisel, A., Lieberwirth, R., Svoboda, S., Günther, K., Röder, C., Himcinschi, C., Irmer, G., Weißmantel, S., *Wear behaviour of hydrogen free diamond-like carbon thin films in diesel fuel at different temperatures*. Diamond and Related Materials, 2014. 44: p. 78-87.
131. Ferrari, A.C. and J. Robertson, *Interpretation of Raman spectra of disordered and amorphous carbon*. Physical Review B, 2000. 61(20): p. 14095-14107.
132. Ferrari, A.C., *Determination of bonding in diamond-like carbon by Raman spectroscopy*. Diamond and Related Materials, 2002. 11(3-6): p. 1053-1061.
133. Ferrari, A.C. and J. Robertson, *Raman spectroscopy of amorphous, nanostructured, diamond-like carbon, and nanodiamond*. Philosophical Transactions of the Royal Society of London. Series A: Mathematical, Physical and Engineering Sciences, 2004. 362(1824): p. 2477-2512.
134. Casiraghi, C., A.C. Ferrari, and J. Robertson, *Raman spectroscopy of hydrogenated amorphous carbons*. Physical Review B, 2005. 72(8): p. 085401.
135. Ferrari, A.C., *Raman spectroscopy of graphene and graphite: Disorder, electron-phonon coupling, doping and nonadiabatic effects*. Solid State Communications, 2007. 143(1-2): p. 47-57.
136. Cançado, L.G., Jorio, A., Martins Ferreira, E. H., Stavale, F., Achete, C. A., Capaz, R. B., Moutinho, M. V. O., Lombardo, A., Kulmala, T. S., Ferrari, A. C., *Quantifying Defects in Graphene via Raman Spectroscopy at Different Excitation Energies*. Nano Letters, 2011. 11(8): p. 3190-3196.

137. Tay, B.K., Shi, X., Tan, H. S., Yang, H. S., Sun, Z., *Raman studies of tetrahedral amorphous carbon films deposited by filtered cathodic vacuum arc*. *Surface and Coatings Technology*, 1998. 105(1-2): p. 155-158.
138. Reimer, L., *Introduction*, in *Scanning Electron Microscopy: Physics of Image Formation and Microanalysis*. 1998, Springer Berlin Heidelberg: Berlin, Heidelberg. p. 1-12.
139. Goldstein, J., Newbury, D., Echlin, P., Joy, D, Lyman, C., Lifshin, E., Sawyer, L., Michael, J., *The SEM and Its Modes of Operation*, in *Scanning Electron Microscopy and X-ray Microanalysis: Third Edition*. 2003, Springer US: Boston, MA. p. 21-60.
140. Zhou, W., Apkarian, R., Wang, Z., Joy, D., *Fundamentals of Scanning Electron Microscopy (SEM)*, in *Scanning Microscopy for Nanotechnology: Techniques and Applications*, W. Zhou and Z.L. Wang, Editors. 2007, Springer New York: New York, NY. p. 1-40.
141. Joy, D.C., *SMART – a program to measure SEM resolution and imaging performance*. *Journal of Microscopy*, 2002. 208(1): p. 24-34.
142. Stokes, D., *Principles and Practice of Variable Pressure: Environmental Scanning Electron Microscopy (VP-ESEM)*. 2008: Wiley.
143. SEM. [cited 2014 18/8]; Available from: <http://nanoart21.org/sem.html>.
144. Inkson, B.J., *2 - Scanning electron microscopy (SEM) and transmission electron microscopy (TEM) for materials characterization*, in *Materials Characterization Using Nondestructive Evaluation (NDE) Methods*. 2016, Woodhead Publishing. p. 17-43.
145. Scheu, C. and W.D. Kaplan, *Introduction to Scanning Electron Microscopy*, in *In-Situ Electron Microscopy*. 2012, Wiley-VCH Verlag GmbH & Co. KGaA. p. 1-37.
146. Leonard, D.N., G.W. Chandler, and S. Seraphin, *Scanning Electron Microscopy*, in *Characterization of Materials*. 2002, John Wiley & Sons, Inc.
147. Cardell, C. and I. Guerra, *An overview of emerging hyphenated SEM-EDX and Raman spectroscopy systems: Applications in life, environmental and materials sciences*. *TrAC Trends in Analytical Chemistry*, 2016. 77: p. 156-166.
148. Abd Mutalib, M., Rahman, M. A., Othman, M. H. D., Ismail, A. F., Jaafar, J., *Chapter 9 - Scanning Electron Microscopy (SEM) and Energy-Dispersive X-Ray (EDX) Spectroscopy*, in *Membrane Characterization*. 2017, Elsevier. p. 161-179.
149. Girão, A.V., G. Caputo, and M.C. Ferro, *Chapter 6 - Application of Scanning Electron Microscopy–Energy Dispersive X-Ray Spectroscopy (SEM-EDS)*, in *Comprehensive Analytical Chemistry*, A.P.R.-S. Teresa and C.D. Armando, Editors. 2017, Elsevier. p. 153-168.
150. Orloff, J., *Focused Ion Beam Characterization Techniques*, in *Reference Module in Materials Science and Materials Engineering*. 2016, Elsevier.

151. Utlaut, M., 4 - *Focused ion beams for nano-machining and imaging A2 - Feldman, Martin*, in *Nanolithography*. 2014, Woodhead Publishing. p. 116-157.
152. Wilhelmi, O., Reyntjens, S., Van Leer, B., Anzalone, P., Giannuzzi, L., *Chapter Twenty - Focused Ion and Electron Beam Techniques*, in *Handbook of Silicon Based MEMS Materials and Technologies*. 2010, William Andrew Publishing: Boston. p. 323-325.
153. Ngo, S., Lowe, C., Lewis, O., Greenfield, D., *Development and optimisation of focused ion beam/scanning electron microscopy as a technique to investigate cross-sections of organic coatings*. *Progress in Organic Coatings*, 2017. 106: p. 33-40.
154. Mahamid, J., Schampers, R., Persoon, H., Hyman, A., Baumeister, W., Plitzko, J., *A focused ion beam milling and lift-out approach for site-specific preparation of frozen-hydrated lamellas from multicellular organisms*. *Journal of Structural Biology*, 2015. 192(2): p. 262-269.
155. Barker J., R.J., Piggott M., Fay M., Parmenter C., Davies A., Weston N., Snape C. E., Scurr D. J., Angel-Smith S., *The characterisation of Diesel Internal Injector Deposits by Focused Ion-Beam Scanning Electron Microscopy (FIB-SEM), Transmission Electron Microscopy (TEM), Atomic Force Microscopy (AFM) and Raman Spectroscopy*. *SAE Int. J Fuels Lubr.*, 2015. 2015-01-1826.
156. Hooghan, K.B.N., *Device Edits and Modifications*, in *Introduction to Focused Ion Beams: Instrumentation, Theory, Techniques and Practice*, L.A. Giannuzzi and F.A. Stevie, Editors. 2005, Springer US: Boston, MA. p. 87-106.
157. Kant, K. and D. Losic, *Focused Ion Beam (FIB) Technology for Micro- and Nanoscale Fabrications*, in *FIB Nanostructures*, Z.M. Wang, Editor. 2013, Springer International Publishing: Cham. p. 1-22.
158. Stevie, F.A., L.A. Giannuzzi, and B.I. Prenitzer, *The Focused Ion Beam Instrument*, in *Introduction to Focused Ion Beams: Instrumentation, Theory, Techniques and Practice*, L.A. Giannuzzi and F.A. Stevie, Editors. 2005, Springer US: Boston, MA. p. 1-12.
159. Brocks, J., Love, Gordon D., Snape, C., Logan, G., Summons, R., Buick, R., *Release of bound aromatic hydrocarbons from late Archean and Mesoproterozoic kerogens via hydrolysis*. *Geochimica et Cosmochimica Acta*, 2003. 67(8): p. 1521-1530.
160. Septon, M., Meredith W., Sun C-G., Snape C., *Hydrolysis as a preparative method for compound specific carbon isotope analysis of fatty acids*. *Rapid Comm. in Mass Spectrometry*, 2005. 19: p. 323-325.
161. Ascough, P.L., Bird, M. I., Brock, F., Higham, T. F. G., Meredith, W., Snape, C., Vane, C. H., *Hydrolysis as a new tool for radiocarbon pre-treatment and the quantification of black carbon*. *Quaternary Geochronology*, 2009. 4(2): p. 140-147.
162. Rombola, A., Fabbri, D., Meredith, W., Snape, C., Dieguez-Alonso, A., *Molecular characterization of the thermally labile fraction of biochar by hydrolysis and pyrolysis-GC/MS*. *Journal of Analytical and Applied Pyrolysis*, 2016. 121: p. 230-239.

163. Hübschmann, H.J., *Handbook of GC/MS: Fundamentals and Applications*. 2009: Wiley.
164. Gilbert, J., McCaskill, D., Fishman, V., Brzak, K., Markham, D., Bartels, M., Winniford, B., Bano Mohsin, S., Godbey, J., Akinbo, O., Lewer, P., *Industrial Applications of High-Resolution GC/MS*. *Comprehensive Analytical Chemistry*, 2013. 61: p. 403-429.
165. Grayson, M.A., *A History of Gas Chromatography Mass Spectrometry (GC/MS)*, in *The Encyclopedia of Mass Spectrometry*. 2016, Elsevier: Boston. p. 152-158.
166. Hedden, P., *The Use of Combined Gas Chromatography-Mass Spectrometry in the Analysis of Plant Growth Substances*, in *Gas Chromatography/Mass Spectrometry*, H.F. Linskens and J.F. Jackson, Editors. 1986, Springer Berlin Heidelberg: Berlin, Heidelberg. p. 1-22.
167. Hussain S. Z., M.K., *GC-MS: Principle, Technique, and its Application in Food Science*. *INT J CURR SCI*, 2014. 13(E 166-126).
168. Athanasiou, L.S., D.I. Fotiadis, and L.K. Michalis, *6 - Plaque Characterization Methods Using Computed Tomography*, in *Atherosclerotic Plaque Characterization Methods Based on Coronary Imaging*. 2017, Academic Press: Oxford. p. 115-129.
169. Ying, X., N.J. Barlow, and M.H. Feuston, *Chapter 63 - Micro-Computed Tomography and Volumetric Imaging in Developmental Toxicology A2 - Gupta, Ramesh C*, in *Reproductive and Developmental Toxicology (Second Edition)*. 2017, Academic Press. p. 1183-1205.
170. Heverhagen, J.T., *Chapter 16 - Physics of Computed Tomography Scanning A2 - Newton, Herbert B*, in *Handbook of Neuro-Oncology Neuroimaging (Second Edition)*. 2016, Academic Press: San Diego. p. 145-149.
171. Lin, S.-H., K.C. Chen, and Y.K. Yang, *Chapter 90 - Single-Photon-Emission Computed Tomography Studies with Dopamine and Serotonin Transporters in Opioid Users A2 - Preedy, Victor R*, in *Neuropathology of Drug Addictions and Substance Misuse*. 2016, Academic Press: San Diego. p. 966-973.
172. T., B., *Introduction*, in *Computed Tomography: From Photon Statistics to Modern Cone-Beam CT*. 2008, Springer Berlin Heidelberg: Berlin, Heidelberg. p. 1-13.
173. Walther, T., *Chapter 4 - Transmission Electron Microscopy of Nanostructures*, in *Microscopy Methods in Nanomaterials Characterization*. 2017, Elsevier. p. 105-134.
174. Tang, C.Y. and Z. Yang, *Chapter 8 - Transmission Electron Microscopy (TEM)*, in *Membrane Characterization*. 2017, Elsevier. p. 145-159.
175. Instruments, Z., *Zeta-20 Optical Profiler*, Z.O.M. PDF, Editor. 2012.
176. Koch, C., *Conventional and Advanced Electron Transmission Microscopy*, in *In-Situ Electron Microscopy*. 2012, Wiley-VCH Verlag GmbH & Co. KGaA. p. 39-69.
177. D. Suneel, S.A.P. *Nanotechnology*. 2017 [cited 2017 9th September].
178. Sahoo, P., *1 - Surface topography A2 - Davim, J. Paulo*, in *Tribology for Engineers*. 2011, Woodhead Publishing. p. 1-32.

179. Mani, G., 2 - *Surface properties and characterization of metallic biomaterials A2 - Wen, Cuie*, in *Surface Coating and Modification of Metallic Biomaterials*. 2015, Woodhead Publishing. p. 61-77.
180. Bert, J.A. and L.J. Painter, *JFTOT - A New Fuel Thermal Stability Test (A Summary of Coordinating Research Council Activity)*. 1973, SAE International.
181. Clark, R.H. and L. Thomas, *An Investigation of the Physical and Chemical Factors Affecting the Performance of Fuels in the JFTOT*. 1988, SAE International.
182. Datschefski, G. and T.G.R. Farthing, *Evaluation of JFTOT Tube Deposits by Carbon Burnoff*. 1985, SAE International.
183. Kendall, D.R. and J.S. Mills, *The Influence of JFTOT Operating Parameters on the Assessment of Fuel Thermal Stability*. 1985, SAE International.
184. Pidol, L., Starck, L, Jeuland, N., Allouche, Y., *Selection of the Most Promising Alternative Fuels for Aircraft Development: ALFA-BIRD Proposal*. 2011, SAE International.
185. Belian, T.C. and B.K. Bailey, *Automotive/Fuel Cooperative Research - Past, Present and Future*. 2000, SAE International.
186. Henderson, H.T. and A.C. Nixon, *New Techniques for Measurement of Jet Fuel System Deposits*. 1970, SAE International.
187. Dam, C.Q., Long, M.C., Shafer, S.F., Tomaseski, J.E., *Thin film coating for fuel injector components*. 2004, Google Patents.
188. He, J., Hsieh, C., Wu, Y., Schmelzer, T., Wang, P., Lin, Y., Marko, M., Sui, H., *Cryo-FIB specimen preparation for use in a cartridge-type cryo-TEM*. *Journal of Structural Biology*, 2017. 199(2): p. 114-119.
189. Sanna, M. and M. Medda, *FIB/TEM analysis supported by  $\mu$ -probing approach to identify via marginality*. *Microelectronics Reliability*, 2012. 52(9): p. 2050-2053.
190. Soldati, A., Baqué, L., Troiani, H., Cotaro, C., Schreiber, A., Caneiro, A., Serquis, A., *High resolution FIB-TEM and FIB-SEM characterization of electrode/electrolyte interfaces in solid oxide fuel cells materials*. *International Journal of Hydrogen Energy*, 2011. 36(15): p. 9180-9188.
191. Bailey, S., *A Study of Polyisobutylene and its Derivatives at High Temperatures*, in *Chemical Engineering*. 2016, Nottingham University.
192. Snape, C., Axelson, D., Botto, R., Delpuech, J., Tekely, P., Gerstein, B., Pruski, M., Maciel, G., Wilson, M., *Quantitative reliability of aromaticity and related measurements on coals by  $^{13}\text{C}$  n.m.r. A debate*. *Fuel*, 1989. 68(5): p. 547-548.
193. Ulyanova, E.V., et al., *Fine structure of Raman spectra in coals of different rank*. *International Journal of Coal Geology*, 2014. 121: p. 37-43.
194. S., Z., *Fatty acid patterns of phospholipids and lipopolysaccharides in the characterisation of microbial communities in soil: a review*. *Biol Fertil Soils* 1999. 29: p. 111- 129.
195. Lloyd M. Wenger, C.L.D., Joseph M. Evensen, James R. Gormly, Paul J. Mankiewicz, *Impact of modern deepwater drilling and testing fluids*

- on geochemical evaluations. *Organic Geochemistry* 2004. 35: p. 1527-1535.
196. Uguna, C., Carr, A., Snape, C., Meredith, W., *Retardation of oil cracking to gas and pressure induced combination reactions to account for viscous oil in deep petroleum basins: Evidence from oil and n-hexadecane pyrolysis at water pressures up to 900 bar.* *Organic Geochemistry*, 2016. 97: p. 61-73.
  197. Tariq, M., et al., *Identification, FT-IR, NMR (1H and 13C) and GC/MS studies of fatty acid methyl esters in biodiesel from rocket seed oil.* *Fuel Processing Technology*, 2011. 92(3): p. 336-341.
  198. Meredith, W., et al., *The use of model compounds to investigate the release of covalently bound biomarkers via hydropyrolysis.* *Organic geochemistry*, 2006. 37(12): p. 1705-1714.
  199. Schaffer, M., Mahamid, J., Engel, B., Laugks, T., Baumeister, W., Plitzko, J., *Optimized cryo-focused ion beam sample preparation aimed at in situ structural studies of membrane proteins.* *Journal of Structural Biology*, 2017. 197(2): p. 73-82.
  200. Tuccitto, N., Giambianco, N., Marletta, G., Licciardello, A., *ToF-SIMS investigation of FIB-patterning of lactoferrin by using self-assembled monolayers of iron complexes.* *Applied Surface Science*, 2008. 255(4): p. 1075-1078.
  201. Hayashi, S., Takahashi, T., Kanehashi, K., Kubota, N., Mizuno, K., Kashiwakura, S., Sakamoto, T., Nagasaka, T., *Chemical state of boron in coal fly ash investigated by focused-ion-beam time-of-flight secondary ion mass spectrometry (FIB-TOF-SIMS) and satellite-transition magic angle spinning nuclear magnetic resonance (STMAS NMR).* *Chemosphere*, 2010. 80(8): p. 881-887.
  202. Sui, T., Song, B., Dluhos, J., Lu, L., Korsunsky, A., *Nanoscale chemical mapping of Li-ion battery cathode material by FIB-SEM and TOF-SIMS multi-modal microscopy.* *Nano Energy*, 2015. 17: p. 254-260.
  203. Priebe, A., G. Audoit, and J.-P. Barnes, *A novel PFIB sample preparation protocol for correlative 3D X-ray CNT and FIB-TOF-SIMS tomography.* *Ultramicroscopy*, 2017. 173: p. 10-13.
  204. Oran U., U.E., Wirth T., Unger W.E.S., *Poly-Dimethyl-Siloxane (PDMS) contamination of Polystyrene (PS) Oligomers Samples: A Comparison of Time-of-Flight Static Secondary Ion Mass Spectrometry (ToF-SSIMS) and X-ray Photoelectron Spectroscopy (XPS) Results.* *Applied Surface Science*, 2004. 227(1): p. 318-324.
  205. Vickerman J. C., B.D., Henderson A., *The Static SIMS Library.* Surface Spectra Manchester 1997.
  206. Delcorte A., B.S., Poleuris C., Troosters M., *Improvement of Metal Adhesion to Siliconfilms: A ToF-SIMS Study.* *Adhesion Aspects of Thin Films*, 2004. 2: p. 155-166.
  207. S, K. *Multiwalled Carbon Nanotube Forest grown Via Chemical Vapour Deposition from Iron Catalyst Nanoparticles by ToF-SIMS.* *Surface Science Spectra*, 2015. 22(29).
  208. Link, D.D., J.P. Baltrus, and P. Zandhuis, *Isolation and Identification of Nitrogen Species in Jet Fuel and Diesel Fuel.* *Energy & Fuels*, 2007. 21(3): p. 1575-1581.

209. Velaers, A.J. and S. de Goede, *The Properties and Injector Nozzle Fouling Performance of Neat GTL and GTL/EN590 Diesel Blends in Various Diesel Engines*. 2012.
210. Sander Z.H., *Heat Transfer Fluid Dynamics, and Auto-oxidation Studies on th Jet Fuel Thermal Oxidation Tester (JFTOT)*, in *Mechanical Engineering*. December 2012, University of Dayton.
211. Valantin, C., Benoit, R., D, M. P., Lacroix, F., Gomez, E., Phalip, P., Morcel, J., Tricoche, D., Hocine, N., *SEM-EDX analysis and TOF-SIMS 3D imaging of a textile/rubber interface undergoing fatigue loading*. *Applied Surface Science*, 2016. 360: p. 623-633.